Large deformation shear and elongation rheology of polymers for electrospinning and other Industrial Processes

Deepak Ahirwal

Large Deformation Shear and Elongation Rheology of Polymers for Electrospinning and other Industrial Processes

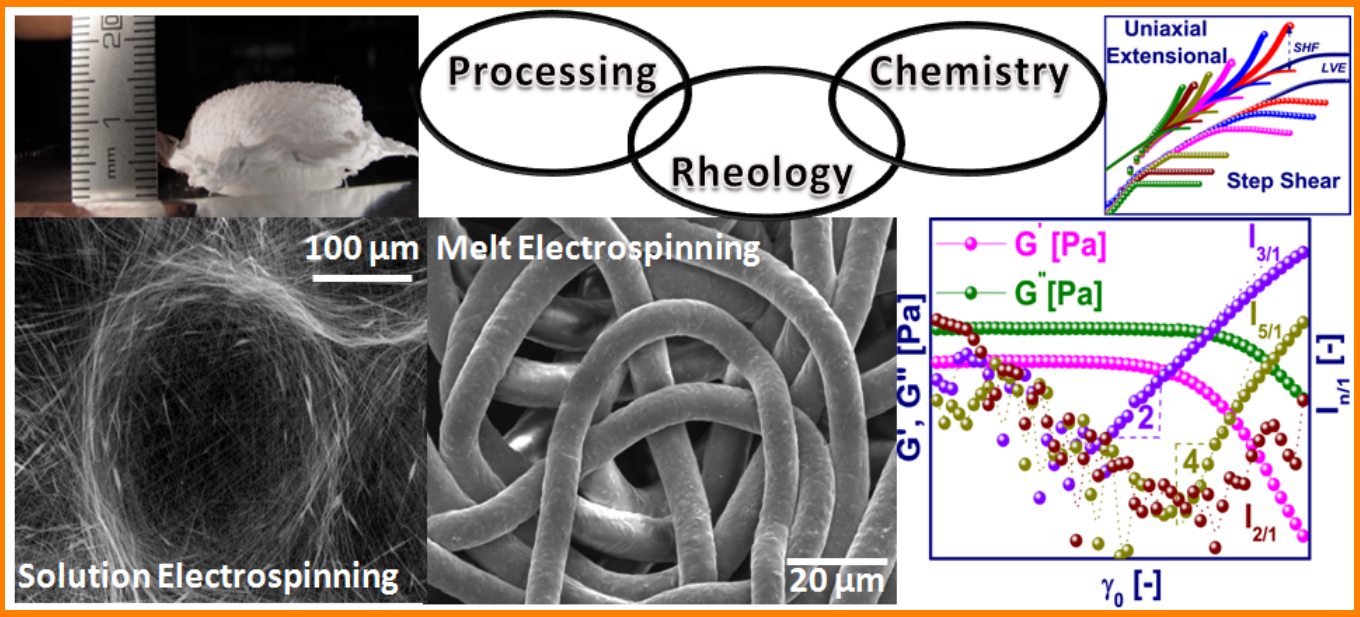

Deepak Ahirwal

UNIVERSITÉ DE STRASBOURG

Karlsruhe Institute of Technology

December 2013

Large Deformation Shear and Elongation Rheology of Polymers for Electrospinning and other Industrial Processes

A thesis submitted for the degree of

Doctor of Engineering

University of Strasbourg, France

&

Karlsruhe Institute of Technology, Germany

DISSERTATION

Deepak Ahirwal

Directors of Thesis:

Prof. Guy Schlatter

Prof. Manfred Wilhelm

External Examiners:

Prof. Frédric Bossard

Prof. Christian Friedrich

Internal Examiner:

Prof. Norbert Willenbacher

Karlsruhe, 2013

Résumé

Les objectifs de cette thèse concernent la caractérisation des polymères à l'état fondu via la rhéologie non linéaire dans les modes de cisaillement ou en élongationnel et les procédés faisant intervenir de fortes élongations tel que l'électrospinning en voie solvant et en voie fondue. Pour atteindre le premier objectif, nous nous sommes concentrés sur la caractérisation des polymères fondus enchevêtrés dans les régimes viscoélastiques linéaires et non linéaires. L'influence de la masse moléculaire, M_w et de sa distribution MWD, la présence de longues chaînes branchées (LCB) ou encore l'addition de nanoparticules dans la matrice de polymère à l'état fondu ont été étudiées en utilisant des techniques rhéologiques en cisaillement et en élongationnel. Dans le cas des écoulements de cisaillement oscillatoires à grandes amplitudes (LAOS), nous avons proposé de nouveaux paramètres mécaniques qui ont permis de définir les relations structure-propriétés des différents systémes étudiés.

Pour étudier l'influence de la masse moléculaire, des polystyrène (PS) monodisperse atactique ont été synthétisés par voie anionique. Les mesures de cisaillement oscillant ont été effectuées à petites et grandes déformations. La contrainte résultante en grandes déformations a été analysée par la méthode de rhéologie par transformation de Fourier (FT). Dans le régime viscoélastique linéaire, la viscosité au plateau de cisaillement, η_0, a été mesurée et utilisée pour caractériser les effets des enchevêtrements sur le poids moléculaire. En outre, les propriétés viscoélastiques linéaires des PS à l'état fondu ont été simulées à l'aide du modéle de Likthmann-McLeish. Pour le régime viscoélastique non linéaire, un nouveau paramètre non linéaire, caractérisant la non-linéarité à taux de cisaillement nul, μ_0, a été introduit. Ce nouveau paramètre présente une plus grande sensibilité à la masse moléculaire que η_0. En outre, les propriétés viscoélastiques non-linéaires ont été simulées en utilisant le modéle de Giesekus. Pour étudier l'influence de la distribution du poids moléculaire, des mélanges de PS monodisperses ont été préparés. Dans le régime viscoélastique linéaire, le comportement qualitatif des modules élastique et visqueux en fonction de la fréquence de sollicitation [$G'(\omega)$ et $G''(\omega)$] était similaire pour les mélanges et les PS

monodisperses. Cependant, deux pics distincts attribués des dynamiques de relaxation des chaînes de polymère ont été observés dans le cas des spectres du paramètre non linéaire $Q_0(\omega)$ obtenu par FT. Il a été conclu que le paramètre viscoélastique non linéaire, $Q_0(\omega)$, est plus sensible à la distribution de masse moléculaire que les paramètres obtenus généralement par viscoélasticité linéaire. Pour étudier l'influence des ramifications le long des chaînes de polyméres, des mélanges de polyoléfines ramifiées linéaires et branchées ont été utilisés. Pour les expériences de cisaillement oscillatoire en petites et grandes déformations, la contrainte normale a été mesurée en plus de la contrainte de cisaillement. De nouveaux paramètres ont été introduits via l'analyse par rhéologie par transformation de Fourier FT et par la méthode de décomposition de la contrainte (SD). En outre, des mesures d'extension uniaxiale ont été effectuées et comparées aux résultats de simulation obtenus par le modèle de fonction de contrainte moléculaire (MSF). Différents comportements ont été observés pour les mélanges de polyéthylènes branchés (PE) et de polypropylènes branchés (PP). L'utilisation des nouveaux paramètres décrits dans le présent travail permettent une meilleure compréhension de la relation structure- propriété des matériaux industriels présentant des taux de branchement (LCB) différents. Pour étudier l'influence de l'ajout de nanoparticules (nanotubes de carbone) dans une matrice polymère, des mélanges de polyéthylène (PE) et des nanotubes de carbone (CNT) ont été préparés en utilisant un processus en deux étapes pour une dispersion uniforme de particules. Les mesures ont été effectues en petites et grandes déformation sous écoulement de cisaillement oscillatoire. La formation d'un réseau de percolation des CNT a été étudiée dans les deux régimes viscoélastiques linéaires et non linéaires. Un minimum est observé lorsque la non-linéarité intrinsèque, Q_0, est tracée en fonction de la fraction en masse ϕ_w des nanotubes (MWCNT). Ce minimum correspond au seuil de percolation pour les composites PE / MWCNTs. La formation du réseau de percolation a présenté une forte incidence sur le régime viscoélastique non linéaire par rapport au régime viscoélastique linéaire. Ainsi, le tracé de la courbe $Q_0(\phi_w)$ fournit une meilleure sensibilité pour la détection du seuil de percolation par rapport aux méthodes décrivées des mesures en viscoélasticité linéaire.

Le second objectif de la thèse a concerné le procédé d'électrospinning permettant l'élaboration d'échafaudages (scaffolds) nano/micro-fibreux trouvant des applications dans le domaine de l'ingénierie tissulaire. Nous avons étudié le procédé en voie solution et en voie fondue. Ce procédé, visant à former les nanofibres sous l'action d'un champ électrostatique intense, est généralement reconnu pour obtenir des scaffolds de faible épaisseur (pas plus de 100 microns). Cependant, pour certaines applications, telle que la régénération osseuse, il est nécessaire de faire des scaffolds nanofibreux ayant une épaisseur de l'ordre du cm et présentant des pores de grandes tailles per-

mettant une infiltration des cellules osseuses. Nous avons démontré pour la première fois la capacité de produire par électrospinning des mousses de poly(ϵ-caprolactone) nanofibreuses dont l'épaisseur est de l'ordre du cm. Ces échafaudages ont été obtenus grâce à l'auto-assemblage dynamique des nanofibres sous la forme de motifs en nid d'abeille. Ceci entrane une structuration hiérarchique dans l'épaisseur du scaffold sous la forme de colonnes poreuses dont la taille varie de quelques microns à quelques centaines de microns. Nous avons aussi montré que cette morphologie colonnaire spécifique conduit à des propriétés mécaniques adaptée à la manipulation et à l'implantation in vivo. Pour atteindre notre objectif final, un procédé original permettant l'électrospinning en voie fondue, et donc sans solvant, a été développé. Ceci a été motivé par le fait que la présence de solvant résiduel, même l'état de trace, peut affecter la croissance cellulaire dans le cas d'applications pour l'ingénierie tissulaire. Avec le nouveau dispositif, il a été possible de fabriquer des scaffolds sans solvant. L'influence des divers paramètres de procédé sur le diamètre des fibres et la morphologie des scaffolds a été étudiée. La tension appliquée a été identifié comme le paramètre le plus important qui influe sur le diamètre de la fibre. La température du collecteur, a quant à lui, affecté la morphologie globale des scaffolds. En particulier, des morphologies à porosité ouverte tout à fait originales ont pu être développées grâce au contrôle de la rupture des fibres au moment de leur dépôt sur le collecteur.

Zusammenfassung

Die Ziele dieser Doktorarbeit sind die Charakterisierung von Polymerschmelzen durch die Benutzung von hauptsächlich nichtlinearen scherrheologischen und Dehnrheologischen Techniken, die Herstellung von „Gewebegersten“ mit hervorragenden physikalischen und mechanischen Eigenschaften mit Hilfe des Lösungs-Elektrospinnen, um dies bei der Gewebekonstruktion anzuwenden, und die Entwicklung eines Schmelzen-Elektrospinn Aufbaus zur Herstellung von lösungsmittelfreien „Gewebegerüsten“.

Um das erste Ziel zu erreichen, fokussierten wir uns auf die Charakterisierung von verzweigten Polymerschmelzen im linear und nicht-linearem viskoelastischen Bereich. Der Einfluss von dem Molekulargewicht M_w der Molekulargewichtverteilung (MWD), der Langkettenverzweigung (LCB) und das Hinzufgen von Partikel zur Polymermatrix auf die Eigenschaften der Polymerschmelzen wurde untersucht mittels von scherrheologischen und dehnrheologischen Techniken. Die resultierenden Struktur-Eigenschaft Beziehungen wurden etabliert durch die Benutzung von neu eingeführten mechanischen Parametern in oszillierenden Scherströmungen mit großer Amplitude (LAOS).

Um den Einfluss des Molekulargewichts festzustellen wurden anionisch synthetisierte monodisperse ataktische Polystyrol (PS) schmelzen gewählt. Oszillatorische Schermessungen wurden bei kleinen und großen Deformationen durchgeführt. Die Antwort der Schubspannung bei großen Deformationen wurde analysiert mit der bekannten Technik der Fourier Transformations (FT) Rheologie. Im linear viskoelastischen Bereich wurde die Null-Scherraten-Viskosität η_0 gemessen und benutzt, um den Effekt der Verzweigungen auf das Molekulargewicht zu analysieren. Im Weiteren wurden die linear viskoelastischen Eigenschaften der PS-schmelzen mit Hilfe des Likthmann-McLeish Modells simuliert. Im nichtlinearen viskoelastischen Bereich wurde ein neuer nichtlinearer Materialparameter die Null-Scherraten Nichtlinearitt μ_0 eingeführt. Dieser neue Materialparameter zeigte eine größere Sensitivität bezüglich des Molekulargewichts relativ zu η_0.

Weiterhin wurden die nichtlinearen viskoelastischen Eigenschaften mittels des Giesekus Models simuliert. Um den Einfluss der Molekulargewichtsverteilung zu untersuchen wurden Mischungen von monodispersen PS durch Mischen in Lösung hergestellt. Im linear viskoelastischen Bereich war das qualitative Verhalten des linearen dynamischen Spektrums [$G'(\omega)$ und $G''(\omega)$] der Mischungen hnlich wie das der monodispersen PS schmelzen. Jedoch wurden zwei klare Frequenzspitzen welche zu den Kettendynamiken der langen und der kurzen Ketten gehören im nichtlinearen Frequenzspektrum $Q_0(\omega)$ beobachtet. Daraus wurde gefolgert, dass der nicht-lineare viskoelastische Materialparameter $Q_0(\omega)$ mehr sensitiver ist bezüglich der Unterscheidung zwischen monodispersen PS Schmelzen und binären Mischungen von PS Schmelzen verglichen mit anderen linearen viskoelastischen Materialparametern. Um den Einfluss der Langkettenverzweigung zu untersuchen wurden Mischungen von linearen und langkettenverzweigte Polyolefine benutzt. Bei oszillierenden Scherströmungen mit kleiner und großer Amplitude wurden auch die Normalspannung zusätzlich zu den Schubspannungen gemessen. Neue Materialparameter wurden eingeführt basierend auf der FT-Rheologie und der Spannungszerlegung (Stress Decomposition SD) Analyse der Normal- und Schubspannungsmessungen. Desweiteren wurden einachsige Dehnungsmessungen durchgeführt und verglichen mit Simulation mit dem Molecular Stress Function (MSF) Modell. Es wurden verschiedene Verhalten beobachtet für PE und PP Mischungen, von welchen angenommen wird, dass sie von den verschiedenen Arten der Langkettenverzweigung (LCB) der jeweiligen Systeme stammen. Die Verwendung der in dieser Arbeit vorgeschlagenen und beschriebenen Materialparameter hat das Potential ein besseres Verständnis der Struktur-Eigenschaft Beziehungen in industriellen LCB Materialien zu ermöglichen.

Um den Einfluss des HHinzufügens von Nanopartikeln (Kohlenstoffnanoröhrchen) zur Polymermatrix zu untersuchen, wurden Mischungen von Polyethylen (PE) und Kohlenstoffnanorhrchen (CNT) mittels eines zwei Stufen Prozesses, um eine gleichmäßige Verteilung der Partikel zur gewährleisten, hergestellt. Oszillatorische Schermessungen wurden bei kleinen und großen Deformationen durchgefhrt. Die Formierung von Perkolation Netzwerken wurde in beiden im linearen und im nichtlinearen viskoelastischen Bereich studiert. Ein Minimum wurde beobachtet wenn die intrinsische Nichtlinearität Q_0 als eine Funktion des Massenanteils an Vielwandigen Kohlenstoffnanorhrchen (MWCNTs) ϕ_w aufgetragen wurde. Dieses Minimum von $Q_0(\phi_w)$ korrespondiert mit der Perkolationgrenze der PE/MWCNT's Gemische. Die Entwicklung des Perkolationsnetzwerkes scheint einen groen Effekt auf den nichtlinearen viskoelastische Bereich zu haben relativ gesehen zum linear viskoelastischen Bereich. Wir erwarten, dass die Verwendung der $Q_0(\phi_w)$

Kurve eine bessere Sensitivität bei der Detektion der Perkolationsgrenze liefern wird im Vergleich zu den linearen viskoelastischen Eigenschaften.

Um das zweite Ziel bezüglich der Herstellung von Gewebegerüste zu erreichen wurde eine einschritt Lösungs-Elektrospinntechnologie benutzt. Aus dem Elektrospinnen resultieren normalerweise Gewebegerüste die eine hundert Mikrometer dick sind und Porengrößen im Bereich von Mikrometern haben. Jedoch ist es für einige Anwendungen, Gewebeherstellung eingeschlossen, notwendig cm dicke nanofibrillen Gewebegerüste mit großen Porengrößen , welche die Infiltration von Zellen erlauben, herzustellen. Wir zeigen iin dieser Arbeit zum ersten Mal die Fähigkeit bioresorbierbare poly(ϵ- caprolacton) nanofibrille cm dicke Schäume herzustellen durch die Benutzung des Lösungselektrospinntechnik. Diese Gewebegerste wurden erhalten durch die dynamische Selbstordnung der elektrogesponnenen Nanofasern in Bienenwabenmustern, welche eine einmalige säulenartige hierachische Struktur erzeugte mit sowohl Mikroporen und Mesoporen mit bis zu einigen hundert Mikrometern Größe. Diese spezifische Morphologie hatte auch die mechanischen Eigenschaften von dicken Gewebegerüsten und war deswegen brauchbar für die Handhabung und Implantierung *in vivo*.

Um das letzte Ziel zu erreichen, wurde ein einmaliger Schmelze-Elektrospinnversuchsaufssbau entwickelt. Die Motivation Gewebegerüste ohne Lösemittel herzustellen ist hergeleitet von der Tatsache, dass für einige Anwendungen in der Gewebekonstruktion sogar die Prsenz von einigen *ppm* von restlichen Lösemittel das Wachstum von Gewebe auf den Gewebegersten beeinflussen kann. Mit dem neu entwickelten Aufbau ist es möglich Gewebegerüste ohne Lösemittel herzustellen. Der Einfluss von mannigfaltigen Prozess- und Materialparametern auf den Faserdurchmesser und die Fasermorphologie wurden untersucht. Die angelegte Spannung wurde als wichtigster Parameter identifiziert, um den Faserdurchmesser zu beeinflussen und die Kollektortemperatur hatte den größten Effekt auf die resultierende Morphologie.

Wir erwarten, dass die neu eingeführten Parameter (Null-Scherraten intrinsische Nichtlinearität durch die Analyse der oszillatorischen Schubspannung und die Null-Scherungs intrinsische Nichtlinearität berechnet aus der ersten Normalspannungsdifferenz) unter oszillierende Scherströmungen mit großer Amplitude für eine breite Menge an komplexen Fluiden benutzt werden kann. Die neue Selbstordnungstechnik, um hierarchische 3D cm dicke Gewebegerüste mittels Lösungs-Elektrospinnen herzustellen eröffnet neue Möglichkeiten für Anwendungen der Gewebekonstruk-

tion. Die ermutigenden Resultate bei der Entwicklung von lösemittelfreien Gewebegerüsten durch die Nutzung der Schmelzen-Elektrospinnentechnologie ermöglichen aufregende neue Möglichkeiten für Anwendungen bei der Gewebeherstellung.

Abstract

The goals of this thesis are the characterization of polymer melts using mainly non-linear shear and extensional rheological techniques, the fabrication of scaffolds with excellent physical and mechanical properties using the solution electrospinning technology for tissue engineering applications and the development of melt electrospinning equipment to facilitate the fabrication of solvent free scaffolds. To achieve the first goal, we focused on the characterization of entangled polymer melts in the linear and nonlinear viscoelastic regimes. The influence of molecular weight, M_w, molecular weight distribution (MWD), long-chain branching (LCB) and addition of particles to the polymer matrix on polymer melt properties were investigated using shear and extensional rheological techniques. The resulting structure-property relationships were established using newly introduced mechanical parameters under large amplitude oscillatory shear (LAOS) flow.

To investigate the influence of the molecular weight, anionically synthesized, monodisperse atactic polystyrene (PS) melts were chosen. Oscillatory shear measurements were performed at small and large deformations. The stress response at large deformation was analyzed using well established Fourier Transformation (FT) rheology technique. In the linear viscoelastic regime, the zero shear-rate viscosity, η_0, was measured and used to characterize the entanglements effects on the molecular weight. Furthermore, the linear viscoelastic properties of PS melts were simulated using the Likthmann-McLeish model. In the non-linear viscoelastic regime, a new non-linear material parameter, the zero shear-rate nonlinearity, μ_0, was introduced. This new material parameter displayed a higher sensitivity to the molecular weight relative to the η_0. Furthermore, the non-linear viscoelastic properties were simulated using the Giesekus model. To investigate the influence of molecular weight distribution, blends of monodisperse PS were prepared using solution mixing. In the linear viscoelastic regime, the qualitative behaviour of the linear dynamic frequency spectrum [$G^{'}(\omega)$ and $G^{''}(\omega)$] for the blends was similar to the monodisperse PS melts. However, two distinct peaks belonging to the large and small polymer chain dynamics were ob-

served in non-linear frequency spectrum [$Q_0(\omega)$]. It was then concluded that the non-linear viscoelastic material parameter, $Q_0(\omega)$, is more sensitive to differentiate between monodisperse PS melt and binary blends of PS melts compared to other linear viscoelastic material parameters. To investigate the influence of long-chain branching, blends of linear and long-chain branched polyolefins were used. Normal stresses were measured in addition to shear stresses at small and large deformation amplitudes under oscillatory shear flow. New material parameters were introduced based on FT-Rheology and Stress Decomposition (SD) analysis of normal and shear stress measurements. Furthermore, uniaxial extensional measurements were performed and compared to simulation results using the Molecular Stress Function (MSF) model. Different behaviours were observed for the PE and PP type blends, which are believed to arise from the different types of long chain branching (LCB) present in each of the systems. The use of the new material parameters proposed and described within the present work has the potential to allow for a better understanding of structure-property relationship in industrial LCB materials. To investigate the influence of the addition of nano-particles (carbon nanotubes) to the polymer matrix, blends of polyethylene (PE) and carbon nanotubes (CNTs) were prepared using a two-step process for a uniform dispersion of particles. The measurements were performed at small and large deformation amplitudes under oscillatory shear flow. The influence of the percolation network formation were studied in both the linear and non-linear viscoelastic regimes. A minimum is observed when the intrinsic nonlinearity, Q_0, was plotted as a function of the weight fraction of multi-walled carbon nanotubes (MWCNTs), ϕ_w. The minimum in $Q_0(\phi_w)$ corresponds to the percolation threshold for the PE/MWCNTs composites. The formation of the percolation network have large effect on the nonlinear viscoelastic regime relative to the linear viscoelastic regime . We anticipate, the use of $Q_0(\phi)$-curves will provide a better sensitivity in detecting the percolation threshold compared to other linear viscoelastic properties.

To achieve the second goal related to scaffold fabrication, single-step solution electrospinning technology was used. Electrospinning usually results in the formation of scaffolds that are a few hundred microns in thickness with pore sizes in the micron range. However for some applications including tissue engineering, it is necessary to make cm-thick nanofibrous scaffolds with large pore sizes that allow for cell infiltration. Here, we demonstrated for the first time the ability to produce of bioresorbable poly(ϵ-caprolactone) nanofibrous cm-thick foams using the solution electrospinning technique. These scaffolds were obtained through the dynamic self-assembly of electrospun nanofibers into honeycomb patterns, which resulted in a unique columnar hierarchi-

cal structure with both micropores and mesopores of up to several hundreds of microns in size. This specific morphology also had the mechanical properties of thick scaffolds and are, therfore, suitable for handling and implanting *in vivo*.

To achieve our final goal, a unique melt electrospinning set-up was developed. The motivation to fabricate the scaffolds without solvent is derived from the fact that for some applications in tissue engineering even the presence of a ppm amount of residual solvent can affect the cell culture growth on the scaffolds. With the newly developed set-up, it was possible to fabricate the scaffolds without solvent. The influence of various process and material parameters on the fiber diameter and fiber morphology were investigated. The applied voltage was identified as the most important parameter influencing the fiber diameter. The collector temperature had the largest effect on the resulting morphology.

We anticipate, the new introduced parameters (zero shear-rate intrinsic nonlinearity calculated by the analysis of oscillatory shear stress, and zero strain intrinsic nonlinearity calculated by the analysis of first normal stress difference) under large amplitude oscillatory shear flow can be applied to the wide range of complex fluids. The novel self-assembling technique to fabricate the hierarchical 3-dimensional cm-thick scaffolds using solution electrospinning opens up new possibilities for tissue engineering applications. The encouraging results obtained in developing solvent free scaffolds using melt electrospinning technology enables new possibilities for tissue engineering applications.

Contents

List of Figures

List of Tables

Nomenclature

α	Giesekus model nonlinear parameter
β	nonlinear parameter in MSF model
β_p	percolation scaling exponent
$\dot{\gamma}$	applied strain-rate
$\dot{V}$	flow rate
ϵ	dielectric permittivity
η	shear viscosity
η^*	complex viscosity
η_0	zero shear-rate viscosity
γ	applied strain
γ_s	surface tension
μ_0	zero shear-rate intrinsic nonlinearity (shear stress)
$\mu_0^{N_1}$	zero shear-rate intrinsic nonlinearity (first normal stress difference)
$\nu_{n/1}$	n^{th} Chebyshev viscous intensity relative to fundamental viscous intensity
ω	angular frequency
σ	stress
τ_a	arm relaxation time
τ_d	reptation relaxation time

τ_e entanglement relaxation time

τ_f fragmental relaxation time

τ_R Rouse relaxation time

τ_s stretch relaxation time

$\underline{\underline{\sigma}}$ extra stress tensor

ζ dimensionless whipping term in solution electrospinning process

a tube diameter

a_0 equilibrium tube diameter

C concentration

c_v constraint release parameter

d fiber diameter

D_{avg} average fiber diameter

De Deborah number

$e_{n/1}$ n^{th} Chebyshev elastic intensity relative to fundamental elastic intensity

f_{max}^2 maximum stretch (a nonlinear parameter in MSF model)

$G^{''}$ viscous modulus

$G^{'}$ elastic modulus

G^* complex modulus

G_g glassy modulus

G_N^0 plateau modulus

h planck constant

h_t terminal fiber diameter of solution electrospun fiber

I electric current

$I_{3/1}$ 3^{rd} Fourier intensity relative to fundamental intensity for shear stress

$I_{5/1}$ 5^{th} Fourier intensity relative to fundamental intensity for shear stress

M molecular weight

M_c critical molecular weight

M_e entanglement molecular weight

m_e mass of electron

M_n number-average molecular weight

M_w weight-average molecular weight

M_z z-average molecular weight

M_{z+1} z+1-average molecular weight

N_1 first normal stress difference

N_2 second normal stress difference

$N^1_{4/2}$ 4^{th} Fourier intensity relative to fundamental intensity for first normal stress difference

Oh Ohnesorge number

p isotropic pressure

$Q_0^{3/1}$ zero strain intrinsic nonlinearity based on $I_{3/1}$

$Q_0^{5/1}$ zero strain intrinsic nonlinearity based on $I_{5/1}$

Q_0^{ν} zero strain intrinsic viscous nonlinearity

Q_0^{e} zero strain intrinsic elastic nonlinearity

$Q_0^{N_1}$ zero strain intrinsic nonlinearity based on $N_1^{4/2}$

q_v volume charge density

S_a normalized arm relaxation time

S_b normalized backbone average molecular weight

T	temperature
T_c	crystallization temperature
T_g	glass transition temperature
T_m	melting temperature
V	velocity of electron
V_s	applied voltage on syringe
Wi	Weissenberg number
Z	number of entanglement
V_h	hydrodynamic volume

Chapter 1

Introduction

Polymeric materials brought a paradigm shift for the development of pioneering innovations to meet society's biggest challenges. This fact can be realized by the growth in cumulative global consumption over the last six decades. The yearly worldwide plastic production has exploded from 1.5 million tonnes in 1950 to 300 million tonnes in 2011[3]. Worldwide the drivers of growth in the demand for plastics are manifold. Economic growth, population growth and the increasing wealth in newly industrialized and in developing countries play an important role. The share of plastics has been increasing at the expense of the other bulk materials. This is partly a result of new needs, which can best be fulfilled by plastics (e.g., safety devices such as airbags, mulch films for agriculture and certain medical devices and fabrication of scaffolds for tissue engineering applications). Another important driver is material substitution, e.g. the replacement of glass by polymers in consumer goods such as computer screens and inroads made by plastics into the traditional applications of paper/board in packaging and metals (e.g. in consumer goods and buildings). Here, the costs for production and processing of the competing materials play an important role.

Polymeric materials are commonly classified into three categories: thermoplastics, elastomers, and thermosets. This categorization is based on the thermo-mechanical properties of the polymeric materials as a consequence of their molecular structure. *Thermoplastics* are linear or branched polymers that become fluid when heat is applied. They can be molded and transformed using the processing techniques such as injection molding and extrusion. Currently, this class occupy the major proportion of polymeric materials used in industry. Thermoplastics can be further classified into crystalline and amorphous. *Elastomers* are cross-linked polymers with a low density of cross-linking points that can be easily deformed, reaching extensions of up to ten times their original

dimensions and rapidly recovering their original size when the applied tension is released. The cross-linking restricts their ability to flow, though cross-linking provides the ability to recover into their original size when the applied tension is released. *Thermosets* are rigid materials with a high density of cross-linking which severely restricts the chain movements. This work is focused only on the characterization and processing of the thermoplastics [polyethylene (PE), polypropylene (PP), polystyrene (PS) and poly(ϵ-caprolactone)].

It is utmost important for the polymer industries to tune the thermoplastic polymeric material properties depending on the processing techniques and applications. The most frequent ways in the industry to tailor the properties of the thermoplastics polymeric materials are to change the (i) molecular size, M, (ii) molecular weight distribution (MWD), (iii) branching [short chain branching (SCB) and long chain branching (LCB)] and (iv) addition of nanofillers to the polymeric matrix (polymer nanocomposites).

- **Molecular Weight and Molecular Weight Distribution (MWD):** Many properties of polymers depend on their size, which is expressed in term of molecular weight, M. In general, polymers do not have a unique molecular weight. Instead, they have a distribution of molecular weights. The distribution of molecular weights can be characterized in terms of different molecular weight averages. The most basic average is the number-average molecular weight, M_n:

$$M_n = \frac{\sum n_i M_i}{\sum n_i} \tag{1.1}$$

where n_i is the fraction of molecules having the molecular weight, M_i. Generally, the preferred way to describe the composition of a mixture is in term of weight fractions (w_i) rather than the number fractions of molecules. This motivated the use of weight-average molecular weight, M_w :

$$M_w = \frac{\sum w_i M_i}{\sum w_i} \tag{1.2}$$

Higher moments can also be used to provide additional information about the shape of distribution. The next two after M_w are:

$$M_z = \frac{\sum w_i M_i^2}{\sum w_i M_i} \tag{1.3}$$

$$M_{z+1} = \frac{\sum w_i M_i^3}{\sum w_i M_i^2} \tag{1.4}$$

For distributions with a single maximum, M_n is normally close to the maximum. M_w is always greater than M_n, except for a monodisperse polymer where all molecules have the same molecular weight and $M_w = M_n$. The ratio M_w/M_n is known as the polydispersity index (PDI) which provides a measure of the width of the distribution. The width of the number-average molecular weight distribution, expressed as its standard deviation, σ_n, is related to the ratio M_w/M_n as follows:

$$\frac{\sigma_n}{M_n} = \sqrt{\frac{M_w}{M_n} - 1} \tag{1.5}$$

Figure 1.1 shows the log-normal distribution and all the averages which are used to describe the typical distributions. The average molecular weight, M_w, is 100 kg/mol and PDI is 3. It could be observed that the higher moments provide the information about higher molecular weight and always greater than the M_w.

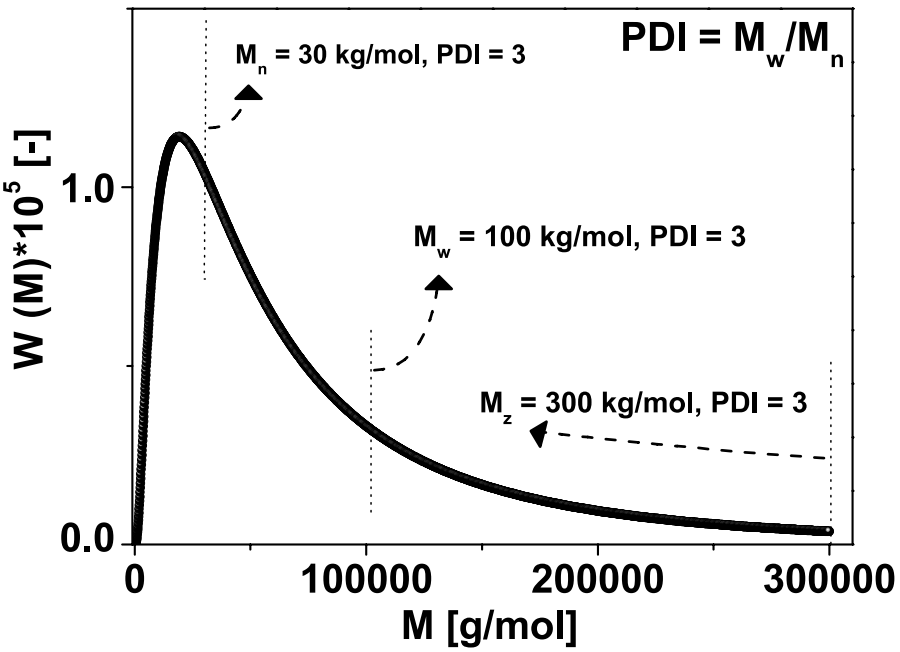

Figure 1.1: log-normal distribution with mean $\sqrt{M_w M_n}$, and standard deviation of $\sqrt{log(PDI)}$, where M_w = 100 kg/mol and PDI = 3.

- **Branching:** Polymers can be synthesized with the different topologies of macromolecules (Fig. 1.2). The most important structural variable influencing the properties of polymers after the molecular weight and its distribution is branching. The branching can be cate-

gorized into two categories: short-chain branching (SCB) [branches with fewer than six carbon atoms] and long-chain branching (LCB). The short-chain branching is well known to be particularly critical in its effects on the morphology and solid-state properties of semi-crystalline polymers such as polyethylene, while long-chain branching has a profound effect on melt rheology[4].

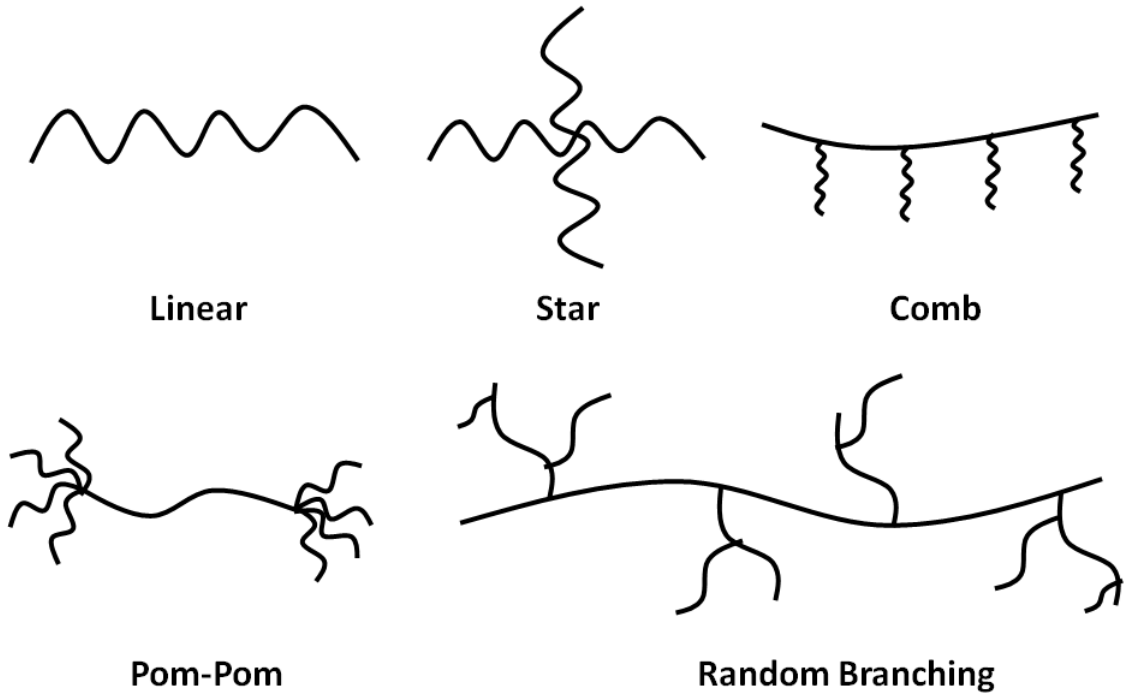

Figure 1.2: Sketches illustrating various structures: linear, star, comb, Pom-Pom, and randomly branched polymers.

- **Polymer Nanocomposites:** The mixing of nanofillers with polymers has opened up a new pathways for engineering flexible composites that exhibit advantageous electrical, optical, or mechanical properties. Different types of nanofillers are utilized to improve the properties of polymeric materials, e.g. graphene, carbon nanotubes, graphite platelets, carbon nanofibers, natural fibers (hemp or flex)[5].

It is crucial for the polymer industries to understand the effects of above discussed parameters (M_w, PDI, LCB, and addition of nanofillers) on the properties of polymer melts. This motivated the development of numerous methods to characterize the influence of these parameters, such as Size Exclusion Chromatography (SEC)[6], Nuclear Magnetic Resonance (NMR)[7,8] and rheological methods[9,4]. Among these techniques, the rheological methods are widely used in the polymer

industry because of two reasons. First, rheological properties are both very sensitive to certain aspects of the structure and much simpler to use than analytical methods such as SEC and NMR. Second, it is the rheological properties that govern the flow behaviour of polymers when they are processed. Consequently, the rheological properties helps in establishing the structure-processing relationship which is of significant interest to the polymer industry.

Rheology is the science of *deformation* and *flow*. The rheology has a key position in polymer research, being an important link in the so-called *chain of knowledge* reaching from the production of polymers to their end-use properties [10]. The rheological methods are used to perform the quality control on polymers used as raw material, consistency monitoring and troubleshooting of products, fingerprinting of different structures, new material development, product performance prediction, design and optimization of different processing techniques.

Many processing techniques are used to produce the day-to-day products using the polymeric materials, e.g, electrospinning, melt spinning, blow moulding, film casting, melt extrusion and thermoforming [11,4]. Generally, this thesis is focused to the characterization of polymeric materials for industrial processes. However, a particular attention is focused to the electrospinning process to fabricate the scaffolds for the tissue engineering applications.

Electrospinning or electrostatic spinning [12,13,14] technology enables the production of continuous polymer micro/nano fibers from either a polymer solution or melt using high electric field. The electrospinning technology has its roots almost 300 years ago. In 1745, Bose described aerosols generated by the application of high electric potentials to drops of fluids [15]. Then, in 1882, Lord Rayleigh investigated the question of how many charges were needed to overcome the surface tension of a drop [16]. Next, Morton received the first US patent for the electrospinning of artificial fibers in 1902 [17]. Finally, in 1934, Formhals patented the electrospinning of plastics [18]. However, the practice of electrospinning technology remained latent until the 1970. In the early 1980, Larrondo and Manley [19] demonstrated the feasibility of electrospinning a polymer melt instead of a solution. A melt extruder was used to deliver a polyethylene melt to a charged capillary. The electrospun fibers were about 10 μm in diameter. In the 1990, great interest in electrospinning research was generated when Doshi and Reneker [20] reintroduced this technique as a facile way to fabricate submicron fibers. Since then, it has been shown that almost all materials that can be spun from melt or solution by conventional methods can be electrospun into fibers. One of the reasons

for the interest in this subject is the combination of both fundamental and application-oriented research from different branches of science and engineering. The scope of possibilities presented by electrospinning encompasses a multitude of new and interesting concepts, which are developing at exponential rate.

The recent developments towards large scale productions combined with the simplicity of the process enables this technology very attractive for many applications, e.g. filters[21], tissue engineering applications[22], regenerative medicine[23], microfluidic cell incubators or immunoassays[24], photovolotic devices[25], catalyst supports[26], composite reinforcements[27] and photonic devices[28]. Other alternative techniques for the production of ultrathin polymer fibers include, most notably, melt blown and multicomponent processes[29]. Both these methods use polymers to make fibers with diameter of less than 500 nm. In the melt-blown technique, polymer melts are pushed, under relatively high pressure, through an array of nozzles. Fibers are formed from the melt under rapid cooling in the countercurrent. Multicomponent fibers, which consist of segments of different polymers, are fabricated by extrusion techniques, for example, by handling with water jets. Although both methods have significantly higher productivity than electrospinning and yield finer fibers from the melt, electrospinning is much more flexible in terms of achieving controlled fiber diameters and for processing of all kinds of polymers and additives. As a result of this, several industries are already using electrospinning technology to deliver consumer products, e.g. Donoldson Corporation (filtration solutions), Cella Energy (use electrospun fibers for hydrogen storage in clean energy applications). Furthermore, electrospinning provides many interesting possibilities for the nanostructuring of materials.

1.1 Main Objectives

The objectives of the thesis were:

- The influence of entanglements on the linear and non-linear viscoelastic material properties at small and large deformations under oscillatory shear flow for monodisperse PS melts and its blends.

- The influence of long-chain branching on the linear and non-linear viscoelastic material properties at small and large deformations under oscillatory shear and uniaxial extensional flow for industrial polyolefin.

- The influence of percolating network on the linear and non-linear viscoelastic material properties at small and large deformations under oscillatory shear for polymer composites of PE with carbon nanotubes.

- Fabrication of hierarchical cm-thick scaffolds for tissue engineering applications using the single-step solution electrospinning technology.

- The development of melt-electrospinning set-up, and fabrication of scaffolds without residual solvent.

1.2 Organization of Thesis

In the following section, first a brief introduction to essential tensors needed to understand the rheological methods were described. In addition, supplementary characterization techniques principle for polymer melts and fabricated scaffolds were discussed. In chapter 2, various constitutive equations are presented for the prediction of linear and non-linear viscoelastic properties of polymer melts. In chapter 3, different techniques are introduced to analyse the Large Amplitude Oscillatory Shear (LAOS) flow response. Furthermore, the LAOS responses (shear stress and first normal stress) are simulated using the Giesekus Model and analyzed using various techniques available in the literature. In chapter 4, linear viscoelastic and nonlinear viscoelastic properties are discussed under oscillatory shear flow for the monodisperse polystyrene (PS) and blends of the monodisperse polystyrene (PS) melts. In chapter 5, the characterization of long-chain branching using oscillatory shear and extensional rheology is discussed. Particularly, normal stresses were measured at large deformation oscillatory shear for the first time and analysed using a FT-Rheology and Stress-Decomposition (SD). Many new parameters were introduced based on the FT-Rheology analysis of oscillatory shear and first normal stress. In chapter 6, a new analysis is proposed to characterize the percolation threshold in polymer composites of carbon nanotubes using FT-Rheology. Chapter 7 describes a new method to fabricate the 3D cm-thick scaffolds which has tremendous potential for tissue engineering applications. In chapter 8, a melt electrospinning set-up design is discussed, which was built within this theis. The processing and material parameter (viscosity) were optimized to obtain the desired fiber morphology. In chapter 9, the summery and future perspective of this thesis are presented.

1.3 Flow Kinematics and Stress Tensor of Deformable Bodies

A mathematical description of arbitrary deformations is required to understand and develop constitutive equations for describing the flow of polymeric materials. This purpose has been achieved with the introduction of deformation gradient and the velocity gradient tensors. To understand these tensors we consider a three-dimensional material body before and after an arbitrary deformation as shown in Figure 1.3. Consider a vector is embedded in the material. The vector coordinates is represented by $\underline{r}$ before the deformation. On applying the deformation, the vector is rotated and stretched such that its new coordinate are given by $\underline{r}'$. A quantity that provides complete information about the relative displacement of any material element in a very small volume of the fluid is called deformation gradient tensor, $\underline{\underline{F}}$.

$$\underline{\underline{F}} \equiv \begin{bmatrix} \frac{\partial r_1'}{\partial r_1} & \frac{\partial r_2'}{\partial r_1} & \frac{\partial r_3'}{\partial r_1} \\ \frac{\partial r_1'}{\partial r_2} & \frac{\partial r_2'}{\partial r_2} & \frac{\partial r_3'}{\partial r_2} \\ \frac{\partial r_1'}{\partial r_3} & \frac{\partial r_2'}{\partial r_3} & \frac{\partial r_3'}{\partial r_3} \end{bmatrix}$$

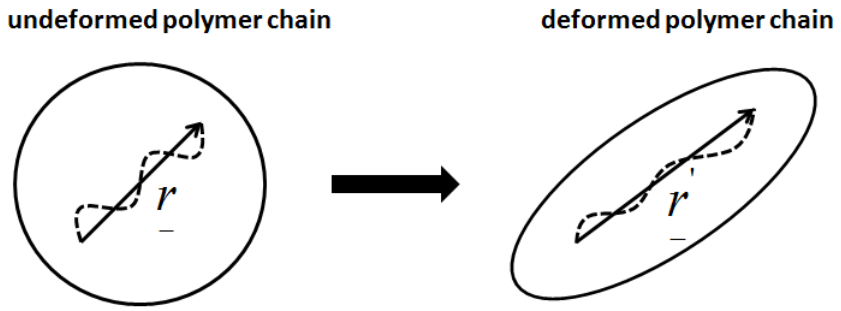

Figure 1.3: The deformation gradient, $\underline{\underline{F}}$, for an arbitrary three-dimensional deformation.

The time derivative of $\underline{\underline{F}}^{-1}$ is equal to:

$$\frac{\partial}{\partial t}\underline{\underline{F}}^{-1} = \underline{\underline{F}}^{-1} \cdot \underline{\nabla}\,\underline{v} \tag{1.6}$$

where $\underline{\nabla}\,\underline{v}$ is a velocity gradient. The velocity gradient describes the steepness of velocity variation as one moves from point to point in the flow at a given instant in time.

The stress tensor arises as a result of applied deformation on the material. The physical significance of stress tensor may be illustrated best by considering the three forces acting on three

faces (one force on each face) of a small cube element of fluid, as schematically shown in Figure 1.4. The force acting on each face with a arbitrary direction may be resolved in three components directions. The total stress tensor, $\underline{\underline{T}}$, of incompressible fluids under deformation or in flow can be divided into two parts:

$$\underline{\underline{T}} = -p\underline{\underline{\delta}} + \underline{\underline{\sigma}} \tag{1.7}$$

where $\underline{\underline{\delta}}$ is the unit tensor, $\underline{\underline{\sigma}}$ is a extra stress tenor that vanishes in the absence of deformation or flow, and p is the isotropic pressure. Note in Eq. 1.7 that p has a negative sign since it acts in the direction opposite to a normal stress, which by convention is chosen as pointing out of the cube.

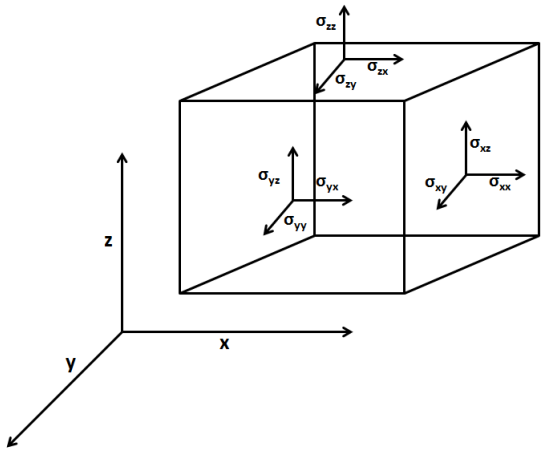

Figure 1.4: Stress components on a cube.

1.3.1 Simple Shear

Simple shear is a common flow in nature, for example the flow of water down a pipe consists locally of shear flow. Likewise, the flow of a polymer melt though an extruder and a die is shear. A fluid between two plates experiences simple shear if the top plate is moved with constant velocity (Fig. 1.5). The viscosities of polymer melts and solutions are always quantified by a shear flow. The extra stress tensor under simple shear is given as:

$$\underline{\underline{\sigma}} = \begin{bmatrix} \sigma_{xx} & \sigma_{xy} = \sigma_{yx} & 0 \\ \sigma_{yx} = \sigma_{xy} & \sigma_{yy} & 0 \\ 0 & 0 & \sigma_{zz} \end{bmatrix}$$

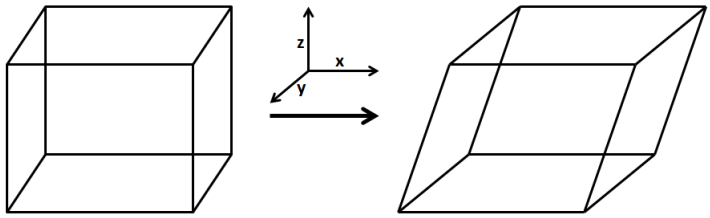

Figure 1.5: Shear flow: The element has a force applied to its top surface in the x-direction. Newtonian flow in a pipe is an example of local shearing flow due to the parabolic velocity profile through the pipe.

The shear stress is shear flow is just σ_{xy}. The 1^{st} normal stress difference and 2^{nd} normal stress difference are defined:

$$N_1 = \sigma_{xx} - \sigma_{yy}, \qquad N_2 = \sigma_{yy} - \sigma_{zz} \tag{1.8}$$

respectively. The first normal stress difference can be visualised as tension in the streamlines. A melt being stirred can produce a force towards the centre of the container causing the famous rod-climbing phenomena[30].

1.3.2 Uniaxial Extension

In an uniaxial extension the sample is elongated at both ends with a constant velocity in the direction of deformation x to generate a steady uniaixal extension (Fig. 1.6). A material line oriented along any axis of the cube is stretched or compressed but not rotated. Thus, deformation tensor and velocity tensor only contain diagonal elements. The extra stress tensor under uniaxial extension is given as:

$$\underline{\underline{\sigma}} = \begin{bmatrix} \sigma_{xx} & 0 & 0 \\ 0 & \sigma_{yy} & 0 \\ 0 & 0 & \sigma_{zz} \end{bmatrix}$$

1.4 Supplementary Characterization Techniques

The supplementary techniques which were used in this study include:

- Differential Scanning Calorimetry (DSC)

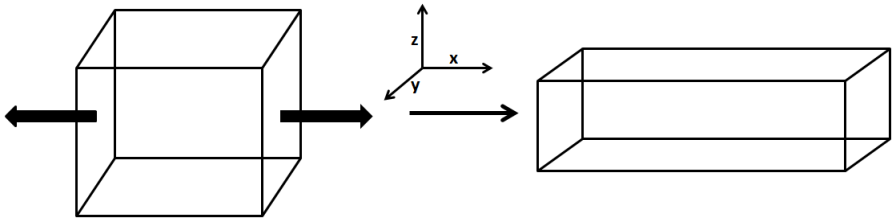

Figure 1.6: Uniaxial extension: The element is stretched in the x-direction causing a reduction of element size in the y and z directions.

- Light Scattering
- Gel Permeation Chromatography (GPC)
- Scanning Electron Microscopy (SEM)

1.4.1 Differential Scanning Calorimetry (DSC)

Differential Scanning Calorimetry is a thermo-analytical technique that records changes in heat flow as a function of time or temperature[31]. This technique is most often used for characterizing the T_g (glass transition temperature) , T_m (melting temperature) , T_c (crystallization temperature) , and heat of fusion of polymers. The sample and a reference are exposed to a temperature program, usually a linear ramp with or without plateaus, and the heat flow is adjusted in such a way that the temperature T , of the sample and reference coincide at all times. In contrast to other calorimetric techniques, the temperature difference, $\triangle T$, between the sample and reference is always zero, yet the heat flow is different for the sample when a thermodynamic transition occurs. Usually the first order phase transitions like melting or freezing processes appear in the thermogram as peaks, while second-order transitions, like the glass transition, leads to steps in the baseline. It is important to note that the glass transition is not a second order transition in the conventional Ehrenfest sense since it is not an equilibrium transition[31]. Yet a change in heat capacity is typically associated with the glass transition, which is why it appears step-like in a DSC experiment.

1.4.2 Light Scattering

The determination of the weight average molecular weight is done using light scattering. The basic principle is that light passing through a polymer solution is scattered by the polymer molecules, which are large enough to cause significant scattering, but still small compared to the wavelength

of the light. It is necessary to choose a solvent having a refractive index that is sufficiently different from that of polymer. The Low Angle Laser Light Scattering (LALLS) is useful for the absolute determination of molecular weight, while MutliAngle Laser Light Scattering (MALLS) can determine the mean-square radius of gyration and the second virial coefficient. While light scattering can measure over a wide range of molecular weight, it is less sensitive to low-molecular weight material.

1.4.3 Gel Permeation Chromatography (GPC)

Gel permeation chromatography (GPC) is a widely used method to obtaining information about the molecular weight and its distributions[32]. Generally, a mixture of different constituents dissolved in a solvent, the eluent, is pressed through a column of densely packed filler particles, the stationary phase, which are able to undergo certain interactions with the solutes. In GPC sample fractions are separated with respect to their different molecular size or more specifically to their hydrodynamic volume, V_h . The stationary phase consists of particles with a particular pore size. Due to diffusion into these pores, small solute molecules remain in the column for a longer time. The time is called the retention time and depends on the hydrodynamic volume and thus on the size of the macromolecule. Using a calibration curve for which the experimental relation between the hydrodynamic volume and molecular weight has been determined based on polymer standards, a sample of unknown molecular mass can be analyzed. GPC is a relative but straight forward technique that yields the full molecular weight distribution for polymers, specifically the first moments of this distribution (M_n, M_w, M_z). The detection of short-chain branching such as those resulting from the use of an $\alpha-$olefin co-monomer with ethylene, is difficult because short-chain branches have only a moderate effect on the size of the molecule and thus on the GPC separation. However, by combining GPC with infrared spectrometry[33] or with nuclear magnetic resonance[34] short-chain branching could be revealed. For architectures with long chain branching, the analysis is made complicated by the fact that the size of a molecule depends on the branching structure as well as on the molecular weight. The combination of GPC with MALLS along with a UV detector has been used to study the long chain branching in isotactic polypropylene[35] and in polyethylene[36].

1.4.4 Scanning Electron Microscopy (SEM)

Scanning electron microscopy (SEM)[37] uses electrons instead of light to create highly magnified images of a specimen. SEM has distinct advantages over traditional light microscopes in terms of resolution and depth of field. The resolution of a light microscope is about 400 nm which is due to the wavelength limitation of visible light (400-800 nm). Electrons have much smaller wavelength according to the De Broglie relationship (Eq. 1.9) and are capable to give a clear discrimination in the range of nano meters.

$$\lambda = \frac{h}{m_e V} \tag{1.9}$$

where h is the Planck constant $6.63 * 10^{-34}\ J \cdot s$ and m_e is the mass of a electron and V is the velocity of the electrons.

A pictorial description of a typical SEM is shown in Figure 1.7. The filament is heated resistively by a current to achieve a temperature between T = 2000-2700 K. This results in an emission of thermionic electrons from a tungsten cathode. Then, the electron are accelerated towards an anode with a set energy typically ranging from a few hundred to 100,000 eV. The electron beam is focused by one or two condenser lenses into a spot sized 1 to 5 nm. On its trajectory the beam passes through pairs of scanning coils, which deflect the beam horizontally and vertically, such that it scans in a raster fashion over a rectangular area of the sample surface. The electrons that come in contact with the sample surface lose energy by repeated scattering and absorption over an area extending from less than 100 nm to around 5 μm on the specimen surface. Energy exchange between the electron beam and the sample results in emission of secondary and backscattered electrons as well as emission of electromagnetic radiation from the sample. The secondary and backscattered electrons detected are then amplified by a photomultiplier tube to produce an image; secondary electrons are good for obtaining morphological information from sample surface, while backscattered electrons are useful for illustrating contrasts in composition in multiphase samples[37]. The combination of higher magnification, large depth of focus, greater resolution, and ease of sample preparation makes the SEM one of the most commonly used technique for fibre analysis.

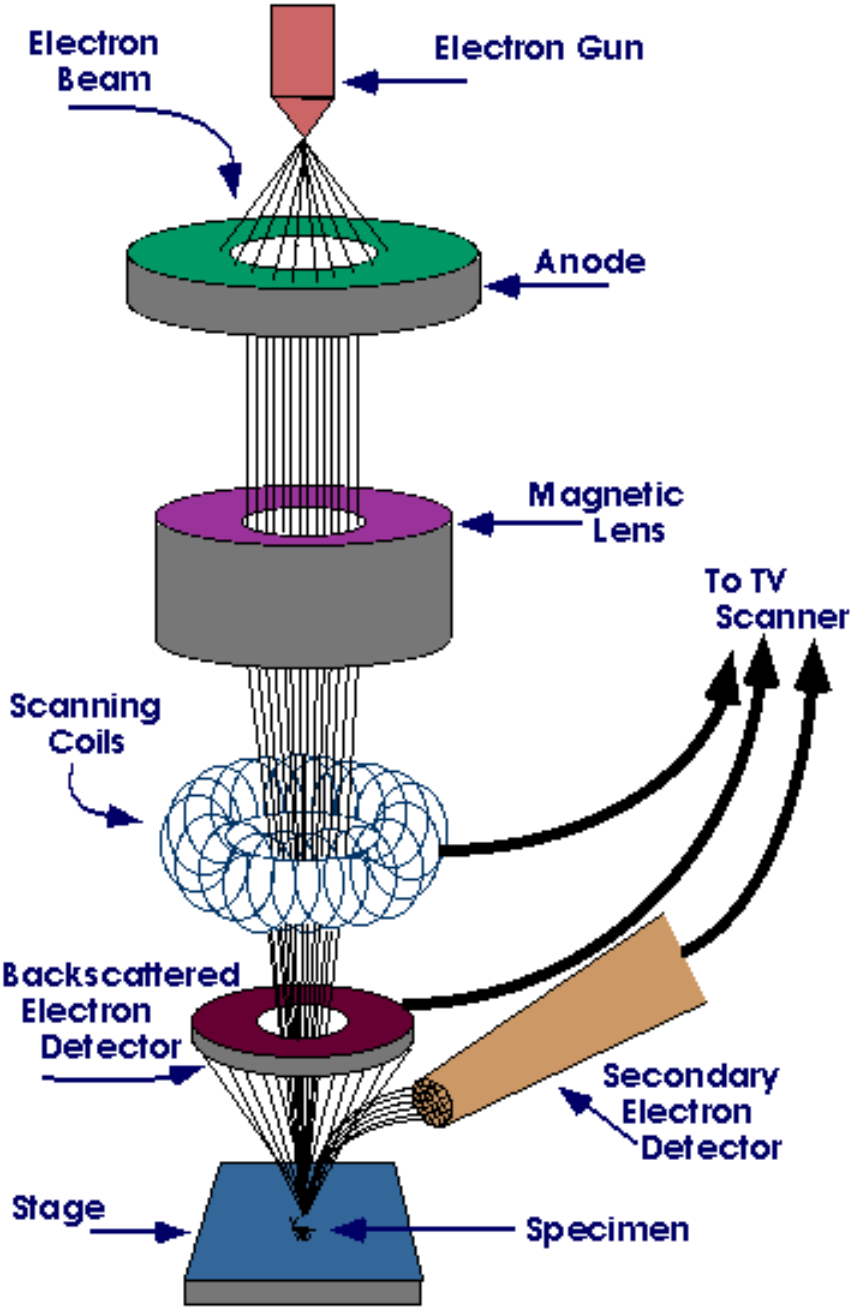

Figure 1.7: Pictorial illustration of the principles and constructions of SEM (figure is taken from webpage[1]).

Chapter 2

Constitutive Models to Predict the Linear and Nonlinear Viscoelastic Response of Polymer Melts

A material subjected to mechanical loading may respond by storing energy (elastic deformation), dissipating energy (viscous deformation), or a combination of the two (viscoelastic deformation). The response of ideal elastic solid to deformation (pure elastic deformation) can be modeled by Hooke's model. The stress response is proportional to the imposed strain, γ and is independent of the strain-rate, $\dot{\gamma}$. In contrast, the stress response of ideal viscous liquid is proportional to the imposed strain-rate [Newtonian model] and the total strain is irrelevant. Polymer materials, amongst others, shows the viscoelastic behavior, i.e., the stress response is a function of both imposed strain and strain-rate.

$$\text{Hook's model:} \qquad \sigma = G_0\gamma \tag{2.1}$$

$$\text{Newtonian model:} \qquad \sigma = \eta\dot{\gamma} \tag{2.2}$$

where G_0 and η are intrinsic material properties.

In the linear viscoelastic regime, the viscosity is independent of shear rate. Polymer melts exhibit this behaviour at very low shear rates, and the limiting value at low shear-rate of the viscosity is called zero shear-rate viscosity, η_0 . This material parameter plays an important role in polymer rheology, both as an indicator of molecular weight and as a key parameter in molecular theories. The most interesting feature of $\eta_0(M_w)$ is its strong dependence on molecular weight.

Based on $\eta_0(M_w)$ dependence on molecular weight, polymer melt systems are divided into two categories: (i) unentangled polymer systems (ii) entangled polymer systems. For unentangled polymer systems $\eta_0(M_w)$ is proportional to molecular weight, but for entangled polymer systems, a steep increase is observed in a exponent where $\eta_0(M_w) \propto M_w^{3.4-3.6}$. This dramatic change happens after a critical molecular weight, M_c, for each polymers[4]. This significant increase in the dependence of molecular weight is attributed to entanglement coupling of polymers chains, which takes effect when the molecules become sufficiently long (after M_c) that they seriously impede motions of each other. In this work, our studies is focused to entangled polymer systems.

In the nonlinear viscoelastic regime, the polymer melts display extensional hardening in extension and shear thinning in shear. The extensional hardening helps to stabilize the processes and shear thinning leads to improved processability. These remarkable properties of polymer melts above entanglement molecular weight make polymers an important class of material for processing applications.

The aim of theoretical rheology is to develop constitutive equations that relate stress within the material to its deformation history. Constitutive equations together with mass and momentum conservation can be used to predict the flow of the material. Molecular rheology aims to derive and understand these constitutive equations from the underlying microscopic physics of the material. The topology of the chain can vary from a simple linear chain to a complex branched structure. Chemically identical materials with the same molecular weight but different topologies often have radically different rheology. Conversely, materials with different chemistries but with molecules of globally the same shape often exhibit evidence of universal behaviour. In this thesis, our focus is mainly on entangled polymeric systems.

The dynamics of the entangled polymeric systems can be modeled by the two approaches. The first treats the physics as collective effects, without seeking to capture the topological nature of constraints explicitly. Starting with the Rouse theory[38], collective corrections introduced to the monomer mobility lead both to slowing down and to local anisotropy. An example is the approach of Williams and co-workers[39]. The second approach treats the entanglements phenomenologically, but as serious topological constraints. The most successful of these has been the *tube model*. The basic idea is to convert a many-body problem into a single-body problem (test chain) in an effective field (tube like region). The tube is invoked to represent the sum of all topological non-

crossing constraints active with neighbouring chains, and the tube radius, a, is of the order of the end-to-end length of a chain of molecular weight M_e (entanglement molecular weight). In this way, only chains of higher molecular weight than M_e are strongly affected by the topological constraints (Fig. 2.1). The tube was first invoked by Edwards[40] in an early model for the trapped entanglements in a rubber network. The consequences of this idea towards melt dynamics were first explored by de Gennes[41], again in the context of networks. A free chain in a network would be trapped by the tube of radius a defined by its own contour. This would suppress any motion perpendicular to the tube's local axis beyond a distance of a, but permit both local curvilinear chain motions and centre-of-mass diffusion along the tube. De Gennes coined the term 'reptation' for this snake-like wriggling of the chain under Brownian motion. The theory gives immediately a characteristic timescale for full disengagement from the tube by curvilinear centre-of-mass diffusion. This disengagement time τ_d is proportional to the cube of the molecular weight of the trapped chain. This arises from combining the Fickian law of diffusive displacement of length L with time τ_d , $\tau_d \sim L^2$, recognizing that path length $L \sim M_w$; with one extra power arising from the proportionality of the total drag to molecular weight[42].

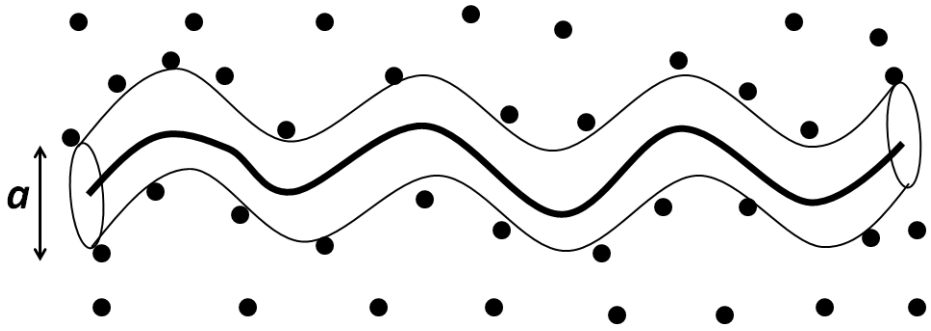

Figure 2.1: A tube-like region of constraint arises around any selected polymer chain in a melt due to the topological constraints of other chains (small circles) in its neighbourhood.

2.1 Constitutive Models for the prediction of Linear Viscoelastic Properties

The advantages of performing the experiments in the linear viscoelastic regime are, (i) experiments in this regime are relatively easy to realise, (ii) an isotropic material response is often insensitive to the geometry of the deformation and (iii) the experiments can probe polymer materials over a

wide range of timescale. The most fundamental rheological experiment for a viscoelastic material is step shear-strain test, i.e, relaxation-test. In this test, a sample is subjected to a step shear strain of magnitude, γ_0, at time $t = 0$. The shear stress is measured as a function of time, and the ratio of the stress to the applied strain defines the relaxation modulus, $G(t)$.

$$G(t) = \sigma(t)/\gamma_0 \tag{2.3}$$

Figure 2.2 shows the typical stress relaxation curve for a highly entangled, monodisperse linear homopolymer. The distinct relaxation mechanism can be observed for the polymer melt. At short times there is a glassy zone in which the polymer is very stiff and has very high 'glassy modulus', G_g . The typical value for polymer melts lies around $G_g \approx 10^9$ Pa. In this regime the dynamics of polymer melts is governed by fragmental relaxation time, τ_f . This is followed by 'transition zone' in which additional mechanisms of relaxation come into play (entanglement relaxation time, τ_e) , and this leads to plateau zone, in which very little relaxation occurs (Rouse relaxation time, τ_R) . Finally, at long times, a new mechanisms of relaxation take place (reptation relaxation time, τ_d), and in this 'terminal zone', the stress falls towards zero, which it must finally do in any liquid. The value of $G(t)$ in the zone of constant modulus is called the *plateau modulus*, G_N^0. The typical value for the plateau modulus lies in the range $G_N^0 \approx 10^5 - 10^6$ Pa.

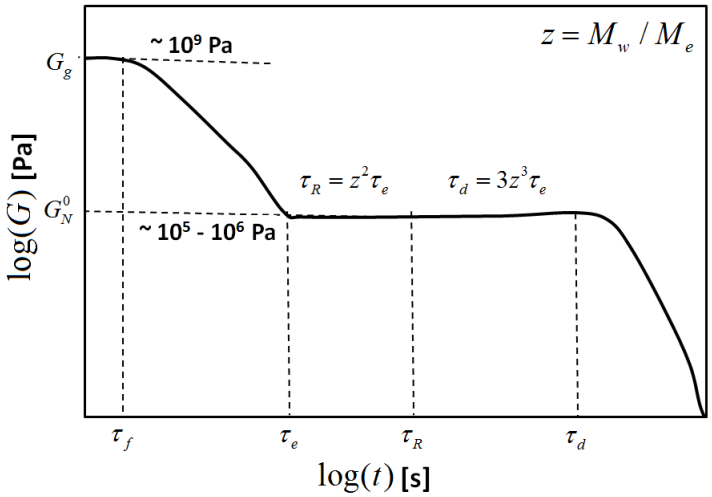

Figure 2.2: Stress relaxation curve for a linear, entangled, monodisperse polymer sample.

In the linear viscoelastic regime, using the Boltzmann superposition principle[4], the stress response can be expressed as:

$$\sigma(t) = \int_{-\infty}^{t} G(t - t')d\gamma(t') = \int_{-\infty}^{t} G(t - t')\dot{\gamma}(t')dt' \tag{2.4}$$

where $d\gamma(t^{'})$ is the shear strain that occurs between $t^{'}$ and, $dt^{'}$, and $\dot{\gamma}$ is the shear rate during this period. Next, two classes of models were discussed. At first, a phenomenological model and then the models based on tube theory[38,42].

2.1.1 Maxwell Model

The Maxwell model is the simplest realization of the viscoelastic liquids where a spring is connected in series with a dashpot (Fig. 2.3). For a step experiment, the applied deformation (γ) and

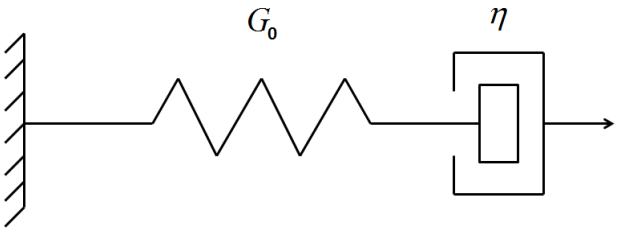

Figure 2.3: Maxwell liquid where a Newtonian subunit (dashpot) and an elastic subunit (spring) are arranged in series.

deformation rate ($\dot{\gamma}$) can be obtained as:

$$\gamma = \gamma_s + \gamma_{dp} \tag{2.5}$$

$$\dot{\gamma} = \dot{\gamma}_s + \dot{\gamma}_{dp} \tag{2.6}$$

At time $t > 0$, $\dot{\gamma} = 0$. Using the Newtonian and Hook laws respectively for pure viscous and elastic response, the equation 2.6 can be written as:

$$0 = \frac{\dot{\sigma}}{G_0} + \frac{\sigma}{\eta} \tag{2.7}$$

The expression of stress can be determined by solving the differential equation as:

$$\sigma(t) = G_0\gamma \exp\left(-\frac{G_0}{\eta}t\right) \longrightarrow G(t) = G_0 \exp\left(-\frac{G_0}{\eta}t\right) \tag{2.8}$$

By introducing the oscillatory deformation rate, $\dot{\gamma} = \gamma_0\omega_1 \cos(\omega_1 t)$, and relaxation modulus expression from the Maxwell model into the stress expression (Eqn. 2.4). The expression of elastic modulus $G^{'}$, and viscous modulus $G^{''}$, can be calculated as :

$$G^{'}(\omega) = \frac{G_0(\omega\tau)^2}{[1 + (\omega\tau)^2]} \tag{2.9}$$

$$G^{''}(\omega) = \frac{G_0\omega\tau}{[1 + (\omega\tau)^2]} \tag{2.10}$$

At low frequency, $G^{'} \propto \omega^2$ and $G^{''} \propto \omega$ which points towards validity of the Maxwell model in terminal regime for polymer melts (see in chapter-4).

2.1.2 Models Based on the Tube Theory

To interpret the linear viscoelastic data, one needs a quantitative molecular theory that can relate the rheological properties of a polymer to its molecular structure. Here, at first, we have described the basic mechanisms of relaxation that have been found to be most essential in developing models capable of predicting the linear viscoelastic properties of linear polymer melts. Moreover, the repation model[38] and Likhtman-McLeish model[43] were described for qualitative and quantitative prediction of the linear viscoelastic properties of linear polymer melts.

- **Reptation:** The tube model can be used to provide predictions for the linear viscoelastic properties. This is achieved by assuming that shortly after a step strain the polymer stress is due to chains trapped in oriented tube segments. A tube segment orientation is completely renewed when a free end of the chain passes through it. This relaxation process is illustrated in Figure 2.4.

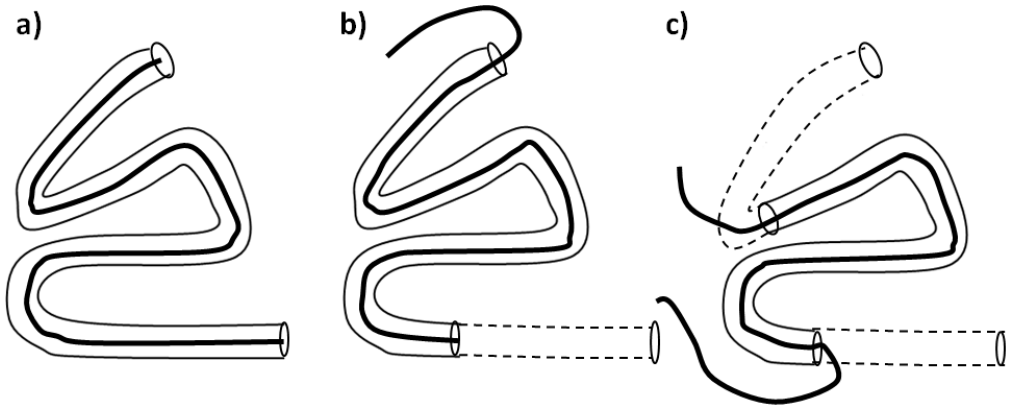

Figure 2.4: Pictorial description of the reptation process. The polymer chain escapes its tube by a snake-like diffusion process.

Immediately after the deformation all the chains are trapped in deformed tube (Fig. 2.4a). As the chain begins to move one chain end passes through some tube segments and these sections of oriented tube are lost (Fig. 2.4b). Since the new configurations taken by the emerging chain end are chosen without any constraint on their direction, they carry no stress.

The tube segments are destroyed from both ends as the chain moves back and forth due to diffusion (Fig. 2.4c).

- **Contour Length Fluctuations:** Since the tube diameter is much wider than the diameter of the chain, and the chain meanders within the tube, the chain is 'wrinkled up' within its tube as shown in Fig. 2.5b. The degree of wrinkling changes constantly, due to Brownian motion. When the chain gets slightly unwrinkle, it pushes its ends out again, but these ends emerge into new, randomly created, tube segments, and the stress associated with the now-vacated, end tube segments is lost (Fig. 2.5c). Thus, the occupied tube (contour length or primitive path) fluctuates in length due to the Brownian motion of the polymer molecules, and stress is thereby relaxed.

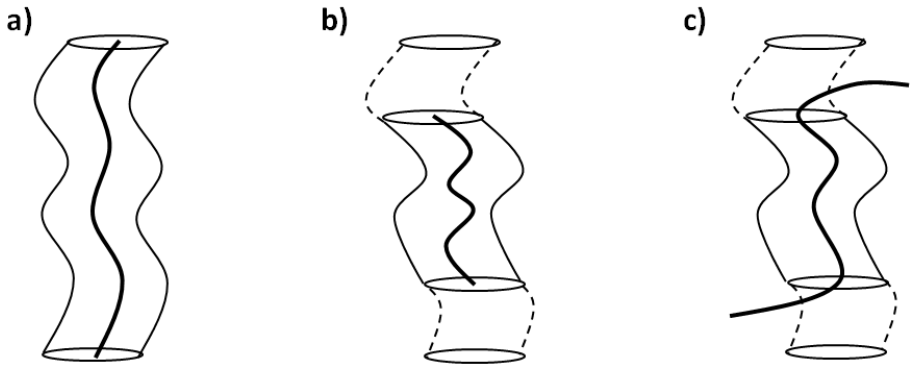

Figure 2.5: Pictorial description of contour length fluctuation. (a) the polymer chain in tube, (b) the chain ends contract due to thermal fluctuations and some tube is lost, and (c) the chain expand again and they are free to explore new directions.

- **Constraint Release:** While reptation and contour length fluctuation is considered for the chain motion of a chosen single chain (the test chain), the surrounding chains are undergoing similar motions. Thereby, constraints via entanglements on the test chain are released by the movement of surrounding chains and vice versa (Fig. 2.6). This effect is called constraint release (CR) and is especially important for branched or polydisperse linear polymers. This is because short chain can relax constraints much faster via diffusion than long chain via reptation[4].

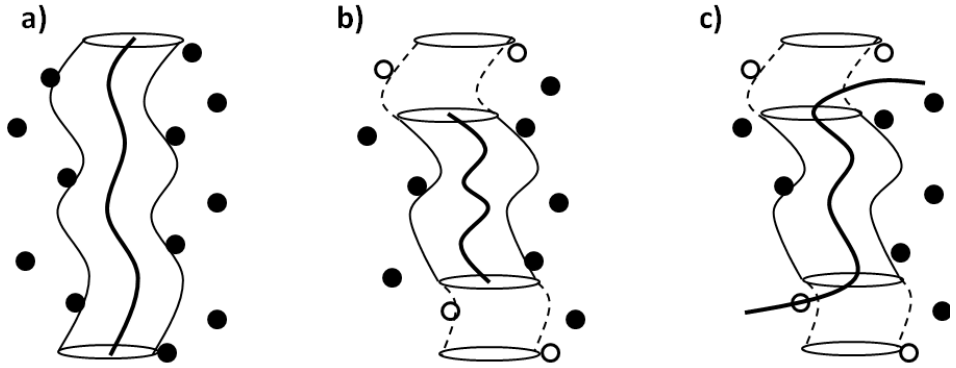

Figure 2.6: Pictorial description of constraint release, the tube is confined by the constraints of the surrounding chains. By the motion of surrounding chains (filled black sphere) the entanglement are released.

Repation model

The relaxation modulus of polymers can be predicted in the framework of the tube model. The first model to describe the linear polymer dynamics in the linear regime was the reptation model[38]. This model was based on the concept of reptation theory developed by de Gennes[41] and Doi and Edwards[38]. The reptation model consists of three main assumptions: first is that all other chains surrounding one particular chain are replaced by an effective field (the mean field), which acts as a tube around the particular chain and prohibits its motion in directions perpendicular to the primitive path. The second assumption is that longitudinal motion along the tube is allowed via reptation, which is simultaneous motion of all monomers; i.e., the polymer chain is replaced by the flexible rod with fixed length and only one degree of freedom. The third is that chain ends are not affected by topological constraints from other chains and, via reptation, occupy new tube segments selected from an isotropic distribution. Using these assumptions, Doi and Edwards[38] derived the following expression for the relaxation modulus:

$$G(t) = G_0 \sum_{p \quad odd}^{\infty} \frac{8}{p^2\pi^2} \exp\left(-\frac{p^2 t}{\tau_d}\right) \tag{2.11}$$

where p represents the number of mode and τ_d is known as the reptation time. Although, the reptation model is successful in predicting the qualitative behaviour in linear viscoelastic regime, quantitative prediction requires incorporation of several missing relaxation processes from the reptation model.

Likhtmann-McLeish model

The Likhtman-McLeish (LM) model[43] incorporated several missing relaxation processes from the reptation model such as (i) contour length fluctuation (ii) constraint release (iii) longitudinal stress relaxation along the tube. The validity of the developed theory was shown by describing the linear viscoelastic response of several linear polystyrene (PS) and polybutadine (PB) polymers. The proposed expression of relaxation modulus where all the relaxation processes were combined:

$$G(t) = G_e\left(\frac{4}{5}\mu(t)R(t) + \frac{1}{5Z}\sum_{p=1}^{Z-1}\exp\left(\frac{-p^2t}{\tau_R}\right) + \frac{1}{Z}\sum_{p=Z}^{N}\exp\left(-\frac{2p^2t}{\tau_R}\right)\right) \tag{2.12}$$

In this expression, the first term contains $\mu(t)$ which is equal to the fraction of the tube segments that was not visited by a chain end during time, t, and constraint release described by $R(t)$. The second term consists of the longitudinal modes relaxation, and the third represents the fast Rouse motion inside the tube. The detailed illustration of each term could be found elsewhere[43]. In the chapter 4, the linear viscoelastic response of monodisperse linear polystyrene (PS) is fitted with a REPTATE software[44], which implemented the full LM-model. In the software, the following model parameters should be chosen carefully: (i) Rouse time of entanglement segment, τ_e, (ii) plateau modulus, G_e, (iii) entanglement molecular weight, M_e, (iv) constraint release parameter, c_v, where $c_v = 0$ means there is no constraint release. The Rouse relaxation time (τ_R) and reptation relaxation time is calculated by the following equations where Z (number of entanglements) is equal to M_w/M_e:

$$\tau_R = \tau_e Z^2 \tag{2.13}$$

$$\tau_d = 3\tau_e Z^3\left(1 - \frac{2C_1}{\sqrt{Z}} + \frac{C_2}{Z} + \frac{C_3}{Z^{3/2}}\right) \tag{2.14}$$

with the following constants $C_1 = 1.69$, $C_2 = 4.17$ and $C_3 = -1.55$. The following constants value were proposed by Likhtman and McLeish[43] in order to obtain a reasonable description of the linear viscoelastic properties for polymeric systems.

2.2 Constitutive Models for Prediction of the Non-linear Viscoelastic Properties

The stress response of the polymer melts to a large or rapid deformation is nonlinear. This implies that the deformation exceeds the limit of linear viscoelasticity, and the polymer chains start to disentangle and orient along the flow. Therefore, material response is a function of the applied

deformation, deformation rate and the kinematics of the deformation. Thus, the Boltzmann superposition principle is no longer valid, and nonlinear viscoelastic behaviour cannot be predicted from linear properties. The understanding and development of constitutive equations to describe the nonlinear viscoelastic properties is important because in most industrial processes, polymer materials are subjected to large or rapid deformations in shear and elongation. The applied large or rapid deformations in elongation leads to extensional hardening which helps to stablize the processes, and at the same time shear thinning is observed. Therefore, to optimize industrial processes and tailor the material properties, an elaborate knowledge of flow behaviour at large deformations is necessary. In the following, two classes of models, one based on dumbbell theory and second based on tube theory (molecular rheology) are described.

2.2.1 Dumbbell Theory: Giesekus Model

The Giesekus equation belongs to a class of constitutive models based on anisotropic drag[45]. It constitutes an extension of the dumbbell theory for dilute solutions efficiently described by the upper-convected Maxwell (UCM) model[46]. It incorporates the contribution of the surrounding oriented molecules to the dumbbell relaxation in the UCM equation by introducing an empirical parameter α associated with the magnitude of the anisotropic drag. The Giesekus equation reads:

$$\tau \overset{\nabla}{\underline{\underline{\sigma}}} + \underline{\underline{\sigma}} + \frac{\alpha}{G_0} \underline{\underline{\sigma}} \cdot \underline{\underline{\sigma}} = 2G_0 \tau \underline{\underline{D}} \tag{2.15}$$

in which the $\overset{\nabla}{\sigma}$ denotes the upper-convected time derivative of the stress tensor σ defined as

$$\overset{\nabla}{\underline{\underline{\sigma}}} = \frac{\partial \underline{\underline{\sigma}}}{\partial t} + \underline{v} \cdot \frac{\partial \underline{\underline{\sigma}}}{\partial r} - \underline{\kappa} \cdot \underline{\underline{\sigma}} - \underline{\underline{\sigma}} \cdot \underline{\kappa}^T \tag{2.16}$$

where $\underline{v}$ is the velocity field tensor and $\underline{\kappa} = (\nabla \underline{v})^T$ is the transpose of the velocity gradient tensor. The parameter α determines the magnitude of the anisotropic drag and $0 \leq \alpha \leq 1$. For $\alpha = 0$, the UCM model is recovered. G_0 and τ are obtained from linear viscoelastic data. The rate of deformation tensor $\underline{\underline{D}}$ is defined as:

$$\underline{\underline{D}} = \frac{1}{2} \left(\nabla \underline{v} + (\nabla \underline{v})^T \right) \tag{2.17}$$

2.2.2 Models Based on the Tube Theory

To incorporate nonlinear rheological effects into the tube model, one must include the effects of large deformations on molecular configuration. The most important effects that influence the

non-linear viscoelastic response are *orientation* of tube segments, *retraction* of the tube segments within the tube and finally the *convective constraint release* caused by flow induced movement of chains relative to each other resulting in loss of entanglements between chains (Fig. 2.7).

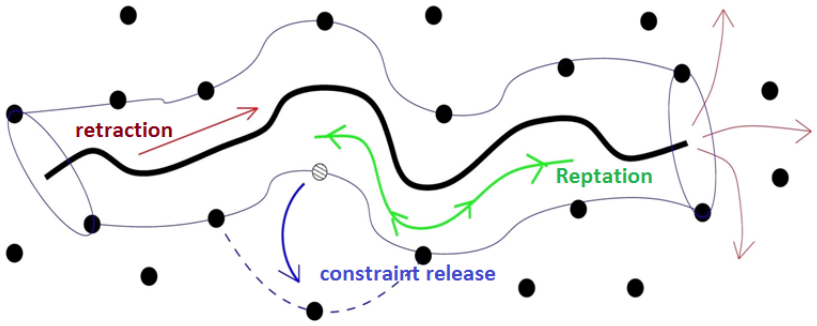

Figure 2.7: Typical relaxation processes within a nonlinear deformation.

- **Retraction:** The relaxation that is unique to the nonlinear regime is retraction within the tube. The retraction relaxation process is illustrated in Fig. 2.8. A large deformation induces a large tension on the test and matrix chains. The test chain can relieve some of this tension rather quickly by crinkling up within the deformed tube. This crinkling, or retraction, is rapid because it does not require the test chain to escape the tube. This means it requires only a Rouse-like motion, but not reptation. The longest relaxation time which describes the retraction process is called *retraction time* or *stretch relaxation time*, τ_s.

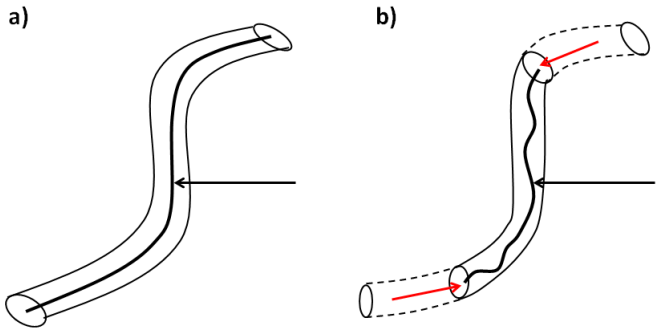

Figure 2.8: The chain relaxes its contour length towards equilibrium through retraction along the tube, driven by the chain's entropic spring force.

- **Convective Constraint Release:** In the linear viscoelastic regime, the constraint release occurs when the matrix chains relax by the same mechanisms as the test chains,

thereby releasing constraints on the test chains. In the nonlinear viscoelastic regime, a new relaxation for the test chain appears, that of chain retraction. Since the matrix chains also undergo chain retraction, this too must lead to constraint release. Because the flow *convects* the matrix chains past the test chain, and so releases the constraints imposed by the matrix chains on the test chain at a rate proportional to the flow rate (Fig. 2.9). Hence, Marrucci[47] who first recognized the importance of this phenomenon and modeled successfully called this nonlinear process *convective constraint release* (CCR).

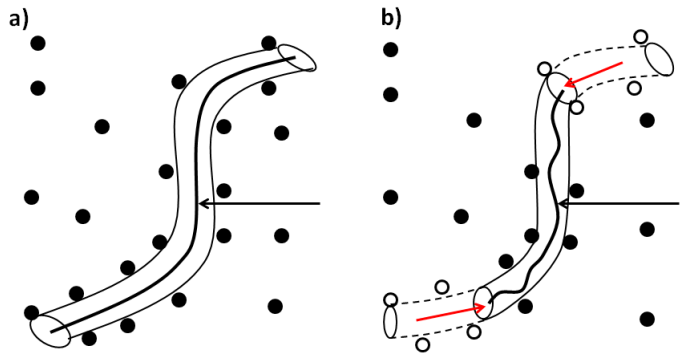

Figure 2.9: As the test chain retracts it releases the constraints that it was imposing on neighbouring chains.

Doi-Edwards Model

The kinetic theory of Doi and Edwards[38] model incorporates the entanglement interaction for entangled linear polymer melts via the tube concept. In this model, the relaxation of polymer chains occurs by two mechanisms the first is *chain retraction* by equilibration along the tube contour, which is supposed to be a fast process governed by the Rouse time, τ_R, of the chains, where the Rouse time is proportional to the square of the molar mass. The second relaxation process is the chain diffusion by *reptation* out of the tube with a reptation or disengagement time, τ_d, which is proportional to the third power of the molar mass. Doi and Edwards[38] noticed that since $\tau_s = 2\tau_R$ is expected to be much smaller than the reptation time, τ_d, then for flows that are fast compared to the rate of reptation $1/\tau_d$, but slow compared to the rate of retraction $1/\tau_s$, one can assume that the chains remain completely retracted during flow, means there is no chain stretch. Under this assumption Doi and Edwards[38] derived the famous constitutive equation that bears their name:

$$\underline{\underline{\sigma}}(t) = \int_{-\infty}^{t} m(t-t')\underline{\underline{S}}^{IA}_{DE}(t')dt' \tag{2.18}$$

where, the $\underline{\underline{S}}^{IA}_{DE}(t')$ denotes the strain measure of the Doi-Edwards theory with the independent alignment assumption:

$$\underline{\underline{S}}^{IA}_{DE}(t') = \frac{15}{3}\langle\frac{u'u'}{u'^2}\rangle \tag{2.19}$$

where u' is the length of the deformed unit vector $u = (u_x, u_y, u_z)$ and $\langle\ \rangle$ denotes an average over all possible orientations. A highly accurate approximation for this strain measure was proposed by Currie[4]:

$$\underline{\underline{S}}^{IA}_{DE} \equiv \left(\frac{5}{J-1}\underline{\underline{B}}\right) - \left[\frac{5}{(J-1)(I_2+13/4)^{1/2}}\right]\underline{\underline{C}} \tag{2.20}$$

where

$$J \equiv I_1 + 2(I_2 + 13/4)^{1/2} \tag{2.21}$$

where I_1 and I_2 are the Finger tensor two scaler invariants. For monodisperse polymer melts and solutions, the Doi-Edwards model seems to give an acceptable description of material behaviour in step-shear experiments. The biggest failure of the Doi-Edwards model is in steady-state shear flow where it predicts excessive shear thinning. In addition, in extensional flow, the DE theory predicts extensional thinning, rather than the extensional thickening often observed experimentally. The Doi-Edward model also leads to an incorrect prediction of the dependence of the zero-shear viscosity on the polydispersity[46,48,4].

Molecular Stress Function (MSF) Model

The MSF model[49,50,51] is a single tube segment model which quantitatively describes the nonlinear rheology of linear and LCB polymer melts. According to the MSF model, which allows not only for chain orientation as described by the orientation tensor, but also for chain stretching, the strain measure is expressed as product of the square of relative stretch, f^2, and the respective orientation tensor components S^{DE}_{IA} as given by

$$\underline{\underline{S}}^{MSF} = f^2\underline{\underline{S}}^{DE}_{IA} \tag{2.22}$$

In the MSF model, chain stretch is considered as a consequence of the tube diameter decreasing from its equilibrium value a_0 to a value a(t, t') with increasing deformation and the molecular stress function $f = f(t, t')$ is inversely proportional to the tube diameter a (Fig. 2.10):

$$f(t, t') = \frac{a_0}{a(t, t')} \tag{2.23}$$

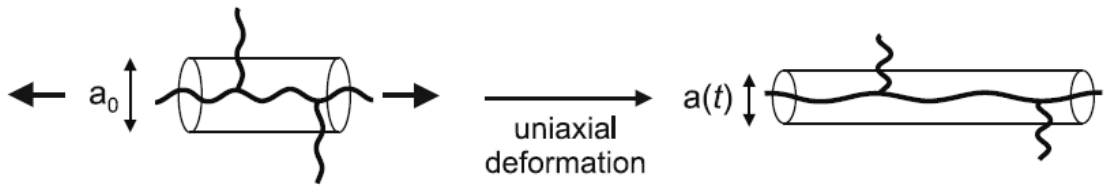

Figure 2.10: Influence of uniaxial deformation on the tube diameter a.

Assuming constraint release (CR) a dissipative process, a more general form of evolution equation of f^2 was proposed[50,51]:

$$\frac{\partial f^2}{\partial t} = \frac{\beta f^2}{1 + \frac{\beta - 1}{f^4}} \left[(\underline{\underline{\kappa}} : \underline{\underline{S}}) - \frac{1}{f^2 - 1} CR \right] \tag{2.24}$$

where β is a nonlinear parameter of the model. For the case of irrotational flows such as uniaxial, biaxial, and planar extension, the time evolution equation for f^2 can be written as [50,51]:

$$\frac{\partial f^2}{\partial t} = \dot{\epsilon} \frac{\beta f^2}{1 + \frac{\beta - 1}{f^4}} \left[S_{11} + m S_{22} - (1 + m) S_{33} - \frac{f^2 - 1}{f^2_{max} - 1} \sqrt{S_{11} + m^2 S_{22} + (1 + m)^2 S_{33}} \right] \tag{2.25}$$

where $m = -0.5$ for uniaxial, $m = 1$ for equibiaxial and $m = 0$ for planar deformations.

Pom-Pom Model

McLeish and Larson[52] developed a nonlinear viscoelastic theory for Pom-Pom molecular architecture which are idealized branched polymers with multiple branches, but only two branch points (Fig. 2.11). The motivation behind the development of this model was to capture the intricate behavior of polymers at large deformations in extension and shear simultaneously, which had been the challenge until this point. In this model, the two dominant relaxation processes, backbone re-orientation and backbone stretch relaxation, are determined from the branch disentanglement time. The re-orientation relaxation time, τ_d, is the average time it takes the backbone to reptate via its branch points diffusing along the backbone tube, out of a tube of unstretched length. The backbone stretch relaxation time, τ_s, is the time necessary for the path length of the backbone to return from some displaced length to its equilibrium length. The original differential form of McLeish and Larson[52] was improved with the flow induced local branch-point displacement correction[53] and modification of backbone reorientation time for very fast non-linear flows[54]. Therefore, the revised Pom-Pom model equations are as follows:

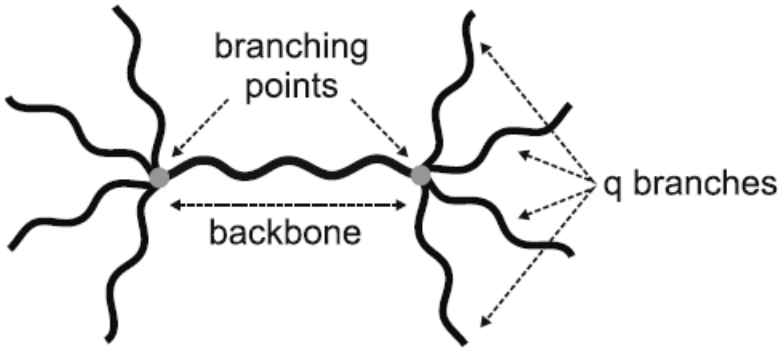

Figure 2.11: Pom-Pom molecule.

$$\text{stress :} \qquad \underline{\underline{\sigma}} = G_0 \phi_b^{\beta} \lambda^2(t) \underline{\underline{S}}(t)$$

$$\text{orientation :} \qquad \underline{\underline{S}}(t) = \underline{\underline{A}}/\mathbf{tr}A$$

$$\dot{\underline{\underline{A}}} - \underline{\underline{\kappa}} \cdot \underline{\underline{A}} - \underline{\underline{A}} \cdot \underline{\underline{\kappa}} = -\frac{1}{\tau_b}\left(\underline{\underline{A}} - I\right)$$

$$\text{stretch :} \qquad \frac{D\lambda(t)}{Dt} = \lambda(t)\underline{\underline{\kappa}} : \underline{\underline{S}} - \frac{1}{\tau_s}\left[\lambda(t) - 1\right]\exp(v^*(\lambda(t) - 1))$$

$$\text{time scales :} \qquad \tau_s = \frac{5}{2} q s_b \phi_b^{\beta-1} \tau_a \qquad \tau_d = \frac{75}{2\pi^2} q s_b^2 \phi_b^{2(\beta-1)} \tau_a$$

$$\text{reversing flow correction:} \frac{1}{\tau_d^*} = \begin{cases} \dfrac{1}{\tau_d} & \text{for } 1 \le \lambda \le q \\ \dfrac{1}{\tau_d} + \dfrac{\dot{\lambda}}{\lambda} - \underline{\underline{\kappa}} : \underline{\underline{S}} & \text{for } \lambda < 1 \end{cases}$$

where S_b and S_a are the dimensionless molecular weights of the backbone and arms, respectively, τ_a is the arm relaxation time, ϕ_b is the backbone fraction in the Pom-Pom molecule, $v^* = 2/(q-1)$ [see McLeish[42]] and $\beta = 2$.

2.3 Concluding Remarks on Various Constitutive Models Discussed in the Chapter 2

Various constitutive models used to predict the linear and nonlinear viscoelastic properties of polymer melts were discussed in this chapter. For the linear viscoelastic properties, Maxwell model provides the adequate prediction but no molecular insights can be revealed. This motivated the development of molecular theories, where the viscoelastic properties could be correlated with the macromolecule characteristics. The repation model was the first attempt to develop such theory, which predicted the qualitative behavior of linear polymer dynamics over a wide frequency

range. However, because of several missing relaxations, quantitative prediction is not possible. The Likhtman-McLeish model has incorporated the other possible mechanism of relaxation to predict quantitatively the linear viscoelastic response of linear polymers.

To predict the non-linear viscoelastic properties, one of the simplest description has been provided by the Giesekus model which is a phenomenological model. To understand the non-linear phenomena from macromolecule perspective, molecular theories were developed by incorporating large deformation effects on the dynamics of polymer chains. The Doi-Edwards model was the first detailed molecular theory for the nonlinear rheology of polymer melts. Since then, it serves the basis for almost all theories for the dynamics and rheology of entangled polymers. The Doi-Edwards model fails to capture commonly observed phenomena at large deformation, such as extensional hardening, excessive shear thinning in steady state shear flow.

The shortcomings of Doi-Edwards model are successfully overcome by the Pom-Pom and Molecular Stress function (MSF) models. Both incorporates, retraction of chain and convective constraint release along with the repation of polymer chains. The MSF model is more robust to predict the uniaxial and shear properties of model as well as industrial polymeric systems. However, MSF model is an integral model which is computational expensive. In contrast, the Pom-Pom model has a molecular parameter (branching, q) embedded in its formulation which makes it possible to study the effect of branching on various types of flows.

Chapter 3

FT-Rheology and Stress-Decomposition Techniques For the Analysis of Large Amplitude Oscillatory Shear Responses

Dynamic oscillatory shear tests are common in rheology to investigate the wide range of complex fluids. The oscillatory shear tests have many advantages over other rheological methods, such as the viscous and elastic mechanical properties can be simultaneously probed, oscillatory shear does not involve any sudden jumps in the shear-rate, therefore, a relatively easy flow to generate. The oscillatory shear tests broadly divided into two regimes on the basis of a stress response, small amplitude oscillatory shear (SAOS) and large amplitude oscillatory shear (LAOS) regime. In the SAOS regime, the stress is proportional to the applied deformation and rate of deformation. Whereas, in the LAOS regime, the stress is a nonlinear function of the applied deformation and rate of deformation. More specifically, the SAOS tests are employed frequently for probing the linear viscoelastic properties of complex fluids because of the easy estimation of the length and time scale of polymer melts. However, most processing operations are carried out at a large or rapid deformations. This facilitated the development of test protocols for the LAOS regime.

Recently, LAOS has been frequently used to characterize the nonlinear viscoelastic properties of soft matters[55,56,57,58]. The renewal of tremendous interest in exploring the LAOS flow response is due to the development of high sensitivity Fourier Transform (FT) rheology[59,60,61,62]. The development and use of extremely sensitive detection method was successful in overcoming the software and hardware limitations. Especially, the use of 'oversampling' with high performance

Analog-to-Digital Converter (ADC) card, electrical and mechanical shielding, and special FT algorithm[62]. The combination of all these improvements led to exceptionally high signal to noise ratio $S/N \approx 10^7$ as demonstration by Wilhelm et al.[57].

The Giesekus model simulations were performed to simulate the oscillatory shear responses under SAOS and LAOS flows. In the SAOS regime, the stress response is sinusoidal with the excitation frequency of $\omega/2\pi$ and the first normal stress difference response is sinusoidal with the twice of excitation frequency (Fig. 3.1). However, in the LAOS regime ($\gamma_0 = 10, \omega_1 = 0.1$ Hz), the responses are complex but periodic. In addition, the elastic storage modulus, $G^{'}$, and viscous dissipation modulus, $G^{''}$, variation as a function deformation amplitude, γ_0, is displayed in Figure 3.1. The elastic and viscous modulus are independent of applied deformation amplitudes in the SAOS regime. Whereas, both the material parameters displayed a dependance on the applied deformation amplitude in the LAOS regime. In addition, it should be kept in mind that in the LAOS regime the complete stress response cannot be represented by the elastic and viscous modulus, but the higher order harmonics contribution should be incorporated.

Numerous methods were developed to quantify the nonlinearity in the LAOS shear stress response. The methods involve FT-Rheology[62], Lissajous-Bowditch curves (stress vs strain or stress vs strain rate)[11,56], decomposition into characteristic waveforms[63], generalized 'storage' and 'loss' modulus when decomposing the nonlinear stress data[64], Chebyshev polynomials using decomposing stress data[65] and further development of Chebyshev polynomials by[66], dimensionless graphs[67] and LAOS response decomposition into Sequence of Physical Process (SPP)[68]. Next, a detailed description of the FT-Rheology and Stress-Decomposition are provided for the LAOS responses analysis. Furthermore, the nonlinear material parameters derived from the FT-Rheology and Stress-Decomposition are discussed to quantify the nonlinearity under LAOS flow.

3.1 FT-Rheology

The FT-Rheology is based on Fourier transformation of oscillatory shear stress and first normal stress differences. The Fourier transformation of any real or complex time signal, $s(t)$, and the corresponding inverse transform of a frequency dependent spectrum $S(\omega)$ are usually defined in the following way:

$$S(\omega) = \int_{-\infty}^{\infty} s(t) \exp^{-i\omega t} dt, \qquad s(t) = \frac{1}{2\pi} \int_{-\infty}^{\infty} S(\omega) \exp^{+i\omega t} d\omega \tag{3.1}$$

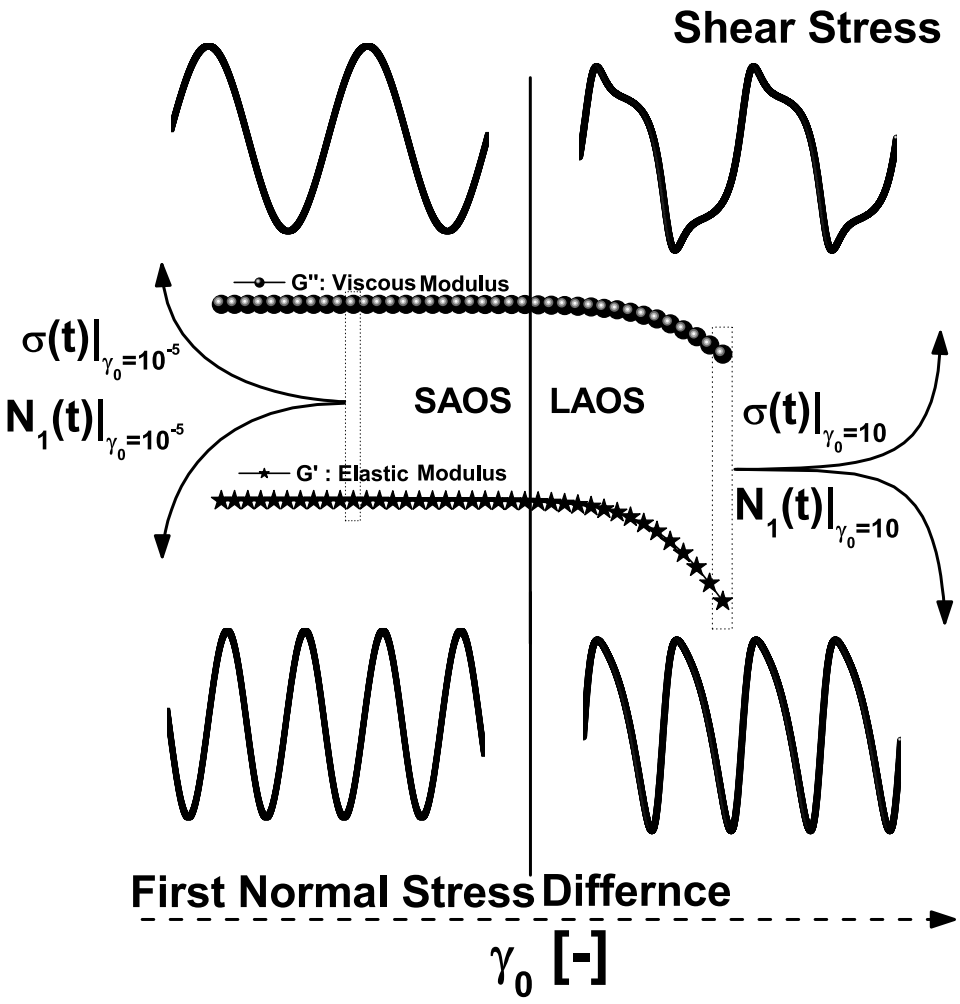

Figure 3.1: The simulated stress and first normal stress difference response using Giesekus Model where $\tau = 1$ s, $\omega_1 = 0.1$ rad/s, $\alpha = 0.5$, and $G = 1$ Pa.

To implement FT-Rheology, a half-sided, discrete, complex Fourier transformation is applied to the shear stress signal $\sigma(t)$. To obtain highly resolved, artifact-free spectra with a low noise level, the time signal has to be acquired with sufficient care. In particular, mechanical and electrical shielding are typically used in combination with data oversampling techniques to increase significantly the quality of the raw time data[59,60,61,62].

In general the Fourier transformation is an invertible, linear, complex transformation over the infinite interval from $-\infty$ to $+\infty$. The Fourier transformation is a linear mathematical transformation defined on any signal $s(t)$ which we use to quantify mechanical nonlinearities. By supplying a "monochromatic" or single input frequency, $\omega_1/2\pi$, we ensure that any output from the system at frequencies other than $\omega_1/2\pi$ is associated with nonlinearity in the system response. These two aspects should be clearly separated. Any linear superposition of different signals in the time domain

will also lead to a linear superposition in the frequency domain since a Fourier transformation is a mathematically linear operation.

In the case of discrete and digitized sampling, the data is taken point by point with a fixed increment t_{dw} (the dwell time, or inverse sampling rate) over a total acquisition time $t_{aq} = t_{dw}N$. Thus, both time and amplitude have discrete values. Since the peaks in the FT-Rheology spectrum are in principle infinitely narrow, a long acquisition time t_{aq} over multiple cycles will decrease the observed line width and increases the signal-to-noise (S/N) ratio. The S/N-ratio can be defined as the ratio of the amplitude of the highest peak (="signal") divided by the standard deviation of the noise (="noise"). The noise level is the average value measured in a spectral window where no peak is anticipated. Typically about 5-50 cycles of the fundamental deformation frequency are acquired at a given strain amplitude, to achieve high $S/N \approx 10^7$. This leads to a number of acquired time data points N in the range of 1000-10,000. In most experiments, the time data $s(t)$ is not measured continuously but discretely after fixed time steps and is then digitized via a k-bit analog-to-digital converter (ADC) having 2^k discrete values for representing the measured signal. Typically a 100-200 kHz, 16-bit ADC prior to oversampling is used for FT-Rheology experiments.

A fast Fourier transformation (FFT) is a very common and particularly fast algorithm for discrete Fourier transformation (DFT) but is not suitable for FT-Rheology. While the more general discrete FT algorithm is formulated for an arbitrary numbers of points N, the simplest and most common FFT algorithms, e.g. the butterfly, require $N = 2^n$ data points. This restriction leads to fixed discrete values for the acquisition time t_{aq} and thus for the spectral resolution $\triangle\nu = 1/t_{aq}$. As a result, the fundamental frequency $\nu_1 = \omega_1/2\pi$ or the odd multiples at $(2k+1)\omega_1/2\pi$ are rarely located exclusively at a single data point having the precise frequency corresponding to integer multiples of the fundamental excitation within the FT-Rheology spectra. The application of a butterfly FFT can therefore introduce misleading results for the intensities and phases of the spectral intensities. For example the intensity of a higher harmonic cannot be read out at exactly the expected frequency value. A maximum error of up to a factor 2 might be introduced this way. More advanced FFT-algorithms exist that can provide an FT for arbitrary number of data points, and the most fundamental discrete Fourier transform (DFT) algorithms also allow for arbitrary data points. It is therefore important to report if the applied algorithm does simple zero-filling to generate artificially 2^n temporal data points prior to the transformation into frequency space[59,60,61,62].

3.1.1 Shear Stress

An adequate mathematical representation for a time-dependent oscillatory shear stress response is a Fourier series, and the term FT-Rheology refers to the practice of representing the periodic oscillatory stress response as:

$$\sigma(t;\omega,\gamma_0) = \gamma_0 \sum_{n}^{\infty} \left[G_n^{'}(\omega,\gamma_0)\sin(n\omega t) + G_n^{''}(\omega,\gamma_0)\cos(n\omega t) \right] \tag{3.2}$$

This FT framework is mathematically robust and reduces to the linear viscoelastic framework in the limit of small deformations. Figure 4.7 shows Fourier transformations of the stress responses simulated using the Giesekus model at the applied deformation amplitudes of $\gamma_0 = 10^{-5}$ and 10^{1}. On applying the Fourier transformation on stress response at the applied deformation amplitude of $\gamma_0 = 10^{-5}$, only the fundamental Fourier intensity, $I_{1/1}$, is observed. This implies the stress response is proportional to the applied deformation and deformation-rate. This is the typical Fourier spectrum of material response in the SAOS regime (linear viscoelasticity). However, the appearance of multiple odd Fourier harmonics are observed at the applied deformation amplitude of $\gamma_0 = 10^{2}$. Obviously, such a large amount of higher harmonics contribution can lead to complex interpretation.

Hyun et al.[69] subdivided the nonlinear oscillatory shear tests into two sub-regimes, Medium Amplitude Oscillatory Shear (MAOS) and LAOS. The MAOS is an intermediate regime between the SAOS and LAOS. In this regime, the following scaling law, $I_{n/1} \propto \gamma_0^{n-1}$, is valid for odd natural number ($n = 3, 5, ...$). The validity of this scaling law for the $I_{3/1}(\gamma_0)$ was reported for both the viscoelastic constitutive equations [Giesekus model[70], Molecular Stress Function (MSF) model[71], Pom-Pom model[72]] and experiments[69,73,74].

The Giesekus model is used to simulate the shear stress as a function of γ_0 at Deborah number ($De = \omega\tau$) equal to one. Then, the FT-Rheology technique is applied to analyze the shear stress response. Figure 3.3 illustrates the variation of odd higher harmonics, $I_{3/1}(\gamma_0)$, $I_{5/1}(\gamma_0)$ and $I_{7/1}(\gamma_0)$ as a function of γ_0. All the odd harmonics displayed the scaling $I_{n/1} \propto \gamma_0^{n-1}$ over the deformation amplitude range of $\gamma_0 = 0.1 - 1$, i.e, the MAOS regime. This is followed by the deviation from the scaling, i.e, the LAOS regime.

The third higher harmonic, $I_{3/1}(\gamma_0)$, is frequently used to quantify the nonlinearity in the nonlinear viscoelastic regime[55,57,58]. In the Giesekus model simulations the sensitivity for the detection

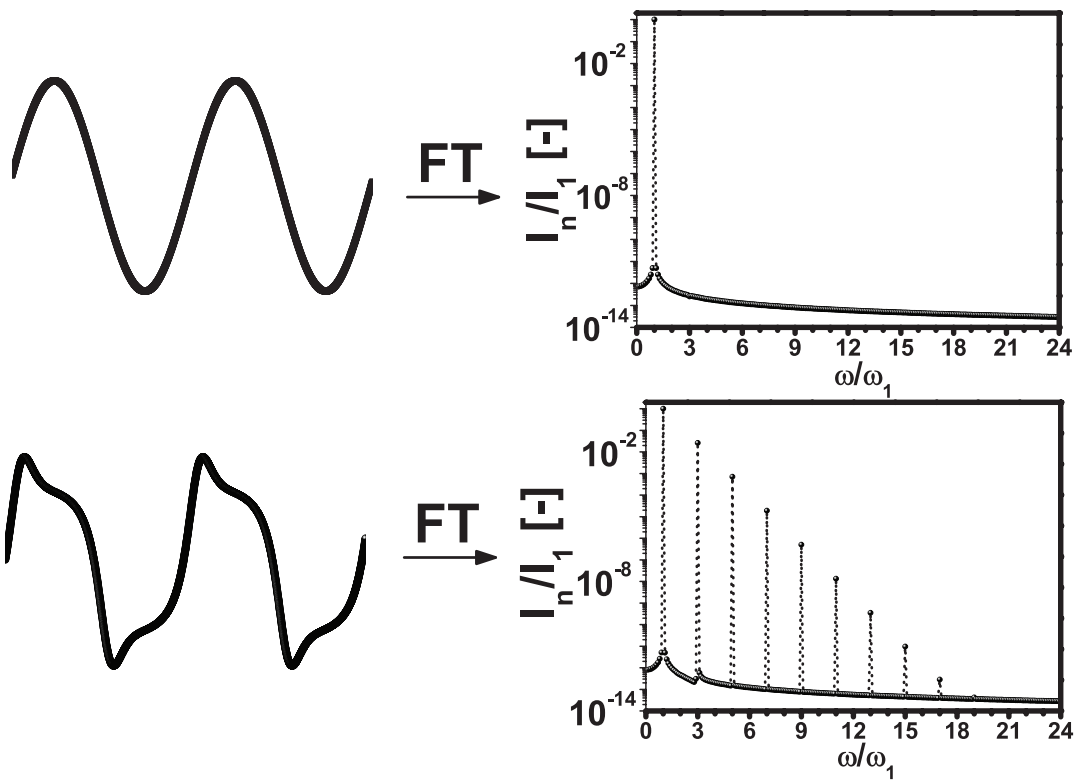

Figure 3.2: The Fourier transformation of simulated shear stress response using the Giesekus model at applied deformations, $\gamma_0 = 0.000001$ (SAOS), $\gamma_0 = 10$ (LAOS), with following parameters: $\tau = 1$ s, $\omega_1 = 0.1$ rad/s, $\alpha = 0.5$, and $G = 1$ Pa.

of higher harmonic is $S/N \approx 10^{-14}$ (Fig. 4.7). However, for the experimental measurements using the ARES G2 rheometer (TA Instruments) the typical sensitivity is $S/N \approx 10^{-5}$. The influence of the difference in signal-to-noise ratio between the simulations and experiments can be realized by comparing a experiment and a simulated strain sweep (Fig. 3.4). The significant difference is observed at the lower limit of deformation amplitudes. In the lower limit of deformation amplitudes, the experimental data are noisy and linearly regretted data follow the scaling $I_{3/1}(\gamma_0) \propto \gamma_0^{-1}$. However, the simulated $I_{3/1}(\gamma_0)$ follow the scaling $I_{3/1}(\gamma_0) \propto \gamma_0^2$. This difference in scaling exponent can be explained by the difference in the signal-to-noise ratio of experiments and simulations. In experiments, no $I_3(\gamma_0)$ was detected below $I_{3/1} < 10^{-5}$. However, I_1 is detectable and following the scaling, $I_1 \propto \gamma_0$. As a result the scaling exponent of -1 is obtained.

Motivated by the square scaling law $I_{3/1}(\gamma_0) \propto \gamma_0^2$ Hyun and Wilhelm[73] introduced a new nonlinear parameter $Q(\gamma_0)$ which is defined as follows:

$$Q(\gamma_0) = \frac{I_{3/1}}{\gamma_0^2} \tag{3.3}$$

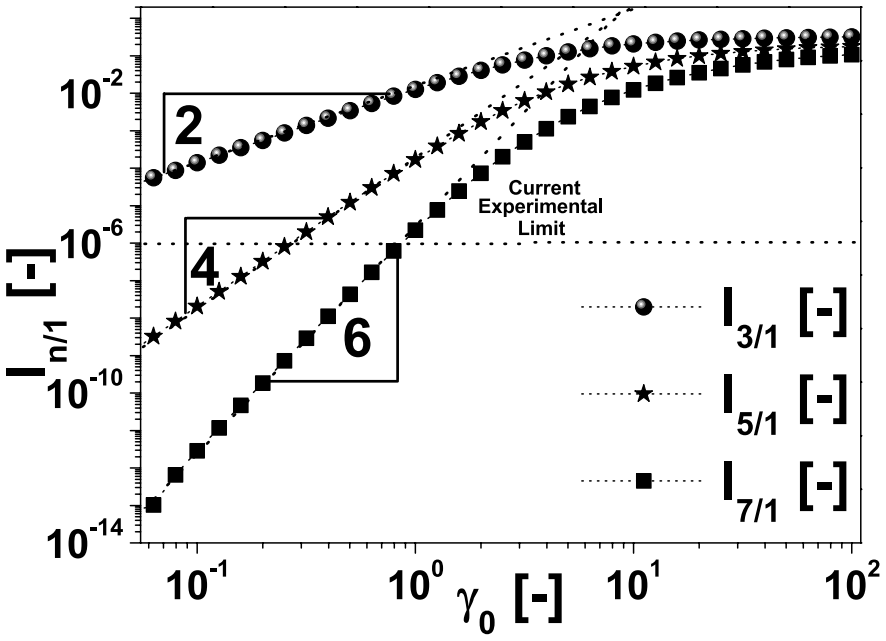

Figure 3.3: The variation of $I_{3/1}(\gamma_0)$, $I_{5/1}(\gamma_0)$, and $I_{7/1}(\gamma_0)$ as a function of applied deformation amplitudes, γ_0, where the stress response is simulated using the Giesekus model with following parameters: $\tau = 1$ s, $\omega_1 = 1$ rad/s, $\alpha = 0.5$, and $G = 1$ Pa.

By convention, the absolute strain amplitude value used in Eq. 3.3, not the % strain amplitude. Figure 3.5 illustrates the variation of $I_{3/1}(\gamma_0)$ and $Q(\gamma_0)$ as a function of applied strain amplitudes, γ_0, and nonlinear parameter (Giesekus model), α. One of the advantage of plotting the $Q(\gamma_0)$ instead of the $I_{3/1}(\gamma_0)$ as a function of γ_0 is the qualitative similarities with the well known rheological quantities, viscosity, $\eta(\dot{\gamma})$ or first normal stress coefficient, $\psi^1(\dot{\gamma})$. Similar to these rheological quantity, the $Q(\gamma_0)$ also approaches to a constant value at small deformation limit (Fig. 3.5b). As in the case of $\eta(\dot{\gamma}_0)$ and $\psi^1(\dot{\gamma})$, the limiting value at small shear-rate, $\dot{\gamma}$, are called zero shear-rate viscosity, η_0, and zero shear-rate first normal stress coefficient, ψ^1_0, respectively. Similarly, the limiting value at small strain was named zero strain nonlinearity or intrinsic nonlinearity, Q_0, which is defined as follows[73]:

$$Q_0(\omega) = \lim_{\gamma_0 \to 0} Q(\gamma_0, \omega) \tag{3.4}$$

The zero strain intrinsic nonlinearity, $Q_0(\omega)$, is frequently used to characterize the nonlinear viscoelastic effects in soft matters. For examples, the characterization of the topology (linear and comb) in PS melts[73,75], polydispersity in industrial linear PE melts[76], droplet size in dilute

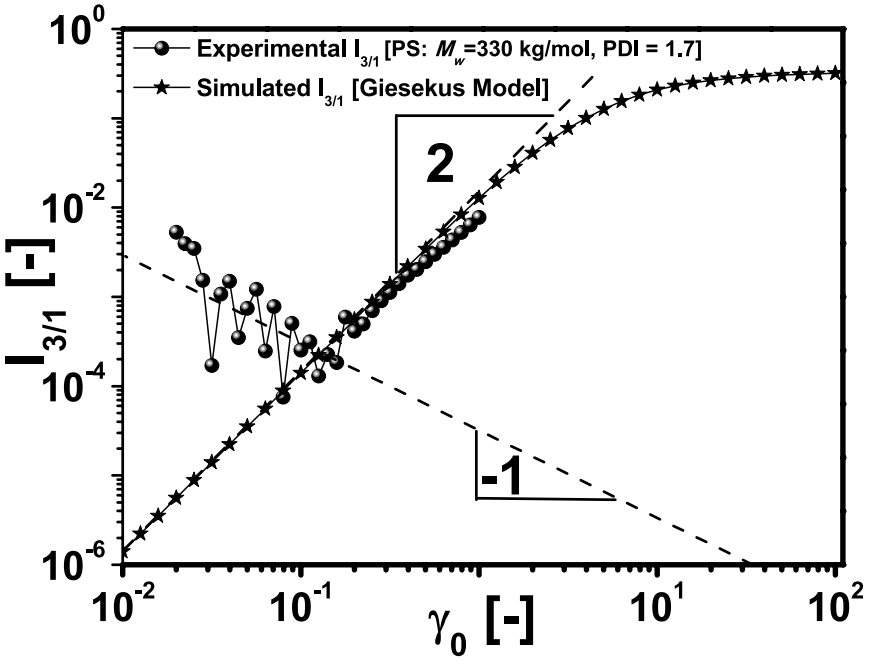

Figure 3.4: The variation of $I_{3/1}(\gamma_0)$ as a function of applied deformation amplitudes, γ_0, for the experiment and simulation at T=180°C. The following parameters were used for the Giesekus model simulation: $G_0^N = 2 * 10^5$ Pa, $\tau = 1.5$ s, $\omega_1 = 1$ rad/s, $\alpha = 0.3$.

monodisperse emulsions[74], droplet size distribution in polydisperse emulsions[58] and the polymer composites of PCL/MWCNTs[77].

Recently, a interesting analytical solution for Q_0 was proposed in terms of tube model parameters using the MSF model[71]. The authors showed that the zero strain intrinsic nonlinearity is proportional to $Q_0 \propto (\alpha_{Doi} - \beta)$, where α_{Doi} is the tube orientation parameter, and β is the backbone stretching parameter. One of the interesting result coming out of their study was that only the terminal relaxation of the backbone and, if present, the terminal relaxation of the entangled branches were related to the nonlinearity Q_0.

Hyun and Wilhelm[73] observed striking differences between the linear and comb PS melts by measuring the $Q_0(\omega)$. One of the remarkable difference was the appearance of two maximums in case of comb polymer melts. Whereas, the linear polymer only showed a single maximum. Kempf et al.[75] correlated the two maximums in case of the comb polymer melts to the backbone and arm relaxation time. In addition, corresponding frequency belongs to the minimum (between the two maximums) was correlated with Rouse relaxation time of backbone. Here, the Giesekus model is used to simulate the zero strain intrinsic nonlinearity Q_0 as a function of angular frequency, ω

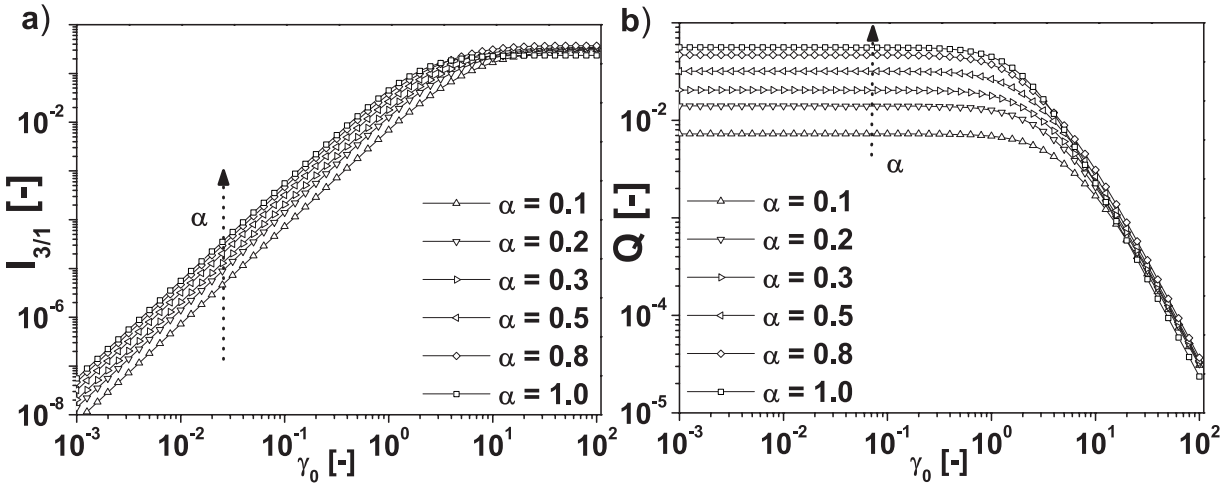

Figure 3.5: The variation of $I_{3/1}(\gamma_0)$ and $Q(\gamma_0)$ as a function of applied deformation amplitudes, γ_0, and Giesekus model nonlinear parameter, α, for following model parameters: τ = 1 s, ω_1 = 1 rad/s, and G = 1 Pa.

and α (Fig. 3.6a). The qualitative behaviour is similar at all the α and quantitatively a increase in the α leads to a increase in $Q_0(\omega)$. This implies the Giesekus model parameter, α, which is a measure of degree of anisotropy in the flow, has a inverse relation with the backbone stretching in the tube model [$Q_0 \propto (\alpha_{Doi} - \beta)$]. The appearance of only one maximum implies its ability to simulate the polymer melts whose response is only dominated by largest relaxation time scale. In addition, at the small frequency limit a square scaling, $Q_0 \propto \omega^2$, and at the large frequency limit a inverse scaling, $Q_0 \propto \omega^{-1}$ are observed. The square scaling at the small frequency limit using the Doi-Edwards model was derived by Pearson and Rochefort[78]. Motivated by the scaling law $Q_0 \propto \omega^2$ at low frequencies, we introduced a new nonlinear parameter μ which is defined as follows:

$$\mu = \frac{Q_0}{\omega^2} \tag{3.5}$$

Figure 3.6b shows the nonlinear parameter μ as a function of ω and α. In the low frequency limit the nonlinear parameter μ is approaching a constant value and at high frequencies μ-thinning is observed. The μ-thinning is defined as the decreases of μ-parameter as the frequency is increased. The limiting value at low frequencies is called zero shear-rate intrinsic nonlinearity, μ_0 which is defined as follows:

$$\mu_0 = \lim_{\omega \to 0} \mu(\omega) \tag{3.6}$$

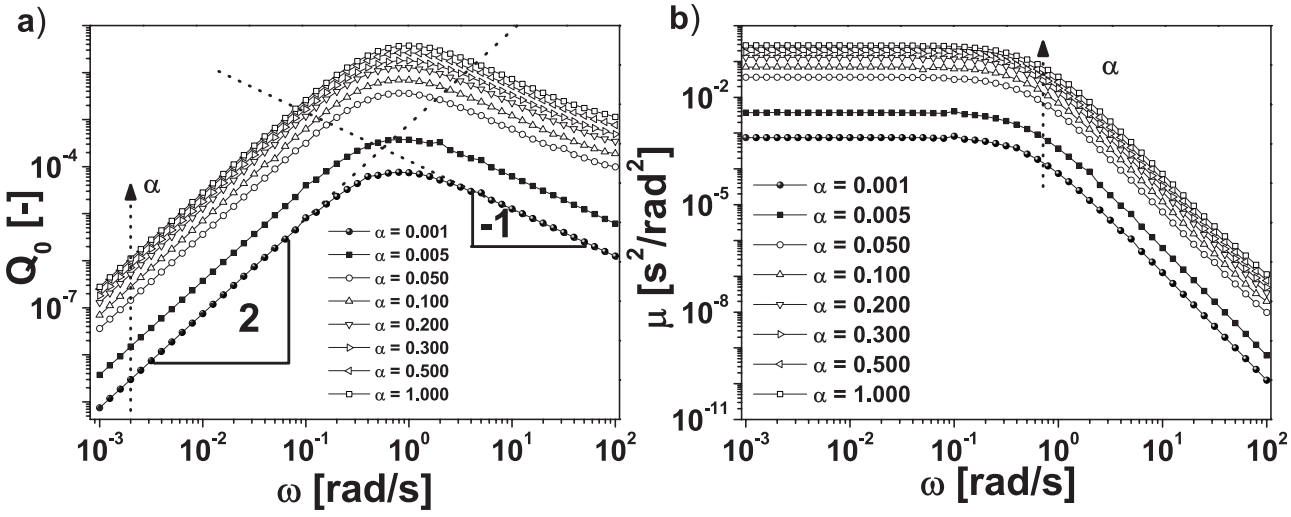

Figure 3.6: The variation of $Q_0(\omega)$ and $\mu(\omega)$ as a function of applied angular frequency, ω, and Giesekus model nonlinear parameter, α, for following model parameters: τ = 1 s and G = 1 Pa.

Figure 3.7 illustrates the variation of maximum zero strain intrinsic nonlinearity, Q_0^{max}, and zero shear-rate intrinsic nonlinearity, μ_0, as a function of α (Giesekus model nonlinear parameter). The following extracted power law relations $Q_0^{max} = 0.05\alpha^{0.8}$ and $\mu_0 = 0.10\alpha^{0.73}$ are displayed. The higher scaling exponent for the Q_0^{max} compared to the μ_0 illustrate the higher sensitivity for determining the nonlinear parameter, α.

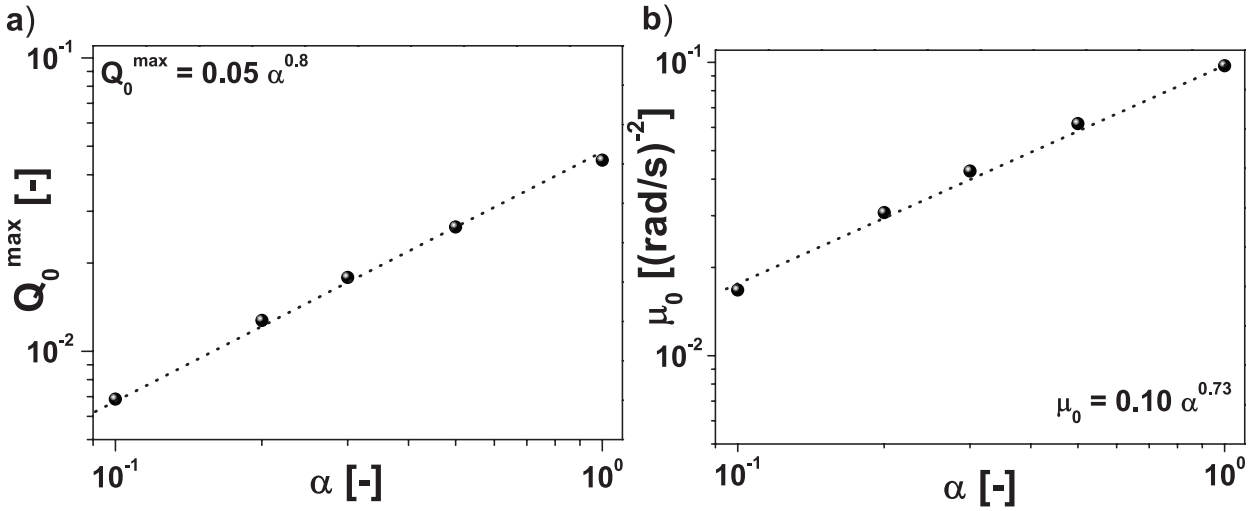

Figure 3.7: The variation of $Q_0^{max}(De = 1)$ and μ_0 as a function of Giesekus model nonlinear parameter, α, for following model parameters: τ = 1 s and G = 1 Pa.

3.1.2 Normal Stress Difference

Until now most of the focus was on the analysis of shear stress under LAOS flow. Whereas, the analysis of normal stress difference were ignored. This is often due to lack of accurate measurements of the normal stress difference during oscillatory shear. However, the normal stress may become larger than shear stress at high deformations, and thus it is important that we have a good understanding of the normal stress behaviour. Furthermore, with the advancement in the instrumentation, it has become possible to get more reliable data under oscillatory shear. For polymeric materials, the normal stress oscillates with a frequency that is twice the imposed frequency with a non-zero mean value[79,80]. Figure 3.8 shows the first normal stress difference responses and respective Fourier spectrums. In the linear regime, the first normal stress difference shows only the fundamental harmonic at the twice of excitation frequency. However, in the nonlinear regime, the resulting response is distorted and higher order even harmonics are observed in the Fourier spectrum.

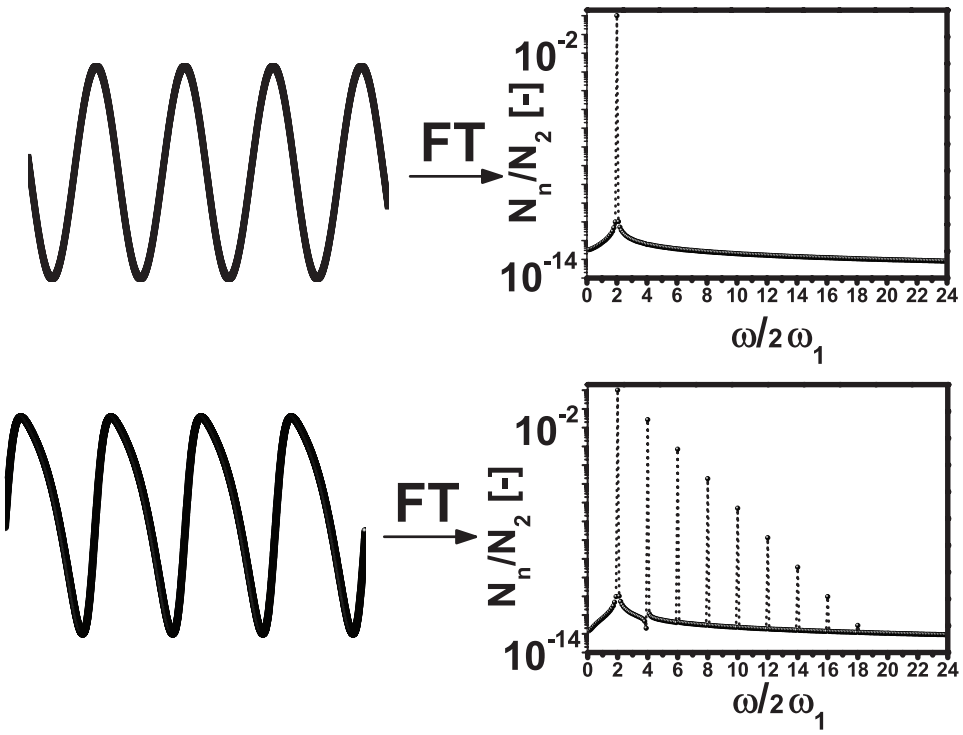

Figure 3.8: The Fourier transformation of simulated first normal stress response using the Giesekus model at applied deformations, $\gamma_0 = 0.000001$ (SAOS), and $\gamma_0 = 10$ (LAOS) with following parameters: $\tau = 1$ s, $\omega_1 = 1$ rad/s, $\alpha = 0.5$, and $G = 1$ Pa.

The normal stress differences under oscillatory shear condition can be written as the sum of constant term and an oscillating term with a phase angle ($\delta_{i,2}$). The normal stress differences in time domain can be represented by Fourier series as follows:

$$N_i = N_{i,0} + N_{i,2}^{'} \sin(2\omega t) + N_{i,2}^{''} \cos(2\omega t) + N_{i,4}^{'} \sin(4\omega t) + N_{i,4}^{''} \cos(4\omega t) + ... \tag{3.7}$$

where i is either the first ($i = 1$) or second ($i = 2$) normal stress difference. It is well known that the second normal stress difference ($i = 2$) in steady shear flow is typically smaller than the first ($i = 1$) by roughly an order of magnitude and its difficult to measure[81]. In the SAOS regime, the first normal stress can be calculated from the shear properties ($G^{'}$, $G^{''}$) by the phenomenological models as follows[81]:

$$\frac{N_{1,0}}{\gamma_0^2} = G^{'}(\omega) \tag{3.8}$$

$$\frac{N_{1,2}^{'}}{\gamma_0^2} = \left[G^{''}(\omega) - \frac{1}{2} G^{''}(2\omega) \right] \tag{3.9}$$

$$\frac{N_{1,2}^{''}}{\gamma_0^2} = \left[-G^{'}(\omega) + \frac{1}{2} G^{'}(2\omega) \right] \tag{3.10}$$

Figure 3.9a shows the fourth higher harmonic relative to fundamental harmonic, $N_{4/2}$, as function of applied deformation amplitudes, γ_0, and α. The square scaling, $N_{4/2} \propto \gamma_0^2$, is observed at low deformation amplitudes limit and at the higher deformation amplitudes $N_{4/2}$ deviates from the scaling. The $N_{4/2}$ increases with α over the simulated deformation amplitude range. Motivated by the square scaling we proposed Q^{N_1} which is defined as follows:

$$Q^{N_1} = \frac{N_{4/2}}{\gamma_0^2} \tag{3.11}$$

Figure 3.9b shows the Q^{N_1} as a function of applied deformation amplitudes, γ_0, and α. At the low deformation limit the Q^{N_1} is independent of applied deformation amplitudes. This motivated us to introduce a new intrinsic nonlinearity $Q_0^{N_1}$ which is defined as follows:

$$Q_0^{N_1}(\omega) = \lim_{\gamma_0 \to 0} Q^{N_1}(\gamma_0, \omega) \tag{3.12}$$

Figure 3.10a illustrates the variation of $Q_0^{N_1}(\omega)$ as a function of ω and α. The maximum is observed at $\omega = 1$ s and a square scaling law is observed, $Q_0^{N_1}(\omega) \propto \omega^2$, at the small frequency limit. The qualitative behavior is similar to the simulated intrinsic nonlinearity $Q_0(\omega)$ except at

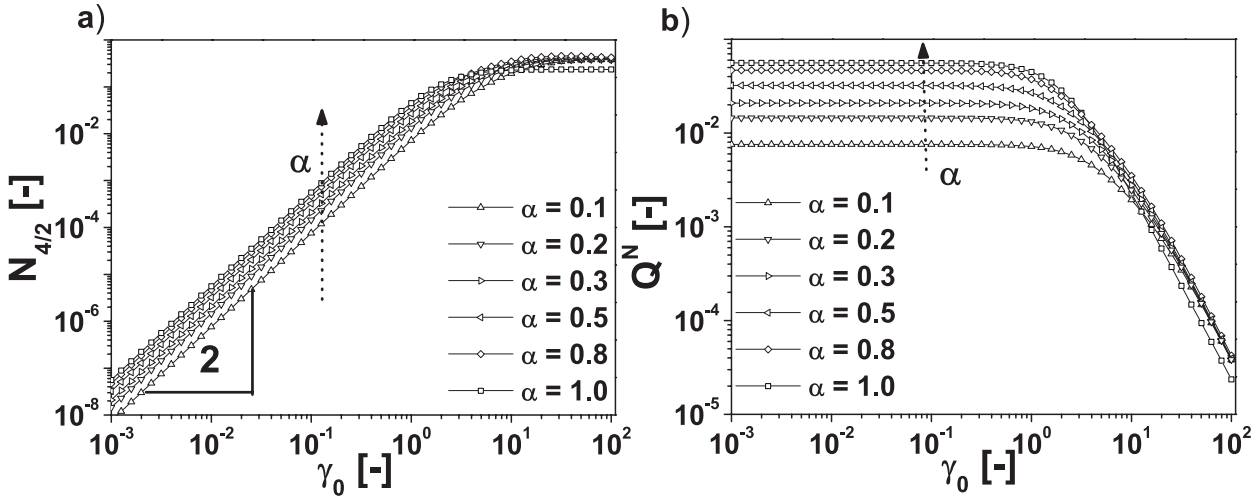

Figure 3.9: The variation of $N_{4/2}(\gamma_0)$ and $Q^N(\gamma_0)$ as a function of applied deformation amplitudes, γ_0, and Giesekus model nonlinear parameter, α, for following model parameters: τ = 1 s, ω_1 = 1 rad/s, and G = 1 Pa.

the large frequency limit. At the large frequency limit $Q_0(\omega)$ displayed the scaling law [$Q_0(\omega) \propto \omega^{-1}$], but in the case of $Q_0^{N_1}(\omega)$ the value seems to converge to one constant value for simulated α. Motivated by the square scaling in the low frequency limit, we introduced a new nonlinear parameter μ^{N_1} which is defined as follows:

$$\mu^{N_1} = \frac{Q_0^{N_1}(\omega)}{\omega^2} \tag{3.13}$$

Figure 3.10b illustrates the variation of $\mu^{N_1}(\omega)$ as a function of ω and α. The $\mu^{N_1}(\omega)$ displayed a increase with α over the simulated deformation amplitudes range. In the low frequency limit $\mu^{N_1}(\omega)$ is independent of applied frequency. This motivated us to introduce a intrinsic zero shear-rate nonlinearity, $\mu_0^{N_1}$, by the analysis of first normal stress measurements. The $\mu_0^{N_1}$ is defined as follows:

$$\mu_0^{N_1} = \lim_{\omega \to 0} \mu^{N_1}(\omega) \tag{3.14}$$

Figure 3.11 illustrate the variation of $Q_{0,max}^{N_1}$ and $\mu_0^{N_1}$ as a function of α. The $Q_{0,max}^{N_1}$ displayed a monotonically increasing trend with α. The $\mu_0^{N_1}$ displayed a increasing trend but the changes in the parameter is significantly small in the range $\alpha = 0.5 - 1$.

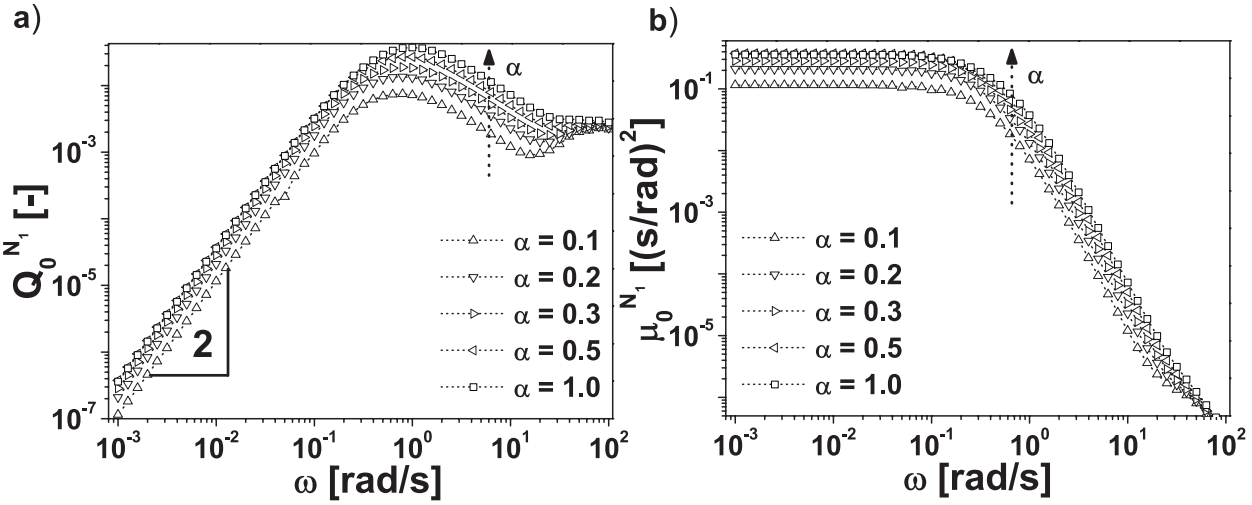

Figure 3.10: The variation of $Q_0^{N_1}(\omega)$ and $\mu_0^{N_1}(\omega)$ as a function of applied angular frequency, ω, and Giesekus model nonlinear parameter, α, for following model parameters: $\tau = 1$ s and $G = 1$ Pa.

3.2 Stress Decomposition

In the SAOS regime (linear viscoelastic regime), the material is commonly characterized by the viscoelastic moduli $G^{'}(\omega)$ and $G^{''}(\omega)$ which has clear physical meaning. However, these linear viscoelastic moduli are not uniquely defined once the material response become nonlinear[82,64,65]. Although the FT framework is mathematically robust and reduces to the linear viscoelastic framework in the limit of small deformations, it suffers from two drawbacks. First, although FT-Rheology is a very sensitive indicator of nonlinearity, as quantified by the $I_{3/1}(\gamma_0, \omega)$[62], the FT framework does not result in a clear physical interpretation of the higher-order coefficients. Second, the use of the first harmonic coefficients $G_1^{'}(\gamma_0, \omega)$ and $G_1^{''}(\gamma_0, \omega)$ as measures of the viscoelastic moduli in the nonlinear regime (and which is often the output of commercial rheometers) is arbitrary and often fails to capture the rich nonlinearities that are apparent in the raw data signal[56].

The decomposition of stress response into characteristic response functions was the first step towards the physical interpretation of complex nonlinear response[63]. Klein et al.[63] used sine, square, and triangular waveforms as a set of 'basis functions' and represented stress response as a superposition of different physical phenomena. One of the shortcoming of using the basis functions was their non-orthogonality. Similarly, the so-called geometrical interpretation (also referred to as stress decomposition) introduced by Cho et al.[64] also suffers from non-orthogonality of the resulting material measures.

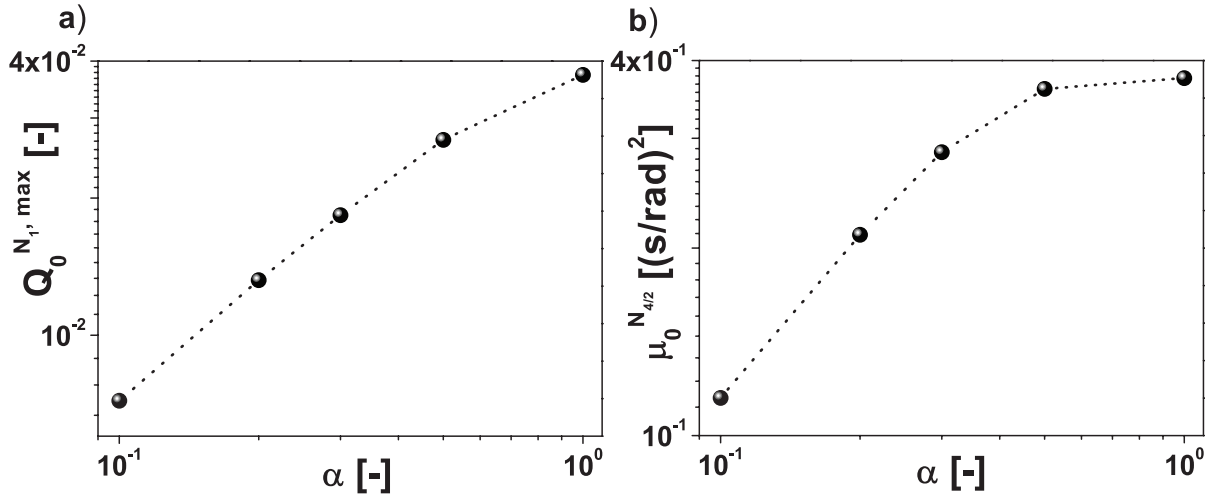

Figure 3.11: The variation of $Q_0^{N_1,max}(De = 1)$ and $\mu_0^{N_1}$ as a function of Giesekus model nonlinear parameter, α, for following model parameters: $\tau = 1$ s and $G = 1$ Pa.

To interpret LAOS data in a meaningful way, Ewoldt et al.[65] improved the method of stress decomposition which uses symmetry arguments to decompose the generic nonlinear stress response into superposition of an elastic stress $\sigma^{'}(x)$, where $x = \gamma/\gamma_0 = \sin(\omega t)$, and viscous stress $\sigma^{''}(y)$, where $y = \dot{\gamma}/\omega\gamma_0 = \cos(\omega t)$. The total oscillatory stress is the sum of the two contributions, $\sigma = \sigma^{'}(t) + \sigma^{''}(t)$. This decomposition is based on the idea that the elastic stress $\sigma^{'}$ should exhibit odd symmetry with respect to x and even-symmetry with respect to y, whereas viscous stress $\sigma^{''}$ should exhibit even-symmetry with respect to x and odd-symmetry with respect to y. The elastic and viscous stresses are related directly to the Fourier decomposition as follows:

$$\sigma^{'} = \frac{\sigma(\gamma,\dot{\gamma}) - \sigma(-\gamma,\dot{\gamma})}{2} = \gamma_0 \sum_{n\ odd} G_n^{'}(\omega,\gamma_0)\sin(n\omega t) \tag{3.15}$$

$$\sigma^{''} = \frac{\sigma(\gamma,\dot{\gamma}) - \sigma(\gamma,-\dot{\gamma})}{2} = \gamma_0 \sum_{n\ odd} G_n^{''}(\omega,\gamma_0)\cos(n\omega t) \tag{3.16}$$

Thus, in contrast to the closed loops formed by the total stress σ vs. γ or σ vs. $\dot{\gamma}$ (Fig. 3.12), plotting elastic stress $\sigma^{'}$ vs. x or viscous stress $\sigma^{''}$ vs. y produces single-valued functions of applied deformation and deformation-rate (Fig. 3.13). Fig. 3.13 illustrates this stress decomposition using the simulated LAOS response using the Giesekus model. Cho et al.[64] suggested a polynomial regression fit to these lines of elastic and viscous stress. However, the material properties represented by the polynomial coefficients are not unique since they depend on the order of the polynomial arbitrarily chosen by user. For example, given an unknown smooth function $F(x)$, a

regression fit to a first order polynomial $F = a_0 + a_1 x$ will always result in different coefficients a_0, a_1 than a regression fit to the higher order polynomial $F = a_0 + a_1 x + a_2 x^2 + ...$ except in the limit of $x \ll 1$ or if the unknown function is itself a linear function. Thus, fitting higher order terms affects the values of lower order terms, and a polynomial regression fits do not result in unique values for quantifying nonlinearity. A framework which breaks down beyond the limit $x \ll 1$ is not suitable for quantifying a nonlinear (viscoelastic) response.

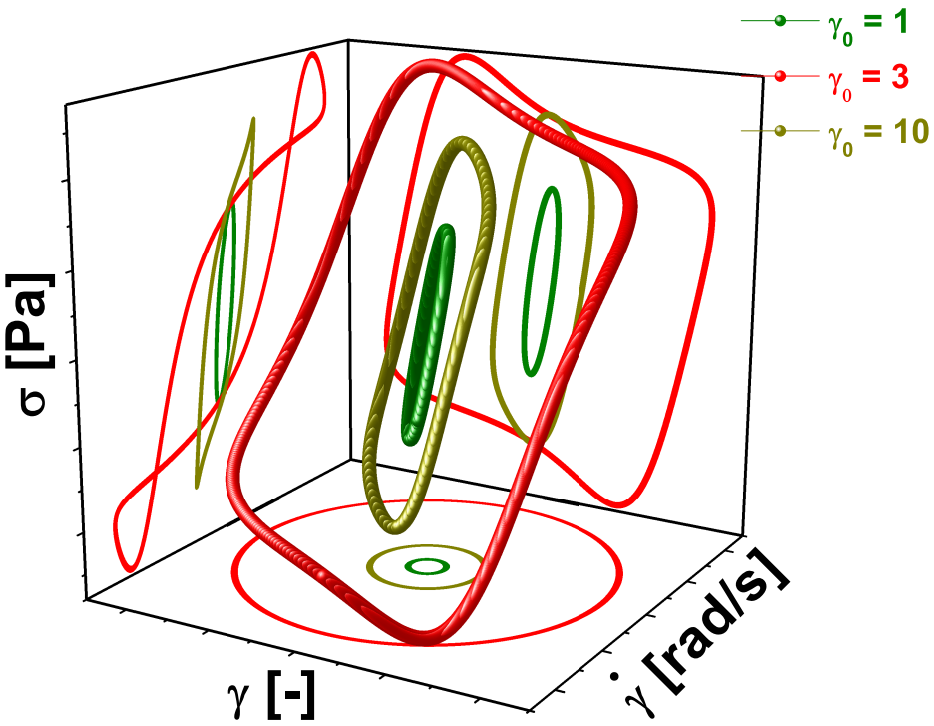

Figure 3.12: The simulated stress response at $\gamma_0 = 1$, 3, and 10, and $\omega_1 = 1$ rad/s using the Giesekus model with following parameters: $\tau = 1$ s, $\alpha = 0.5$, and $G = 1$ Pa,

Ewoldt et al.[65] chosen the Chebyshev polynomials of first kind among the various available orthogonal polynomial basis functions (Laguerre, Hermite, Jacobi, Legendre, and Chebyshev of the first and second kind). The particular choice exhibit (i) orthogonality over a finite domain (ii) odd symmetry about $x = 0$ and (iii) a bounded range for higher-order contributions. Laguerre and Hermite polynomials are eliminated because of their limits of orthogonality ([0,∞] and [−∞∞]), which contradicts the finite domain criteria. Jacobi polynomials are not appropriate, as they do not have symmetry about $x = 0$. Ultraspherical and Chebyshev (second kind) are ill-suited for LAOS due to their values at $x = \pm 1$. Finally, Legendre polynomials are eliminated because they are not directly related to the time-domain Fourier coefficient, thus implementation with previously

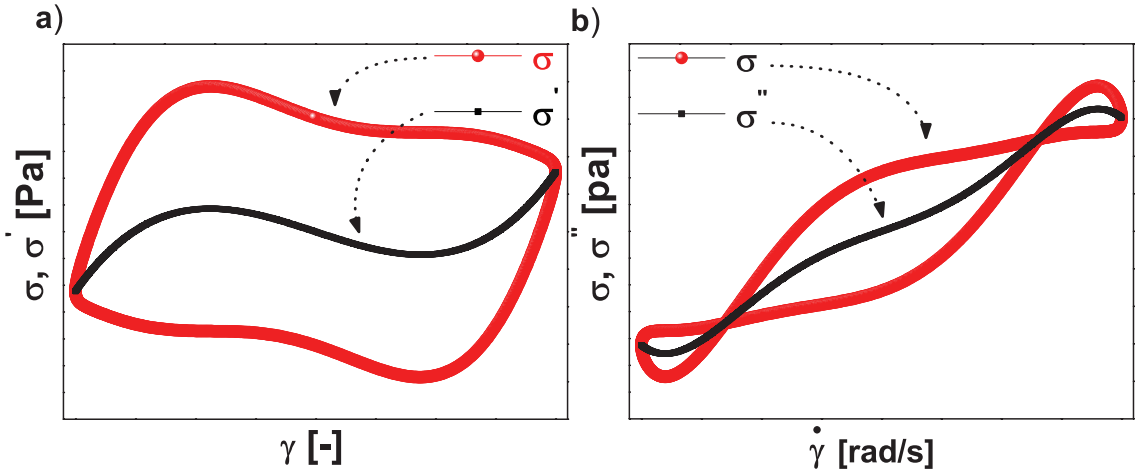

Figure 3.13: The simulated stress response at $\gamma_0 = 10$, and $\omega_1 = 1$ rad/s using the Giesekus model with following parameters: $\tau = 1$ s, $\alpha = 0.5$, and $G = 1$ Pa, (a) the total stress, σ, and elastic stress, σ^e, as a function deformation, γ, (b) the total stress, σ, and viscous stress, σ^v, as a function deformation-rate, $\dot{\gamma}$.

reported LAOS data and comparison with other LAOS interpretations would be unnecessarily complicated. Using this basis set, the elastic and viscous contributions to the measured stress response can be written as:

$$\sigma^{'}(x) = \gamma_0 \sum_{n:\ odd} e_n(\omega, \gamma_0) T_n(x) \tag{3.17}$$

$$\sigma^{''}(y) = \gamma_0 \omega \sum_{n:\ odd} v_n(\omega, \gamma_0) T_n(y) \tag{3.18}$$

where $T_n(x)$ is the n^{th}-order Chebyshev polynomial of the first kind, and $x = \gamma/\gamma_0$, $y = \dot{\gamma}/\gamma_0\omega$ provide the appropriate domains of [-1,+1] for orthogonality. The functions at each order are orthogonal and therefore the coefficients e_n, v_n are independent of each other. The $e_n(\omega, \gamma_0)$ is the elastic Chebyshev coefficients and $v_n(\omega, \gamma_0)$ is the viscous Chebyshev coefficients.

In the linear regime, the equations 5.4, 5.5 recover the linear viscoelastic result such that $e_1 \rightarrow G^{'}$ and $v_1 \rightarrow \eta^{'} = G^{''}/\omega$. The interpretation of any deviation from linearity, i.e. the $n = 3$ harmonic, as follows. A positive contribution of the third-order polynomial $T_3(x) = 4x^3 - 3x$ results in a higher elastic stress at the maximum dimensionless deformation, $x \rightarrow 1$ than is represented by the first-order contribution alone. Thus $e_3 > 0$ corresponds to intra-cycle stain-stiffening of the elastic stress, whereas $e_3 < 0$ indicates strain-softening. Similarly, a positive value for v_3 represents intra-cycle shear-thickening of the viscous stress, and $v_3 < 0$ describes shear-thinning.

These physical interpretations are not apparent in the time-domain (Fourier coefficients) but become immediately apparent from the sign of the Cheybyshev coefficients. The deliberate use of Chebyshev polynomials allowed the coefficients e_n and v_n to be calculated from the Fourier coefficients. The relationships between the Chebyshev coefficients in the strain or strain-rate domain and the Fourier coefficients in the time domain are thus given by:

$$e_n = G_n^{'}(-1)^{\frac{n-1}{2}} \qquad n : odd \tag{3.19}$$

$$v_n = G_n^{''}/\omega \qquad n : odd \tag{3.20}$$

Figure 3.14 illustrates the variation of $e_{3/1}(\gamma_0, \omega)$ as a function of applied deformation amplitudes, γ_0, and α. The $e_{3/1}(\gamma_0, \omega)$ is negative at the small deformation amplitudes limit $\gamma_0 = 10^{-2} - 10^{0}$ and positive at the large deformation amplitudes. The $e_{3/1}(\gamma_0, \omega) < 0$ implies a elastic softening and $e_{3/1}(\gamma_0, \omega) > 0$ a elastic thickening. In the low deformation amplitude limit the viscoelastic material exhibit the elastic softening and at large deformation it exhibit the elastic thickening at the applied frequency of $\omega/2\pi$. In the low deformation limit the square scaling $e_{3/1}(\gamma_0, \omega) \propto \gamma_0^2$ is observed. This motivated us to introduce the a nonlinear parameter Q^e which is defined as follows:

$$Q^e = \frac{e_{3/1}(\gamma_0, \omega)}{\gamma_0^2} \tag{3.21}$$

The Q^e at low deformation limit would approach a constant value similar to Q and Q^{N_1}. This motivated us to introduce intrinsic elastic nonlinearity Q_0^e which is defined as follows:

$$Q_0^e = \lim_{\gamma_0 \to 0} Q^e \tag{3.22}$$

Figure 3.15 illustrates the variation of $v_{3/1}(\gamma_0, \omega)$ as a function of applied deformation amplitudes, γ_0, and α. The $v_{3/1}(\gamma_0, \omega)$ was positive at the small deformation amplitudes limit, $\gamma_0 = 10^{-2} - 10^{1}$ and negative at the large deformation amplitudes. The $v_{3/1}(\gamma_0, \omega) < 0$ implies a viscous thinning and $v_{3/1}(\gamma_0, \omega) > 0$ a viscous thickening. In the low deformation amplitude limit the viscoelastic material exhibit the viscous thickening and at large deformation it exhibit the viscous thinning at the applied frequency of $\omega/2\pi = 1/2\pi$ Hz. In the low deformation limit the square scaling $v_{3/1}(\gamma_0, \omega) \propto \gamma_0^2$ is observed. This motivated us to introduce a nonlinear parameter Q^v which is defined as follows:

$$Q^v = \frac{v_{3/1}(\gamma_0, \omega)}{\gamma_0^2} \tag{3.23}$$

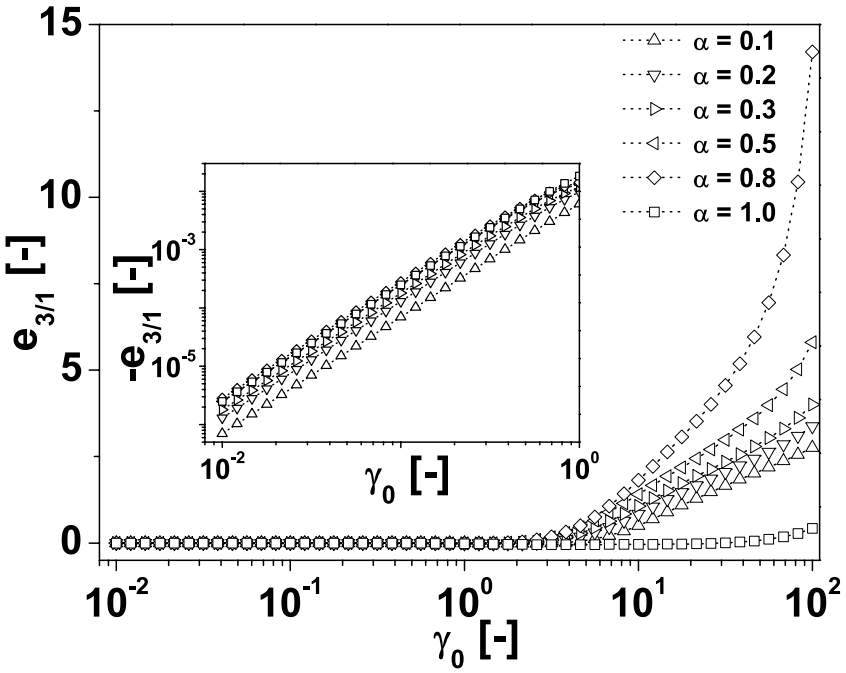

Figure 3.14: The variation of simulated $e_{3/1}(\gamma_0)$ as a function of γ_0 at applied angular frequency of $\omega_1 = 1$ rad/s. The following Giesekus model parameters were used for simulation: $\tau = 1$ s, $\alpha = 0.5$, and $G = 1$ Pa.

The Q^v at low deformation limit would approach a constant value similar to Q and Q^{N_1}. This motivated us to introduce intrinsic elastic nonlinearity Q_0^v which is defined as follows:

$$Q_0^v = \lim_{\gamma_0 \to 0} Q^v \tag{3.24}$$

Figure 3.16 illustrates the variation of $Q_0(\omega)$, $Q_0^e(\omega)$ and $Q_0^v(\omega)$ as a function of applied angular frequency, ω. The curves are shown only for one particular value of $\alpha = 0.5$ (Giesekus model non-linear parameter) because qualitative behaviour was similar for all the α values. The viscoelastic material in the simulated angular frequency range can be divided into four regime based on the sign of intrinsic elastic and viscous nonlinearity.

- Regime I: $Q_0^e > 0$ (elastic stiffening) and $Q_0^v < 0$ (viscous thinning)
- Regime II: $Q_0^e > 0$ (elastic stiffening) and $Q_0^v > 0$ (viscous thickening)
- Regime III: $Q_0^e < 0$ (elastic softening) and $Q_0^v > 0$ (viscous thickening)
- Regime IV: $Q_0^e < 0$ (elastic softening) and $Q_0^v < 0$ (viscous thinning)

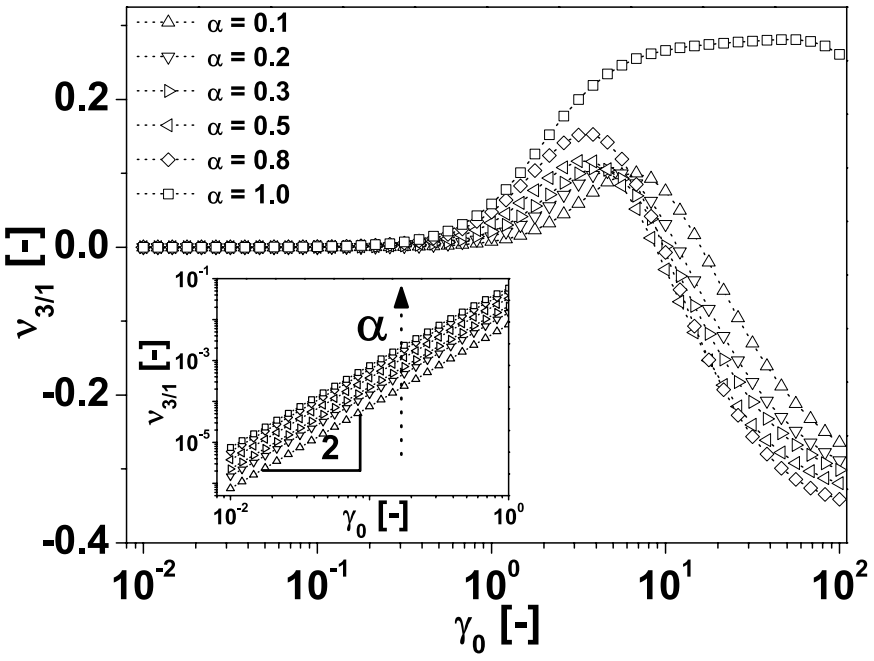

Figure 3.15: The variation of simulated $\nu_{3/1}(\gamma_0)$ as a function of γ_0 at applied frequency of $\omega_1 = 1$ rad/s. The following Giesekus model parameters were used for simulation: $\tau = 1$ s, $\alpha = 0.5$, and $G = 1$ Pa.

Recently, Ewoldt and Bharadwaj[83] proposed four intrinsic measures ($[e_1]$, $[\nu_1]$, $[e_3]$ and $[\nu_3]$) derived from the SD analysis in MAOS regime:

$$e_1(\gamma_0, \omega) = G^{'}(\omega) + [e_1](\omega)\gamma_0^2 + o(\gamma_0^4) \tag{3.25}$$

$$\nu_1(\gamma_0, \omega) = G^{''}(\omega) + [\nu_1](\omega)\gamma_0^2 + o(\gamma_0^4) \tag{3.26}$$

$$e_3(\gamma_0, \omega) = [e_3](\omega)\gamma_0^2 + o(\gamma_0^4) \tag{3.27}$$

$$\nu_3(\gamma_0, \omega) = [\nu_3](\omega)\gamma_0^2 + o(\gamma_0^4) \tag{3.28}$$

The proposed intrinsic nonlinearity in this chapter are directly correlated with the intrinsic measures proposed by Ewoldt and Bharadwaj[83]:

$$Q^e(\gamma_0, \omega) = \frac{e_{3/1}}{\gamma_0^2} = \frac{[e_3](\omega)\gamma_0^2 + o(\gamma_0^4)}{G^{'}(\omega) + [e_1](\omega)\gamma_0^2 + o(\gamma_0^4)} \frac{1}{\gamma_0^2} \tag{3.29}$$

$$Q^{\nu}(\gamma_0, \omega) = \frac{\nu_{3/1}}{\gamma_0^2} = \frac{[\nu_3](\omega)\gamma_0^2 + o(\gamma_0^4)}{G^{''}(\omega) + [\nu_1](\omega)\gamma_0^2 + o(\gamma_0^4)} \frac{1}{\gamma_0^2} \tag{3.30}$$

$$Q_0^e(\omega) = \frac{[e_3](\omega)}{G^{'}(\omega)} \tag{3.31}$$

$$Q_0^{\nu}(\omega) = \frac{[\nu_3](\omega)}{G^{''}(\omega)} \tag{3.32}$$

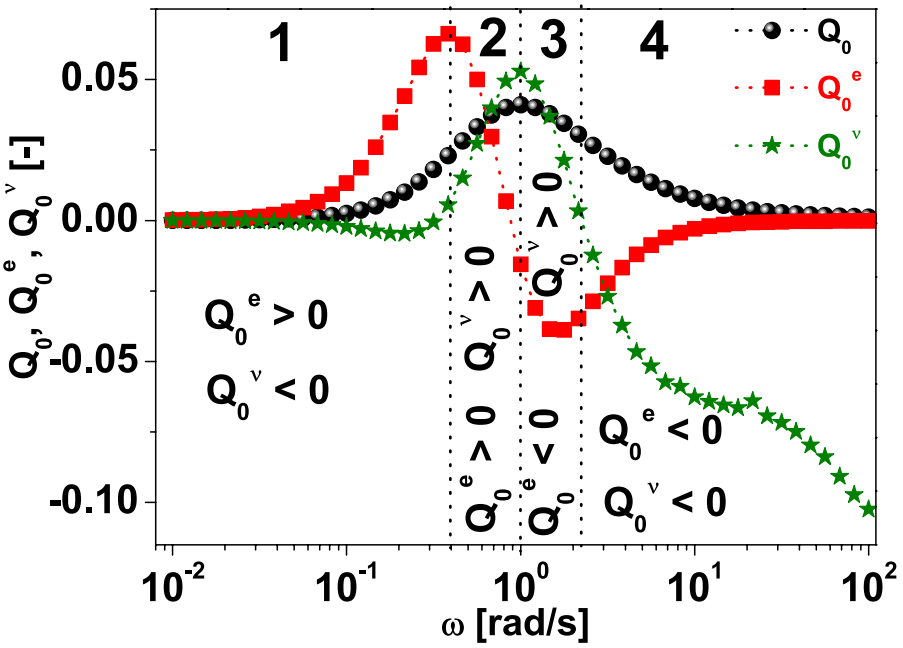

Figure 3.16: The variation of $Q_0(\omega)$, $Q_0^e(\omega$, and Q_0^v as a function of ω.

Figure 3.17 illustrates the variation of $Q_0^e(\omega)$ and $Q_0^v(\omega)$ as a function of α at $De = 1$ where $De = \omega\tau$. The $Q_0^e(\omega)$ is negative and decreasing with increasing α. However, $Q_0^v(\omega)$ displayed following power law $Q_0^v(\omega) \propto \alpha$. The scaling exponent for Q_0^v is higher than the Q_0^{max} and μ_0, which implies the highest sensitivity for nonlinear parameter determination.

3.3 Conclusions of Chapter 3

Large Amplitude Oscillatory Shear (LAOS) responses (shear and first normal stress difference) were simulated using the Giesekus model. The responses were analyzed using the FT-Rheology and Stress-Decomposition techniques. The zero strain intrinsic nonlinearity, $Q_0(\omega)$, observed to follow the scaling, $Q_0(\omega) \propto \omega^2$, at the limit of small frequencies. Furthermore, at large frequency limit the following scaling, $Q_0(\omega) \propto \omega^{-1}$ was observed. Motivated by the square scaling at the low frequency limit, we introduced a new zero shear-rate nonlinearity, μ_0. The μ_0 is only a function of nonlinear parameter, independent of applied strain and frequency. The μ_0 is monotonically increasing with nonlinear parameter, α.

The nonlinearity in first normal stress difference response were quantified using the fourth order higher Fourier harmonic relative to fundamental Fourier harmonic, $N_{4/2}$. At small deformation amplitudes, γ_0, limit the following scaling, $N_{4/2} \propto \gamma_0^2$, was observed. Motivated by this

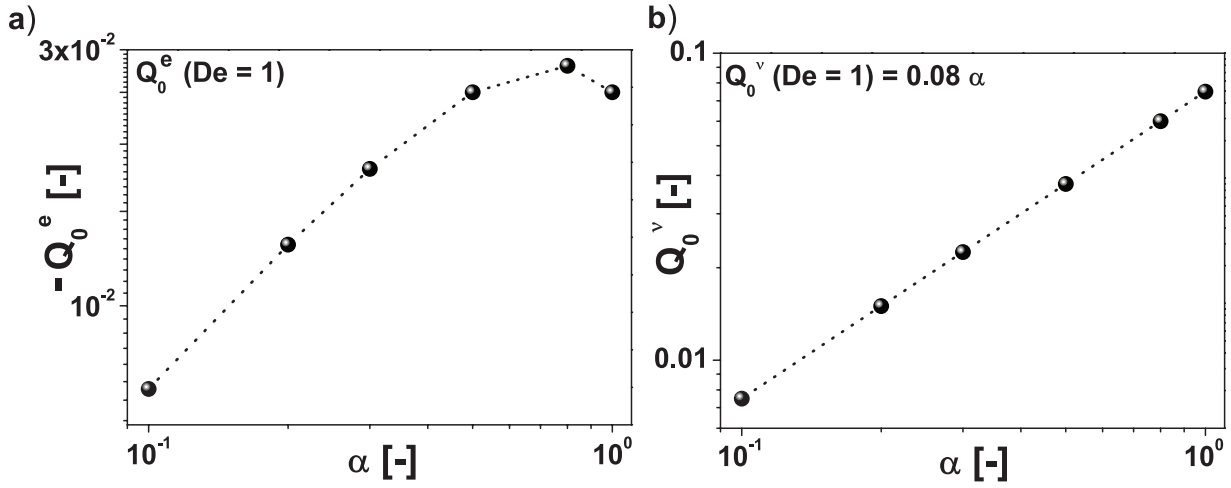

Figure 3.17: The variation of Q_0^e and Q_0^ν as a function of nonlinear parameter, α, at Deborah number equal to one, (a) Q_0^e vs. α, (b) Q_0^ν vs. α.

scaling, a new zero strain intrinsic nonlinearity, $Q_0^{N_{4/2}}(\omega)$, was introduced. Furthermore, this zero strain intrinsic nonlinearity at small frequency limit also observed to follow the square scaling, $Q_0^{N_{4/2}}(\omega) \propto \omega^2$. Similar to zero shear-rate nonlinearity, μ_0, a new zero shear-rate nonlinearity, $\mu_0^{N_{4/2}}$, based on the first normal stress measurement is introduced.

The shear stress response were also analyzed using the Stress-Decomposition method. The Chebyshev elastic third order harmonic relative to Chebyshev elastic fundamental harmonic, $e_{3/1}(\gamma_0, \omega)$, and Chebyshev viscous third order harmonic relative to Chebyshev viscous fundamental harmonic, $\nu_{3/1}(\gamma_0, \omega)$, also observed to follow the square scaling with applied deformation amplitudes. The square scaling motivated the introduction of zero strain intrinsic elastic nonlinearity, $Q_0^e(\omega)$, and zero strain intrinsic viscous nonlinearity, $Q_0^{\nu_{3/1}}(\omega)$. Interestingly, the $Q_0^{\nu_{3/1}}(\omega)$ as a function of Giseksus model nonlinear parameter, α, observed to follow the power law, $Q_0^{\nu_{3/1}}(\tau\omega = 1) \propto \alpha$ at Deborah number equal to one. This can be used to predict the nonlinear parameter, α, with one single strain sweep at the angular frequency of $\omega = 1/\tau$.

Chapter 4

Linear and Non-linear Viscoelasticity of Monodisperse Polystyrene Melts and its Blends using FT-Rheology

The effects of entanglement on the viscoelastic properties of flexible linear polymers is an active area of research in polymer physics[4,43,42]. One of the significant influences of entanglement is the zero shear-rate viscosity, η_0, dependence on molecular weight, M_w, where the following power law $\eta_0 \propto M_w^{3.4-3.6}$ holds for the entangled linear polymer melts[4]. The reptation theory[38] qualitatively predicts the dynamics of entangled monodisperse linear polymers in the linear viscoelastic regime. However, for quantitative prediction of the linear viscoelastic properties, Likhtman and McLeish[43] added several missing relaxation mechanisms (contour-length fluctuations and constraint release) in the reptation theory (details were described in chapter-2).

In addition to the molecular weight, molecular weight distribution is one the key parameter which has an influence on rheological properties. Remarkable progress has been made in interconnecting the viscoelastic properties with the molecular weight and molecular weight distribution[84,85,86,87]. While most of the scientific literatures focuses on the linear viscoelasticity, in this study, the nonlinear viscoelasticity of linear polymers (polystyrene) and blends of monodisperse linear polymers are investigated under the Large Amplitude Oscillatory Shear (LAOS) flow.

The Fourier-Transform (FT)-Rheology technique is used to analyze the stress response under LAOS flow. In FT-Rheology, the intensity of third Fourier harmonic relative to fundamental Fourier harmonic, $I_{3/1}$, has been frequently used to quantify the nonlinear viscoelasticity.

In LAOS, for a range of applied deformation amplitudes, a square scaling law, $I_{3/1} \propto \gamma_0^2$, was observed both experimentally[73,58] and by simulation of various nonlinear constitutive equations (Giesekus model[70], Pom-Pom model[72], Molecular Stress Function (MSF) model[71]). Motivated by this scaling law Hyun and Wilhelm[73] introduced a new nonlinear parameter $Q(\gamma_0, \omega) = I_{3/1}/\gamma_0^2$. At low deformation amplitudes limit, the Q-parameter converges to a constant value which they called zero strain intrinsic nonlinearity, $Q_0(\omega) := \lim_{\gamma_0 \to 0} Q(\gamma_0, \omega) = \lim_{\gamma_0 \to 0} I_{3/1}/\gamma_0^2$. The zero strain intrinsic nonlinearity, $Q_0(\omega)$, was used to characterize the branching effects for linear and comb polystyrenes (PS)[73] and polydispersity effects in industrial polyethylene (PE)[76].

To study the effect of entanglement on the nonlinear viscoelasticity, the zero strain intrinsic nonlinearity, $Q_0(\omega)$, is measured for monodisperse linear PS and its blends. The non-linear parameter, $\mu(\omega) = Q_0(\omega)/\omega^2$, at small frequency limit is observed to be independent of frequency for linear monodisperse PS polymer melts. This facilitated the experimental measurements of zero shear-rate intrinsic nonlinearity, μ_0, a new material parameter which was introduced in the previous chapter using the Giesekus model simulations. Similar to the zero shear-rate viscosity scaling, $\eta_0 \propto M_w^{3.4-3.6}$, a interesting scaling is observed for the intrinsic zero shear-rate nonlinearity, $\mu_0 \propto M_w^{8.85\pm0.15}$. Furthermore, the nonlinear viscoelastic master-curve, $Q_0(a_T\omega)$, was found to be a more effective way to detect the relaxation processes of long and short chains in binary blends relative to linear viscoelastic master-curve [$G^{'}(a_T\omega)$ and $G^{''}(a_T\omega)$].

4.1 Materials and Methods

4.1.1 Materials

The monodisperse PS with various molecular weights were synthesized by Dr. Kempf (member of our lab, currently working at 3M Germany) using anionic polymerization. The mixtures were prepared for the study of polydispersity effect by solution mixing using the THF (tetrahydrofuran). After mixing, excess amount of methanol was added for precipitation of the polymers. Methanol of 800 ml was added to every PS/THF solution of 100 ml. The precipitated polymers were filtered and dried at 50°C for 24 hours in the vacuum oven. For the prepared binary blends bi-model molecular weight distribution (Fig. 4.1a) were observed. The molecular weight distribution for quaternary blend is shown in Fig. 4.1b. For the polymer synthesized by radical polymerization where a uni-model molecular distribution was observed (Fig. 4.1c). The detailed specification of

the investigated materials are displayed in table 8.1.

Table 4.1: Characteristics of the investigated PS materials

Polymers	Blends	Weight Fraction (ϕ)	M_w [kg/mol]	M_w/M_n	Synthesis Method
PS-62k	Monodisperse	$\phi_{62k} = 1$	62	1.03	Anionic Polymerization
PS-79k	Monodisperse	$\phi_{79k} = 1$	79	1.04	Anionic Polymerization
PS-110k	Monodisperse	$\phi_{110k} = 1$	110	1.07	Anionic Polymerization
PS-179k	Monodisperse	$\phi_{179k} = 1$	179	1.09	Anionic Polymerization
PS-133k	Polydisperse	$\phi_{133k} = 1$	133	1.66	Free Radical Polymerization
B-PS-101k	PS-62k + PS-110k	$\phi_{62k} = 0.5$ $\phi_{110k} = 0.5$	101	1.14	Solution Blending
B-PS-103k	PS-79k + PS-110k	$\phi_{79k} = 0.5$ $\phi_{110k} = 0.5$	103	1.08	Solution Blending
B-PS-163k	PS-110k + PS-179k	$\phi_{110k} = 0.5$ $\phi_{179k} = 0.5$	163	1.13	Solution Blending
B-PS-109k	PS-62k + PS-79k + PS-110k + PS-179k	$\phi_{69k} = 0.25$ $\phi_{79k} = 0.25$ $\phi_{110k} = 0.25$ $\phi_{179k} = 0.25$	109	1.35	Solution Blending

4.1.2 Rheological Measurement Protocol

The rheological measurements were carried out on a strain controlled rheometer (ARES-G2, TA instruments) using a cone and plate geometry (13 mm , $\alpha = 0.1$ rad) under a nitrogen environment (99.8% vol) to reduce the degradation. The dynamic frequency sweep tests (SAOS) were performed over the temperature range from 140 to 200 °C. The LAOS experiments were performed on an ARES-G2 rotational rheometer from TA instruments using an implemented FT-Rheology

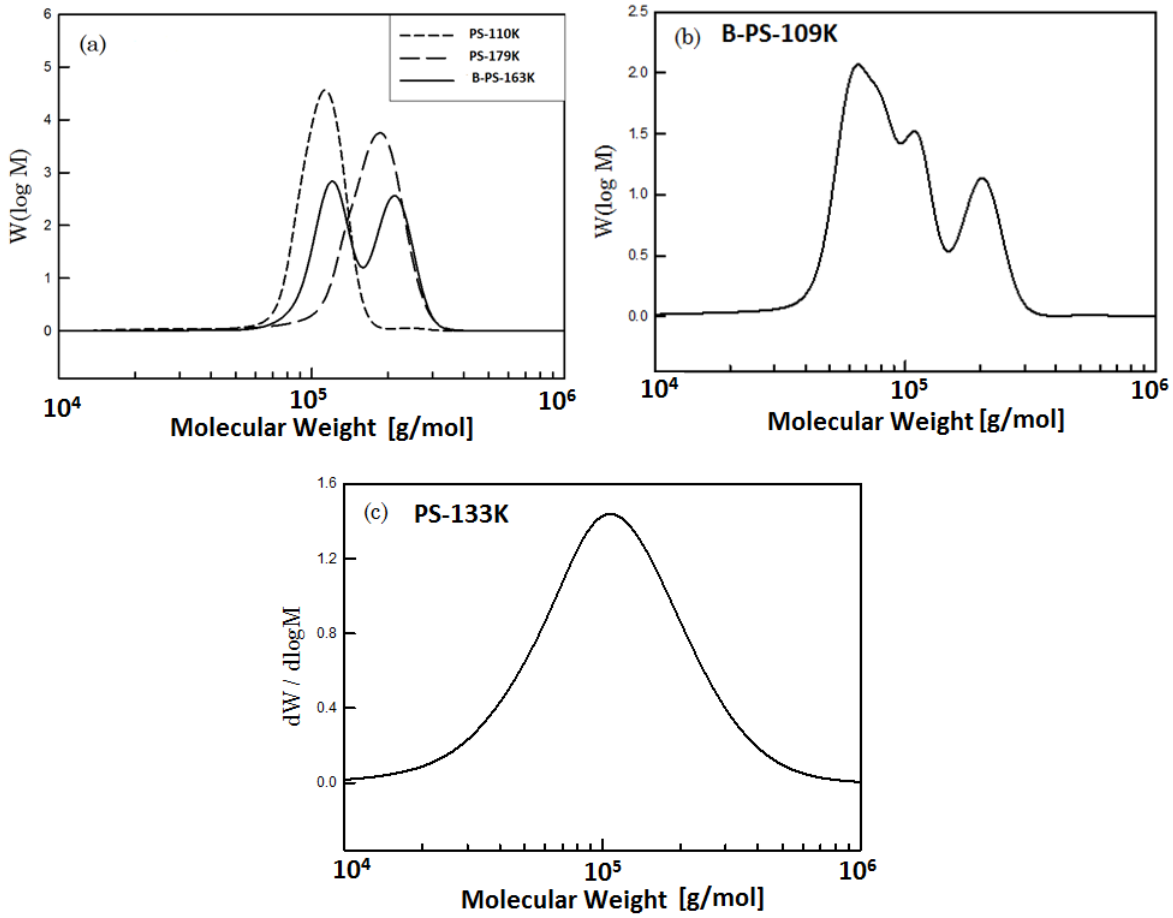

Figure 4.1: The molecular weight distribution of (a) monodisperse PS (M_w = 110k, 179k) and binary blends of PS-110K and PS-179K, (b) Quaternary blends of PS-62K, PS-79K, PS-110K, and PS-179K and (c) PS-133K (polymer synthesized using radical polymerization).

module. The samples were press-molded under vacuum at 200°C into 13 mm discs for the oscillatory shear experiments.

4.2 Results and Discussion

The time-temperature superposition (TTS)[88] was used to increase the range of time or frequency over which the linear behaviour could be determined. The low-temperature experiments were performed to probe the faster relaxation processes of the polymer and high-temperature experiments were performed to probe the terminal relaxation processes. The validity of TTS in linear viscoelastic regime was demonstrated for several polymer systems[4,81,88]. Figure 4.2 illustrates the linear mastercurve using the TTS principle. The data was shifted along the frequency

axis, and the horizontal shift factors for all PS samples were fitted with the *WLF* equation[4,81,88]: $\log a_T = \left[-C_1(T - T_{ref})\right] / \left[C_2 + (T - T_{ref})\right]$ with T_{ref} = 180°C, C_1 = 5.150 and C_2 = 124.6 °C (Fig. 4.3).

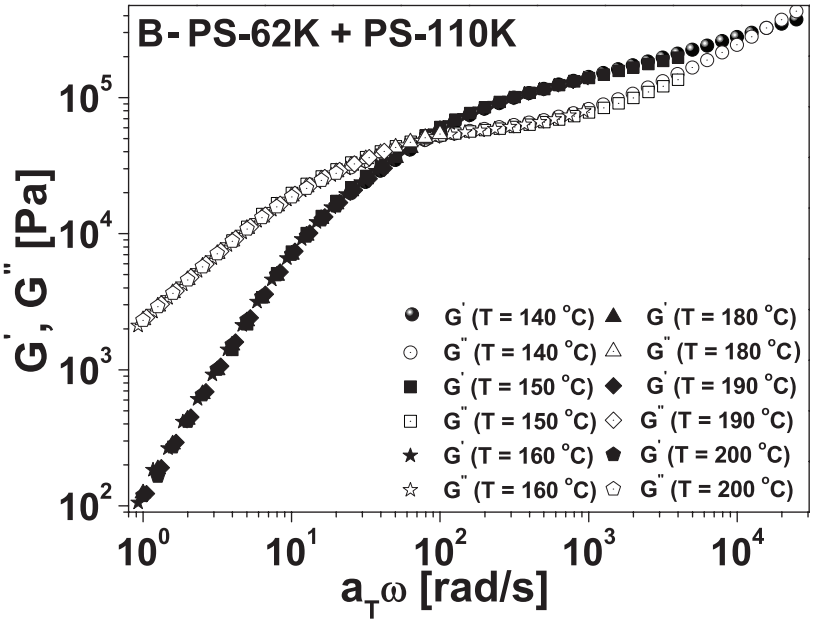

Figure 4.2: Master curve obtained using the time-temperature superposition (TTS) in the linear viscoelastic regime.

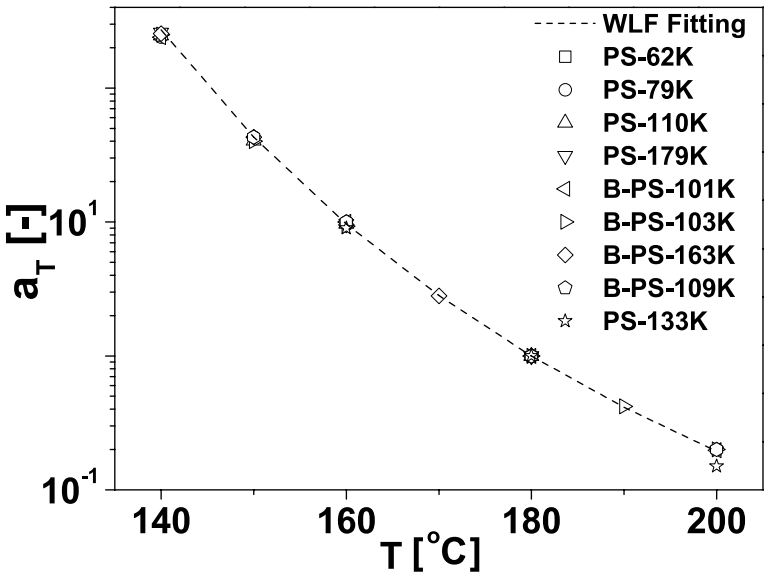

Figure 4.3: The horizontal shift factor, a_T, vs. temperature for the monodisperse PS and blends along with WLF fitting. The following WLF parameters were used: C_1 =5.15 and C_2 = 124.6 °C.

Small Amplitude Oscillatory Shear (SAOS) is the technique most often used to determine the linear viscoelastic characteristics of a polymer melt. Figure 4.4 illustrates the variation of the storage modulus, $G^{'}$, and the viscous modulus, $G^{''}$, as a function of angular frequency, ω, for the monodisperse linear polymer melts. For comparison purpose, the master curves were shifted vertically in an arbitrary manner. For all the linear PS melts, a plateau in $G^{'}(\omega)$ is observed. As the molecular weight increases, the plateau first becomes well defined and then lengthens continuously. The longer the molecules, the longer the delay between the time when Rouse modes of relaxation occur in the transition zone, and the time when reptation modes become possible at much lower frequencies.

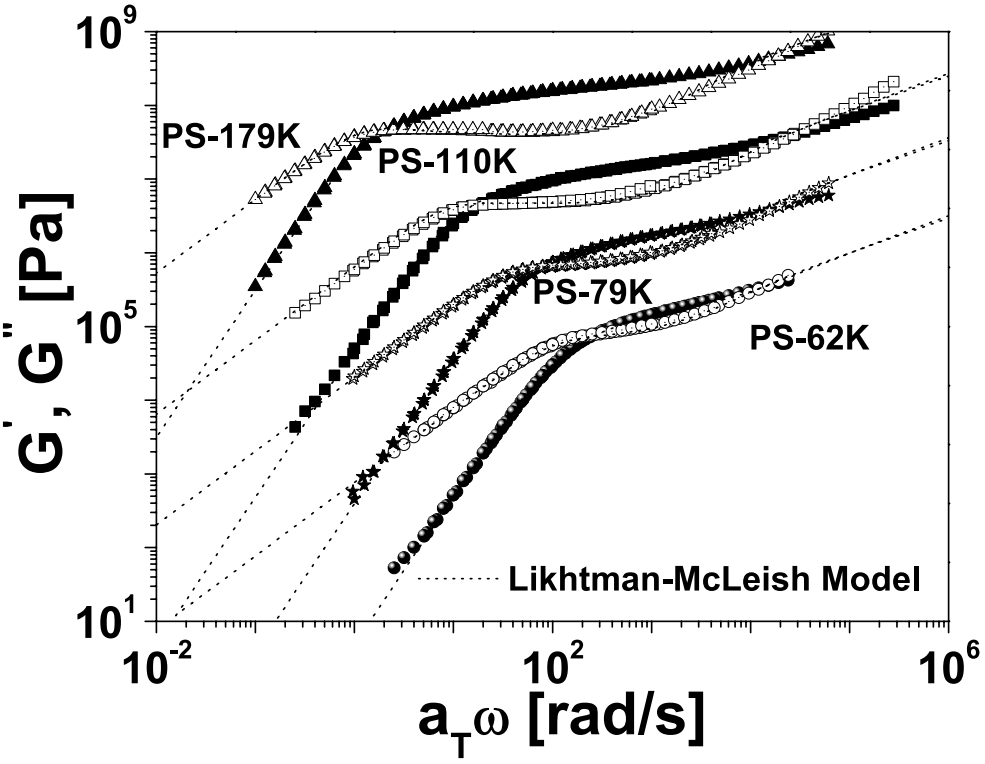

Figure 4.4: The linear master curve of monodisperse PS melts and prediction of Likthman-McLeish model.

To simulate the linear viscoelastic properties of the monodisperse linear polymer melts, the Likthman-McLeish model[43] was used. The two model parameters, reptation time, τ_d, and Rouse relaxation time, τ_R, are sufficient to describe quantitatively the linear viscoelastic properties for monodisperse linear polymer melts over a wide range of frequencies. The calculated reptation time and Rouse relaxation time are displayed in table 4.2. These time scales were determined by fitting the dynamic frequency spectrum with the following tube parameters for the PS: τ_e =

$3.8 * 10^{-4}$ s, $G_e = 3.0 * 10^5$ Pa, $M_e = 16.518$ kg/mol and $c_\nu = 0.1$ at 180 °C.

Table 4.2: Predicted relaxation times using Likhtman-McLeish model

Polymers	τ_d [s]	τ_R [s]
PS-62k	0.005842	0.00542
PS-79k	0.017474	0.00879
PS-110k	0.06203	0.01705
PS-179k	0.6063	0.04514

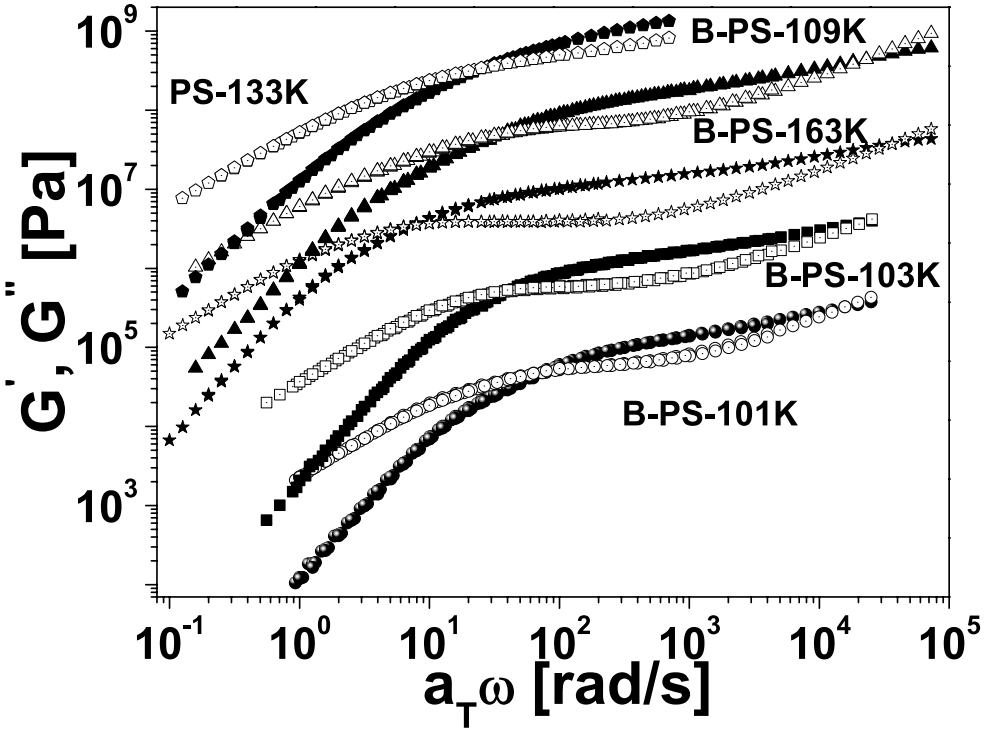

Figure 4.5: The linear master curves for the blends and polydisperse PS-133K.

The blends of monodisperse PS systems provide an effective way to study the effect of polydispersity on linear and nonlinear viscoelastic properties. Watanable et al.[84] studied the linear viscoelasticity of binary mixtures of monodisperse polymers with significant differences in molecular weights of long and short polymer chains. Since the molecular weight of one component was much higher than that of the other, it was possible to observe two distinct peaks in the loss modulus. However, when the molecular weights of the two monodisperse polymers were similar, as is in our case it is difficult to distinguish between the monodisperse PS and binary blends linear

master curves (Fig. 4.5).

To investigate non-linear viscoelasticity, large deformation amplitudes were applied under oscillatory shear flow. The resulting stress response was analyzed using FT-Rheology. To quantify the non-linear viscoelasticity of linear PS and blends, the analysis of $I_{3/1}(\gamma_0, \omega)$ (experimentally) as a function of deformation amplitude and frequency were carried out.

A square scaling, $I_{3/1}(\gamma_0, \omega) \propto \gamma_0^2$, is observed for the monodisperse PS melts and its blends in the deformation amplitude range of $\gamma_0 = 0.3 - 2$ over a wide range of frequencies. This square scaling was previously observed for wide variety of complex fluids[73,55,56,57,58]. The experimental measurements of $I_{3/1}(\gamma_0, \omega)$ for one of the blends is displayed in Figure 4.6. This square scaling has facilitated the determination of zero strain intrinsic nonlinearity, $Q_0(\omega)$, a material parameter in nonlinear viscoelastic regime.

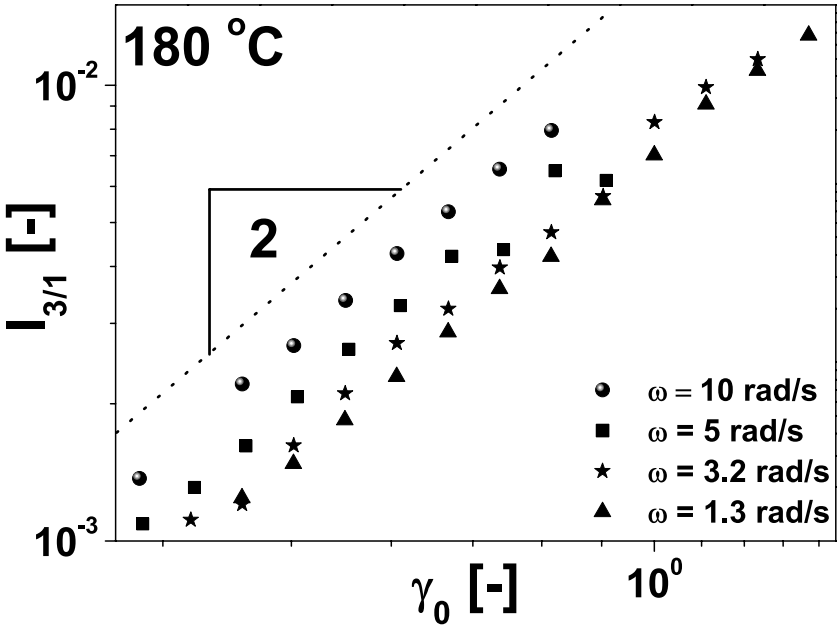

Figure 4.6: Nonlinearity $I_{3/1}$ versus strain amplitude, γ_0 for B-PS-101K at T = 180 °C. Since $I_{3/1}$ is severely affected by noise at low strain amplitude which belongs to linear regime, only reliable data points which show the square scaling $I_{3/1} \propto \gamma_0^2$ were selected.

The experimental measurements under LAOS were performed over the angular frequency range ω=1-10 rad/s. In this range of frequencies the square scaling $I_{3/1}(\gamma_0, \omega) \propto \gamma_0^2$ were observed (Fig. 4.6). To obtain a master curve over the wide range of frequencies, the TTS principle is applied. Hyun and Wilhelm[73] demonstrated the validity of TTS in non-linear viscoelastic regime for zero

strain intrinsic nonlinearity, $Q_0(\omega)$. Figure 4.7 illustrates the nonlinear mastercurve using the TTS principle for the binary blend (B-PS-62K + PS-110K). For the monodisperse PS and its blends the TTS principle validity is observed.

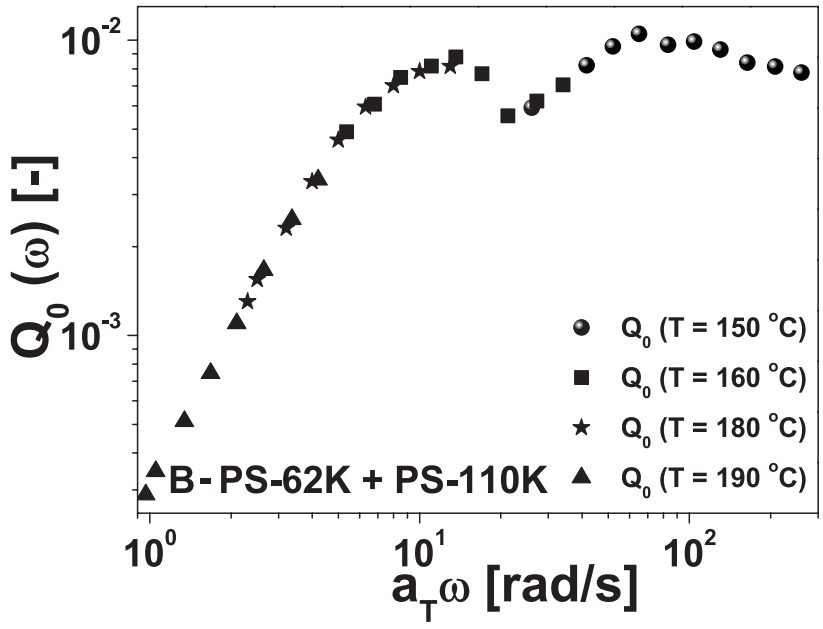

Figure 4.7: Nonlinear master curve obtained using the time-temperature superposition (TTS) in the nonlinear viscoelastic regime.

Figure 4.8 illustrates the variation of Q_0 as a function of angular frequency, ω, and its prediction by the nonlinear Giesekus model for monodisperse PS samples. The model parameters, relaxation time, τ_d, and plateau modulus, G_n, were determined from the linear master curves fitted by the Likthman-McLeish model. The nonlinear parameter, α (Giesekus model), was determined by fitting of nonlinear master curves. The α parameter for PS-62K, PS-79K and PS-110K is 0.335. However, the α parameter for PS-179K is 0.48 which is higher than the other monodisperse PS polymers. The experimental nonlinear mastercurve for PS-179K display higher maximum values relative to all other investigated materials and, due to this, the value of α was higher for PS-179K. At higher excitation frequencies, the deviation between the prediction (Giesekus model) and experiment is significant. This can be explained by higher mode contribution (Rouse relaxation) to the intrinsic nonlinearity, Q_0, as in single mode Giesekus model simulations only the reptation relaxation time is used.

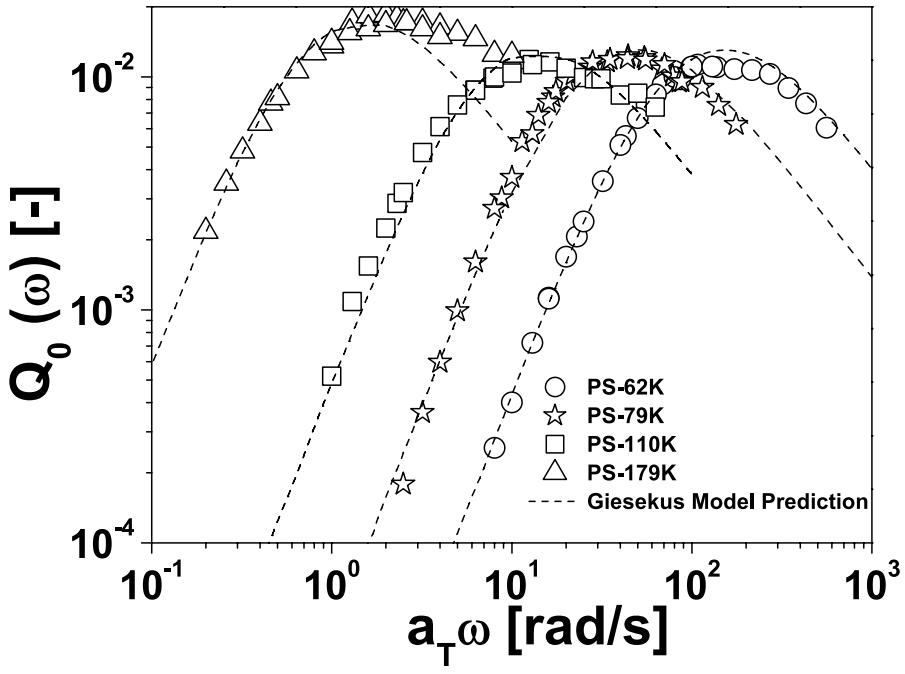

Figure 4.8: The nonlinear master curve ($Q_0(a_T\omega)$ vs. $a_T\omega$) and its prediction using the Giesekus model.

Figure 4.9a illustrates the variation of complex viscosity, $|\eta^*|$, as a function of applied angular frequency, ω, and molecular weight. The limiting value of the $|\eta^*|$ at the small ω is observed to be independent of the frequencies. This limiting value is called zero shear-rate viscosity, η_0. The η_0 displayed the following scaling with average molecular weight of PS chains $\eta_0 \propto M_w^{3.50\pm0.08}$ (Fig. 4.9b). The observed value of scaling exponent was in well agreement with the reported values for the PS linear polymer melts[4,81]. Figure 4.9c illustrates the variation of shear-rate nonlinearity, μ, as a function of the applied frequency and molecular weight. The qualitative trend is similar to the complex viscosity, $|\eta^*|(\omega)$. However, the zero shear-rate intrinsic nonlinearity, $\mu_0(M_w)$, shows the following scaling towards molecular weight, $\mu_0 \propto M_w^{8.85\pm0.15}$ (Fig. 4.9d).

The dependence of zero shear-rate intrinsic nonlinearity, $\mu_0(M_w)$, on molecular weight is significantly higher than the zero shear-rate viscosity, $\eta_0(M_w)$. This steeper increase in scaling exponent for material parameter (μ_0) defined in the MAOS flow regime relative to material parameter defined in the SAOS flow regime, provides a more effective way to quantify the effects of molecular

weight on the viscoelastic properties.

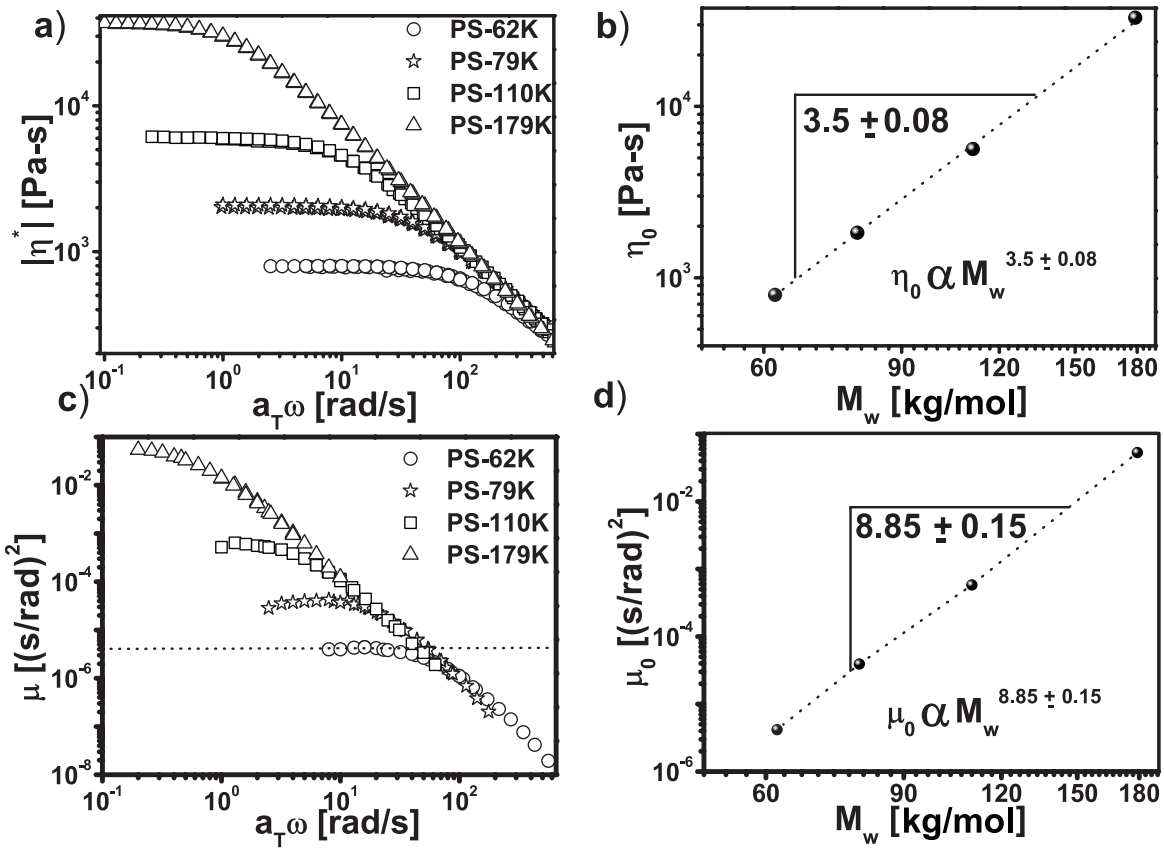

Figure 4.9: The variation of modulus of complex viscosity, $|\eta^*|(a_T\omega)$, and shear-rate nonlinearity, $\mu(a_T\omega)$, as a function ω for monodisperse PS melts, (a) $|\eta^*|$ vs. $a_T\omega$, (b) η_0 vs. M_w, (c) $\mu(a_T\omega)$ vs. $a_T\omega$, (d) μ_0 vs. M_w.

Hyun and Wilhelm[73] and Kempf et al.[75] observed that the nonlinear viscoelastic mastercurve, $Q_0(\omega)$, was more sensitive relative to linear mastercurve $(G^{'}(\omega), G^{''}(\omega))$ for the detection of relaxation processes in linear and branched polymers. The qualitative behaviour of linear mastercurves is similar for all the blends and monodisperse PS systems used in this study. However, the nonlinear mastercurve showed significant differences (Fig. 4.10). In the nonlinear mastercruves of the binary blends two distinct peaks are observed which correspond to the two monodisperse PS polymers (Fig. 4.10a-c) used to formulate the binary blends. The comparison also reveals that $Q_0(\omega)$ values in the low frequency limit are lower for blends correspond to the high molecular weight, M_w, PS polymers for all three binary blends. This observation can be explained by a increased contribution from the convective constraint release relaxation process. Since rapid motion of short chains will release constraints on the long chains in the melts, allowing them to begin relaxing by

constraint release more rapidly than they can relax by their own reptation.

Figure 4.10d illustrates the quaternary blends as well as polydisperse PS (PS-133K, PDI = 1.66) mastercurves. For quaternary blends, in the low frequency limit $Q_0(\omega)$ is suppressed even further relative to the binary blend (B-PS-110K+PS-179K). This can be explained by an even higher degree of convective constraint release because of the presence of small chains (PS-62K, PS-79K, and PS-110K). In conclusion, the non-linear master-curves displayed more resolution for differentiation between the monodisperse PS and blends compared to the classical linear master-curves.

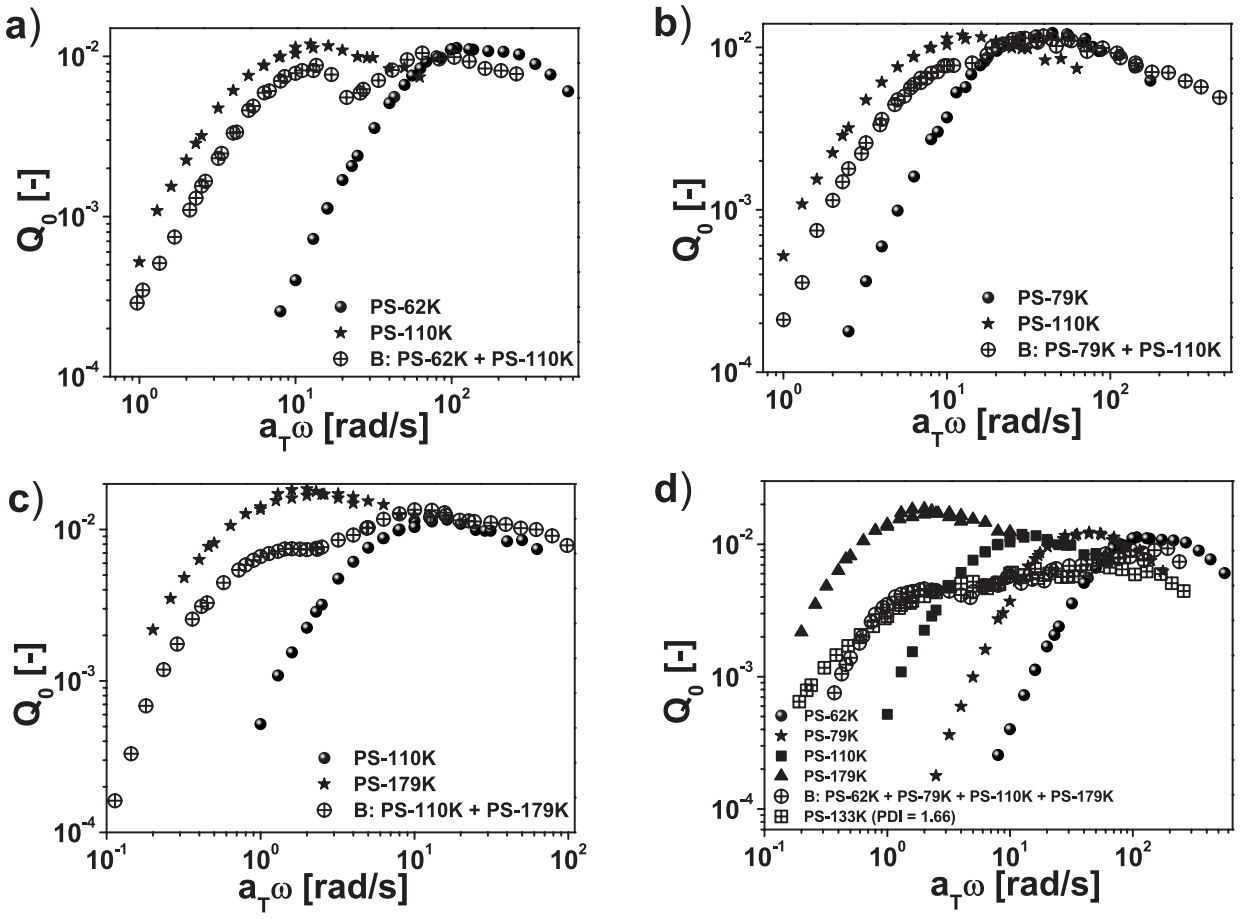

Figure 4.10: The nonlinear master curve of blends and polydispers PS (PS-133K), (a) blends of PS-62K and PS-110K, (b) blends of PS-79K and PS-110K, (c) blends of PS-110K and PS-179K, (d) blends of PS-62K, PS-79K, PS-110K, and PS-179K.

4.3 Concluding Remarks on the Characterization of Monoddisperse PS melts and its Blends using FT-Rheology

Linear monodisperse polystyrene (PS) melts and their blends were investigated under oscillatory shear flow in the linear and nonlinear viscoelastic regime. The linear viscoelastic properties of monodisperse PS polymer melts were predicted by the Likthman-McLeish model, and the nonlinear viscoelastic properties by the Giesekus model. A new material parameter, zero shear-rate intrinsic nonlinearity, $\mu_0 = \lim_{\gamma_0\omega\to 0} I_{3/1}/\gamma_0^2\omega^2$, was introduced and obtained for monodisperse PS polymer melts. A scaling of $\mu_0 \propto M_w^{8.85}$ was obtained with the molecular weight of monodisperse PS polymer melts. Interestingly, the entanglement effects on μ_0 are significantly higher than the zero shear-rate viscosity, η_0. The η_0 follow the scaling $\eta_0 \propto M_w^{3.5}$ for entangled polystyrene PS melts. In conclusion, the higher scaling exponent of 8.85 for material parameter in the nonlinear viscoelastic regime (MAOS regime) presents a more effective way to quantify the effects of molecular weight on linear PS polymer melts. Distinct peaks were observed for the binary blends in the nonlinear viscoelastic regime [$Q_0(\omega)$ as a function of ω]. These peaks can be associated to the dynamics of small and big polymer chains. In contrast, in the linear viscoelastic regime no distinct peaks were observed in $G^{''}(\omega)$. This analysis displays the high sensitivity of FT-Rheology in characterizing the effects of molecular weight and molecular weight distribution for polymer melts.

Chapter 5

Large Amplitude Oscillatory Shear and Uniaxial Extensional Rheology of Blends from Linear and Long-Chain Branched Polyolefins

Long Chain Branching (LCB) has profound effects on the processability of polymeric materials such as polyethylene (PE) and polypropylene (PP), which together comprise a substantial market. To have a significant effect on processing, branches must be longer than about twice the entanglement length in the melt[4]. Therefore, it is crucial for polyolefin industries to understand the effects of the type and amount of LCB. This motivated the development of numerous methods to characterize branching, such as, Size Exclusion Chromatography (SEC)[6], Nuclear Magnetic Resonance (NMR)[?] [8] and rheological methods[9]. However very low LCB concentrations (less than 0.1 per 1000 carbon atoms) are not easily detected by SEC and NMR,[89,90] although a combination of these methods can significantly reduce the detection threshold, e.g., SEC-Multiangle Laser Light Scattering (MALLS), SEC-MALLS[36] and SEC-FTIR[33]. In contrast, rheological measurements are very sensitive to even small amounts of LCB[91,92,93]. The combination of the excellent sensitivity of rheology, along with recent theoretical developments in predicting the flow of industrial complex polymers,[94,95,96,42] as well as the bridge between flow response and polymerization models,[97,98] provided us the opportunity to make a breakthrough in the design of new materials with optimized processing.

Rheological methods for measuring the amount of LCB involve measurement of the zero shear rate viscosity, η_0 [99]. This is a sensitive way to detect the LCB but due to the long relaxation time of branched polymers, it is not always accessible [100]. The long-chain branching index (LCBI) [90] and Dow Rheology Index (DRI) [[101]] is frequently used in industry to characterize the long-chain branching in PE. However, LCBI fails for materials with high branching index and DRI is only valid for materials with similar narrow MWD. Based on the oscillatory shear rheology measurements, the reduced van Gurp-Palmen plot ($\delta_0(|G^*(\omega)|)$) is used to characterize the long-chain branching and polydispersity influence on polymeric materials [102,103]. Recently, thermo-rheological techniques were also found to be a sensitive tool to characterize the LCB [104,105]. However, the absence of an increase in flow activation energy (E_a) does not exclude the possibility of a low level of LCB [106].

All the methods discussed above are performed at small deformations, where the stress is proportional to the applied deformation. However, in most of industrial processes, polymer are subjected to large or rapid deformations in shear and elongation. The applied large or rapid deformations in elongation lead to extensional hardening which helps to stabilize the processes. At the same time shear thinning is observed which leads to improved processability and low energy consumption. Therefore, to optimize the industrial processes and tailor the material properties, an elaborated knowledge of flow behaviour at large deformations is necessary.

The rheological methods used for characterization of polymer melts at large deformation or rapid deformation involves, uniaxial extensional transient viscosity, η_E^+, measurements and large amplitude oscillatory shear. In elongation, the polymer melt is subjected to uniaxial extension and the strain hardening factor (SHF) is estimated. The SHF is the ratio of the time dependent elongational viscosity , $\eta_E^+(t, \epsilon)$, to η_{DE}^+, where η_{DE}^+ is the tensile stress growth coefficient determined using the Doi-Edwards model [38], where stretching of macromolecules is not taken into consideration [75]. The SHF displays an increasing trend with increasing degree of long-chain branching [4,107]. The major drawback with the SHF is that for linear topologies and materials with a very small amount of branching, there is no significant strain hardening. This restricts the use of SHF to more highly branched topologies that show significant extensional hardening. Recently, Large Amplitude Oscillatory Shear (LAOS) has been used to characterize the nonlinear behaviour of different soft matters [69,56,73,55,58,57]. The interest in LAOS flow to characterize soft matters are attributed to the development of several methods to analyze the complex periodic flow response,

such as, FT rheology[62] and Stress Decomposition (SD)[64], which was further developed to describe higher order moduli in a meaningful way using Chebyschev polynomials[65] and the Sequence of Physical Process (SPP) framework[108]. In particular, much attention has been focused to FT-Rheology, where the stress response is analyzed in Fourier space. Schlatter et al.[109] and Vittorias et al.[110] investigated various linear and branched materials using FT-Rheology. They showed that FT-Rheology is more sensitive to characterize the long-chain branching than the linear viscoelastic analysis. The third Fourier harmonic relative to fundamental Fourier harmonic ($I_{3/1}$) has been used frequently to quantify the nonlinear behaviour in LAOS flow. In LAOS, for a range of applied deformation amplitudes, a square scaling law $I_{3/1} \propto \gamma_0^2$ was observed both experimentally[73,58] and by simulation of various nonlinear constitutive equations (Giesekus model[70], Pom-Pom model[72], Molecular Stress Function (MSF) model[71]). Motivated by this scaling law Hyun and Wilhelm[73] introduced a new nonlinear parameter $Q(\gamma_0, \omega) = I_{3/1}/\gamma_0^2$. The Q-parameter at low deformation amplitudes limit converge to a constant value which they called intrinsic nonlinearity $Q_0(\omega) := \lim_{\gamma_0 \to 0} Q(\gamma_0, \omega) = \lim_{\gamma_0 \to 0} I_{3/1}/\gamma_0^2$. The intrinsic nonlinearity $Q_0(\omega)$ were used to characterize the branching effects for linear and comb polystyrene (PS)[73] and polydispersity effects in PE[76]. Furthermore, the Non-Linear Factor (NLF) was used by Filipe et al.[111] to characterize the LCB. The NLF is the absolute value of the ratio of fundamental Fourier coefficient to third Fourier coefficient $|G_1^{'}/G_3^{'}|$ at the applied deformation amplitudes $\gamma_0 = 10$ and excitation frequency $\omega/2\pi = 0.1$ Hz.

We tailored the properties of PE and PP in a systematic way by blending a long-chain branched PE with a linear PE and a long-chain branched PP with a linear PP. Small amplitude oscillatory shear (linear viscoelastic regime) was used to calculate the flow activation energies. At medium amplitude oscillatory shear (non-linear viscoelastic regime)[69,73,55], new intrinsic nonlinear material parameters, based on the first normal stress and shear stress measurements will be introduced. Additionally, under LAOS flow ($\gamma_0 = 10$, $\omega/2\pi = 0.1$ Hz), new parameters will be introduced to characterize the influence of addition of LCB in PP and PE blends. In extensional flow, the uniaxial extensional measurements were performed over a wide range of deformation rates. Furthermore, these results were then compared to simulations using the Molecular Stress Function (MSF) model[96]. Significant differences were observed in the flow response of PP and PE blends when subjected to different kinds of deformations. These differences were explained by differences in the type of branching in PP and PE.

5.1 Materials and Methods

5.1.1 Materials

Four different commercial PE and PP grades were selected for the study. The linear (L) and long-chain branched (LCB) blends were formulated carefully by Dr. Filipe from Borealis Linz, Austria. The table 8.1 summarizes the results of the molecular and rheological characterization.

Table 5.1: Characteristics of the blends of a linear and a long-chain branched polyethylene and polypropylene

Polymer	Blends	L:LCB [wt. %]	M_w [kg/mol]	M_w/M_n	η_0 [Pa-s]	T_m [°C]
i-PP (L)	PP-1	100:0	301	2.9	11046	155
	PP-2	90:10	291	2.9	10496	155
+	PP-3	60:40	311	3.7	13472	160
	PP-4	20:80	341	5.2	14410	160
i-PP (LCB)	PP-5	0:100	312	4.6	24898	163
LLDPE (L)	PE-1	100:0	202	16	61786	131
	PE-2	90:10	177	13.32	87759	130
+	PE-3	80:20	172	12.60	169398	129
	PE-4	70:30	174	12.30	170925	129
	PE-5	60:40	175	11.42	212066	129
LDPE (LCB)	PE-6	0:100	144	7.59	1213	119

The blends were prepared in a twin screw extruder equipped with co-rotating screws, a water cooling bath and a pelletizer. The extrusion for PP blends were conducted at a temperature of 230°C, and for PE blends were conducted at a temperature of 210°C. To avoid a degradation of the molecules during the blend composition, a stabilizer was added. The zero shear-rate viscosity, η_0, was determined at 190°C. The steady-state was reached for all the PP-blends, but for the PE-blends, the steady state was not reached. To determine η_0 for PE-blends, the dynamic frequency sweep data were fitted with multi-mode Maxwell model, and determined using $\eta_0 = \sum_{i=1}^{N} G_i \tau_i$. Where, N is number of modes, and G_i and τ_i are the Maxwell parameter calculated by fitting the dynamic frequency spectrum (table 5.3).

Wasserman et al.[106] reported the following scaling with the molecular weight for linear PE, $\eta_0^L = 3.40 \cdot 10^{-15} M_w^{3.6}$ at 190°C. Whereas Eckstein et al.[112] reported following scaling with the molecular weight for linear i-PP, $\eta_0^L \propto M_w^{3.5}$ at 190°C. The branched polymers display deviation from the above scaling, and this deviation has been used extensively to infer the long-chain branching structures[113,107,114]. Gabriel et al.[113] concluded from investigations on a number of PE that slightly long-chain branched PE with starlike molecular structure displayed higher viscosity than the linear PE of similar molecular weight, whereas low viscosity has been observed for treelike branching. The similar conclusion has been drawn by Auhl et al.[107,114] for long-chain branched PP synthesized using electron-beam and gamma irradiation.

In case of the PE blends, the ratio is $\eta_0^L/\eta_0^{LCB} > 1$, which implies a treelike topology for long-chain branched PE. However, for the PP blends, the ratio is $\eta_0^L/\eta_0^{LCB} < 1$, which implies a starlike topology for long-chain branched PP. These topological structures for the PP and PE were concluded from the above discussion.

5.1.2 Molecular Characterization

Molecular weight distribution were measured by high-temperature size-exclusion chromatography (SEC) with GPC IR5 from PolymerChar and a Infrared (IR) detector by Ms. Neuhaus from University of Darmstadt, Germany. The polymer molecules are fractionated in the SEC by their hydrodynamic volume, which depends on the density in the dissolved state, the molar mass, and long-chain branching. The SEC experiments were carried out at 150 °C, and the eluent was TCB (1,2,4-trichlorobenzene, Merck). The conventional calibration with linear PE standards was used for molar mass determination of the PE blends, and linear PP standards was used for molar mass determination of the PP blends. The columns used for separation are: Shodex (3xGPC-UT-806M, pore size 10000A; 1xGPC-UT-807, pore size 20000). The software used for the control was PolymerChar GPC IR and for the data processing was PSS WinGPC Unity 7.4.0.

5.1.3 Rheological Characterization Methods

Oscillatory shear and uniaxial extensional flow measurements were performed on an ARES-G2 rotational rheometer from TA Instruments. Oscillatory shear measurements in the linear regime were performed using a cone and plate geometry (13 mm and 25 mm, $\alpha = 0.1$ rad) over the temperature range from 135 to 230 °C using angular frequency range from $\omega = 10^{-1}$ to $\omega = 10^2$

rad/s at each measurement temperature. The extensional experiments were performed at 180 °C for the PP-blends and at 145 °C for the PE-blends using the Extensional Viscosity Fixture (EVF) from TA instruments. The extensional rates were varied in the range $\dot{\epsilon} = 0.1 - 10\ s^{-1}$. The LAOS experiments were performed on an ARES-G2 rotational rheometer from TA instruments at 190°C using an implemented FT-Rheology module. Strain amplitudes were applied in the range $\gamma_0 = 0.01 - 10$ at an excitation frequency of 0.1 Hz. Furthermore, the LAOS experiments were also performed on a Rubber Process Analyzer (RPA)-2000, which is a dynamic testing instrument with grooved biconical die geometry to prevent slippage. The test cavity is closed and pressurised for the duration of the test using an elastomeric seal between die and seal plate. The measurements were performed at $\gamma_0 = 10$ and $\omega/2\pi = 0.1$ Hz with the RPA-2000 rheometer. The samples were press-molded under vacuum at 190°C into 13 and 25 mm discs for the shear experiments and into $20 \times 10 \times 0.7$ mm bars for the extensional experiments.

5.2 Results and Discussion

In the linear viscoelastic regime (under oscillatory shear), the flow activation energies were calculated for the PP and PE blends. Oscillatory shear responses (shear stress, first normal stress) were simulated using a single mode Pom-Pom model[52] at large deformation amplitudes. The resulting responses were analyzed using well developed FT-Rheology[62] and stress-decomposition using orthogonal Chebyshev polynomial techniques[65]. The qualitative behaviour of higher harmonics with applied deformation amplitudes, γ_0, and branching, q, were simulated via single mode Pom-Pom model. The qualitative trend for nonlinear parameters variation with branching were compared with experiments on the PE and PP blends. In extensional flow, the uniaxial extensional viscosity were measured, and then simulated using the MSF model[96,115] to characterize the PE and PP blends.

5.2.1 Linear Viscoelasticity

The thermo-rheological behaviour of polymer melts plays an important role for process optimization and also provides an insight into the molecular structure[116]. The thermo-rheological behaviour of a polymer is frequently quantified using dynamic frequency spectrum at different temperatures. Usually, the thermo-rheological behavior can be categorized into two broad categories, thermo-rheological simple and thermo-rheological complex response, depending on whether all

relaxation times have the same temperature dependence[117]. Thermo-rheological simple behaviour is obtained if the frequency dependent $G^{'}(\omega)$ and $G^{''}(\omega)$ superimpose at different temperatures, while the thermo-rheological complex materials exhibit a systematic split between the curves with temperature. Far above the glass transition temperature, the thermo-rheological sensitivity is characterized by the flow activation energy, E_a[104]. The flow activation energy, E_a, varies with the molecular structure and branching topography. For example, branched polymers exhibit higher activation energies than linear ones of similar weight-average molecular weight[104]. Therefore, analyzing the temperature dependence of rheological properties is one of the possibilities to get an insight into the branching structure of polymers.

Figure 5.1a shows the van Gurp-Palmen $\delta_0(|G^*|, T)$-curves for blends of the linear *i*-PP and the long chain branched PP at various temperatures. The superposition of these curves at different temperature for each blends is an indication of thermo-rheological simplicity. As the fraction of long-chain branched PP (PP-5) is increased in PP blends, the elasticity of the blends increases. This is evident from the decrease of $\delta_0(|G^*|)$ in the investigated range of complex modulus, $|G^*(\omega)|$, at all temperatures.

The flow activation energy, E_a, can be determined from the phase angle, δ_0, measurements as a function of ω at different temperatures. If ω at distinct δ_0 are plotted on semi-log scale, as a function of $1/T$, a straight line is obtained as indicated in Figure 5.1b. Then, E_a/R (R = gas constant) can be determined from the slope of linear fits according to:

$$\omega(T) = \omega(T_0) \cdot \exp\left[-\frac{E_a}{RT}\right] \tag{5.1}$$

The E_a increased as the fraction of long-chain branched PP (PP-5) in the PP-blends increased (Fig. 5.1c). The calculated E_a for linear PP (PP-1) is 43 kJ/mol which is in agreement with reported value in the limit of 36-44 kJ/mol[112,118]. The E_a of 70 kJ/mol was calculated for long-chain branched PP (PP-5) which is significantly higher than the linear PP (PP-1). It is well established that long-chain branched polymers have higher E_a compared to linear polymers[117,119,116,104], this is consistent with the presented results.

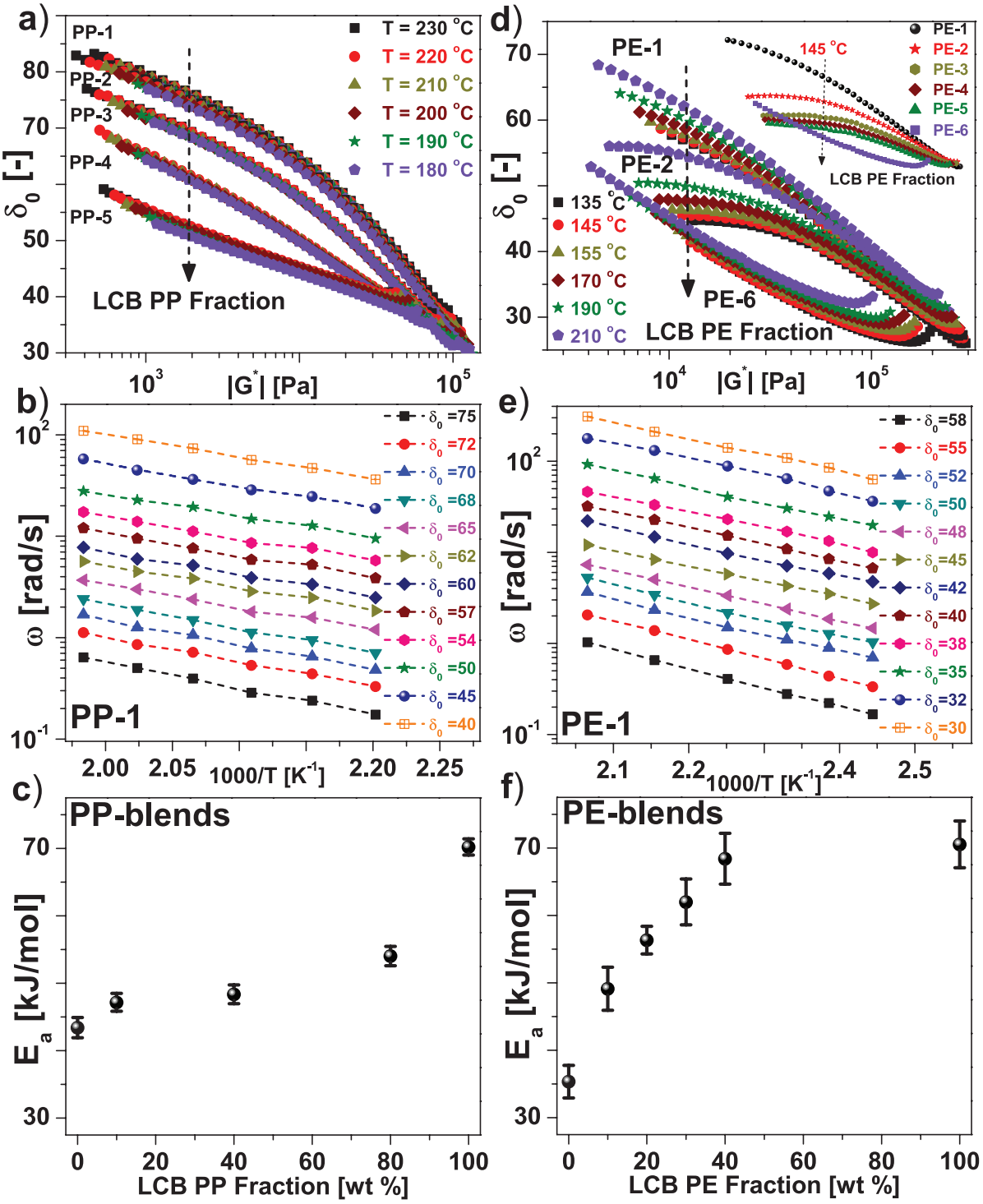

Figure 5.1: Thermo-rheological analysis of polypropylene and polyethylene blends (a) van Gurp-Palmen Plot for polypropylene blends at various temperature(b) determination of activation energy, E_a, at different phase angle, δ_0, of polypropylene (c) activation energy, E_a, variation as we increase the HMS-PP content (d) van Gurp-Palmen Plot for polyethylene blends at various temperature (e) determination of activation energy, E_a, at different phase angle, δ_0, of polyethylene and (f) activation energy, E_a, variation as we increase the LDPE content.

Figure 5.1d shows the van Gurp-Palmen $\delta_0(|G^*|, T)$-curves for blends of the linear PE and the long-chain branched PE at various temperatures. In contrast to PP blends, the PE blends displayed systematic splits in van Gurp-Palmen $\delta_0(|G^*|, T)$-curve with temperatures, typical of pronounced thermo-rheological complexity. It means failure of the time-temperature superposition for the PE blends. Mavridis et al.[120] evaluated the flow activation energy of thermo-rheologically complex polymer like LDPE, which show a split-up in $\delta_0(|G^*|, T)$-curve. They determined empirical vertical and horizontal shift factor and obtained the flow activation energy, E_a. The conversion from thermo-rheological complex behavior to thermo-rheological simple, using the vertical shift factor makes the estimation of activation energy possible. Recently, a method invariant estimation of E_a for thermo-rheological complex polymers was proposed by Kessner et al.[104]. A straight-line is obtained, when ω at distinct δ_0 is plotted on a semi-log scale as a function of $1/T$ (Fig. 5.1e). This implies, the appropriate vertical shift (b_T) of the modulus can lead to thermo-rheological simple behavior for PE-blends. Similar to PP blends, the PE blends also displayed the increase of E_a as the long-chain branched PE fraction in the blends increased (Fig. 5.1f).

In case of branched PE, thermo-rheological complexity were usually showed by several authors[117,116,104]. For the linear PE (PE-1) the calculated flow activation energy is E_a = 35 ± 2.5 kJ/mol, and it showed thermo-rheological complexity. In contrast, in the literature, for the linear PE polymer thermo-rheological simplicity with an E_a of about 27 kJ/mol was found, independent of molar mass and molar mass distribution[106,121]. However, we believe the thermo-rheological complexity and higher value of E_a could be because of significantly high PDI (PE-1, PDI = 16).

In case of the PP blends, addition of 10% of long-chain branched PP has no significant increase (increased by 8%) in the flow activation energy. In contrast, addition of 10% of long-chain branched PE has significant increase (increased by 38%). This difference in the evolution of the flow activation energy on addition of long-chain branched polymer could be attributed to differences in type of branching. Consequently, further experiments were performed in nonlinear-viscoelastic regime (oscillatory and extensional) to justify our hypothesis of differences in the type of branching in long-chain branched polymers (PP and PE).

5.2.2 Non-linear Viscoelasticity: Large Amplitude Oscillatory Shear (LAOS)

To quantify the non-linear viscoelasticity of polymer melts under LAOS flow, the $I_{3/1}(\gamma_0, \omega)$ (calculated by analyzing shear stress response) was frequently used in FT-Rheology[109,110,73,76,55,75].

However, higher order harmonics ($I_{5/1}$, $I_{7/1}$, ..) contribution to nonlinear stress was ignored for polymer melts. As, it can be observed in the Fourier spectrum of shear stress of long-chain branched PP in Figure 5.2, the nonlinear contribution is not only coming from $I_{3/1}(\gamma_0 = 1, \omega/2\pi = 0.1$ Hz), but also from $I_{5/1}(\gamma_0 = 1, \omega/2\pi = 0.1$ Hz). In this work, for the first time, $I_{5/1}(\gamma_0, \omega)$ is analyzed and correlated with extent of branching and type of branching for polymer melt systems.

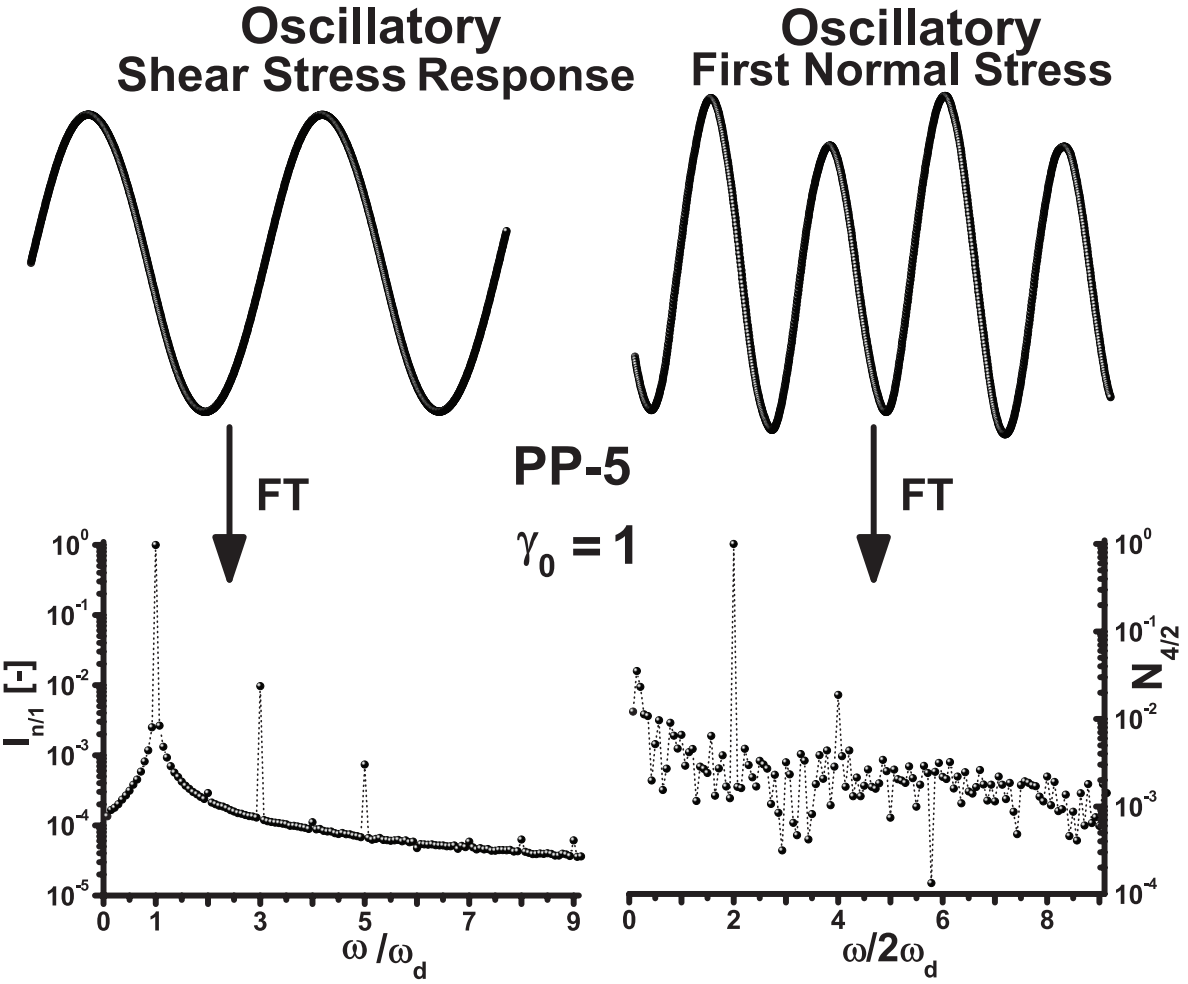

Figure 5.2: Oscillatory shear and first normal stress response with its Fourier Spectrum for long-chain branched PP (PP-5) at $\gamma_0 = 1$ and $\omega_d/2\pi = 0.1$ Hz.

The Fourier spectrum of the first normal stress difference response of long-chain branched PP displayed in Figure 5.2. It can be observed from the spectrum that the non-linear first normal stress difference response can be described by the normalized fundamental harmonic, $N_{2/2}$, and fourth harmonic relative to fundamental harmonic, $N_{4/2}$. The fundamental harmonic of first normal stress difference response under LAOS flow were investigated by few authors [80,79,122,123]. However, to our knowledge, no investigation is performed on higher order harmonics. As it is seen from the

Fourier spectrum, the higher order harmonics also contributes to the nonlinear first normal stress difference response under LAOS flow (Fig.5.2). This motivated the analysis of $N_{4/2}(\gamma_0, \omega)$ for the characterization of long-chain branching and type of branching. At first, the third and fifth harmonics of stress responses, and the fourth harmonic of first normal stress difference responses were simulated using the Pom-Pom model. Then, the experimental results were presented for the PP and PE blends.

LAOS flow simulations using the Pom-Pom model

The normal and shear stresses were simulated using a Pom-Pom model and resulting responses were analyzed using FT-Rheology. The detail of Pom-Pom equations which were used in our simulations is described in chapter 2. Figure 5.3a illustrates the third harmonic relative to the fundamental harmonic, $I_{3/1}$, as a function of applied deformation amplitudes, γ_0, and the branching degree, q. For all simulated values of q, the Medium Amplitude Oscillatory Shear (MAOS) regime is observed where the square scaling law $I_{3/1} \propto \gamma_0^2$ for $I_{3/1}$ is valid[73,55]. Motivated by the square scaling Hyun and Wilhelm[73] introduced a nonlinear parameter, $Q(\gamma_0, \omega) = I_{3/1}/\gamma_0^2$. An increase in $Q(\gamma_0, \omega)$ as a function of deformation amplitudes, γ_0, is called Q-thickening, while a decrease with deformation amplitudes, γ_0, is called Q-thinning. In the limit of small deformation amplitudes, the $Q(\gamma_0, \omega)$ becomes independent of applied deformation amplitudes. The limiting $Q(\gamma_0, \omega)$ is called intrinsic nonlinearity $Q_0(\omega) = \lim_{\gamma_0 \to 0} Q(\gamma_0, \omega)$. The nonlinear parameter, $Q = I_{3/1}/\gamma_0^2$, for q=1, 2, 6 and 12 shows Q-thinning whereas for q=17, Q-thickening behaviour was observed. Both kinds of behaviour were previously observed experimentally for comb topologies[73]. In the MAOS regime, as the degree of branching, q, increased, $I_{3/1}$ and consequently $Q(\gamma_0)$ was seen to decrease. Furthermore, in the LAOS regime, where the ratio of the higher harmonics deviates from the scaling law, $I_{3/1}(\gamma_0, \omega)$ converged towards a constant value that decreased as q increased, in a similar manner to the trend seen in the MAOS regime.

Figure 5.3b shows how $Q_0(\omega)$ varies over a wide range of angular frequencies, ω. It was observed that by increasing the branching degree, q, the $Q_0(\omega)$ at all frequencies decreased. This observation could be explained by the analytical expression derived from the MSF model $Q_0 \propto (\alpha - \beta)$[71], where α is the orientation parameter and β is the stretching parameter. It is clear from this expression that as branching increases, the stretching factor β will also increase causing $Q_0(\omega)$ to decrease. For the Pom-Pom model simulations it was also seen that as the branching degree q increased, molecular stretching increased, which was reflected in a drop in the value of Q_0 at

all frequencies. In addition, it was observed that the qualitative behaviour for the $q = 1$ (linear topology) was different compared to when other values of q were used. This could be explained by the fact that molecular stretching is not considered for the linear polymer in the Pom-Pom model. Furthermore, at ω_d ($\tau_d = 1/\omega_d$), a maximum was observed, which opens up a new possibility to detect the reptation time scale, τ_d, experimentally even for branched system. Next, two interesting results which were obtained by Hyun et al.[72] will be discussed. First, a minimum was observed in the plot of Q_0^{max} as a function of the backbone fraction $\phi_b S_b$, where S_b is the ratio of backbone molecular weight to entanglement molecular weight. Second, the observation of two maxima in the plot of $Q_0(\omega)$ as a function of ω were observed.

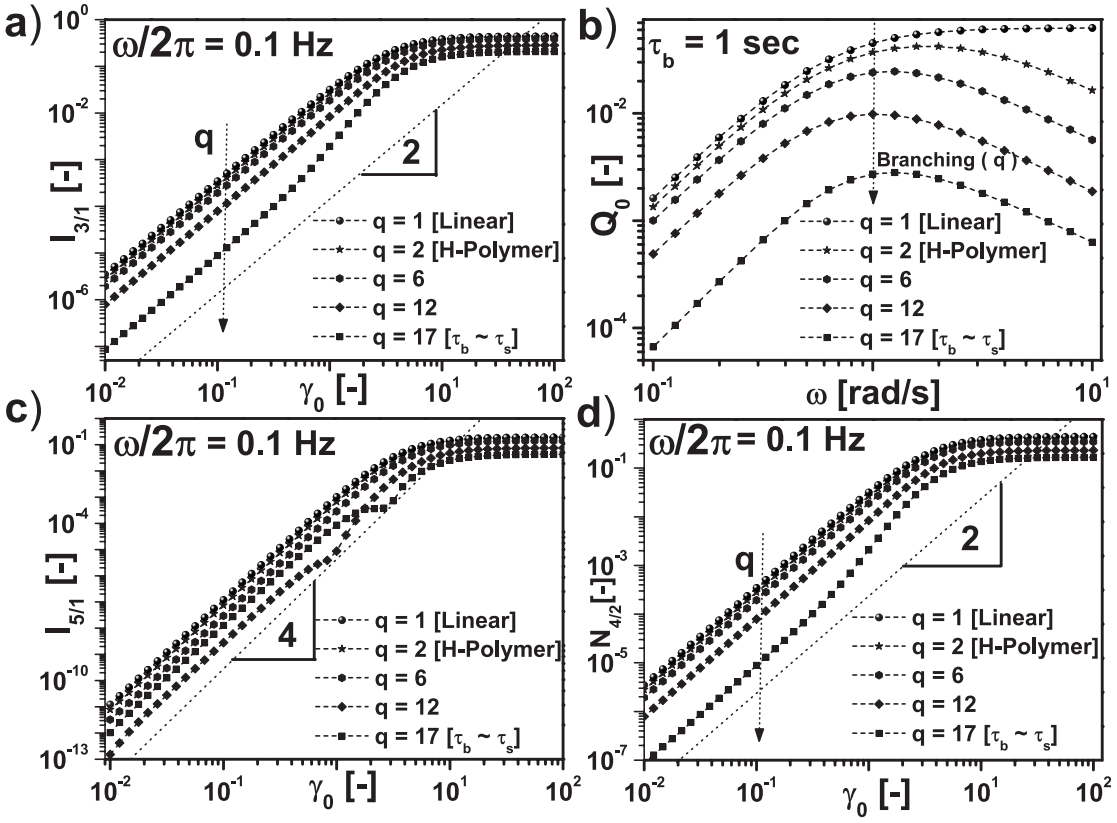

Figure 5.3: Results for LAOS simulations using the Pom-Pom Model for parameters $G_n = 10^5$ Pa, $S_b = 10$, $S_a = 4$, $\tau_d = 1$ sec, and q = 1, 2, 6, 12, 17, for (a) third order Fourier intensity relative to fundamental intensity, $I_{3/1}(\gamma_0, q)$, variation with deformation, γ_0, and branching, q (b) intrinsic nonlinearity based on $I_{3/1}$, ($Q_0(\omega, q)$) variation with ω and branching, q, (c) fifth order Fourier intensity relative to fundamental intensity, $I_{5/1}(\gamma_0, q)$, variation with deformation, γ_0, and branching, q (d) fourth order Fourier intensity relative to fundamental intensity for the first normal stress, $N_{4/2}(\gamma_0, q)$, variation with deformation, γ_0, and branching, q.

The Pom-Pom model is based on the fundamental assumption that all the branches in the Pom-Pom molecules are relaxed and that the nonlinear viscoelasticity results from backbone orientation and stretching, which means that $\tau_a < \tau_s < \tau_d$ where τ_a is the arm relaxation time and τ_s is the stretching relaxation time. The highest allowed value for q is restricted since the ratio τ_s/τ_b cannot exceed one, meaning that for the selected fixed parameters that maximum value for q is $q = 17$. In these simulations, Q_0^{max} decreased monotonically with q up to the physical limit of the simulations, which is in contrast to the simulation shown by Hyun et al.[72] where a minimum was seen in the plot of Q_0^{max} as a function of the backbone fraction $\phi_b S_b = S_b^2/(S_b + 2S_a q)$. The re-investigation revealed that the minimum is based on a region outside the physical limit of the Pom-Pom model. Hyun et al.[72] increased the value of q beyond physical limit where the reptation time τ_d, is less than the stretching time τ_s.[72] also observed a second maximum in the simulation which they compared with experimental data for comb polymers and argued that the second maximum in the simulation relates to the branch relaxation τ_a. In contrast, our simulations results only display one maximum. As the branch relaxation time τ_a, did not enter into the formulation of the differential single mode Pom-Pom model, the appearance of second maximum in the simulations of $Q_0(\omega)$ by Hyun et al.[72] is unclear.

Figure 5.3c shows how the ratio of the fifth harmonic relative to the fundamental harmonic, $I_{5/1}$, varies with the deformation, γ_0, and branching degree, q. For $I_{5/1}$, the expected scaling in the MAOS regime $I_{5/1} \propto \gamma_0^4$ was seen and as the deformation was increased, $I_{5/1}$ then deviated from this scaling and converged to a constant at deformation more than $\gamma_0 = 10$. Motivated by the scaling law in the MAOS regime for $I_{5/1}$, an intrinsic nonlinearity $Q_0^{5/1}$ based on $I_{5/1}$ was introduced:

$$Q_0^{5/1} = \lim_{\gamma_0 \to 0} Q^{5/1} = \lim_{\gamma_0 \to 0} I_{5/1}/\gamma_0^4 \tag{5.2}$$

From Figure 5.3c, it is observed that $I_{5/1}$ at first decreased with increasing branching degree q, but above $q = 12$, $I_{5/1}$ then increased with q in the MAOS regime. However, the qualitative behaviour at all values of q for $I_{5/1}$ was identical in the LAOS regime to the behaviour of $I_{3/1}$ in the LAOS regime. Figure 5.3d shows how the ratio of the fourth higher harmonic relative to the second fundamental higher harmonic $N_{4/2}$ of the first normal stress difference, varies with the deformation γ_0 and branching degree q. In this graph, a square scaling law $N_{4/2} \propto \gamma_0^2$ is observed. Motivated by the scaling law in the simulations for the MAOS regime for $N_{4/2}$, an

intrinsic nonlinearity $Q_0^{N_{4/2}}$ based on normal force $N_{4/2}$ is introduced:

$$Q_0^{N_{4/2}} = \lim_{\gamma_0 \to 0} Q_N^{4/2} = \lim_{\gamma_0 \to 0} N_{4/2}/\gamma_0^2 \tag{5.3}$$

From Figure 5.3d, it was seen that the nonlinear parameter $Q_N^{4/2}$ showed thinning except at $q = 17$ where $Q_N^{4/2}$ thickening was observed. As the branching degree q increased, $N_{4/2}$ decreased in both the MAOS and LAOS simulations which is qualitatively comparable to the behaviour seen for $I_{3/1}$ with increasing q.

To analyze the LAOS data in a physically meaningful way Ewoldt et al.[65] improved the method of Stress Decomposition[64]. The suggested advantage of using this framework over other methods is the definition of the elastic and viscous moduli even at high deformations. Using the Chebyshev polynomials as the basis set, the elastic and viscous contributions to the measured stress response can be written as:

$$\sigma^{'}(x) = \gamma_0 \sum_{n:\ odd} e_n(\omega, \gamma_0) T_n(x) \tag{5.4}$$

$$\sigma^{''}(y) = \gamma_0 \omega \sum_{n:\ odd} v_n(\omega, \gamma_0) T_n(y) \tag{5.5}$$

where $T_n(x)$ is the n^{th}-order Chebyshev polynomial of the first kind, and $x = \gamma/\gamma_0$, $y = \dot{\gamma}/\gamma_0\omega$ provide the appropriate domains of [-1,+1] for orthogonality. The functions at each order are orthogonal and therefore the coefficients e_n and v_n are independent of each other. The $e_n(\omega, \gamma_0)$ are the elastic Chebyshev coefficients and $v_n(\omega, \gamma_0)$ are the viscous Chebyshev coefficients. Similar to FT-Rheology, here we focused our attention to the third order elastic and viscous coefficients relative to fundamental first order elastic and viscous coefficients, respectively. For example, Figure 5.4 shows the variation of the relative third order Chebyshev coefficients obtained by analyzing the decomposed stress response as a function of both deformation and branching degree (q) at an excitation frequency of $\omega/2\pi = 0.1$ Hz. Figure 5.4a shows the ratio of the third elastic nonlinearity relative to the fundamental elastic response. It is interesting to see that this parameter follows a similar scaling $e_{3/1} \propto \gamma_0^2$ as observed for $I_{3/1}(\gamma_0)$. Motivated by the definition of the intrinsic nonlinearity $Q_0(\omega)$ we introduce here the elastic intrinsic nonlinearity Q_0^e, Qualitatively, the behavior of the third elastic nonlinearity $e_{3/1}$ followed a similar pattern as that for the $I_{3/1}$, except at high deformation where this plateau value even exceeded unity which did not occur for $I_{3/1}$.

$$Q_0^e = \lim_{\gamma \to 0} Q^e = \lim_{\gamma \to 0} \frac{e_{3/1}}{\gamma_0^2} \tag{5.6}$$

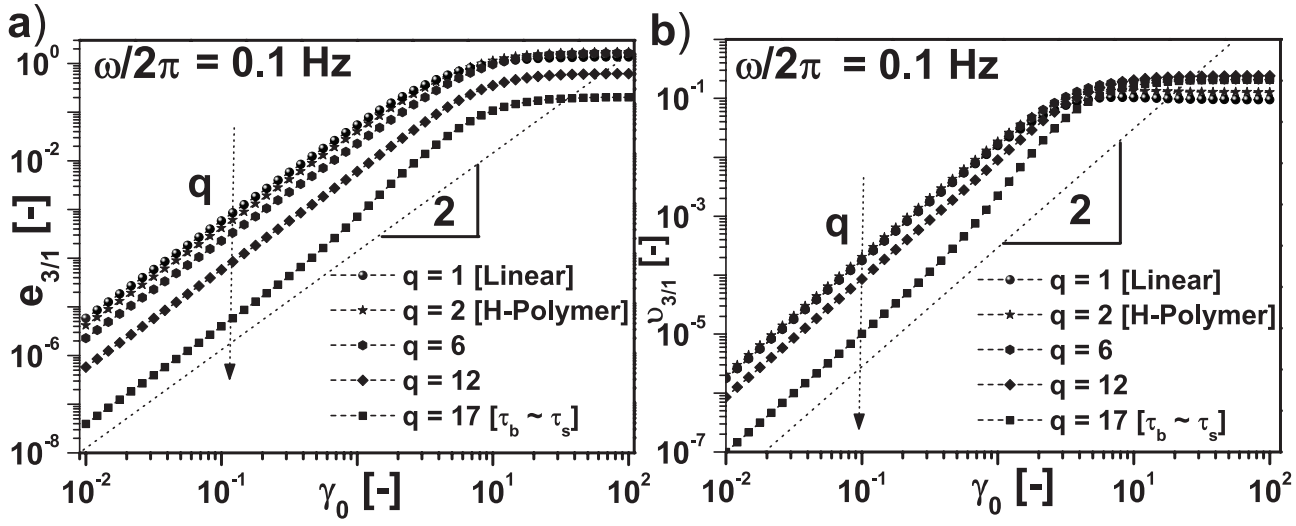

Figure 5.4: Results for LAOS simulations using the Pom-Pom Model for $G_n = 10^5$ Pa, $S_b = 10$, $S_a = 4$, $\tau_d = 1$ sec, and q = 1, 2, 6, 12, 17 for (a) third order elastic Chebyshev coefficient relative to first order elastic coefficient, $e_{3/1}(\gamma_0, q)$, variation with the deformation, γ_0, and branching, q, (b) third order viscous Chebyshev coefficient relative to first order elastic coefficient, $\nu_{3/1}(\gamma_0, q)$, variation with the deformation, γ_0, and branching, q.

Figure 5.4b shows the third viscous nonlinearity relative to the fundamental viscous response, which also followed the scaling $\nu_{3/1} \propto \gamma_0^2$. In a similar fashion as for the elastic response, we introduced here the viscous intrinsic nonlinearity Q_0^ν

$$Q_0^\nu = \lim_{\gamma \to 0} Q^\nu = \lim_{\gamma \to 0} \frac{\nu_{3/1}}{\gamma_0^2} \tag{5.7}$$

Interestingly, the dependence of $\nu_{3/1}$, on the degree of branching in the system was different here compared to the observed dependence for all the other parameters. The parameter, $\nu_{3/1}$ did not change with increasing degree of branching up to $q = 6$, but then decreased when $q = 12$ and 17.

LAOS flow experiments on PP and PE blends

The LAOS experiments were performed at 190 °C for the PP and PE blends. The applied deformation amplitudes range were $\gamma_0 = 0.01 - 10$ at excitation frequency of $\omega/2\pi = 0.1$ Hz. The specific frequency was chosen because Vittorias et al.[110] observed the better differentiation of LCB in industrial PE systems at low excitation frequency ($\omega/2\pi = 0.1$ Hz). This can be explained by the fact that the presence of LCB has significant effect on longest relaxation times.

Figure 5.5a-b shows the ratio of the third and fifth higher harmonic relative to the fundamental harmonic, as a function of γ_0 for the PP-blends. The square scaling law $I_{3/1} \propto \gamma_0^2$, was observed for the PP-blends (Fig. 5.5a). In the MAOS regime ($\gamma_0 = 0.3 - 0.7$), the $I_{3/1}(\gamma_0)$ was increasing as the weight fraction of long-chain branched PP (PP-5) increased. In contrast, the Pom-Pom model simulations revealed that the branching reduces $I_{3,1}(\gamma_0)$.

In this study, $I_{5/1}(\gamma_0)$ was also analyzed to characterize the long-chain branching in PP blends and PE blends. The expected scaling law $I_{5/1} \propto \gamma_0^4$, is observed for the PP-blends only in a limited regime (Fig. 5.5b). Similar to the $I_{3/1}(\gamma_0)$, the $I_{5/1}(\gamma_0)$ also displayed increasing trend as the long-chain branched PP (PP-5) fraction is increased in the blends. The addition of long-chain branhced PP (PP-5) in PP blends had much more pronounced effect on $I_{5/1}(\gamma_0)$ relative to $I_{3/1}(\gamma_0)$. These first results are encouraging because they revel that higher order harmonics (more than the third order), if detectable, might also be effective in characterizing the long-chain branching.

Figure 5.5c-d shows the ratio of the third and fifth higher harmonic relative to the fundamental harmonic, as a function of γ_0 for the PE-blends. The square scaling law $I_{3/1} \propto \gamma_0^2$, were observed for the PE-blends (Fig. 5.5a). In case of the PE-blends, the $I_{3/1}(\gamma_0)$ in MAOS regime ($\gamma_0 = 0.3 - 0.7$) was lowest for the linear PE (PE-1) and long-chain branched PE (PE-6) has a higher value. The lower value of the $I_{3/1}(\gamma_0)$ for linear topology PE (M_w = 202, PDI = 16) relative to the long-chain branched PE (M_w = 144, PDI = 7.59) could be explained by significant higher polydispersity and small amount of branching which was previously confirmed by thermo-rheological analysis. It was surprising that the PE-blends has higher $I_{3/1}$ values than both linear and long-chain branched PE. It was seen that, as the long-chain branched PE (PE-6) content increased in the blends, the $I_{3/1}(\gamma_0)$ decreased. The Pom-Pom model simulation agree with the observation where increase of branching content also decreases the $I_{3/1}(\gamma_0)$. In contrast, PP-blends showed the opposite qualitative behaviour for the $I_{3/1}(\gamma_0)$. The scaling law $I_{5/1} \propto \gamma_0^4$, were observed for the PE-blends (Fig. 5.5d). The qualitative behaviour for the $I_{5/1}(\gamma_0)$ was similar to the PP-blends. It seems that the $I_{5/1}(\gamma_0)$ increases with the long-chain branched weight fraction and the fifth relative harmonic seems to be not affected by the polydispersity.

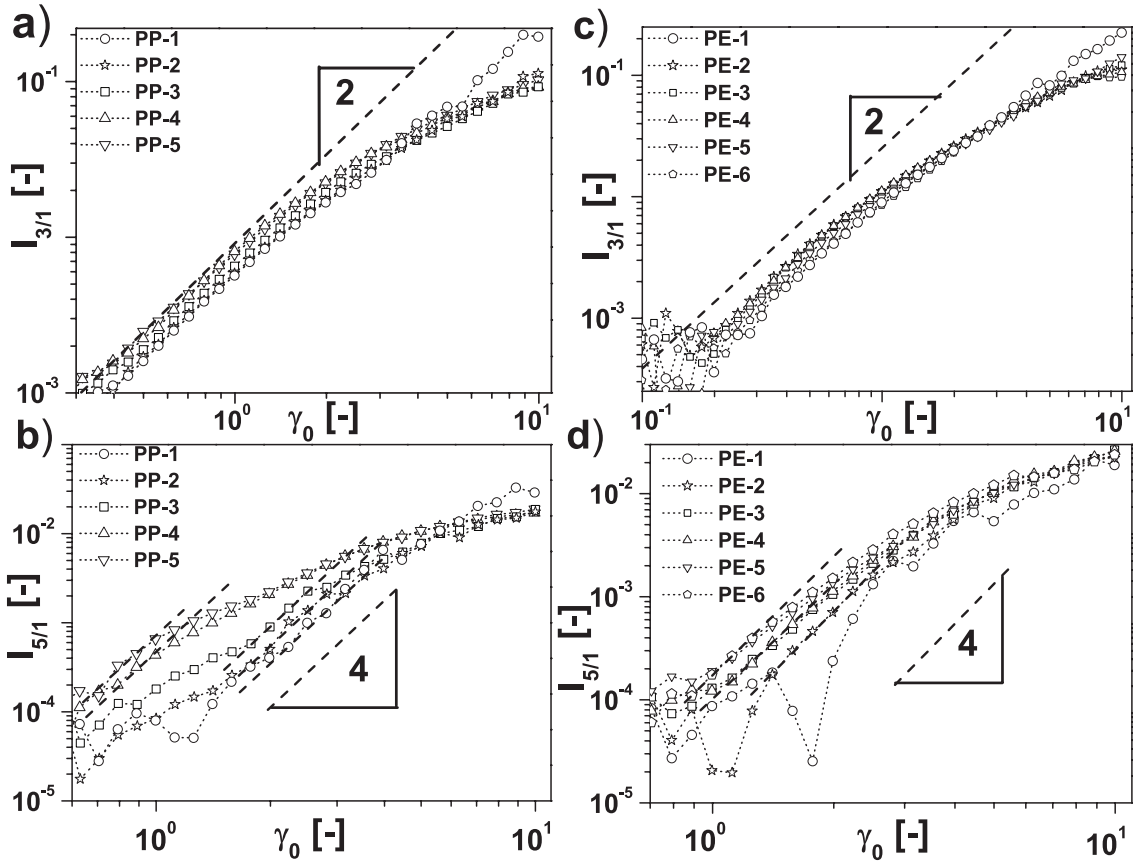

Figure 5.5: Result of FT-Rheology of PP blends and PE blends at $\omega/2\pi = 0.1$ Hz, for the (a) ratio of the third higher harmonic relative to the fundamental harmonic, $I_{3/1}$, as a function of deformation for PP-blends (b) ratio of the fifth higher harmonic relative to the fundamental harmonic, $I_{5/1}$, as a function of deformation for PP-blends (c) ratio of the third higher harmonic relative to the fundamental harmonic, $I_{3/1}$, as a function of deformation for PE-blends(d) ratio of the fifth higher harmonic relative to the fundamental harmonic, $I_{5/1}$, as a function of the deformation for PE-blends.

The first normal stress difference in LAOS was investigated only by very few authors[79,122,123] due to lack of commercial instrumentation. However, recent improvements in instrumentation allowed us to revisit normal stress measurement in LAOS, because long-chain branching increases the elasticity of polymer materials which induces a significant amount of first normal stress during the processing. Figure 5.6a shows the ratio of the fourth higher harmonic relative to fundamental harmonic for first normal stress difference, $N_{4/2}$, as a function of deformation amplitudes, γ_0, for PP-blends. The square scaling law $N_{4/2} \propto \gamma_0^2$ was observed for long-chain branched PP (PP-5) and blend with 80 wt% of long-chain branching fraction (PP-4) in a limited deformation amplitude

range. However, for linear PP (PP-1), and blends with 10 and 40 wt. % long-chain branching fraction, no scaling law was observed. Qualitatively, the first normal stress nonlinearity, $N_{4/2}(\gamma_0)$, showed an increase with long-chain branched PP fraction. Figure 5.6b, shows the variation of $N_{4/2}$ as a function of deformation amplitudes, γ_0, for PE blends. For the PE blends, a square scaling was observed. Qualitatively, the first normal stress nonlinearity, $N_{4/2}(\gamma_0)$, showed a decrease with long-chain branched PE fraction. The contrasting qualitative behaviour of PP and PE blends is attributed to differences in type of branching.

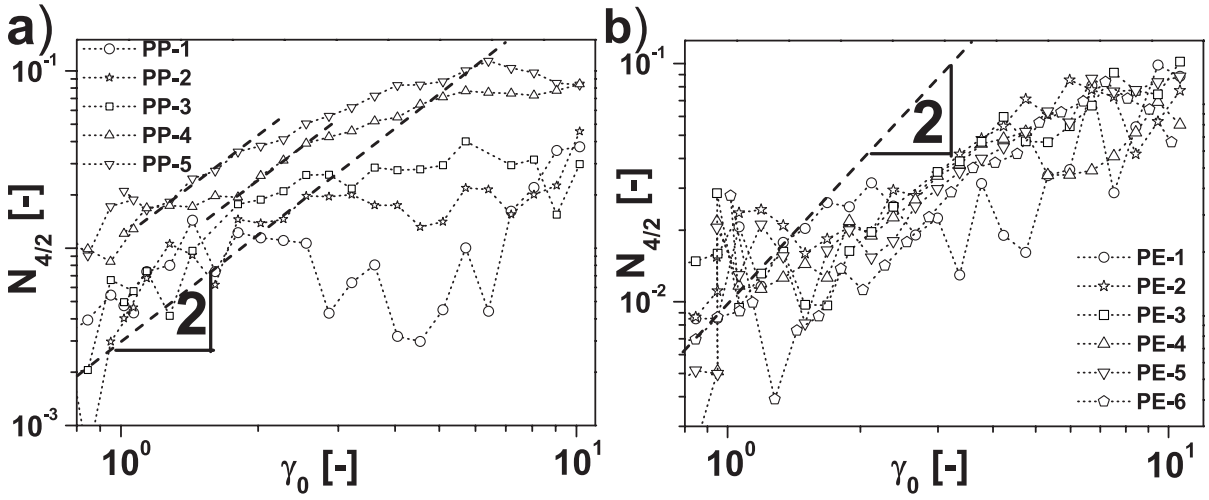

Figure 5.6: Normal stress measurements and its analysis using FT-Rheology for PP-blends and PE-blends (a) fourth higher harmonic relative to fundamental harmonic, $N_{4/2}$, variation as a function of deformation for PP-blends (b) fourth higher harmonic relative to fundamental harmonic, $N_{4/2}$, variation as a function of deformation for PE-blends.

Figure 5.7a shows the ratio of the third elastic Chebyshev coefficient to the first elastic Chebyshev coefficient, $e_{3/1}(\gamma_0)$, as a function of the applied deformation amplitudes, γ_0, for PP-blends. The $e_{3/1}(\gamma_0)$ for the PP-blends have not displayed square scaling law, in contrast, with the simulation of $e_{3/1}(\gamma_0)$ using the single mode Pom-Pom model. For the PP-blends the slopes were higher than 2 at the beginning and then, at high deformation amplitudes, they approached to a constant value. The careful observation of $e_{3/1}(\gamma_0)$ after applied deformation amplitudes of $\gamma_0 = 3$, revels the significant high resolution towards characterization of long-chain branching. At $\gamma_0 = 10$, the maximum resolution were displayed for characterization. The highest $e_{3/1}(\gamma_0 = 10)$ were observed for linear PP (PP-1) and lowest for long-chain branched PP (PP-5). For the PP-blends, even at the deformation amplitude of $\gamma_0 = 10$, and frequency of $\omega/2\pi = 0.1$ Hz, the relative standard

deviation of reproducibility is less than 3 % for the $e_{3/1}$. To confirm our measurements validity at high deformation, the experiments were also performed at RPA-2000 ($\gamma_0 = 10$, $\omega/2\pi = 0.1$ Hz), which is a dynamic testing instrument with grooved biconical die geometry to prevent slippage. The measurements at both instruments agreed well within 10% of deviation for the PP-blends.

The sign of the third order viscous Chebyshev coefficient is related to the inter-cycle decomposed viscous stress[65]. While a positive value for $v_{3/1}$ represents intra-cycle shear thickening of the viscous stress, $v_{3/1} < 0$ describes shear thinning. Figure 5.7b shows the ratio of the third viscous Chebyshev coefficient over the first viscous Chebyshev coefficient, $v_{3/1}$, as a function of the applied deformation γ_0 for PP-blends. Here the square scaling $v_{3/1} \propto \gamma_0^2$ was valid at small deformation amplitudes. PP-blends at first demonstrated instantaneous viscous thickening up to deformations around $\gamma_0 = 2-3$ but then experienced a transition to instantaneous viscous thinning. The $v_{3/1}$ has similar qualitative behavior compared to that for Q_0 based on $I_{3/1}$.

Figure 5.7c shows the ratio of the third elastic Chebyshev coefficient to the first elastic Chebyshev coefficient, $e_{3/1}(\gamma_0)$, as a function of the applied deformation amplitudes, γ_0, for PE blends. Similar to PP blends, the PE blends did not displayed the square scaling. In addition, for PE-blends at $\gamma_0 = 10$, the measurements from both the instruments were in good agreement except for LCB-PE (PE-6) where there was a significant difference were observed between the RPA-2000 and ARES-G2 instruments.

Figure 5.7d shows the experimental ratio of the third viscous Chebyshev coefficient over the first viscous Chebyshev coefficient, $v_{3/1}(\gamma_0)$, variation with applied deformation, γ_0, for PE-blends. Here the square scaling law was also valid and similar qualitative trends were observed as seen for Q_0 based on $I_{3/1}$. For the PE-blends, a transition from viscous thickening to viscous thinning occurred between $\gamma_0 = 3-4$. Interestingly, for both PE and PP blends, the deformation from where instantaneous viscous thinning were observed, the $e_{3/1}(\gamma_0)$ start to show significant resolution for characterization of LCB.

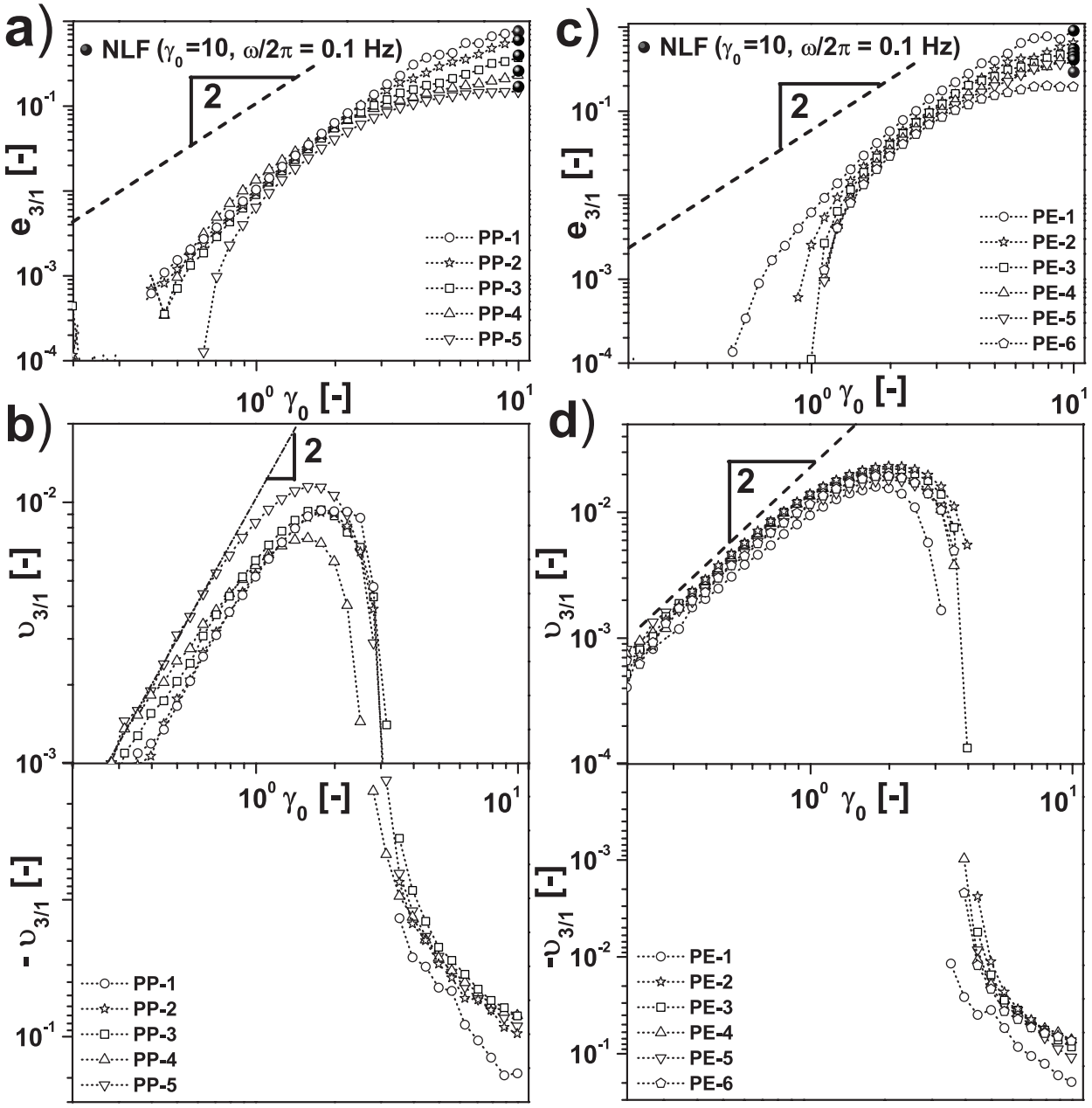

Figure 5.7: Stress-Decomposition analysis of blends at $\omega/2\pi$ = 0.1 Hz (a) third order Chebyshev elastic coefficient relative to first order Chebyshev elastic coefficient variation, $e_{3/1}$ as a function of deformation, γ_0, for PP-blends, (b) third order Chebyshev viscous coefficient relative to first order Chebyshev viscous coefficient variation, $v_{3/1}$ as a function of deformation, γ_0, for PP-blends, (c) third order Chebyshev elastic coefficient relative to first order Chebyshev elastic coefficient variation, $e_{3/1}$ as a function of deformation, γ_0, for PE-blends, (d) third order Chebyshev viscous coefficient relative to first order Chebyshev viscous coefficient variation, $v_{3/1}$, as a function of deformation, γ_0, for PE-blends.

Comparison of different nonlinear mechanical parameters determined in MAOS and LAOS regime to characterize the LCB

The nonlinear oscillatory shear experiments can be subdivided into two regime, (i) Medium Amplitude Oscillatory Shear (MAOS) and (ii) Large Amplitude Oscillatory Shear (LAOS). The advantages of investigating the materials in the MAOS regime are, reliable measurements without getting into the problem of slippage and secondary flow, and determination of intrinsic material parameters, such as, intrinsic nonlinearities, $Q_0^{3/1}$, $Q_0^{5/1}$ (Eq. 5.2), $Q_0^{\nu_{3/1}}$ (Eq. 5.7), $Q_0^{e_{3/1}}$ (Eq. 5.6), and $Q_0^{N_{4/2}}$ (Eq. 5.3). Interestingly, in LAOS regime, a high resolution was observed for characterization of both PP and PE blends at $\omega/2\pi = 0.1$ Hz. The relative standard deviation of reproducibility for $e_{3/1}(\gamma_0)$ is 3 %. To confirm the reliability of measured data for $e_{3/1}(\gamma_0)$, the experiments were also carried out with the RPA-2000 rheometer which is a dynamic testing instrument with grooved biconical die geometry to prevent slippage. The test cavity is closed and pressurised for the duration of test using an elastomeric seal between die and seal plate. The measurements with the two instruments are in well agreement for the PP blends and PE blends, except, for long-chain branched PE (PE-6), where a deviation was observed.

In the MAOS regime, the long-chain branched PP displayed an increase in intrinsic nonlinearity, $Q_0^{3/1}$, by 55 % relative to linear PP. Furthermore, the $Q_0^{3/1}$ for the blends of long-chain branched PP and linear PP displayed a monotonic increase as a function of the long-chain branched fraction (Fig. 5.8a). In comparison, the long-chain branched PE displayed a increase in $Q_0^{3/1}$ by 10 % relative to linear PE. However, for the case of PE-blends, $Q_0^{3/1}$ was higher than both long-chain branched PE as well as linear PE, which is in contrast to PP blends (Fig. 5.8d).

In the MAOS regime, the intrinsic nonlinearity, $Q_0^{\nu_{3/1}}$, displayed a similar qualitative behaviour than the $Q_0^{3/1}$ for both PP an PE blends (Fig. 5.8a and Fig. 5.8d). However, long-chain branched PP displayed an increase by 101 %, and long-chain branched PE displayed an increase by 22 %, in $Q_0^{\nu_{3/1}}$, relative to respective linear topology. The higher resolution (approximately twice increase in resolution) for characterization of both PP and PE blends were achieved by using the $Q_0^{\nu_{3/1}}$, relative to the $Q_0^{3/1}$, if similar relative reproducibility is assumed.

In the MAOS regime, the long-chain branched PP displayed an increase in intrinsic nonlinearity, $Q_0^{5/1}$, by 2800 % relative to linear PP (Fig. 5.8a). Furthermore, the long-chain branched PE displayed a increase by 275 % in $Q_0^{5/1}$ relative to a blend with 10 % of long-chain branched PE

(Fig. 5.8d). The relative changes could not be reported relative to linear PE because following scaling, $I_{5/1} \propto \gamma_0^4$, was experimentally not observed for linear PE. The qualitative behaviour of the $Q_0^{5/1}$ for both the PP and PE blends were similar. However, the differences in qualitative trend were observed in intrinsic nonlinearities, $Q_0^{3/1}$ and $Q_0^{\nu_{3/1}}$ for the PP and PE blends.

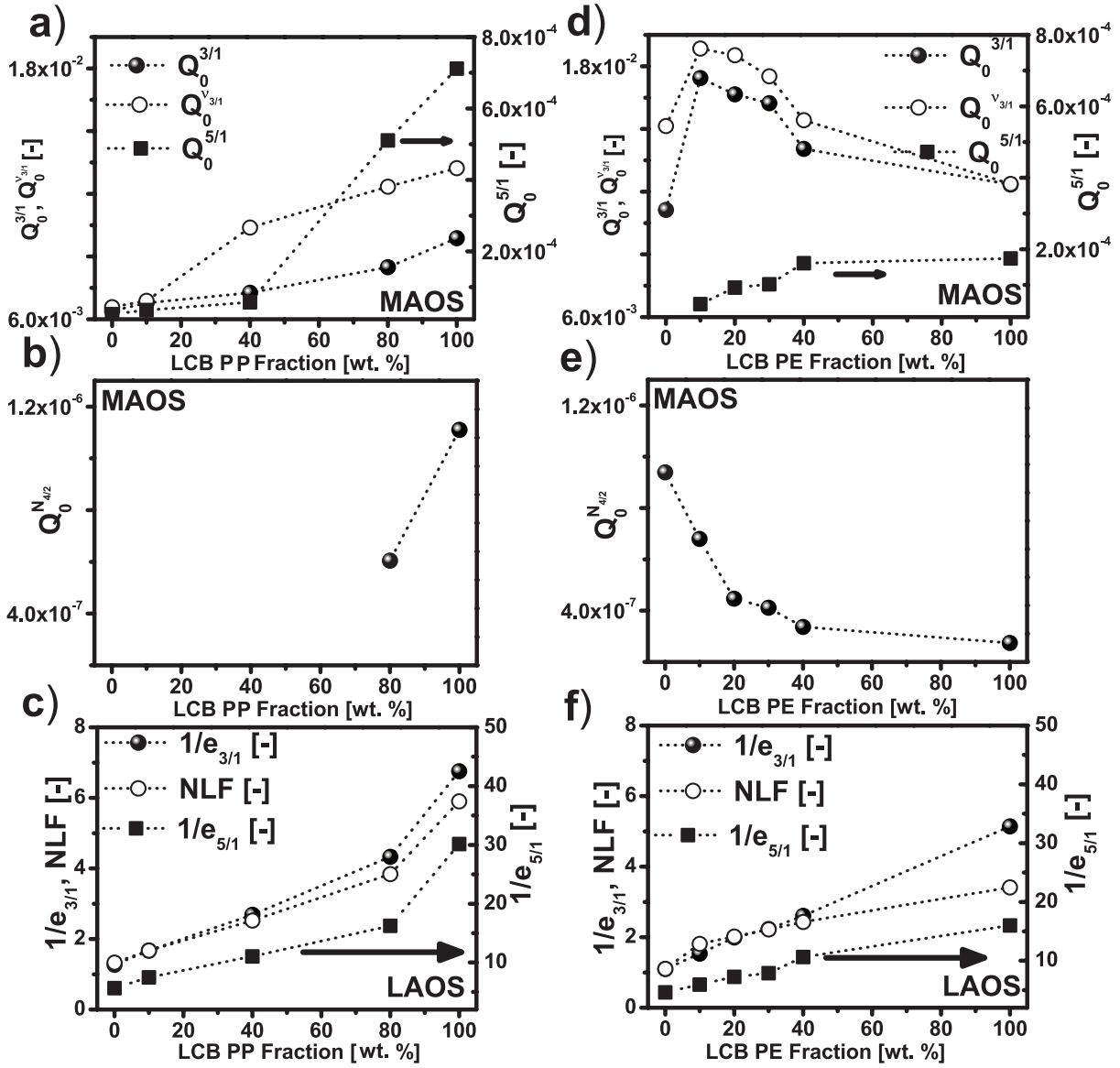

Figure 5.8: Comparison of material parameters derived under MAOS and LAOS flow for characterization of blends, (a) $Q_0^{3/1}$, $Q_0^{\nu_{3/1}}$, and $Q_0^{5/1}$ as a function of long-chain branched PP fraction in PP blends, (b) $Q_0^{N_{4/2}}$ as a function of long-chain branched PP fraction in PP blends, (c) NLF, $1/e_{3/1}$,and $1/e_{5/1}$ as a function of long-chain branched PP fraction in PP blends, at $\gamma_0 = 10$, $\omega/2\pi = 0.1$ Hz, (d) $Q_0^{3/1}$, $Q_0^{\nu_{3/1}}$, and $Q_0^{5/1}$ as a function of long-chain branched PE fraction in PE blends, (e) $Q_0^{N_{4/2}}$ as a function of long-chain branched PE fraction in PE blends, (f) NLF, $1/e_{3/1}$,and $1/e_{5/1}$ as a function of long-chain branched PE fraction in PE blends, at $\gamma_0 = 10$, $\omega/2\pi = 0.1$ Hz.

In the MAOS regime, for the case of the linear PP, and the blends with 10 wt% and 40 wt% fraction of long-chain branched PP, no intrinsic nonlinearity, $Q_0^{N_{4/2}}$ were calculated because at small deformation amplitude limit, the $Q^{N_{4/2}}$, did not converge to a constant value. However, for the long-chain branched PP and the blend with 80 wt% fraction of long-chain branched PP, the $Q_0^{N_{4/2}}$ were calculated and displayed an increasing trend with LCB content (Fig. 5.8b). In case of PE blends, long-chain branched PE displayed a decrease by 70 % (Fig. 5.8e), which in comparison to $Q_0^{3/1}$ and $Q_0^{\nu_{3/1}}$ provides a higher resolution to characterize the PE blends with different long-chain branching fractions. In the MAOS regime, highest resolution for characterization of PP and PE blends was observed for the $Q_0^{5/1}$.

In the LAOS regime, the long-chain branched PP displayed an increase by 430 % in the $1/e_{3/1}$, and 434 % in the $1/e_{5/1}$ relative to the linear PP (Fig. 5.8c). Furthermore, the long-chain branched PE displayed an increase by 365 % in the $1/e_{3/1}$, and 246 % in the $1/e_{5/1}$ relative to the linear PE (Fig. 5.8f). The relative resolution to characterize the blends is significantly higher than the $Q_0^{3/1}$, $Q_0^{\nu_{3/1}}$, and $Q_0^{N_{4/2}}$. Over the investigated applied deformation amplitudes range (SAOS, MAOS, and LAOS), the intrinsic nonlinearity, $Q_0^{5/1}$, displayed highest resolution to characterize the PP blends, and the $1/e_{3/1}$ displayed highest resolution to characterize the PE blends. Both, $Q_0^{5/1}$ in MAOS regime and $1/e_{3/1}$ in LAOS regime are effective parameters to characterize the PP and PE blends. Although $Q_0^{N_{4/2}}$ showed sensitivity towards LCB, however, relative resolution to characterize the PP and PE blends was small compared to $Q_0^{5/1}$ and $1/e_{3/1}$. Therefore, less suited to characterize LCB, then $Q_0^{5/1}$ and $1/e_{3/1}$.

5.2.3 Nonlinear Viscoelasticity: Uniaxial Extensional Experiments and Molecular Stress Function (MSF) Model Simulations

Many industrially relevant processes, such as, extrusion, electrospinning, fiber spinning, film blowing, and ink jet printing are dominated by extensional deformations[11,4]. In extensional flow, the long-chain branched macromolecules experience substantial stretching and orientation. As a result of this, extensional hardening is observed for long-chain branched macromolecules. The uniaxial extensional viscosity measurements are frequently used to characterize the long-chain branching in various polymers[4,124,107,125]. The tube based models (Doi-Edwards (DE) model[38,4] and Molecular Stress Function (MSF) model[96,115]) were used to simulate the transient uniaxial extensional viscosity.

The DE model is based on the following fundamental assumptions: the tube diameter remains the same even after large deformations and that there is an immediate Rouse relaxation of the polymer chain. One of the major failure of the DE model is the prediction of extensional thinning, which is in contradiction with experimental observations where usually extensional hardening is observed for polymer melts in extensional flows. By incorporating the chain stretching in polymer chains Wagner et al.[96] developed the (MSF) model. The MSF model was successful in predicting quantitatively the uniaxial extensional viscosity for various systems[49,50,126].

In this chapter, the degree of extensional hardening is quantified using the Strain Hardening Factor (SHF), which is defined as follows:

$$SHF(\epsilon = 2.7, \dot{\epsilon}) = \frac{\eta_e^+(t, \dot{\epsilon})}{\eta_{DE}^+(t, \dot{\epsilon})} \tag{5.8}$$

where ϵ is the Hencky strain, $\dot{\epsilon}$ is the extensional strain rate, η_e^+ is the tensile stress growth coefficient and η_{DE}^+ is the tensile stress growth coefficient determined using the Doi-Edwards model where stretching of macromolecules is not taken into consideration[75].

Figure 5.9a displays the uniaxial transient extensional viscosity $\eta_e^+(t, \dot{\epsilon})$ measurements and simulation for PP-blends. The measurements were performed at 180 °C and extensional rates $\dot{\epsilon}$, varied in the range of $\dot{\epsilon}$ = 0.1 - 10 s^{-1}. In the case of the linear PP (PP-1) all curves measured at different extensional rates superimpose on the linear viscoelastic curve. This is the usual finding for the linear samples with unimodal molecular weight distribution Gabriel et al.[113]. By addition of 10 wt% long-chain branched PP (PP-2) in linear PP (PP-1), a significant enhancement in extensional hardening was observed. The further increase of the long-chain branched PP fraction in the linear PP displayed even more extensional hardening, and highest extensional hardening were observed for long-chain branched PP (PP-5), as expected.

The Doi-Edwards (DE) and Molecular Stress Function (MSF) models were used to simulate the $\eta_e^+(t, \dot{\epsilon})$ for all the PP-blends. The linear viscoelastic parameters (G_i, τ) were extracted by fitting the dynamic frequency spectrum using the multi mode Maxwell model (table 5.2). The nonlinear parameters in MSF model (f_{max}^2, β) were calculated by fitting the uniaxial transient viscosities $\eta_e^+(t, \dot{\epsilon})$ at all measured extensional rates. The prediction for the linear PP (PP-1), the long-chain branched PP (PP-5) and the blends with 80 % weight fraction of long-chain branched PP (PP-4) were reasonable at all measured extensional rates. In contrast, for the remaining blends (PP-2,

PP-3), the prediction were reasonable only at high extensional rates ($\dot{\epsilon}$ = 1, 3, 10 s^{-1}) but at low extensional rates the prediction showed less extensional hardening relative to the experimental measurements.

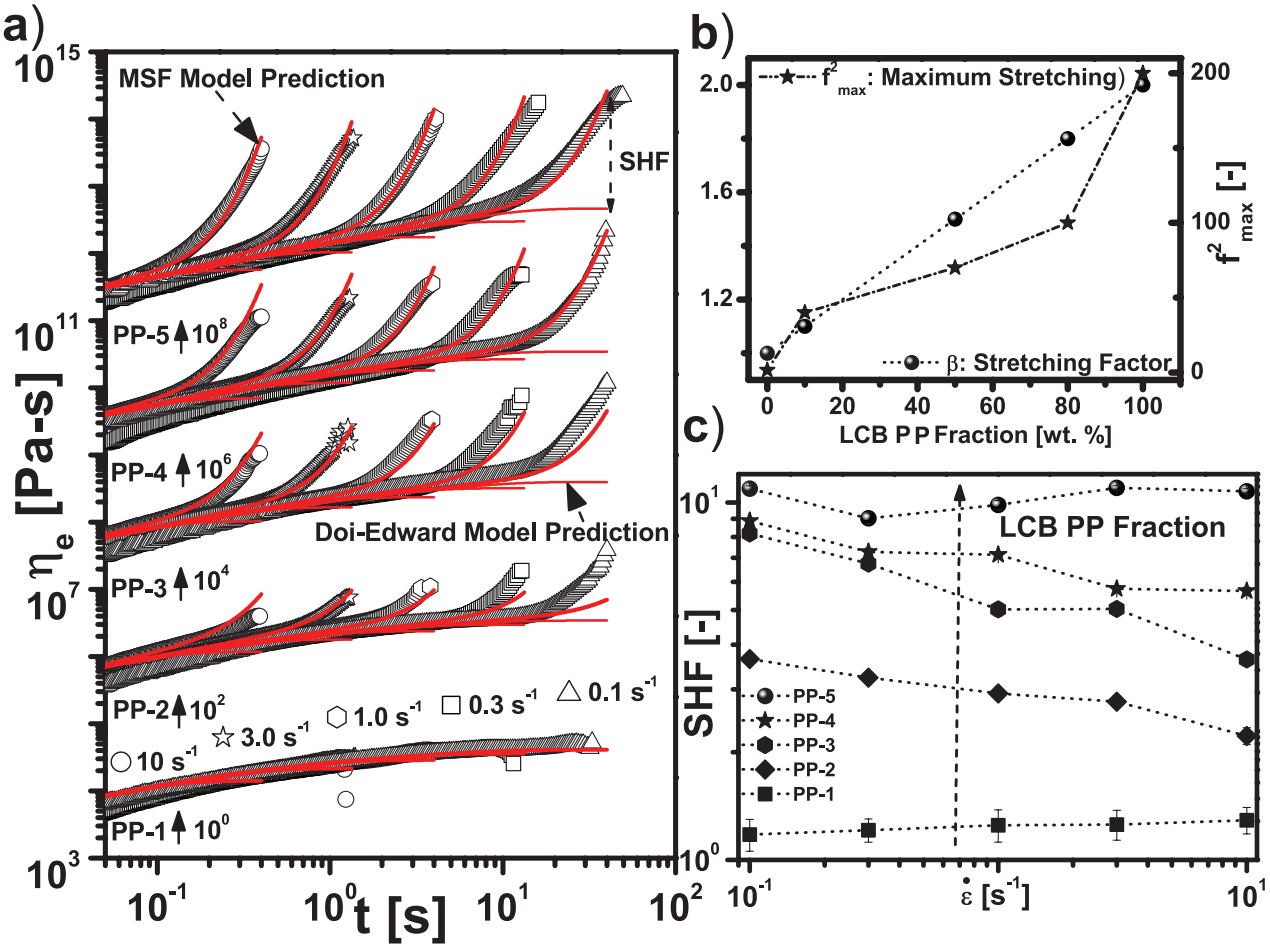

Figure 5.9: Uniaxial extensional measurements using EVF and experimental and modeling parameters, (a) uniaxial extensional measurements and modeling using the MSF model for PP-blends, (b) MSF model parameter variations for PP-blends where β is the stretching parameter and f^2_{max} is the maximum stretching of the macromolecule, and (c) SHF variation with extensional rate $\dot{\epsilon}$ for PP-blends.

The nonlinear parameters (β, f^2_{max}) of the MSF model increased with the long-chain branching PP fraction (Fig. 5.9b). The β values physically represents the slope of the extensional viscosity with time after the start of strain hardening. The β = 2 was obtained for long-chain branched topology (PP-5) and β = 1 for the linear topology (PP-1) which is in good agreement with the previous reported parameter values[51]. The parameter f^2_{max} is related to the square of the maximum relative stretch of the chain segments and determines the steady-state value of the extensional

viscosity. The maximum stretching $f^2_{max} = 200$ was estimated for LCB-PP (PP-5) and $f^2_{max} = 1$ for linear PP (PP-1). The blends have stretching parameter f^2_{max}, in between the long-chain branched and linear topology polypropylene (see Fig. 5.9b).

Figure 5.9c illustrates the SHF dependence on applied extensional rate ($\dot{\epsilon}$) for PP-blends. The SHF for linear PP (PP-1) is monotonically increasing function of extensional rates. However, the SHF for PP blends displayed a decreasing trend with extensional rates. The qualitative trend of SHF as a function of extensional rates is frequently used to characterize the molecular structure. A decrease in strain hardening with increasing strain rate is usually associated with low degrees of long-chain branching of a starlike topology, while the opposite behavior is typical of a high degree of branching with a treelike topology[125,113,127,128,129].

Table 5.2: Multi-mode Maxwell relaxation modes for polypropylene (PP) [T = 180 °C]

PP-1		PP-2		PP-3	
τ_d [s]	G [Pa]	τ_d [s]	G [Pa]	τ_d [s]	G [Pa]
7.745e-4	1.978e+5	1.141e-3	1.520e+5	8.837e-4	1.543e+5
8.092e-3	5.973e+4	9.523e-3	5.199e+4	8.901e-3	4.398e+4
3.354e-2	3.759e+4	4.024e-2	2.991e+4	3.977e-2	2.417e+4
1.325e-1	1.832e+4	1.630e-1	1.309e+4	1.673e-1	1.129e+4
5.326e-1	6.064e+3	6.822e-1	3.959e+3	7.122e-1	3.967e+3
2.247e+0	1.478e+3	2.965e+0	9.326e+2	3.155e+0	1.158e+3
1.115e+1	3.310e+2	1.478e+1	2.028e+2	1.841e+1	3.195e+2
PP-4		PP-5			
τ_d [s]	G [Pa]	τ_d [s]	G [Pa]		
8.658e-4	1.280e+5	5.621e-4	1.482e+5		
8.415e-3	2.851e+4	6.335e-3	2.285e+4		
3.747e-2	1.455e+4	2.437e-2	1.145e+4		
1.590e-1	7.271e+3	8.970e-2	6.266e+3		
6.776e-1	3.094e+3	3.280e-1	3.366e+3		
2.918e+0	1.150e+3	1.226e+0	1.763e+3		
1.659e+1	4.601e+2	4.919e+0	8.958e+2		
-	-	3.278e+1	5.548e+2		

A decreasing extensional hardening with increasing extensional rate as found for the PP blends is typical of metallocene-catalyzed PE with small amount of long-chain branches[113,128]. The similar trend was observed by Auhl et al.[114] for the long-chain branched PP which were irradiated with low doses, and an increase in extensional hardening with increasing extensional rate were observed for high irradiation doses. These changes in qualitative behaviour for extensional hardening with extensional rates were explained by the change in the branching structure with irradiation doses. The PP with low doses of irradiation has a star-like branching structure and with high doses has a tree-like branching structure was proposed.

Stange et al.[125] investigated blends of highly branched PP and linear PP. An increasing SHF with extensional rate was observed for long-chain branched PP. In contrast, for the blends a decreasing trend were observed. As the ratio of zero shear-rate viscosity $\eta_0^L/\eta_0^{LCB} > 1$, which confirmed the tree-like branching for the long-chain branched PP used in the study by Stange et al.[125].

Auhl et al.[107] investigated various long-chain branched PP obtained through electron-beam irradiation and gamma-irradiation. The zero shear-rate viscosity ratio, η_0^L/η_0^{LCB} was more than one for gamma-beam irradiated long-chain branched PP, and less than one for electron-beam irradiated long-chain branched PP at low doses (at first the ratio increases with the irradiation dose) and than approaches to one for high doses. The zero shear-rate viscosity ratio $\eta_0^L/\eta_0^{LCB} > 1$, was explained by the tree-like topology obtained by gamma-irradiation and $\eta_0^L/\eta_0^{LCB} < 1$ by the star-like topology obtained by electron -beam irradiation at low doses. At high doses, the tree-like topology was obtained.

One of the major difference between the blends studied by Stange et al.[125] and the blends studied by us is the polymer topology of the long-chain branched PP. In case of Stange et al.[125] the viscosity ratio was $\eta_0^L/\eta_0^{LCB} > 1$ which was consistent with the tree-like topology of long-chain branched PP. In contrast, here the viscosity ratio is $\eta_0^L/\eta_0^{LCB} < 1$ (η_0^{LCB} = 24898 Pa-s, η_0^L = 11046 Pa-s). This would indicate a star-like topology of long-chain branched PP (PP-5) used in this study.

Figure 5.10a displays the uniaxial transient extensional viscosity $\eta_e^+(t, \dot{\epsilon})$ measurements and simulation for the PE-blends. The measurement were performed at 145 °C and extensional rates $\dot{\epsilon}$, in the range of 0.1 - 10 s^{-1}. Similar to PP-blends, the addition of even 10% of long-chain branched

PE (PE-6) in the linear PE (PE-1), improved the extensional hardening. The MSF model prediction of transient extensional viscosity for the PE blends was excellent. Figure 5.10b displayed the nonlinear parameters (β, f^2_{max}) of MSF model variation with the long-chain branched PE fraction. Similar to the PP-blends, the nonlinear parameters displayed monotonically increasing trend with the long-chain branched PE fraction. Figure 5.10c displays the SHF for the PE-blends as a function of applied elongation rates. In case of linear PE (PE-1), the polymer filament were not able to sustain the tensile stress in the range of 3-10 s^{-1} elongation rates. Consequently, the SHF was not displayed at these elongation rates for linear PE. In contrast to PP-blends, the SHF increased as the elongation rates increased, which clearly points towards the tree like topology for the long-chain branched PE (Fig. 5.11).

Table 5.3: Multi-mode Maxwell relaxation modes for polyethylene (PE) [T = 145 °C]

PE-1		PE-2		PE-3	
τ_d [s]	G [Pa]	τ_d [s]	G [Pa]	τ_d [s]	G [Pa]
1.154e-3	2.952e+5	7.374e-4	3.888e+5	5.888e-4	4.506e+5
9.530e-3	1.031e+5	6.833e-3	9.334e+4	6.518e-3	9.180e+4
4.386e-2	6.647e+4	2.572e-2	6.143e+4	2.486e-2	6.020e+4
1.924e-1	3.797e+4	9.321e-2	3.965e+4	9.176e-2	3.946e+4
8.229e-1	1.737e+4	3.446e-1	2.308e+4	3.498e-1	2.400e+4
3.673e+0	6.552e+3	1.301e+0	1.135e+4	1.398e+0	1.248e+4
2.657e+1	2.620e+3	5.226e+0	5.866e+3	5.837e+0	6.891e+3
-	-	4.620e+1	5.033e+3	5.528e+1	6.927e+3
PE-4		PE-5		PE-6	
τ_d [s]	G [Pa]	τ_d [s]	G [Pa]	τ_d [s]	G [Pa]
8.245e-4	3.289e+5	8.643e-4	3.131e+5	6.244e-4	3.165e+5
7.328e-3	8.150e+4	7.586e-3	7.596e+4	7.588e-3	5.171e+4
2.739e-2	5.181e+4	2.821e-2	4.880e+4	2.946e-2	3.309e+4
9.763e-2	3.458e+4	1.001e-1	3.280e+4	1.102e-1	2.310e+4
3.611e-1	2.159e+4	3.672e-1	2.126e+4	3.994e-1	1.527e+4
1.376e+0	1.199e+4	1.451e+0	1.237e+4	1.430e+0	1.029e+4
5.648e+0	7.116e+3	6.129e+0	7.299e+3	5.389e+0	6.854e+3
5.096e+1	7.429e+3	5.653e+1	7.754e+3	3.488e+1	5.988e+3

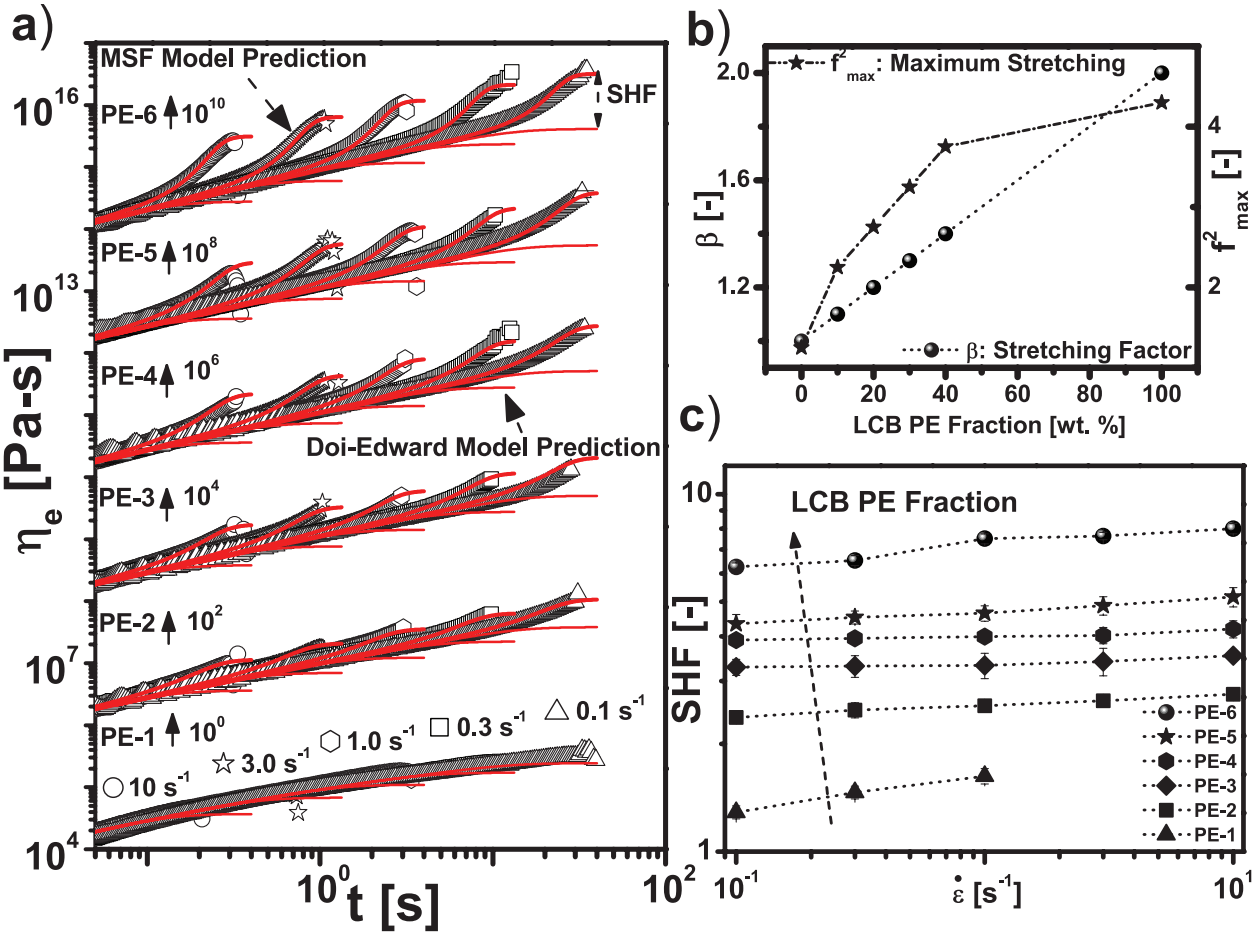

Figure 5.10: Uniaxial extensional measurements using EVF and experimental and modeling parameters, (a) uniaxial extensional measurements and modeling using the MSF model for PE-blends, (b) MSF model parameter variations for PE-blends where β is the stretching parameter and f^2_{max} is the maximum stretching of the macromolecule, and (c) SHF variation with extensional rate $\dot{\epsilon}$ for PE-blends.

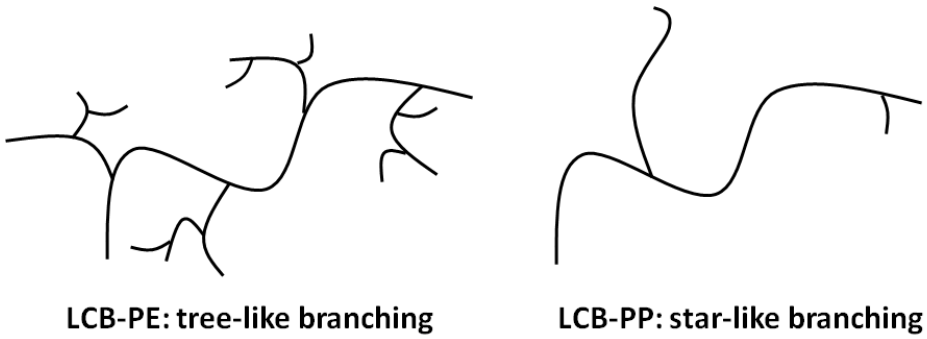

Figure 5.11: The postulated long-chain branching structure for the PP (PP-5) and PE (PE-6).

5.3 Concluding Remarks on the Characterization of LCB Using Oscillatory Shear and Uniaxial Extensional Rheology

Major differences were observed in flow response, both in linear and non-linear viscoelastic regime for PP and PE blends. A starlike topology with few branches for long-chain branched PP, and tree-like topology with high extent of branching for long-chain branched PE are proposed. In the linear viscoelastic regime, the evolution of flow activation energy, as a function of long-chain branched polymer fraction was observed. The difference in evolution is explained by the difference in type of long-chain branching between PP and PE. In the nonlinear viscoelastic regime, the first normal stress differences were measured in oscillating shear, at large deformation amplitudes. For the first time, higher order nonlinearity in the first normal stress measurements , $N_{4/2}(\gamma_0)$, is analyzed as a function of deformation amplitudes. The qualitative behaviour of $N_{4/2}(\gamma_0)$ as a function of deformation amplitudes is opposite for PP and PE blends. Again, these difference is attributed to different type of long-chain branching in PP and PE. The scaling, $N_{4/2} \propto \gamma_0^2$ was observed partly for PP and PE blends and motivated the introduction of a new intrinsic nonlinearity, $Q_0^{N_{4/2}}$. Along with $Q_0^{N_{4/2}}$, the intrinsic nonlinearities, $Q_0^{3/1}$, $Q_0^{5/1}$, and $Q_0^{\nu_{3/1}}$ were used to characterize both PP and PE blends. The highest relative resolutions for the characterization of PP and PE blends were obtained for $Q_0^{5/1}$. In the LAOS regime, $e_{3/1}$ and $e_{5/1}$ at $\gamma_0 = 10$, and $\omega/2\pi = 0.1$ Hz showed the highest resolution to characterize the effect of addition of long-chain branched polymers in PP and PE blends. However, highest relative resolution was obtained for $Q_0^{5/1}$, if measurable. Our hypothesis of proposed structure is further confirmed by uniaxial extensional measurements.

Chapter 6

Non-linear Viscoelasticity of Polymer Composites with Carbon Nanotubes Using FT-Rheology

Polymer composites based on carbon nanotubes[130] (CNTs) attracted enormous interest due to their exceptional electrical[131], mechanical[132,133], and thermal[134] properties at relatively small concentrations in the polymer matrix. The polymer composites based on CNTs have found manufacturing applications in electrostatic painting[135], protective coatings for electronic components[136], radiation shielding[137], and flammability reduction[138]. However, the addition of CNTs into the polymer matrix has consequences for the processing condition (e.g. in mixing, moulding, extrusion, etc) as substantial changes in viscoelastic behavior of the matrix occurs. To optimize the processing condition, it is important to understand the kind of mechanical properties that can be expected by addition of carbon nanotubes in polymer matrix. The change in the mechanical properties will depend primarily on the chemical composition of the polymer, aspect ratio, orientation of CNTs, kind of CNTs, polymer-filler interactions, and degree of dispersion in polymer matrix.

Percolation is a statistical concept that describes the formation of an infinite cluster of connected particles or pathways[139,140]. This concept is widely used to study various phenomena such as flow in porous media, conducting-insulating transitions in composites, and transition from liquid to solid like behavior in polymer composites. To characterize the state of fillers dispersed in a matrix, the percolation scaling law offer the theoretical basis for the properties of composites containing impenetrable particles. The asymptotic variation of a material property (P) is defined as[141,137]:

$P \propto (\phi - \phi_c)^{\beta_p}$, where ϕ is the filler volume fraction, β_p is the critical scaling exponent, and ϕ_c is the percolation threshold concentration, above which a network is formed. The P could be mechanical properties ($G^{'}$, η, δ_0) and electrical property (conductivity). Two material properties are widely used in the application of the percolation theory to describe the dispersion state of CNTs in the polymer matrix: the electrical conductivity and the dynamic elastic modulus. The effects of CNT addition on the linear viscoelasticity of various polymers have been addressed: polystyrene (PS)[137], polycarbonate (PC)[142], poly(methyl methacrylate) PMMA[143], polyethylene (PE)[144], and polypropylene (PP)[145]. Winter et al.[146] described the rheological changes with increasing CNT content in the frame of liquid-solid or liquid-gel transitions. Furthermore, Du et al.[143] provided an perspective for the rheological and conductivity threshold to describe the network formulation by polymer-CNT and CNT-CNT networks using percolation theory. However, most of the industrial processes operate at large deformations where the non-linear behavior is important. Furthermore, under these large deformations relevant changes in the percolation processes occurs, which in consequence has influence on the conductivity behavior as reported by many authors[2,147,148,149,150]. Therefore, to optimize the industrial processes and tailor material properties, an understanding of polymer composites flow behavior under large amplitude oscillatory shear as a model flow for processing conditions.

Recently, Large Amplitude Oscillatory Shear (LAOS) has been used to characterize the non-linear behaviour for polymer nanocomposites[151,152]. Lim et al.[151] investigated the nonlinear viscoelastic behavior of polymer composite systems containing different shaped nanoparticles under LAOS flow. They investigated poly(ϵ-caprolactone)[PCL]/multi-walled carbon nanotubes (MWCNTs) (1D), PCL/organomodified montmorillonite (2D), and PCL/precipitated $CaCO_3$ (3D) composite systems above the percolation threshold. They calculated $Q_0(\omega)$ as a function of the weight fraction of nanoparticles, and compared the linear and nonlinear viscoelastic properties. They observed, that the addition of nanoparticles has a more significant effect on the nonlinear viscoelastic property, $Q_0(\omega)$, compared to the linear viscoelastic property, $G^{'}(\omega)$. Furthermore, Hassanabadi et al.[152] investigated poly(ethylene vinyl acetate) nanocomposites containing two geometrically different nanoparticles (sphere of $CaCO_3$ and platelets of clay) under the uniaxial extensional and LAOS flow. They observed a significant increase in $I_{3/1}(\gamma_0)$ relative to the neat polymer above the percolation threshold. However, below percolation threshold, no significant change was observed for $I_{3/1}(\gamma_0)$.

In this chapter, single and multi walled carbon nanotubes [SWCNTs and MWCNTs] dispersed in a viscous matrix of PE were used. The mechanical response were investigated at small and large deformations under oscillatory shear. Similar to electrical conductivity[2], a minimum is observed for $Q_0(\omega_1/2\pi = 0.1$ Hz) as a function of weight fraction (ϕ_w) of MWCNTs. The networks of CNTs above the percolation have significant higher effect in the nonlinear viscoelastic regime compared to the linear viscoelastic regime. This is confirmed by calculations of the percolation scaling exponent, β, which has higher value in the nonlinear viscoelastic regime compared to the linear viscoelastic regime.

6.1 Materials and Experimental Protocols

6.1.1 Materials:

The MWCNTs were bought from Bayer Material Science AG (Baytubes C150P), whereas the SWCNTs were provided by Prof. Kappes which they prepared by laser vaporization as described in detail elsewhere[153]. The PE sample is an ethylene copolymer with 7 mol% of 1-octene (short chain branching) from DOW (commercial name: Engage-8450). The following data is provided by the supplier for the PE, M_w=100 kg/mol, M_n=45 kg/mol and T_m (meting temperature) = 100 °C.

6.1.2 Nanocomposites Preparation:

The nanocomposites were prepared by Dr. Palza and complete preparation method were described by Palza et al.[2]. A short description of two-step method which were used to improve the dispersion of CNTs is provided here. In the first step, the desired amount of CNT was added to a 1,2-dichlorobenzen (DCB, Acros Organics) solution and dispersed gradually during 3 h using a standard VWR ultrasonic cleaner in order to avoid changes in its aspect ratio. Furthermore, the polymer (15 g) was dissolved in DCB at 120 °C at a concentration of 15 g/L. After the time to dissolve the CNT was elapsed, the CNT solution was heated to 120 °C and added to the polymer solution. The mixture was stirred for 5 min and quickly poured into methanol (Acros Organic) at room temperature and kept it overnight. The precipitate was filtered, dried and putted in an oven with a controlled temperature (≈ 50 °C) vacuum system to remove the solvent. In the second step, the composites prepared by the solution method were additionally melt mixed using HAAKE MiniLab I Micro Compounder from Thermo Scientific with a counter-rotating twin-screw system

at 110 RPM. The mixtures were carried out at 140 °C for 10 min.

6.1.3 Rheological Characterization Method

The rheological measurements were carried out on an ARES-G2 rotational rheometer from TA Instruments. Oscillatory shear measurements in the linear regime were performed using the cone and plate geometry (13 mm and 25 mm, α_r= 0.1 rad) at 140 °C. This particular temperature was chosen because Palza et al.[2] already presented the conductivity measurements at 140 °C for the PE, PE/MWCNTs and PE/SWCNTs. The LAOS experiments were also performed on an ARES-G2 rheometer at 140 °C using an implemented FT-Rheology module. Strain amplitudes over the range $\gamma_0 = 0.001 - 1.5$ were applied at various frequency. The samples were press-molded under vacuum at 180 °C into 13 and 25 mm discs for the experiments.

6.2 Results and Discussion

Palza et al.[2] reported the experimental measurements of electrical conductivity for the PE/MWCNTs and PE/SWCNTs composites at 140 °C under oscillatory shear flow. The electrical percolation threshold for the PE/MWCNTs composites was found to lie between 1-3 wt% of MWCNT content, whereas, for the PE/SWCNTs composites it was not attained (Fig. 6.1). Furthermore, a minimum was observed for the electrical conductivity as a function of weight fraction of MWCNTs in the composites. Below the electrical percolation threshold, drop in DC conductivity on addition of MWCNTs was explained by a scavenger effect of MWCNTs (on impurity and additives) which helps to reduce the impurity contribution to electrical conductivity. In this work, we turn our focus to the mechanical characterization of above discussed composites using the FT-Rheology.

In the linear viscoelastic regime at low frequency, polymer chains are fully relaxed and exhibit typical homopolymer-like terminal behaviour with the scaling properties of approximately $G^{'} \propto \omega^2$. This power law could vary because of polydispersity and long-chain branching. For the neat PE and the polymer composites with MWCNTs weight fractions below 1 wt%, the scaling exponent for $G^{'}(\omega)$ at low frequency is 1.06 (Figure 6.2a). Furthermore, for polymer composites containing 3.0 wt% of MWCNTs the scaling exponent changes to 0.5. On addition of further MWCNTs (6 and 12 wt%), the dependence of $G^{'}(\omega)$ on frequency (at low frequency) is very

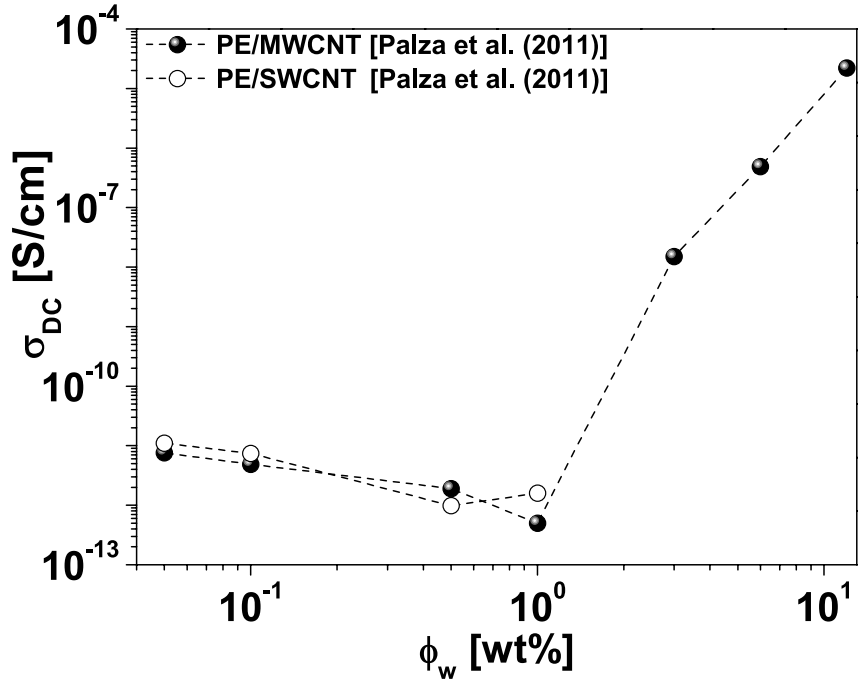

Figure 6.1: The influence of CNT content on the DC conductivity ($\sigma_{DC} \approx |\sigma^*|$ at 0.1 Hz) of PE composites in the melt state at T=140 °C. The data is reproduced from Palza et al.[2]

weak (for 6 wt% the scaling exponent is 0.3, and 12 wt% the scaling exponent is close to 0). For MWCNT composites, the scaling exponent is similar to neat PE until 1.0 wt% of filler content. However, the scaling exponent changes significantly as the MWCNTs weight fraction increases to 3.0 wt% (scaling exponent below 1.0 wt% is 1.06 and above 1.0 wt% is 0.5). This significant change implies large scale polymer relaxation in the nanocomposites is effectively restrained by the presence of the nanotubes. This confirms the formation of percolation network in polymer composites. Further change in scaling exponent implies the more solid-like behavior resulting from the increased interaction between CNT-CNT network formation. Similar to the electrical percolation threshold, the rheological percolation threshold is also between 1-3 wt% of MWCNTs content for the composites. Figure 6.2b shows the $G^{'}(\omega)$ variation with frequency and SWCNTs weight fraction for PE/SWCNTs composites. No significant changes in the linear viscoelastic material parameter, $G^{'}(\omega)$, were observed and the scaling exponent at small frequency remains unchanged. This implies no formation of network and percolation threshold was not attained.

The non-linear viscoelastic behaviour of the PE/MWCNTs and PE/SWCNTs composites were investigated under LAOS flow. The resulting shear stress responses were analyzed using the FT-Rheology. Figure 6.3 shows the $I_{3/1}$ variation with applied deformation for the neat PE polymer

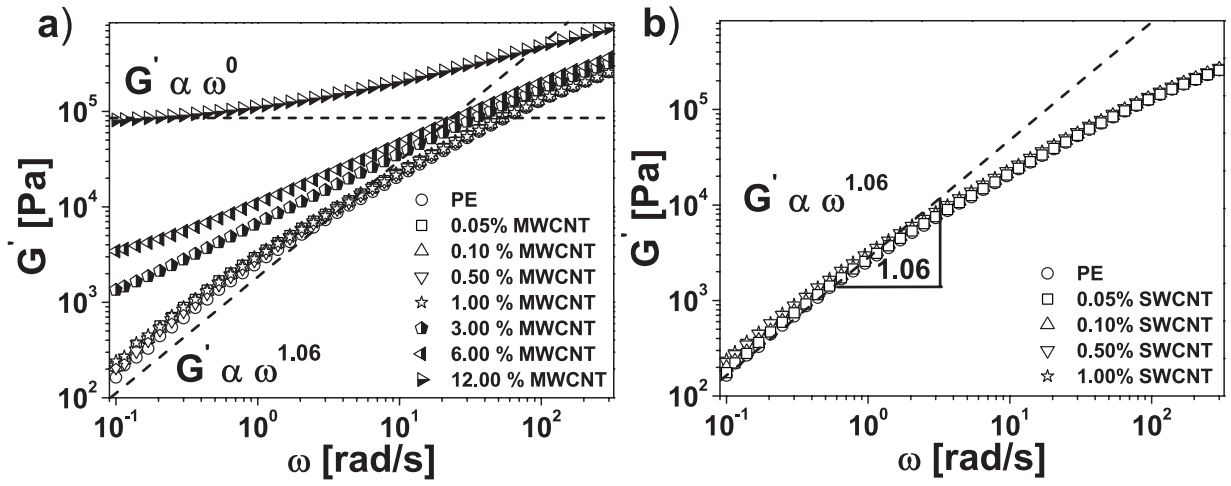

Figure 6.2: The linear viscoelastic property of PE/MWCNTs and PE/SWCNTs composites as a function of ω at 140 °C, (a) $G'(\omega, \phi_w)$ vs. ω for PE/MWCNTs and (b) $G'(\omega, \phi_w)$ vs. ω for PE/SWCNTs.

and polymer composites with MWCNTs content below (1 wt%) and above the percolation threshold (3 wt%, 12 wt%). The square scaling law, $I_{3/1} \propto \gamma_0^2$, is observed for the neat PE polymer as well as for the composites. Surprisingly, the $I_{3/1}$ values for samples below the percolation threshold (1 wt%) were lower than the neat PE melt. For samples above the percolation threshold (3 wt% and 12 wt%) $I_{3/1}$ values were higher relative to neat PE. For the concentration above the percolation threshold (3 wt% and 12 wt%), $I_{3/1}$ starts to appear at much lower deformations relative to neat polymer. The earlier appearance of $I_{3/1}$ implies the nonlinear viscoelastic effect appear at much smaller deformation relative to neat PE.

Figure 6.4a shows the zero strain intrinsic nonlinearity, $Q_0(\omega)$, variation as a function of applied excitation frequency, $\omega/2\pi$, for the PE/MWCNTs composites. The $Q_0(\omega)$ is monotonically increasing with the frequency for the neat PE and PE/MWCNTs composites with a MWCNTs content below the percolation threshold (1 wt%). However, for the PE/MWCNTs composites with a MWCNTs content above the percolation threshold (3 wt%, 6wt% and 12 wt%) the $Q_0(\omega)$ is decreasing as a function of frequency. At any given frequency, a decrease in Q_0 was observed as the MWCNTs concentration increased until the percolation threshold. However, above the percolation threshold $Q_0(\omega)$ increased with the addition of MWCNTs. Figure 6.4b shows the $Q_0(\omega)$ variation with frequency for the PE/SWCNTs composites. It has been already confirmed by the measurements in the linear viscoelastic regime that there is no percolation network formation occurred even for the 1 wt% of SWCNTs addition in PE. The qualitative behavior of $Q_0(\omega)$ with

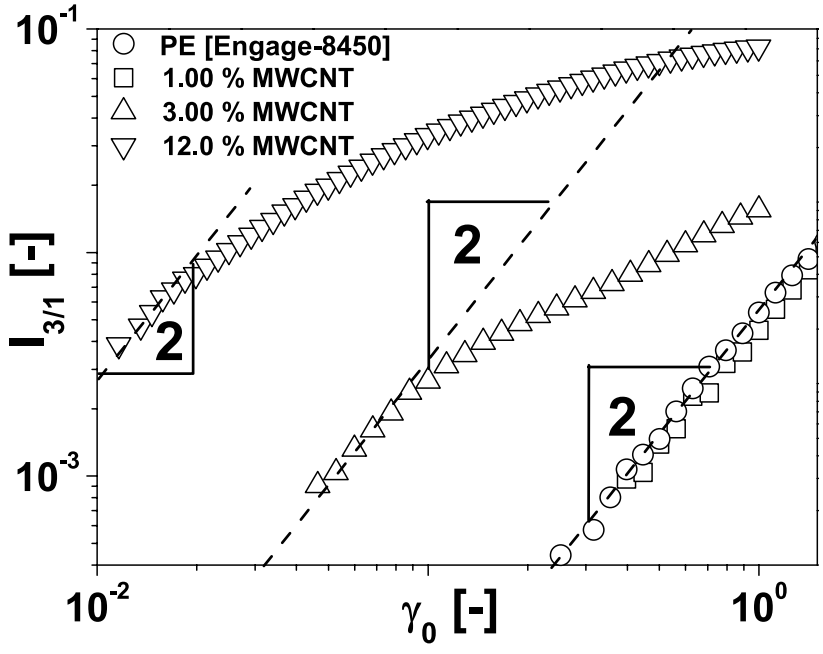

Figure 6.3: Fourier relative intensity of third harmonic ($I_{3/1}$) as a function of applied deformation amplitude, γ_0, at $\omega_1/2\pi$ = 0.1 Hz and 140 °C for different loading of MWCNT dispersed in PE (Engage-84050).

excitation frequency below percolation threshold was similar to the PE/MWCNTs composites.

An increase of $Q_0(\omega)$ below the percolation threshold and decrease above percolation threshold can be explained by a transition from liquid-like behaviour to solid-like behaviour at the percolation threshold. To explain this, at first a qualitative behaviour of typical $Q_0(\omega)$ was discussed for the linear and comb PS polymer melts. The $Q_0(\omega)$ for the linear PS were described in chapter 4 and the comb PS polymer melts were discussed by Hyun and Wilhelm[73] and Kempf et al.[75]. The $Q_0(\omega)$ for the linear PS polymer showed a maxima at the reptation frequency, $\omega_d = 1/\tau_d$. Furthermore, for the branched PS (comb), two maxima were observed respectively at backbone relaxation frequency and branched relaxation frequency, $\omega_a = 1/\tau_a$, where τ_d denote the backbone relaxation time and τ_a the branched relaxation time. In terminal regime, both the linear and branched PS shows increasing trend with ω until ω_d. This is the regime where PS melts display liquid-like behaviour. Whereas, after the ω_d the $Q_0(\omega)$ decreased with the ω, this is the regime where PS melts displays the solid-like behaviour. It was also observed that, as the branches in the combs increased, the steeper decrease was observed in $Q_0(\omega)$ after ω_d. Similar to linear and comb PS polymer melts, the increasing trend were observed for the PE/MWCNTs composites below the percolation threshold, where the liquid-like behaviour was observed. However, decreasing

trend were observed for the PE/MWCNTs composites above the percolation threshold, where the solid-like behaviour was observed. It can also be observed that as the solid-like behaviour of PE/MWCNTs composites increases (on increasing the MWCNTs fraction above percolation threshold), the steeper decreases was observed for $Q_0(\omega)$ as a function of ω.

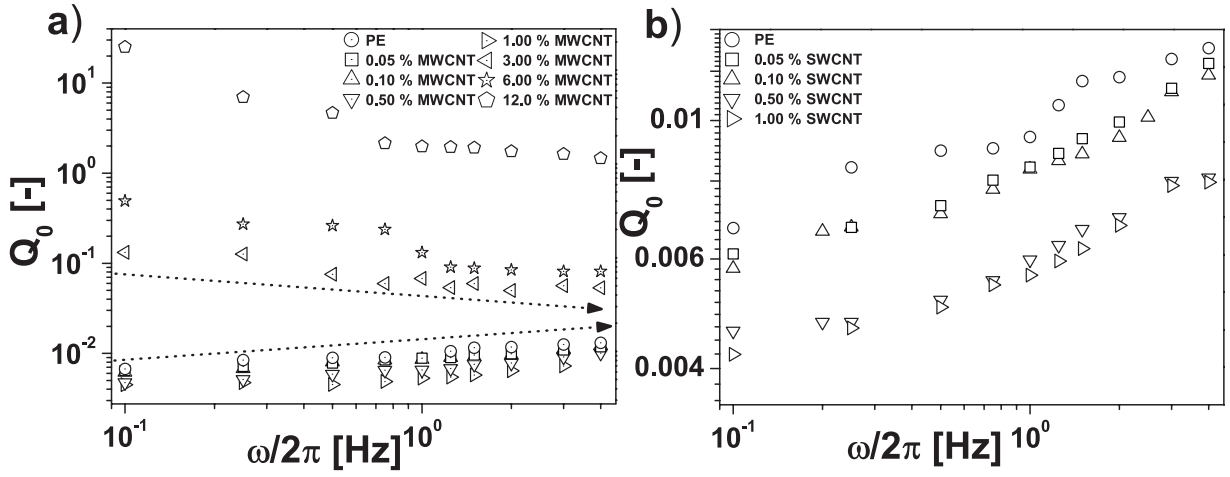

Figure 6.4: The intrinsic nonlinearity, $Q_0(\omega)$ variation as a function of applied frequency, $\omega/2\pi$ and weight fraction of CNTs in PE composites at 140 °C, (a) $Q_0(\omega)$ vs. ω for PE/MWCNTs composites, (b)$Q_0(\omega)$ vs. ω for PE/SWCNTs composites.

It is well established that the addition of nanoparticles into the polymer matrix have significant effect at the small frequency (terminal regime)[137,133]. To characterize the percolation threshold in the nonlinear viscoelastic regime, the frequency of $\omega/2\pi = 0.1$ Hz was chosen in the terminal regime. The specific frequency was chosen for the comparison with the conductivity measurements because Palza et al.[2] presented the conductivity measurements at frequency of $\omega_1/2\pi = 0.1$ Hz. Figure 6.5 shows the variation of $Q_0(\omega, \phi)$ with MWCNT content for the PE/MWCNTs composites at frequency of 0.1 Hz. An interesting phenomenon of minimum was observed for $Q_0(\omega_1/2\pi = 0.1Hz, \phi_w)$ as the MWCNT content was increased. Noteworthy, the tendency observed for Q_0 with CNTs concentration at this frequency is the same as those observed for electrical conductivity during LAOS flow[2].

To explain the decrease for $Q_0(\phi_w)$ below the percolation threshold, first we assumed that the stress response is a function of polymer-polymer and polymer-CNT interactions and CNT-CNT interactions were negligible. The decrease in Q_0 can be explained by the recently derived analytical solution using the Molecular Stress Function (MSF) model. According to this $Q_0(\omega)$ is

proportional to $(\alpha - \beta_{MSF})$, where α is orientation parameter and β_{MSF} is backbone stretching parameter[71]. The interaction between the polymer-CNT induces higher stretching during the LAOS which in turn increases the value of β_{MSF}. This lead to the decrease in $Q_0(\omega_1/2\pi = 0.1$ Hz, $\phi)$. This observation also confirms the validity of the MSF model below the percolation threshold as recently suggested in the literature[152]. The significant increase above the percolation threshold can be explained by the increased contribution coming from the CNT-CNT interactions. In this regime (above percolation), Q_0 is a function of polymer-polymer, polymer-CNT and CNT-CNT interactions but CNT-CNT interaction were the dominating contribution to Q_0.

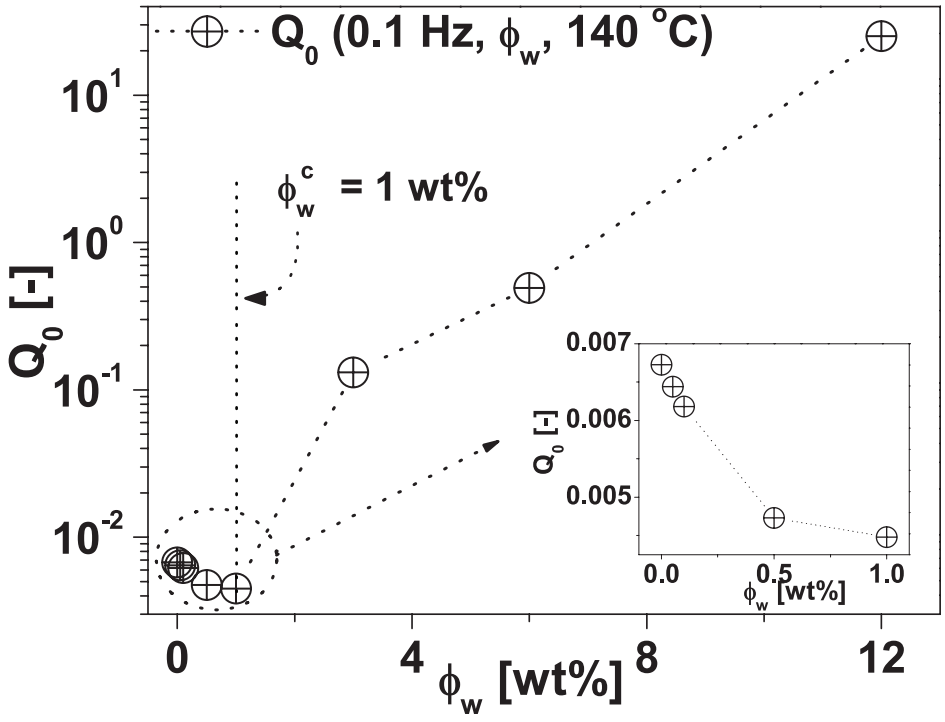

Figure 6.5: The intrinsic nonlinearity, $Q_0(\phi_w)$ as a function of weight fraction of MWCNTs for PE/MWCNTs composites at $\omega/2\pi$ = 0.1 Hz, T=140 °C, and ϕ_w^c = 1 wt%.

Figure 6.6 shows the comparison of $Q_0(\omega)$ variation with CNTs content below the percolation threshold for the PE/MWCNTs and PE/SWCNTs composites. The $Q_0(\omega)$ below the percolation threshold for the PE/MWCNTs composites shows the relatively higher values than the PE/SWCNTs composites. These relative decreased values of $Q_0(\omega)$ for the PE/SWCNTs composites might be explained by more interaction between the polymer-CNT because of higher aspect ratio of SWCNTs.

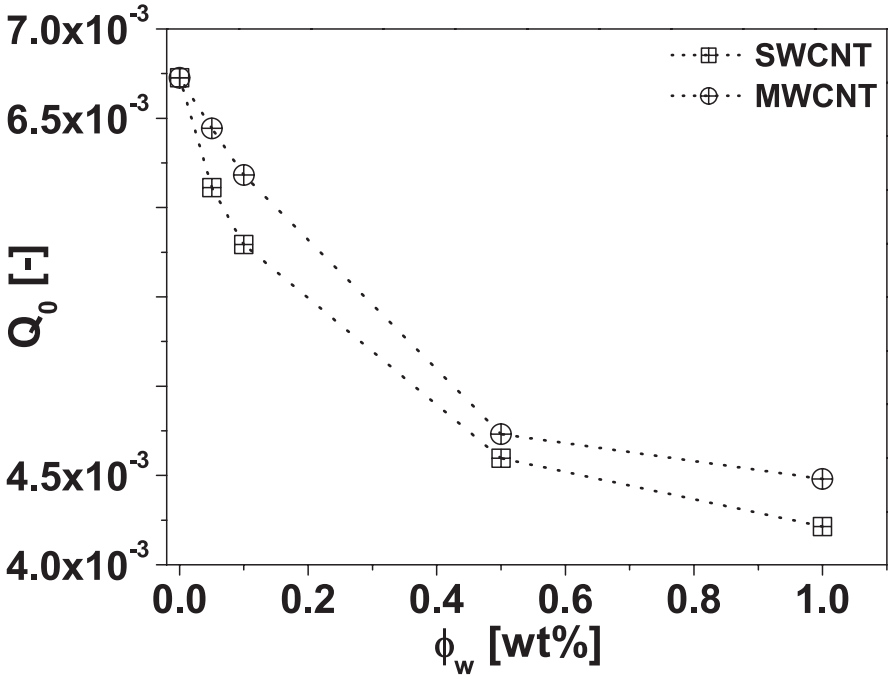

Figure 6.6: The intrinsic nonlinearity, $Q_0(\phi)$, variation as a function of weight fraction of MWCNTs and SWCNTs at $\omega_1/2\pi$ = 0.1 Hz, and 140 °C, in PE composites.

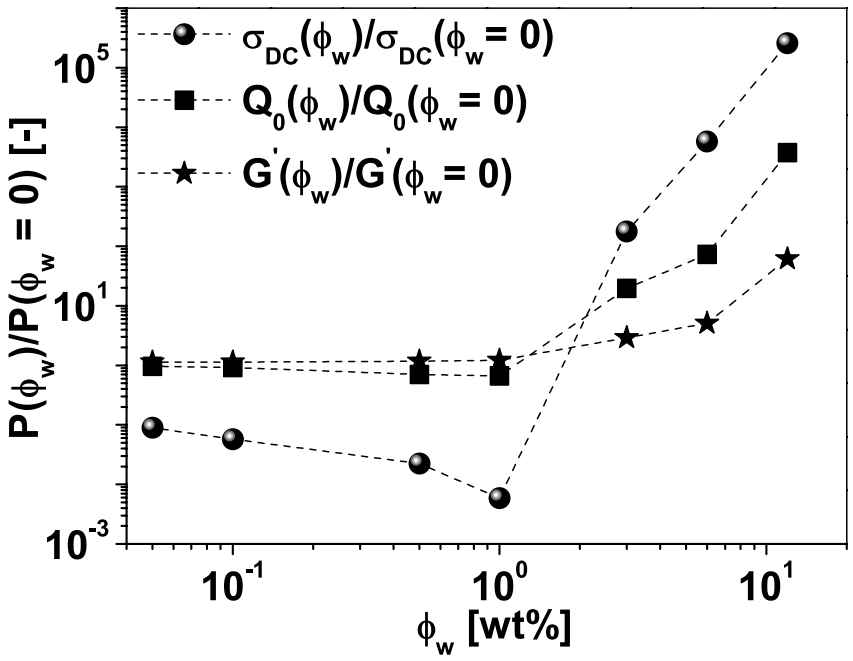

Figure 6.7: The effect of percolating network on conductivity (σ_{DC}) and linear and nonlinear viscoelastic properties for PE/MWCNTs composites at $\omega_1/2\pi$ = 0.1 Hz and T = 140 °C.

The influence of network formation on the electrical conductivity, elastic modulus and intrinsic nonlinearity were compared by normalizing the respective material parameters with the neat PE. Figure 6.7 shows the normalized electrical conductivity (the data is taken from Palza et al.[2]), and material parameters in the linear viscoelastic regime ($G^{'}$) and nonlinear viscoelastic regime (Q_0) variation as a function of ϕ_w. At the onset of the electrical and rheological percolation network, a power law dependence for the material parameters were observed $P \propto (\phi - \phi_c)^{\beta_p}$, where P represents the material parameters and β is the scaling exponent (Fig. 6.7). This scaling has been observed by many authors for wide variety of polymer composites[143,137,154,141]. The determined scaling exponent β_p for electrical conductivity is $\beta_p = 4.3 \pm 0.3$. For rheological measurements in the linear viscoelastic regime ($G^{'}$) is $\beta_p = 1.7 \pm 0.7$ and in the nonlinear viscoelastic regime (Q_0) is $\beta_p = 3 \pm 1$. The scaling exponent, β_p, in the nonlinear viscoelastic regime is one order higher than in the linear viscoelastic regime. This implies network formation has significantly higher effects in the non-linear viscoelastic regime relative to the linear viscoelastic regime.

6.3 Concluding Remarks on the Characterization of Polymer Composites using FT-Rheology

The PE/MWCNTs and PE/SWCNTs composites were prepared carefully using the two step method to ensure the homogeneous dispersion. The observed electrical and rheological percolation threshold for the PE/MWCNTs composites lies between 1-3 wt% of MWCNTs. Whereas, for the PE/SWCNTs composites no percolation threshold was detected between the 0-1 wt% of SWCNTs. A minimum was observed for the $Q_0(\phi_w)$ as a function of MWCNT weight fraction (ϕ_w) around percolation threshold ($\phi_w^c = 1$ wt%). This observation was explained by increased stretching of polymer chain because of interaction between the PE chains and MWCNTs. The asymptotic variation of material parameters in the linear viscoelastic regime and the non-linear viscoelastic regime were observed to follow the scaling $p \propto (\phi - \phi_c)^{\beta_p}$. The calculated scaling exponent using the elastic modulus (linear viscoelastic regime) was $\beta_p = 1.7 \pm 0.7$ and for the zero strain intrinsic nonlinearity, Q_0, (non-linear viscoelastic regime) was $\beta_p = 3 \pm 1$. The higher scaling exponent in the non-linear viscoelastic regime relative to the linear viscoelastic regime implies the higher influence of network formation in the non-linear viscoelastic regime and additionally a higher sensitivity toward the detection of the percolation threshold.

Chapter 7

Solution Electrospinning: Fabrication of Scaffolds for the Tissue Engineering Applications

Tissue engineering[155,156] demonstrated its great potential in both experimental and clinical conditions to regenerate several complex tissues. In fact, it has been clinically applied for trachea, bladder, blood vessels, cartilage, skin, and heart valve[157,158,159]. The basic principle of tissue engineering is to restore and/or replace the damaged tissue through the use of a bioresorbable porous synthetic scaffold that support and guide the formation of new tissues *in vitro* and further implanting them *in vivo*. To facilitate the development of new tissue *in vivo* or *in vitro*, the fabricated scaffold should mimic the extracellular matrix (ECM), a fibrous 3D nanoscale network that provides structural support for developing tissues[160] and a conducive environment for cell proliferation, differentiation and morphogenesis[161].

The choice of scaffold with specific physical and mechanical properties is extremely important for suitable tissue engineering. In the past decade, there has been tremendous interest in exploring the potency of biomimetic scaffolds in tissue engineering, and various nanofabrication techniques were developed to fabricate 3D porous scaffolds: molecular self-assembly[162], solvent casting/salt-leaching[163], gas foaming[164], phase separation[165], solid free-form fabrication (SFF)[166] and electrospinning[167]. Among these techniques, electrospinning is a simple and versatile technology to fabricate the scaffolds.

In this study, solution electrospinning technology is used to fabricate 3D cm-thick hierarchical scaffolds using the self-assembly strategy. At first, we presented the description of electrospinning technology and literature review on influence of various process, solution, and ambient parameters on fibers diameter and fiber morphology. Afterward, fabrication strategy of 3D cm-thick hierarchical scaffolds is discussed using the single step elctrospinning process.

7.1 Solution Electrospinning Process

The fundamental phenomenon behind the electrospinning process is the use of electrostatic forces to draw a viscoelastic solution into fibers in the range of micro to nano scale. In solution electrospinning process, viscolelastic solution is pumped through a needle which is connected to a high potential electrical source. A straight jet was formed, as a consequence of electrical forces, from a conical protrusion, often called a Taylor cone[168], on the surface of pendent drop of solution. The electrically charged jet for few centimeters subjected to uniaxial extension (slow acceleration regime). At the end of this straight segment, a conical shape, with its vertex at the end of the straight segment, was observed (rapid acceleration regime) when properly illuminated. A pictorial description of electrospinning process is provided in Fig. 7.1. In this conical region, the fiber follows a complex path. Images obtained with short exposure time by Han et al.[169] revealed that the jet is continuously bending in this region. Indeed, these multiple bending is responsible for such a high aspect ratio fibers in electrospinning process.

The most important element operating during electrospinning is the rapid growth of a non-axisymmetric or whipping instability that causes bending and stretching of the jet. This is step which is responsible for rapid reduction of diameter of jet and helpful in production of nanofibers. The end of straight segment and the start of the bending instability can be defined as the point at which the jet bends by an amount equal to the projected diameter of the straight segment. A bending perturbation of the axis of the straight jet creates a new set of electrical forces, with components perpendicular to the jet axis, which tend to make the bending perturbation grow. The jet quickly bends through an angle of approximately 90° and the path develops into a series of loops, generating a coil around the original direction of the axis[170,171]. Recently, these loops which forms at rate of 200 - 1560 turns per second are observed with the combination of videography, stereography and methods for illumination of the multiple coils of an electrospinning jet path[172,173].

The possible reasons for whipping instability as described by Shin et al.[174] are (1) small lateral fluctuations in the centerline of the jet result in the induction of a dipolar charge distribution, as the free charge adjusts to screen out the field inside the jet. The dipole interact with the external electric field, producing a torque that further bends the jet, and (2) mutual repulsion of surface charges carried by the jet causes the centerline to bend. The whipping jet is modeled as being the result of competition between several different modes of instability. These modes of instability are Rayleigh instability, axissymmetric instability, and bending mode instability.

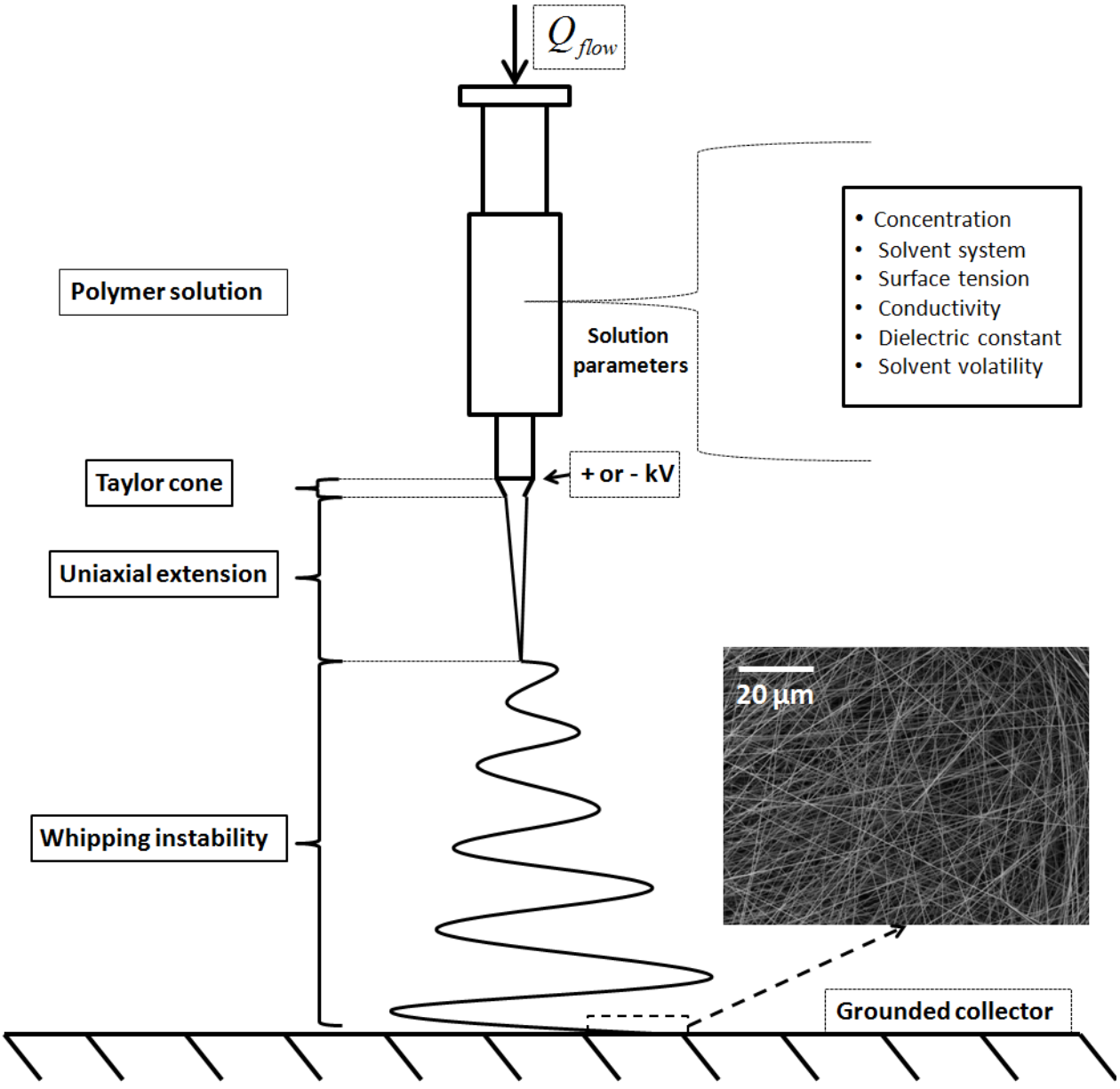

Figure 7.1: Pictorial description of electrospinning process along with how viscoelastic solution gets transformed into the nanofibers.

As the whipping instability is rapid which promotes the nonuniform distribution of surface charges. The area with high local charge density may give rise to secondary jet initiation, resulting in the formation of less frequent branched nanofibers[175]. Branching allows a means to rapidly increasing surface area to accommodate local concentrations of charges. As it is understood till now that the whipping instability is the primary mechanism responsible for reducing nanofiber dimensions upto nano level during electrospinning. However, as Dzenis et al.[176] showed that suppressing this instability using either a secondary electric field or a short gap distance did not result in substantially thick nanofibers being generated. This observation implies that the understanding of the process is still incomplete, and all the factors that governs fiber formation are not yet fully understood.

Efforts to derive equations for the electrospinning process have generated several novel discoveries: a scaling law for the terminal fiber diameter and a Deborah number (*De*) correlation for the formation of fibers (versus droplets or pearl necklace structure). Fridrikh et al.[177] derived a simple analytical model to predict the terminal fiber diameter as a function of surface tension, flow rate, and electric current in the jet.

$$h_t = \left(\frac{\dot{V}}{I}\right)^{2/3} \left(\frac{2\gamma_s \epsilon}{\pi(2\ln\zeta - 3)}\right)^{1/3} \tag{7.1}$$

Where $\dot{V}$ is flow rate, I is electric current, γ_s is surface tension, ϵ is dielectric permittivity, and ζ is dimensionless whipping term.

Yu et al.[178] illustrated the role played by solution elasticity on fiber morphology using *De*. The Deborah number characterized the relaxation time of a solution relative to the processing time scale. In case of electrospinning, the processing time is equal to the rate of whipping. They concluded from their analysis, no fibers were produced for $De < 1$ across all values of Ohnesorge number (*Oh*), a ratio of the viscous to inertial and surface tension forces. The *De* number greater than 6 were found to solely generate uniform fibers, and value between 1 and 6 produced a bead-on-spring morphology.

7.2 Parameters Affecting Diameter and Morphology of Electrospun Fibers

The parameters which can have significant influence on fiber diameter and morphology in electrospinning process is divided into three categories (i) Solution parameters (ii) Process parameters (iii) Environmental parameters. Here we have discussed influence of each parameters on electrospinning process.

7.2.1 Solution parameters

- **Concentration:** The polymer solution with more than 2.5 entanglement per chain are enough to produce uniform fibers[179]. The concentration where polymer solution has enough entanglements ($\leq$ 2.5 entanglement per chain) in a strong enough electric field, leads to uniform nanofibers[180,181,179,182,183]. The concentration has significant effects on final morphology and diameter of fibers[184,185]. An increase in concentration above a critical concentration generally leads to larger diameter, and the morphology changes from beaded fibers to a uniform fibers. He et al.[186] shows that fiber diameter (d) follow a power relation with concentration (C) :

$$d \propto C^{\kappa} \tag{7.2}$$

  where κ is a parameter which varies with polymer systems, for example, power for polyacrylonitrile (PEN) in N,N-dimethylformamide (DMF) solvent is $\kappa = 3.45$ [He et al.[186]], and for polyurethane (PU) in DMF solvent is $\kappa = 3$ [Demir et al.[184]]. The power, κ, changes for different polymer systems because fiber diameter not only depends on concentration but also the solvent quality, spinning conditions and temperature.

- **Solvent system:** The choice of solvent system determines (i) conformation of the dissolved polymer chain (ii) ease of charging the spinning jet (iii) cohesion of the solution due to surface tension forces (iv) rate of solidification of the jet on evaporation of the solvent. Jarusuwannapoom et al.[187] investigated 18 different solvent system for polystyrene (PS) with M_n = 119 kg/mol. Out of 18, only four [DMF, methyl ethyl ketone (MEK), tetrahydrofuran (THF), dichloroethane (DCE)] yielded electrospinnable solution (at 10 - 30% w/v). The dipole moment and conductivity of the solutions were identified as the key properties that determined electrospinnability. Son et al.[188] studied PEO dissolved in five solvents at

different concentrations selected to obtain $[\eta]c \approx 10$ (i.e., entangled semidilute regime). The influence on nanofiber diameter obtained varied widely with the solvent used in electrospinning. The thinner fibers were obtained with solvents with higher dielectric constant.

- **Surface tension:** Surface tension, γ_s, of polymer solution is the primary force which opposes the coulombic repulsion of charges during the formation of Taylor cone. This suggests that electrospinning is possible even at lower voltages, if γ_s of the solution can be reduced. The analytical solution proposed by Fridrikh et al.[177] for the terminal diameter, h_t, shows following proportionality $h_t \propto \gamma^{1/3}$ with surface tension. However it should be kept in mind that surface tension of polymer solution changes with concentration[180] as well as with the chemical nature of the polymer[189]. The low concentration of additive is used by many authors to reduce the surface tension[190,191].

- **Conductivity:** The electrospinning process fundamentally requires the transfer of electric charge from the electrode to the spinning droplet at the terminus of the tip. A minimal electrical conductivity in the solution is therefore essential for electrospinning, solutions of zero conductivity cannot be electrospun. In case, solution conductivity for polymer/solvent system is inadequate, the most frequent way employed to improve the conductivity is addition of little amount of additive. For example, Choi et al.[192] added organosoluble trialkylammonium chlorides to a solution of polyhydroxybuterovalerate (PHBV), and achieved substantial reduction in fiber diameters. Kim et al.[193] were able to increase the conductivity of an aqueous solution of poly(2-acrylamido-2-methyl-1-propanesulfonic acid) by addition of $NaCl$ and $CaCl_2$. The increase of conductivity led to uniform fibers. The acids have also been used to increase solution conductivity, and in some cases also served as the solvent or co-solvent. For example, camphorsulfonic acid[194,195] and HCl[196] have been used in small amounts in solutions, while acetic acid and formic acid have been used as solvents for chitosan[197], and gelatin[198], respectively. Adding ionic species to the solution allows a relatively higher surface charge density to be maintained on the jet and consequently promotes improved fiber extension during the whipping stage.

- **Dielectric constant:** The high dielectric constant of solution, helps in dispersing charge more evenly. This translates into high nanofiber quality and productivity during electrospining[?]. Solvents with the higher ϵ results in smaller average values of d (nm) in electrospinning of PEO carried out in multiple solvents[199]. The extent to which the choice

of solvent affects the nanofiber characteristics is well illustrated in the electrospinning of poly(ϵ-caprolactone) (PCL) from $CHCl_3$/DMF mixed solvent. As the volume fraction of DMF in the mixture is increased from 0 to 10 wt%, the average D_{avg} (at the same polymer concentration) was shown to decrease from 450 nm to 150 nm[200]. This was likely a result of the increased dielectric constant of the solvent due to addition of DMF [$\epsilon_{DMF} \approx 36.7$ and $\epsilon_{CHCl3} \approx 4.8$]. Furthermore, the distribution of D was also affected by the higher volume fractions of DMF in the mixture. Bimodal distributions of D are typically obtained when electrospun from $CHCl_3$ solutions, which changed to narrow unimodal distributions with the addition of DMF into the solvent. This was attributed to multiple splaying of the jet obtained with solvent blends containing DMF. Similar data on the effect of solvent composition on fiber morphology have been reported for PCL electrospun from CH_2Cl_2/DMF solutions[201], for PS electrospun from THF/DMF[202], and PVC electrospun from THF/DMF[203].

- **Solvent volatility:** It is the evaporation of solvent from a jet that yields a solid polymer nanofiber at the collector plate. If the solvent do not evaporate until the fiber reaches on the collector they may fuse together[200]. Using volatile solvents helps avoiding this situation. Electrospinning of PS polymer in several solvents, the average fiber diameter $d(nm)$ was reported to decrease with increasing boiling point of the solvent[204]. The rate of drying is determined primarily by the vapor pressure of the solvent and by the degree of whipping instability that governs the rate at which the surface area to volume ratio of the jet increases during spinning. At a given gap distance, drying rate also depends on temperature in the spinning environment, this may afford some independent control over fiber diameter. The solvent volatility also shown to have effect on fiber morphology of cellulose acetate[205].

7.2.2 Process parameters

- **Electrostatic Potential:** The applied voltage, V_s (kV), provides the surface charge on the electrospinning jet. In general higher voltage leads to greater stretching because of higher columbic forces in the jet as well stronger electric field which leads to reduction of collected fibers[206,207,208]. Higher voltage also encourage faster solvent evaporation to yield drier fibers[209]. Another factor that may influence the diameter of the fiber is the flight time of the electrospinning jet. A longer flight time will allow more time for the fibers to stretch and elongates before it is deposited on the collection plate. Thus, at a lower voltage, the reduced acceleration of the jet and the weaker electric field may increase the flight time of

the electrospinning jet which may favor the formation of finer fibers. In this case, a voltage close to the critical voltage for electrospinning may be favorable to obtain finer fibers[210]. At a higher voltage, it was found that there is a greater tendency for beads formation[180,184,185]. It was also reported that the shape of the beads changes from spindle-like to spherical-like with increasing voltage[185]. Given the increased stretching of the jet due to higher voltage, there should be less beads formation as reported in some cases[187]. The increase in beads density due to increased voltage may be the result of increased instability of the jet as the Taylor Cone recedes into the syringe needle[180,185]. In an interesting observation, Krishnappa et al.[211] reported that increasing voltage will increased the beads density, which at an even higher voltage, the beads will join to form a thicker diameter fiber.

- **Feed Rate:** The feed rate would determine the amount of solution available for electrospinning. For a given voltage, there is a corresponding feed rate if a stable Taylor cone is to be maintained. As the feed rate is increased, there is corresponding increase in the fiber diameter or beads size which could be explained by the fact that the greater volume of solution is drawn away from the needle tip[185]. Experimental measurements indicate the volume charge density q_v on the jet to decrease exponentially with feed rate[177,212]. It is likely that higher feed rates lower the rate of replenishment of charges on the surface of the droplet. Theron et al.[212], however, suggest charge replenishment to be governed by the drift velocity of ions and therefore to be independent of feed rate. The lower values of q_v are therefore likely to be a result of high rates of withdrawal of charges as well as polymer solution from the droplet surface at the higher feed rates.

- **Working distance:** The working distance defines the strength of the electric field as well as time available for evaporation of solvent before it reaches the collector. Increasing the distance results in a decrease in the average fiber diameter[213]. The longer distance means that there is a longer flight time for the solution to be stretched before it is deposited on the collector[210,170]. However, there are cases where at a longer distance, the fiber diameter increases. This is due to the decrease in the electrostatic field strength resulting in less stretching of the fibers[214]. When the distance is too large, no fibers are deposited on the collector[210].

7.2.3 Environmental parameters

- **Temperature:** The temperature of the solution has both the effect of increasing its evaporation rate and reducing the viscosity of the polymer solution. For example, when polyurethane (PU) is electrospun at a higher temperature, the fibers produced have a more uniform diameter[184]. Hardick et al.[215] shown for cellulose acetate fibers that as the processing temperature is increased the average fiber diameter goes down. This may be due to the lower viscosity of the solution and greater solubility of the polymer in the solvent which allows more even stretching of the solution.

- **Humidity:** The most important ambient parameter to affect the morphology of electrospun fibers is humidity. The magnitude of the effect of humidity on the fiber morphology depends greatly on the solvent used. Baumgarten et al.[216] used an acrylic resin in DMF, while Yang et al.[217] used poly(ethylene oxide) in water, and water/ethanol mixes and Casper et al.[218] used polystyrene in tetrahydrofuran. All three saw significant changes in morphology with change in relative humidity. However, because of the different solvents and different polymers used, the results were rather different. Baumgarten et al.[216] typically used a spinning atmosphere of air with a relative humidity between 30 and 40% to electrospin fibers from a 12.5 wt % solution of acrylic resin in DMF. However, when the relative humidity was reduced to less than 5% spinning could only be carried out for 1-2 minutes because the solution at the tip of the capillary dried up. When the relative humidity was greater than 60%, Baumgarten et al.[216] discovered that the solution tangled before reaching the grounded collector because it did not dry properly. Yang et al.[217] had similar results. In their experiment, Yang et al.[217] electrospun a four weight percent solution of 500,000 g/mol average molecular weight poly(ethylene oxide) using water and ethanol/water solutions as the solvent. At 70% relative humidity, solutions with 1:3 and 1:1 water/ethanol ratios formed mostly bead-free fibers. A 3:1 water to ethanol ratio formed mostly beads with only incipient fibers. Solutions made from pure de-ionized water did not form fibers. The product consisted of blobs of polymer with some fiber-like interconnections. However, when the relative humidity was reduced to 48%, the aqueous PEO solution produced mostly uniform fibers with only a moderate number of beads. No results for relative humidity lower than 48% were given. When polystyrene, polycarbonate and poly(methyl methacrylate) are dissolved in volatile solvents and electrospun in a humid environment pores have been found. These pores increase the surface area, which is important in filtration, and can be used as

a cradle for enzymes or for capturing nanoparticles. Therefore, Casper et al.[218] studied the correlation between humidity and fiber morphology. A 35 wt % solution of 190 kg/mol polystyrene (PS) with a polydispersity index of 3.0 was dissolved in tetrahydrofuran (THF) and electrospun under five humidity ranges: 25%, 31-38%, 40-45%, 50-59% and 60-72%. When the humidity was below 25% the fibers were smooth and pore-less. As the humidity increased to the 31-38% range small, round pores were formed with their density increasing in the 40-45% range. When the relative humidity was between 50 and 59% the smaller pores began to coalesce into larger, non-uniform pores. The 60-72 % range gave similar results with even larger pores. Therefore, humidity can create both positive and negative results with many polymer solutions. In solutions in which water is the solvent it is especially important to control the relative humidity.

7.3 New Way to Fabricating 3D cm-thick Hierarchical Foams via Solution Electrospinning

The recent developments towards large scale productions combined with simplicity of the electrospinning process motivated us to explore the fabrication of 3D foams using electrospinning. However, two main issues still have to be addressed concerning electrospinning. First, the random deposition of the fibres results in nonwoven membranes with limited pore size and porosity and moreover, the maximum thickness of produced membranes is limited to few hundreds of microns owing to electrostatic repulsion between incoming and deposited fibres. The first problem of random deposition has been tackled by using various fabrication methods such as rotating[219,220] or structured collectors[221,222,223,224] scanning tip electrospinning[225] or near-field electrospinning[226]. However these methods bring additional complexity which increases the processing cost.

Recently, few studies utilized self-assembling strategy[227] of collected fibers in simple electrospinning to fabricate patterned structure just by tuning processing or environmental or solvent parameters appropriately. The few reported structures using self-assembly strategy were, honeycomb self-assembly for polyethylene oxide (PEO)[228], polyurethane[229], polyacrylonitrile (PAN), polyvinyl alcohol (PVA) and polyethylene oxide (PEO)[230], 3D-spongiform self-assembly for polystyrene[231], alginate-PEO[232], nanopottery self-assembly for PEO[233]. In all the reported honeycomb self-assembly structures, the self-organisation occurs when the fibres contain beads

or thicker parts which are still wet, when landing on the collector. Thus, Yan et al.[230] suggest that a small amount of solvent remaining in the beads leads to a competition between capillary forces that tend to merge the fibres that form the walls of the honeycomb structures and the repulsive electrostatic forces. However, capillary forces act at very short distance compared to the long distance electrostatic forces. On the contrary, the fibres electrospun by Yan et al.[230] did not look wet but contained ionic liquids, which has good conductivity. They suggest that bundles of fibres form before landing on the collector, leading to a non-homogeneous deposition. In all cases, the deposition of the fibres on the collector leads to non-homogeneous electrostatic charge accumulation. However, the mechanism of self-organization and its onset are still unclear.

The problem of the thickness of electrospun scaffolds has proven to be more difficult mainly due to electrostatic charging of the scaffold after a few hundreds of microns, leading to repulsion of the following electrospun fibres. Until now only few articles reported the elaboration of cm-thick scaffold. Among them, one can cite the fabrication of thick cotton-like scaffolds with very low density[234]. However no mechanical characterisation was performed on these scaffolds and due to their very low density, implanting them in vivo might lead to collapse of the structure. *Layered hydrospinning* was also used to form a multilayer scaffold[235] by electrospinning thin membranes on a water surface and superposing them in a final cm-thick scaffold. This technique is however more complex and one can wonder about the manipulation of the scaffold and its possible delamination.

In this work for the first time the fabrication of cm-thick electrospun scaffolds with good mechanical properties and a gradient in porosity and pore size up to several hundreds of microns. These scaffolds are obtained by exploiting the self-assembling properties of polycaprolactone (PCL) nanofibers. The temporal evolution of honeycomb-like structures of PCL fibres was first studied and the organization mechanism is explained from its onset to its development during long time of production. Then, the electrospun jet is focused and the process conditions optimized to exploit the fibre self-assembling in order to control the porosity and force the rapid growth of the scaffold in thickness up to the cm-scale. The unique structure of the scaffold in the form of foam enables the coexistence of high porosity and good mechanical properties.

7.3.1 Materials and Methods

Electrospinning process

Poly(ϵ-caprolactone) (PCL) (M_w = 80 kg/mol, PDI=1.1) was provided by Perstorp (commercial name CAPA 6800). Solutions of 11 wt.% and 13 wt.% in dichloromethane/dimethylformamide (50:50 V:V) were prepared, and a delay of at least 24 hours was taken before electrospinning to ensure good polymer solubilization. Electrospinning was performed using a homemade electrospinning set-up. The polymer solution was delivered to the needle via a silicon feed line with a constant flow rate of 1.2 ml/h using a syringe pump (Harvard Apparatus PHD 2000). The distance between the needle and conductive aluminium collector was 15 cm. A large potential difference was applied between the needle and collector using two power supplies (Spellman SL10). Unless indicated in the text, honeycomb self-assembly experiments were performed with V_{needle}= +10 kV applied on the needle and $V_{collector}$ = -10 kV applied on the collector. To produce the thick scaffold, a poly(methyl metacrylate) (PMMA) plate with a thickness of 3 mm and a round hole that was 25 mm in diameter was placed over the conductive collector. In this case, the applied voltages were V_{needle} = +15 kV and $V_{collector}$ = -15 kV. The environmental parameters were held constant and were similar for all of the experiments (T = 25 °C, HR = 35%).

SEM observation and morphological characterization

The scaffold morphology was observed by scanning electron microscopy (SEM, XL30-ESEM, Philips) at the Institut Pluridisciplinaire Hubert Curien (IPHC, UMR 7178) in Strasbourg. Prior to observation, all the samples were sputtered with gold. Measurements of the fibre diameters and the honeycomb pattern areas were done using the software Image J. For diameter distributions, the diameters of hundred fibres at least were measured, taken on images of random areas of the scaffold, at magnifications 1000 to 10000. For honeycomb pattern area distributions, the function ”polygon selections” of ImageJ software was used to follow the walls of the patterns. Pattern diameters were calculated from areas A and perimeters P of each polygon. Then, equivalent diameter has been obtained by D = 4 A / P. The pattern measurements were performed for 100 patterns per sample, taken in the middle of the sample.

Image analysis of thick scaffolds cross-section for porosity and mesopores size

The image analysis were carried out by Dr. Roland Kadar. Carefully selected regions were considered for the analysis, as could be seen in Figure 7.7e. The selection criterion was based on the

structural symmetry of the material and the feature consistency. At the end, the local coordinate systems z_i of the selected regions are transported into the global vertical z-axis. The porosity estimation is based on the grey intensity scaling of the acquired images. By means of local histograms, the volume of solid material is estimated, with the pixel being the elementary unit area and the image intensity as height. The volume of the 3D foam slice is considered here as total volume whereas the volume of the void space is determined by subtracting the computed volume of the solid material from the total volume. The chosen reference length scale for gray-scale intensity was sample thickness. The local pore size was determined by analysing the grayscale intensity along the segments that follow the selected strands as shown in Figure 5e. Due to noise, the signal was fitted with smoothing function, the difference between successive peaks of the fitted data signals being a measure of the pore size. A non-analytic procedure that consists of locally applied weighed least squares fit, LOESS[236] was used for smoothing. The degree of smoothing can be adjusted via the window of the locally applied weighted least square fit. Further on, a linear dependence of the smoothing factor and the previously described porosity estimation to the window width was applied.

Monte Carlo simulation

To model the first moments of electrospinning of heterogeneous nanofibres, Monte-Carlo simulation has been carried out. The size H of the window in which the fibres are observed is firstly given. On assumes that H is much lower than the radius of curvature of electrospun fibres. Thus, fibres are modelled by straight segments entering in the window with a random angle and a random starting point. For a simulation, we fixed the number of fibres entering in the window, the length of the thicker domain L_thick and the length of the thinner one L_thin (see Figure 7.5).

Computation of electric field over regular honeycomb structures

Comsol^{TM} software was used to compute by finite elements methods the electric field over regular honeycomb structures. The geometry and the boundary conditions are given in Figure 7.6.

Mechanical characterization

Stress-strain behavior under compression was measured at $T = 23 \pm 0.5\ ^{\circ}C$ with a MCR 301 rheometer from Anton-Paar. The normal force range is 0.01 N to 50 N with a resolution of 0.002 N. A scaffold with a thickness of 9 ± 0.5 mm was cut to obtain a sample with a thickness of 9.3

mm, a sample with a thickness of 3.3 mm, collected from the upper part of the scaffold, and a sample with a thickness of 2.8 mm, collected from the lower part of the scaffold. A compression velocity of 0.005 mm/s was imposed, and the normal force and gap were recorded every second.

7.3.2 Self-assembly of electrospun fibers

Electrospinning polycaprolactone (PCL) solutions at 11%wt in dichloromethane/dimethylformamide (DCM/DMF, 50/50) leads to very repeatable self-organisation of beaded nanofibres in the form of honeycomb structure as shown in Figure 7.2 a. When observing at higher magnification (Figure 7.2 b, it clearly appears that beads are mainly located in the walls of the honeycomb patterns whereas very few beads appear inside the patterns. When higher concentrated solutions of PCL are used, such as 13%wt, beads naturally disappear. However, self-assembling into honeycomb structures still occurs Figure 7.2 d.

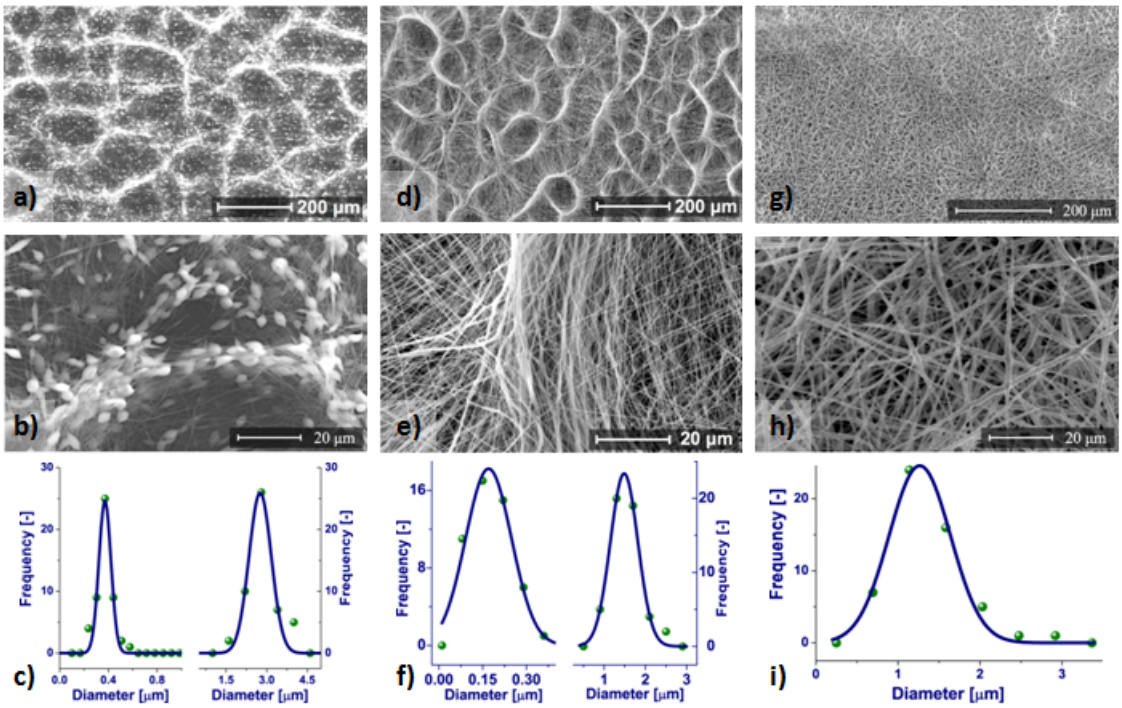

Figure 7.2: Morphologies at scaffold and fibre length scales obtained after 10 min of electrospinning and fibre diameter distribution. (a-c) PCL at a concentration of 11% wt with V_{needle} = 15 kV, $V_{collector}$ = 0 kV. (d-f) PCL at a concentration of 13% wt with V_{needle} = 15 kV, $V_{collector}$ = 0 kV (g-i) PCL at a concentration of 13% wt. with V_{needle} = 5 kV, $V_{collector}$= -10 kV.

A closer look to the organised fibres shows that their diameter distribution is bimodal Figure 7.2 e-f with almost a factor of 10 between thick and thin domains. This bimodal distribution is certainly due to a concentration inhomogeneity of the polymer solution resulting from the mixture of chosen solvents. Indeed, DMF, a poor solvent of PCL with low vapour pressure (5 mbar at 25 $°C$), was added to DCM (vapour pressure 460 mbar at 25$°C$) in order to prevent clogging at the exit of the needle due to its fast evaporation. Furthermore, similarly as what was observed for beads-on-string morphology, the thicker domains are distributed predominantly on the border of the honeycomb patterns, forming the walls between two patterns while thinner fibres are suspended across the patterns. Finally, Figure 7.2 h-i show that a broad but monomodal distribution of the fibre diameter can be obtained by lowering the voltage to +5 kV on the needle and -10 kV on the collector, while keeping the difference of potential constant between needle and collector. Indeed, this leads to a lower electric charge density on the surface of the electrospun jet and limited whipping movements, resulting in lower elongation. In these conditions no self-organisation occurs Figure 7.2 g suggesting that a bimodal distribution of the fibre diameters is a necessary condition for self-organisation.

7.3.3 Temporal evolution of a self-assembled honeycomb patterns

Figure 7.4 and Figure 7.3 shows the self-assembly of electrospun fibers which were evolving as the deposition time is increasing and the universal law's of self-similar pattern growth[237]. Even if honeycomb structures of electrospun fibres have already been observed, the onset of the phenomenon was never shown or explained. To answer this question, and moreover to study the dynamics of self-organisation, experiments were carried out over a wide range of electrospinning times from 1 s to 2 hours. A voltage of +10 kV on the needle and -10 kV on the collector were the optimum condition. SEM observations of the membranes reveal that if self-organisation is only beginning at 2 min, the honeycomb patterns formed after 5 min are growing continuously in size with electrospinning time. Image analysis reveals that the average diameter of the patterns follows a power law $D_{av} \equiv t^{\alpha}$ with $\alpha \equiv 1.2$ (Fig. 7.3d). Moreover, at any time, the pattern area A obeys a lognormal distribution, i.e. $A.P_t(A)$ plotted against $logA$ can be fitted by a normal distribution, with $P_t(A)$ the distribution function of A at time t (Fig. 7.3e). This distribution is time-independent. Indeed, a dynamic scaling of the distribution function of A exists as all the distributions collapse on a single master curve when plotting $A.P_t(A)$ as a function of $log(A/A_{av}, t)$. Where A_{av}, t is the average area at time t. These features are characteristic of the self-similar pattern growth generally observed in

colloids[237] crystals and foams[238].

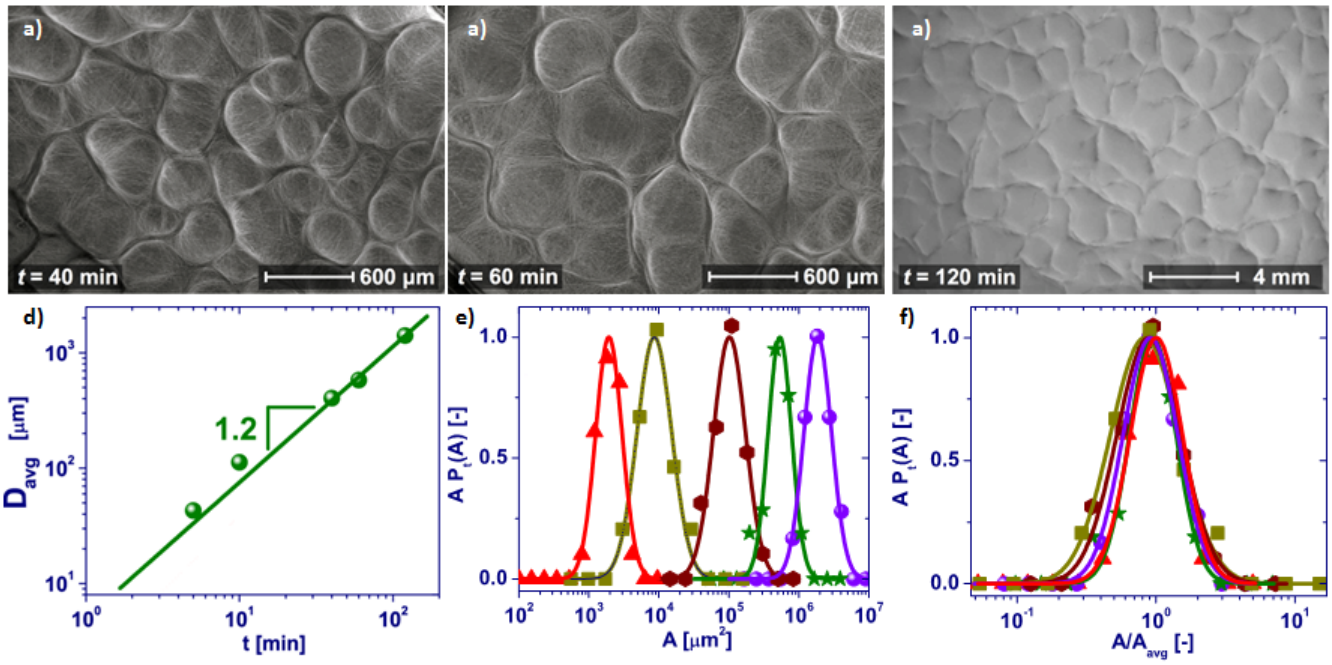

Figure 7.3: Dynamic self-assembly of electrospun fibers and self-similar pattern growth universal laws which are followed by honeycomb patterns (a) Deposition time t = 40 min (b) t = 60 min (c) t = 120 min (d)of average honeycomb pattern diameter Davg with time (e) Dynamic scaling plots of distribution functions of A (f) distribution functions of honeycomb pattern areas A after different electrospinning times: t = 5 min (red triangles), t = 10 min (olive squares), t = 40 min (brown hexagons), t = 60 min (green stars) and t = 120 min (violet spheres).

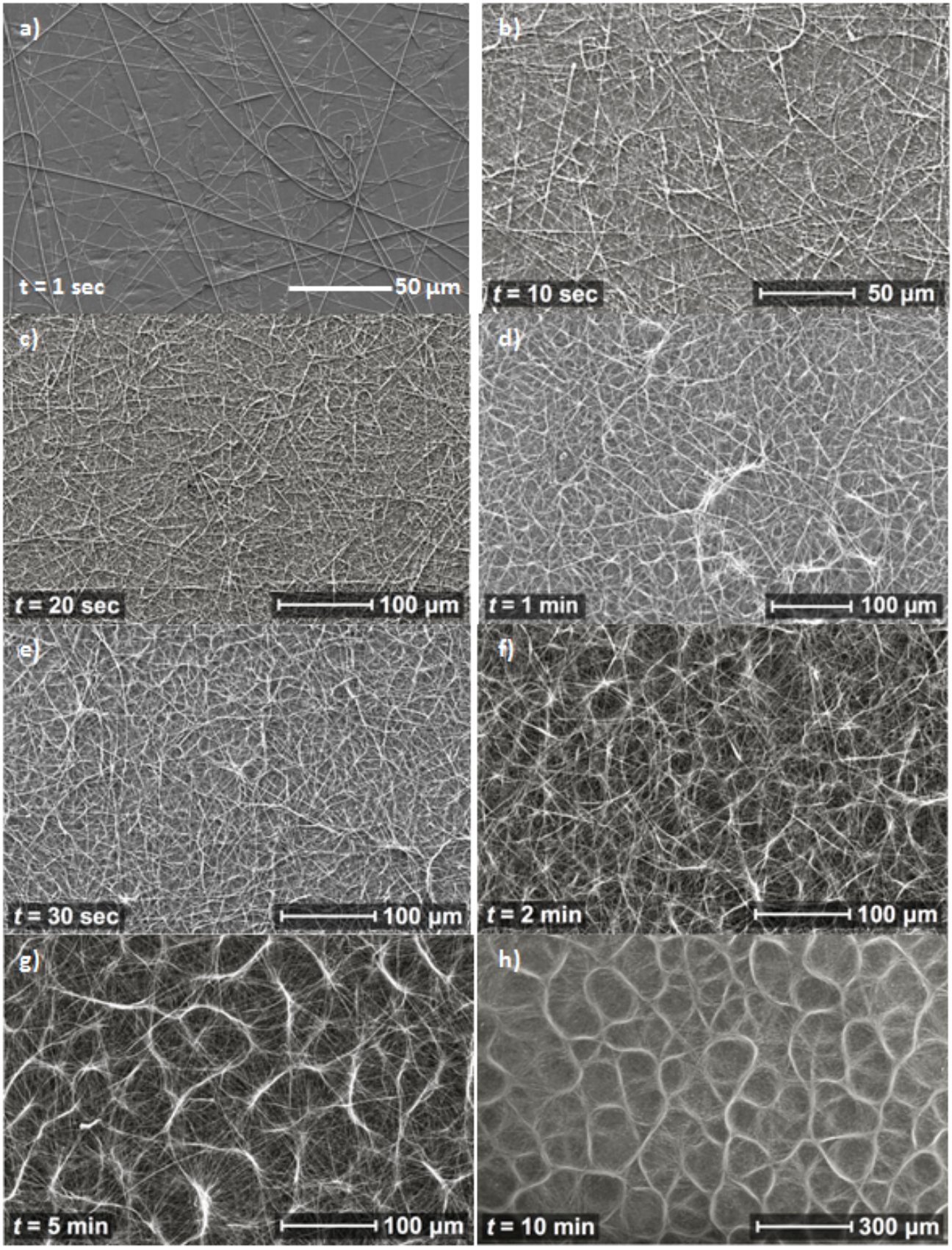

Figure 7.4: Dynamic self-assembly of electrospun fibers (a) Deposition time t = 1 sec (b) t = 10 sec (c) t = 20 sec (d) t = 30 sec (e) t = 1 min (f) t = 2 min (g) t = 5 sec (h) t = 10 min.

7.3.4 Mechanism of self-assembly and its temporal evolution

As it is already indicated with the experiments the most important requirements for the self-assembly is bimodal distribution of electrospun fibers. Figure 7.5 a) shows the bimodal morphology for the Monte Carlo simulation. During the very first moments of electrospinning, the electrospun jet is subject to a homogeneous electric field that induces a pseudo-random deposition. Because of the bimodal distribution of the diameters of the fibers, a heterogeneous rough surface is formed Figure 7.5b,d). Monte Carlo simulations of a random deposition of such fibers revealed that the heterogeneous surface results from the non-uniform distribution of thick domains that form aggregates (Figure 7.5c,e). As also observed by Yan et al.[230] the thick domains are still wet because of the residual DMF. Furthermore, they are in very good contact with the collector, allowing efficient electric charge dissipation. Between these aggregates, thin dry fibers that have diameters 5 to 10 times smaller than those of the thick ones hang in the air and retain their electric charge. Thus, a heterogeneous distribution of electric charges accumulates at the surface of the collector, which forms a perfect template that facilitates the apparition of the first honeycomb layer, similar to the fibers that align between the conductive micro-blocks of a structured collector[239,240]. Because the aggregates are not regularly distributed on the surface of the collector, the honeycomb patterns exhibit a broad size distribution. The walls of the honeycomb pattern are primarily formed by thick wet fibers that are in good contact with the collector, which in turn favors the alignment and deposition of the fibers onto the walls in a self-sustained process.

Figures 7.6 a-d present the results of numerical simulations of the electric field located directly over a regular honeycomb structure. The calculations were performed on an elementary 3D volume (Figures 7.6a). The sizes of the honeycomb edges are in agreement with those observed experimentally (Figures 7.6b). As an example, Figures 7.6 d shows the results obtained for two different honeycomb pattern sizes. The larger honeycomb patterns clearly induce a higher vertical component of the electric field over the sharp edges of the walls, which results in a more efficient deposition. Consequently, for honeycomb structures that exhibit a size polydispersity, while the scaffold thickness increases, the largest patterns take the ascendant over the smaller ones, which gradually disappear, thereby leading to the pattern growth observed in Figures 7.4. In conclusion, the self-organization of electrospun fibers results in the formation of stratified honeycomb layers. The size of the patterns increases with time, forming a pore size gradient in the thickness of the membrane. In the following, we will demonstrate that this efficient dynamic self-organization

provides a considerable advantage for the fabrication of unique 3D cm thick nanofibrous materials with increasing porosity.

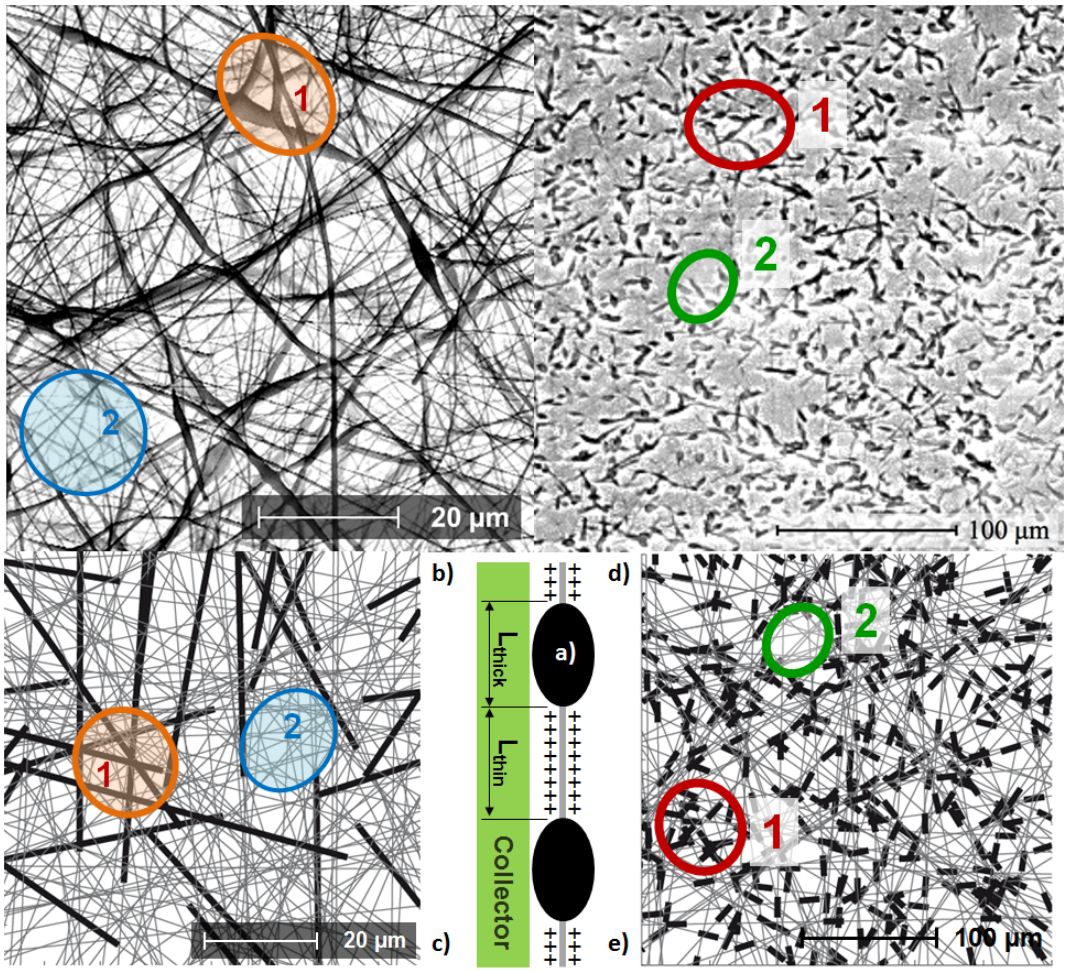

Figure 7.5: (a) Schematic section of a heterogeneous fiber deposited on the collector [b] SEM image showing the very first moments (10 s) of the deposition of irregular electrospun nanofibres, with PCL concentration at 13% wt, V_{needle}= 10 kV and $V_{collector}$ = -10 kV. Region 1 shows the aggregation of thick fiber domains, whereas only thin fibers cover region 2. [c] Monte Carlo simulations of the previous image showing the aggregation of thick fiber domains after a random deposition of 150 fibers with characteristic length L_{thick} =70 μm and L_{thin} = 800 μm. (d) SEM image showing the very first moments (10 s) of the deposition of irregular beaded electrospun nanofibres, with PCL concentration at 11% wt, V_{needle} = 10 kV and $V_{collector}$ = -10 kV. Region 1 shows the aggregation of thick fiber domains, whereas only thin fibers cover region 2. (e) Monte Carlo simulations of the previous image showing the aggregation of thick fiber domains after a random deposition of 150 fibers with characteristic length L_{thick} =15 μm and L_{thin} = 100 μm.

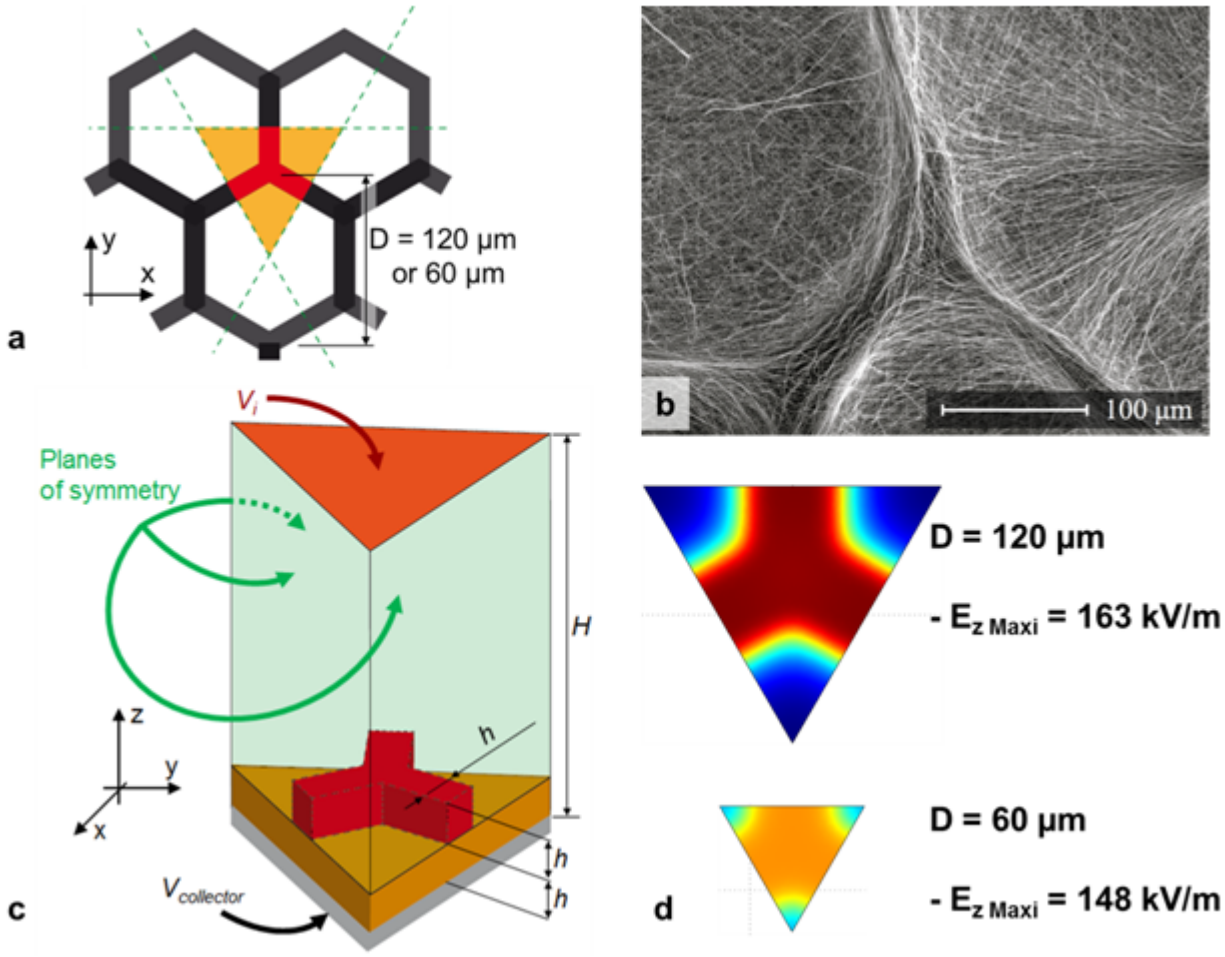

Figure 7.6: (a) Model of a regular honeycomb structure where 3 planes of symmetry (dashed green lines) appear, which permits the study for the elementary triangle domain, (b) SEM micrograph of a honeycomb scaffold showing an elementary domain, (c) 3D geometrical model with boundary conditions for the electric field computation by finite element methods. For the calculations we choose $h = 20\ \mu$m, $H = 200\ \mu$m, distance from needle to collector $D = 15$ cm, $V_{needle} = 10$ kV, $V_{collector} = -10$ kV and $V_i = V_{collector} + V_{needle}H/D$, (d) Electric field z component obtained for two honeycomb pattern sizes ($D = 120\ \mu$m and $60\ \mu$m), $V_{needle} = 10$ kV, $V_{collector} = -10$ kV and given at $z = 25\ \mu$ m.

7.3.5 Fabrication of 3D foams and physical characterization

To reduce the time required for producing a thick scaffold, the electrospun jet is focused on a small surface by placing a 3 mm thick poly(methyl methacrylate) (PMMA) mask with a 25 mm hole over the conductive collector (Figure 7.7 a). Because the presence of the PMMA mask decreases the global electric field, the potential difference between the needle and collector is increased to

30 kV (V_{needle} = 15 kV, $V_{collector}$ = -15 kV). A honeycomb-structured scaffold is deposited inside of the hole in the PMMA plate, and it grows faster as the porosity increases with time because of the growing honeycomb patterns. This phenomenon allows for the fabrication of cm-thick scaffolds with stratified honeycomb layers (Figure 7.7). Furthermore, the walls of the honeycomb structures form a good evacuation path for the electric charges, allowing very long deposition times.

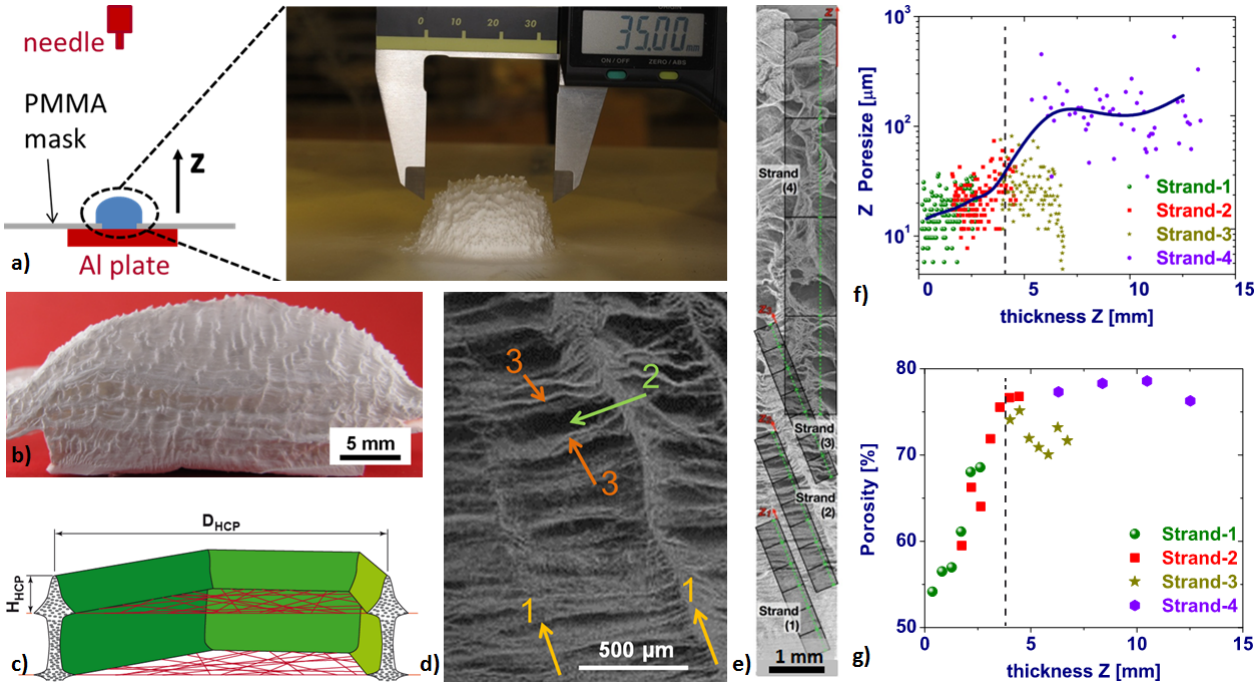

Figure 7.7: Thick scaffolds obtained by focusing the electrospun jet through a PMMA mask. (a) Schematic representation of the set-up and an image of a 3D thick scaffold immediately after electrospinning over the PMMA mask. The top surface of the scaffold shows a rough surface due to the self-assembled honeycomb structures, (b) Cross section of a 15 mm thick scaffold, (c) Schematic representation of a mesopore being formed, (d) SEM image showing the columnar structure of the stratified layers of the mesopores, (e) SEM image showing the entire section of the scaffold, (f) Height of the mesopores versus z obtained from the image analysis of Figure 5e, (g) Scaffold porosity versus z obtained from the image analysis of Figure 5e

Figure 7.7b shows a 15 mm thick scaffold obtained after 5 hours of electrospinning. This sample presents a rough upper surface that results from the last layer of honeycomb patterns. The first 3 mm layer of the scaffold has a diameter of 25 mm, which corresponds to the hole in the mask. Then, the diameter increases slightly due to free boundary conditions. However, the presence of the residual DMF, which possesses a high dielectric constant (ϵ= 40) compared to PMMA (ϵ =

3.5), results in a much higher electric field over the deposited membrane than the PMMA plate, thereby maintaining an efficient focusing of the jet during electrospinning.

Images of cross sections of the sample reveal the internal morphology of thick scaffolds (Figure 7.7 b-e). A columnar structure (Figure 7.7d, arrows 1) clearly appears due to the growth of the honeycomb pattern walls. Between these walls, a succession of mesopores is formed (Figure 7.7d, arrow 2) that are separated by thin membranes (Figure 7.7d, arrows 3). Therefore, the obtained scaffold, which is composed of nearly uniform polyhedral domains separated by thin boundaries, looks like a foam. A statistical analysis of the cross section of Figure 7.7e shows that the height of the mesopore (Figure 7.7f) and the porosity (Figure 7.7g) increase as a function of the vertical z component. However, the maximum porosity obtained from this analysis (~ 80 %) is less than that obtained from gravimetric measurements of the entire sample ($\sim 92 \pm 3\%$). At the employed observation scale, the image analysis only considers the mesopores and neglects the micropores between the nanofibers inside of the membranes and walls.

The formation of thin membranes between the mesopores can be explained by analogy with electrospinning on a micro patterned conductive hole-collector[224]. Over a critical value of the height-to-diameter ratio, H/D, the nanofibers cannot fall onto the hole bottom but cross over it, forming a suspended membrane. In our case, a honeycomb pattern with a diameter D_{HCP} and height H_{HCP} belonging to the upper layer plays a similar role (Figure 7.7c) fibers land preferentially on them, increasing their height. When the critical ratio H_{HCP}/D_{HCP} is reached, the nanofibers form a suspended microporous membrane that closes the honeycomb pattern, thereby forming a mesopore. Because the diameter of the honeycomb patterns increases with deposition time, the height of the walls must increase before the critical ratio H_{HCP}/D_{HCP} is reached. Therefore, the height of the mesopores increases with the thickness of the sample. The critical H/D values for the micro-patterned conductive hole-collector are approximately 1/3[224]. In our case, the H_{HCP}/D_{HCP} ratio is in the range of 1/5 to 1/10, likely because the bottoms of the mesopores are repulsive. A substantial variation in the size of the mesopores and in the porosity is observed at $z \sim 3 - 4mm$ (dashed lines in Figure 7.7f-g), which corresponds to the thickness of the PMMA mask. When the thickness of the deposited fibers reaches the thickness of the mask, the electrospinning process is no longer focused, resulting in a substantial change in the electric field conditions and an abrupt increase in the mesopore size. This result demonstrates that the mask characteristics (thickness, electric permittivity) and applied voltages are important parameters for

controlling the mesopore size of the scaffold and thus the hierarchical porous structure with pore sizes ranging from microns (between nanofibers, inside of the boundaries of the mesopores) to hundreds of microns (mesopores).

7.3.6 Mechanical characterization of 3D foam

The 3D thick scaffolds have a structure that mimics the natural extracellular matrix (ECM) of bone. In addition to morphological properties, tissue engineering applications require scaffolds with mechanical properties that allow facile handling in vitro and implantation in vivo and for creating a good support for the synthesis of the ECM and the formation of new functional tissues. Therefore, the mechanical properties of the obtained electrospun foams were evaluated. The behavior of a scaffold with a thickness of 9 ± 0.5 mm and a porosity of 92% was studied under simple compression. Typical open-cell foam behavior was observed (blue curves of Figures 7.8 a-b). Indeed, the scaffolds exhibit three successive regimes:(i) a linear elastic regime with a modulus of $\hat{E} \sim 35$kPa for strains less than $\epsilon_e \sim 4.5\%$, (ii) a collapse plateau for strains between ϵ_e and $\epsilon_d \sim 75\%$ and (iii) a densification regime beginning from ϵ_d. The images collected during compression illustrate the behavior of the structure at $\epsilon = 0.4$, 17.0 and 29.5% (Figures 7.8 c-e). Figures 7.8 d-e reveal that the collapse plateau is primarily due to buckling of the honeycomb walls. Furthermore, the buckling progressively propagates from the walls that exhibit the highest aspect ratio and are highly loaded (i.e., the walls primarily located in the less dense upper section) to the walls where the aspect ratio and loading are less important (i.e., the walls primarily located in the denser lower section of the scaffold) (Figures 7.8 e). Because the morphology of thick scaffolds can be modeled by the successive superimposition of honeycomb layers of decreasing density, the sample was cut to separately measure the behavior of the upper and lower parts during compression. As expected, the Youngs modulus increased when the porosity decreased; a modulus of 18 kPa and a porosity of 95% were obtained for the upper section, whereas a modulus of 65 kPa and a porosity of 87% were obtained for the lower section. When perfect honeycomb structures are loaded out of plane, their modulus is $\hat{E} = E_{wall}\hat{\rho}/\rho_{wall}$, where E_{wall} is the Youngs modulus of the honeycomb walls and $\hat{\rho}$ and ρ_{wall} are the densities of the foam and wall, respectively[241]. Finally, as expected, the densification regime begins at lower strains ($\epsilon_d \sim 65\%$) for the denser lower section than for the more porous upper section ($\epsilon_d \sim 85\%$). In conclusion, the good mechanical properties observed for 3D thick scaffolds result from their honeycomb-like structure as opposed to an unorganized loose fibrous network with comparable pore size. These properties enable the

facile manipulation and implantation of these materials for tissue engineering applications.

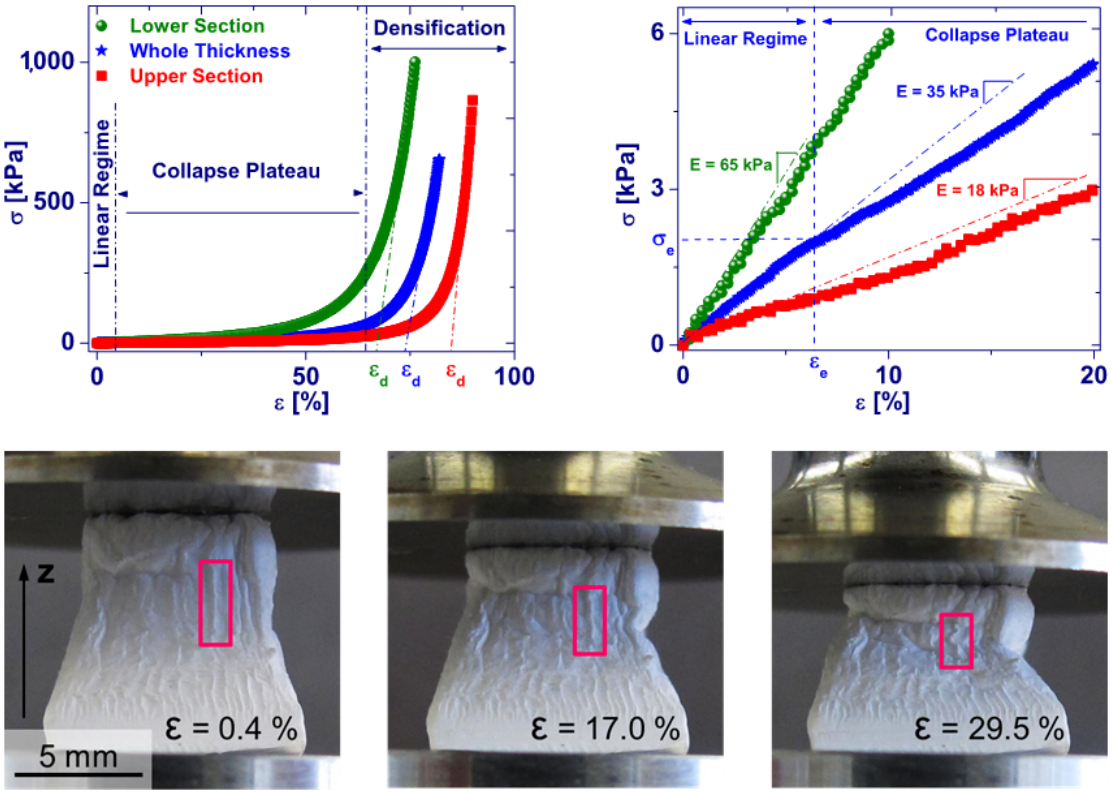

Figure 7.8: Compression properties of electrospun 3D thick foams (a) Stress-strain behaviors of a foam obtained after 4 hours of electrospinning with an initial thickness of 9 ± 0.5 mm; behavior of the entire thickness of the scaffold (blue), behavior of the upper part (red) and lower part (green), (b) Magnified section of the previous graph showing the linear regime of different scaffold domains; entire thickness (blue), upper part (red) and lower part (green) (c-e) Pictures showing the sample with an initial thickness of 9.3 mm between the compression plates, c) at the very first moments when $\epsilon = 0.4\%$, (d) at $\epsilon = 17.0\%$ and (e) at $\epsilon = 29.5\%$

7.4 Conclusion and Future Perspective

In summary, a new process to produce cm-thick 3D foams using a simple electrospinning set-up was developed. This process exploits the self-organization of nanofibers in honeycomb patterns that increase in size with deposition time, leading to increasing porosity. By focusing the electrospun jet, it is possible to force the rapid growth of the scaffold with thicknesses up to the cm scale in only a few hours. Furthermore, these foams, made of PCL, an FDA-approved bioresorbable polymer, exhibit a porosity and pore-size gradient with micro-pores and mesopores in the range of

several hundred microns. In tissue engineering, it has been reported that scaffolds with pore size gradient might be useful, for example, for nerve regeneration as a gradient in porosity and pore size enables myofibroblast migration through the scaffold[242]. Moreover, pore size gradient can also mimic cartilage[243] or natural bone from cortical dense surface to cancellous interior[244,245]. In addition, despite their high porosity, the foams maintain very interesting mechanical properties, which make them ideal materials for tissue engineering applications. Bio-functionalization[246] of the scaffolds by protein adsorption or the Layer by Layer (LbL) technique[247] could be envisaged to further promote cell adhesion and proliferation. Finally, because the honeycomb self-organization of nanofibers has been observed for several other polymers[228,229,230]. it is assumed that the ability to form 3D foams from various polymers will be a general phenomenon. Therefore, the outstanding properties of such foams make them attractive for other applications.

Chapter 8

Melt Electrospinning: Influence of Material and Process Parameters on Fiber Diameters and Morphology

The melt electrospinning is more attractive than solution electrospinning for industrial applications because it is environmentally benign, it eliminates the solvent recovery and treatments costs, it opened a new doors for the fabrication of electrospun fibers based on polyolefin because they did not have any appropriate solvents at room temperature, and owing to weak polymer concentration in solution electrospinning the rate of fiber production could be improved in melt electrospinning. Recently, Dalton et al.[248] showed that melt electrospun fibers can be directly deposited into cell culture which is not possible using solution electrospinning because of presence of cytotoxic nature of solvent. To promote the cell invasion and growth on the fabricated scaffolds, the optimum diameter should be at least 4 μm which translate into 20 μm pore size assuming the random deposition of the fibers[249]. Concluding from the above discussion, the melt electrospun fibers produced using biodegradable and biocompatible polymers, smaller than 5μm would be ideal for several tissue engineering applications.

Larrondo and Manley[19,250,251] way back in 1980's for the first time demonstrated the feasibility of melt electrospinning. They were successful in obtaining the polypropylene fibers in the range 100-50 μm but this range could easily be obtained using conventional fibers spinning process. Due to lack of encouraging results, the interest in the field diminished. Lyon et al.[252] in 2005 were able to reignite the interest in the field by demonstrating 10 fold reduction in the produced

polypropylene fibers from melt electrospinning and Dalton et al.[253] were able to produce fibers in the range 1000-840 *nm* with addition of viscosity reducing additive in polypropylene melt. Recently few polymer systems were used to produce fibers using melt electrospinning polyethylene (PE)[254,255], poly(ϵ-caprolactone) (PCL)[256,257], polylactic Acid (PLA)[258,259], polyurethane (PU)[260], poly(methyl methacrylate) (PMMA)[261].

The morphology and the diameter of fibers produced by melt electrospinning technology depends on the right combination of material, process, and ambient parameters, similar to the solution electrospinning technology. In melt electrospinning, polymers properties play more dominated role than in solution electrospinning. Indeed, the important parameters reported to tune the fiber diameters are molecular weight, tacticity, and melting point of the polymers, electric field strength, distance from the needle, flow rate, and the process temperature (melting point temperature, electrospinning temperature, cooling/collector temperature)[262,253,252,258]. Melt electrospinning also suffers from the drawback such as the production of microfibers. It has to be noted that the fiber diameter obtained during the melt electrospinning, range from sub-micron to micron range and fibers are at least one order of magnitude thicker than the fiber produced by the solution electrospinning. This is due to the low surface charge density and high viscosity of the polymer melts in comparison to the polymer solutions. Until now, no melt electorspun fibers morphological changes were reported as a function of all the parameters discussed above. In this work, we presented the first study to obtain a different morphology of fibers due to mechanical failure of fibers.

Mechanical properties of electrospun fibers has received some attention in exploring the stress-strain behaviour and modulus of elasticity but the modes of fractures of nanofibers was rarely reported. To the best of our knowledge, the first reported failure mode of polyethylene oxide (PEO) solution electrospun fibers was discussed by Zussmann et al.[263]. Highly aligned nanofibers of PE were obtained by high temperature solution electrospinning combined with parallel-electrode collector which resulted in multiple failure of electrospun fibers[264]. The significant increment in fracture energy of PAN solution electorspun fibers were observed by addition of small amount of SWNT and MWNT[265]. In all the above discussed studies the solution electrospun fibers were subjected to extra stretching during the collection by modifying the collector. Furthermore, Zussmann et al.[263] confirmed that the failure modes were not observed on simple collector. However, in case of melt electrospinning, failure of fibers is observed on simple collector [stationary at 0

kV (ground)].

In this work, a unique melt electrospinning set-up was developed and used to fabricate poly(ϵ-caprolactone) (PCL) solvent free scaffolds. The effects of material parameters and process parameters were investigated. The fiber diameters were correlated with the rheological response of the PCL melts. Furthermore, the new morphology of deposited fibers were produced by controlling the collector temperature.

8.1 Material and Methods

8.1.1 Materials

Two commercial grades of poly(ϵ-caprolactone)(PCL) (CAPA-6808 and CAPA-6500) with linear topology and PCL-S which is synthesized in our lab by Ms. Murielle Oster. The PCL-S is a mixture of linear and 3 arm star topology. The molecular weight (M_w) and molecular weight distribution (PDI) were measured by size-exclusion chromatography in chloroform with polystyrene standard, and melting temperature were measured using Differential scanning calorimetry (DSC) which were indicated in Table 8.1. The PCL-CAPA-6808 (L_1) were blended with PCL-S (L_2) in different ratio. To prepare the blends, first master batch solution (solvent: THF) were prepared where weight concentration of PCL-S were 20%, then this master solution were divided into four parts according to desired ratio and using methanol finally PCL were precipitated. The precipitated PCL were kept into vacuum drying at 30 °C for two days. The detail regarding the ratio and melting points were indicated in Table 8.2.

Table 8.1: Characteristics of the investigated homopolymer materials

Polymer	M_w [kg/mol]	M_w/M_n	T_m [°C]
PCL-CAPA-6808	103	1.8	54
PCL-CAPA-6500	107	1.5	53
PCL-S	40	1.2	53

Table 8.2: Characteristics of the investigated blends materials

Blend	L_1:L_2	T_m [°C]
B_1	98:02	53
B_2	94:06	53
B_3	88:12	53
B_4	80:20	53

8.1.2 Rheological Characterization

Oscillatory shear measurements were performed on an ARES-G2 rotational rheometer from TA Instruments. The oscillatory shear measurements were performed on cone and plate geometry (25 mm, α = 0.1 rad) at 110 °C in a frequency range from 10^0 to 10^2. The samples were press-molded under vacuum at 140°C into 25 mm discs for the shear experiments.

8.1.3 Configuration of Melt Electrospinning

A home-made melt electrospinning equipment was developed as shown in Figure 8.1. It consists of six major components, (i) a cylindrical glass (d = 50 cm) which is rapped around with an electrical heater (T = 30-180 °C (ii) a collector (d = 12.5 cm) was grounded and kept at a temperature which was significantly below the melting temperature of PCL polymer using cold water circulation (T = 15-80 °C) (iii) a high voltage power-supply (V = 0-60 kV) (iv) syringe pump (Harvard Apparatus PHD 2000) (v) the syringe holder which can be moved vertically to adjust the working distance (vi) the needle (inner diameter is 1 mm).

One of the important aspect of building a melt-electrospinning apparatus is deciding on the heating source for the system. So far, four distinct methods have been reported in the literature (i) electrically heated[19,250,251], (ii) circulating fluids[256], (iii) heated air[266], and (iv) heat from a laser source[267]. Electrical heating is most frequently employed method for heating source. The disadvantage of electrical heating are its isolation from the high voltage source, and potential disruption with electric field. To overcome these issues, few research group applied the high voltage at collector instead of needle[268,269].

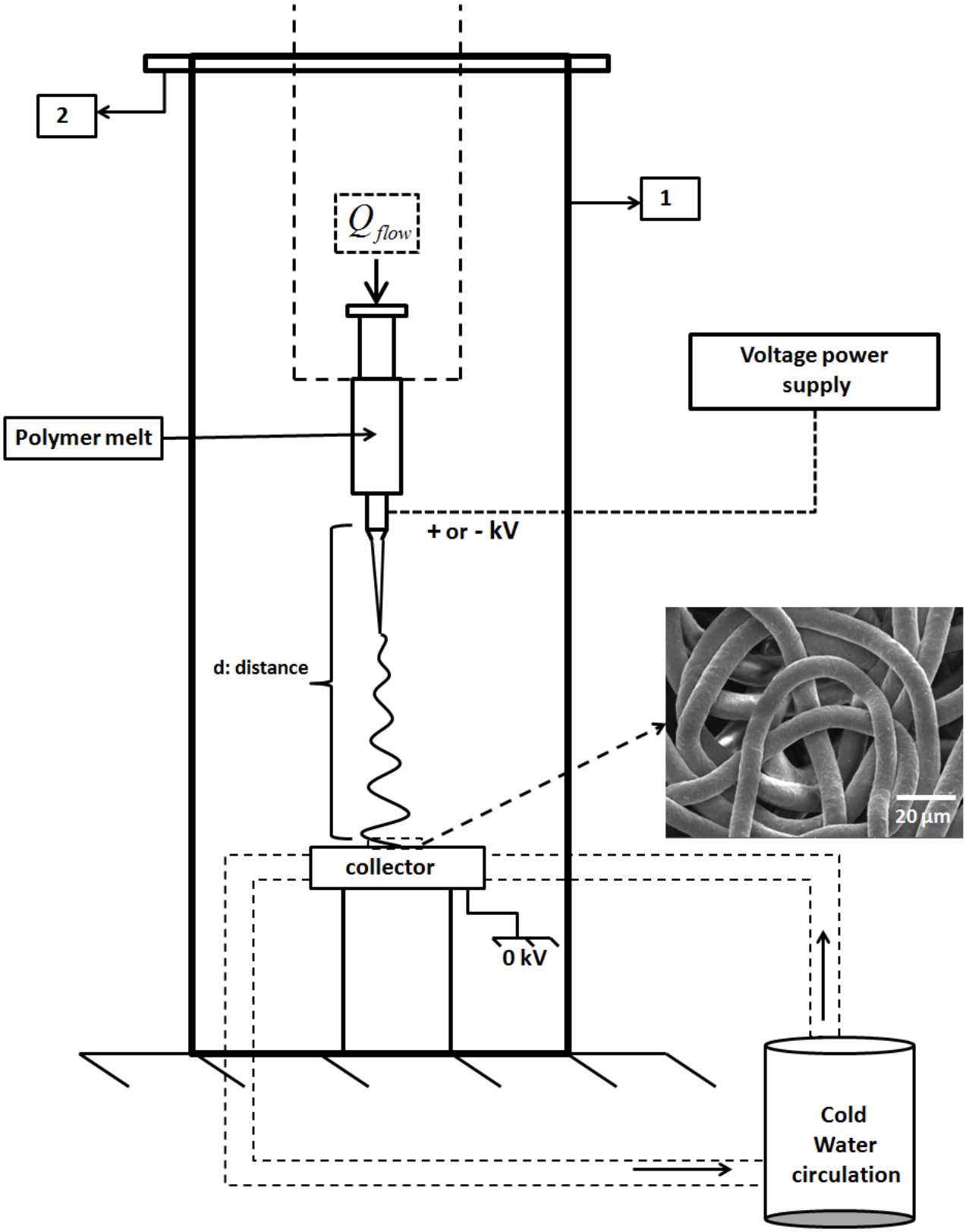

Figure 8.1: Self developed melt-electrospinning set-up with all its components where (1) represents a cylindrical glass (d = 50 cm) which is rapped around with an electrical heater (T = 30-180 °C and (2) is a wooden cover which is connected with the syringe supporter.

One of the disadvantage of all the previously developed set-up is focused heating on the needle. no heating or heating source were operating in between the syringe and collector. Our unique heating strategy avoid the problem of electrical insulation and as can be seen in simulated temperature profile the heating is applied uniformly along the vertical direction. This allows the uniform extension of melt electrospun fibers, which could help to better control the diameter of melt electrospun fibers.

The applied temperature on heater was 140 °C and measured temperature at needle was 110 °C. Furthermore, the temperature at collector was fixed to 15 °C. The applied voltage was varied in the range of 10-35 kV and collector was grounded in all the experiments. The PCL powder or pallets were first press molded at 100 °C and glass syringe was preheated to avoid the bubble formation during the melting.

8.2 Results and Discussion

The electric field and temperature profile for our set-up were simulated using COMSOL^{TM} software by finite element method. The boundary condition for both electric field and temperature simulation is shown in Figure 8.2 and correspond to standard processing parameters used in this study. The temperature profile is plotted between needle and collector, and it could be observed that at a distance of 3.3 cm from the collector, the temperature is 60 ° C which corresponds to the melting point of PCL. Consequently, it could be concluded that the melt electrospun jet is rapidly subjected to cooling by convection during its travel in the air.

Figure 8.3 shows the dynamic complex viscosity, $|\eta^*|$, and van Gurp-Palmen plot for the investigated PCL materials. The two PCL materials which were used for melt electrospinning have similar molecular weight, M_w, but differs in polydispersity. Figure 8.3a illustrates the effect of polydispersity on $|\eta^*|$. The $|\eta^*|$ at all excitation angular frequency, ω, decreased significantly as the polydispersity of PCL polymer melt increased. The decrease in the absolute value of complex viscosity ($|\eta^*|$) with increasing polydispersity in terminal regime could be explained by the larger contribution from convective constraint release relaxation. The small chain in polymer melts were already relaxed and serve as the solvent for big chain and this effectively helps in decreasing the zero shear rate viscosity (η_0)[4]. Figure 8.3b illustrates the van Gurp-Palmen plot which is a very sensitive tool to differentiate polydispersity of polymer melts[102]. Figure 8.3c illustrates the ef-

fect on complex viscosity (η^*) of weight fraction of PCL (M_w = 40000 g/mol) when blended in PCL (M_w = 103000 g/mol, PDI = 1.8). The complex viscosity ($|\eta^*|$) decreased as we increased the weight fraction of PCL (M_w = 40000 g/mol). These observation could also be explained by the dilution effect of small chain ($M_w = 40k$) in the blend. Figure 8.3d illustrates the van Gurp-Palmen plot for the blends. The phase angle (δ_0) decreases as the weight fraction of PCL (M_w = 40000 g/mol) increases except for the case of 12%-L-S. A significant drop were observed for δ_0 in 12%-L-S blend which is surprising.

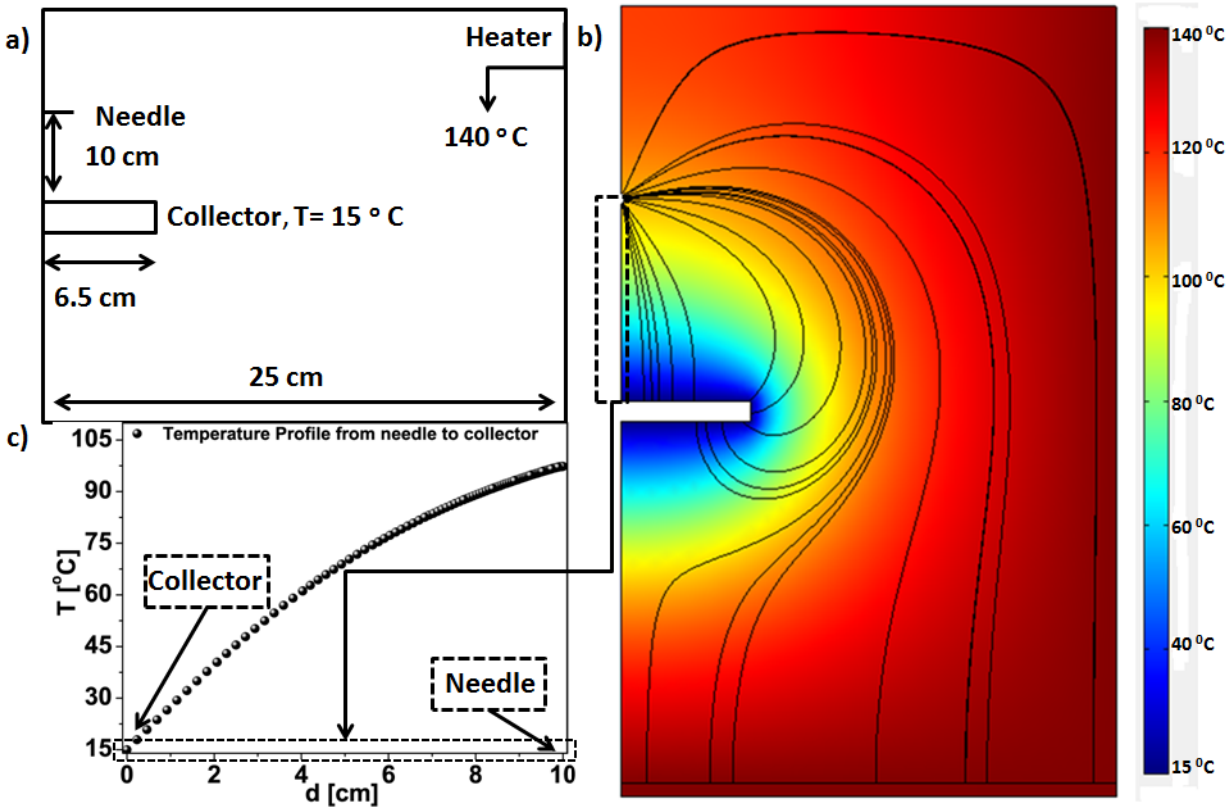

Figure 8.2: COMSOL simulation of temperature and electric field for our melt electropinning set-up (a) geometrical dimensions used for the simulation, (b) temperature and electric field simulation of melt electrospinning set-up and (c) temperature variation at the center from needle to collector.

Figure 8.4 shows the influence of applied voltage on needle, V_s, and polydispersity on melt electrospun fibers average diameter, D_{avg}. The SEM images are shown at two magnification for PCL (PDI = 1.8) and PCL (PDI = 1.5) in Figure 8.5 and Figure 8.6, respectively. The melt electrospun fibers diameter were measured using ImageJ software[270]. D_{avg} of both polymers seems to decrease

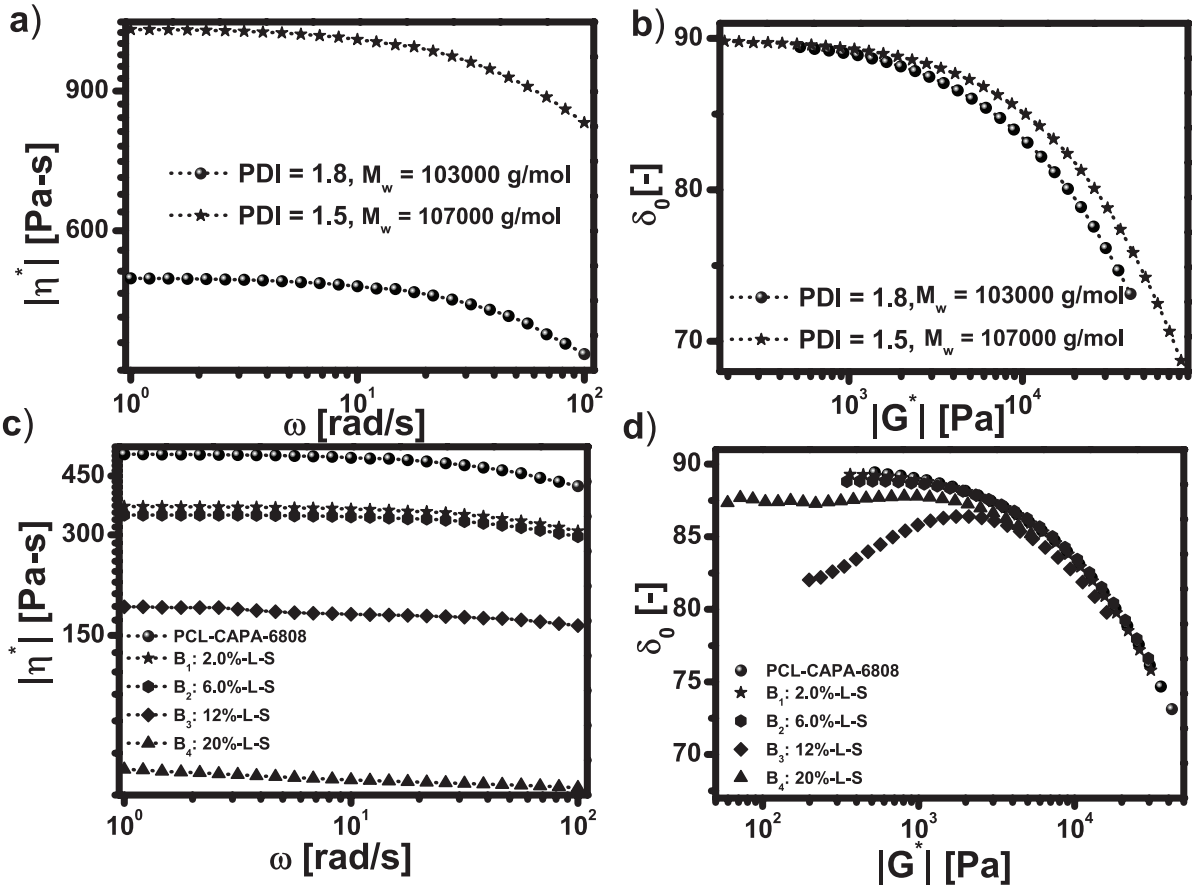

Figure 8.3: Dynamic oscillatory shear rheology of Investigated PCL Materials (a) the complex viscosity (η^*) of linear PCL, (b) the phase difference of linear PCL, (c) the complex viscosity (η^*) of blend of linear and star PCL and (d) the phase difference of blend of linear and star PCL.

by increasing the applied voltage in the range 10-35 kV. An increase in D_{avg} is observed as a function of polydispersity (PDI) of the material in the applied voltage range 10-20 kV. However, in the applied voltage range 25-30 kV, polydispersity influence on D_{avg} is not significant.

The influence of applied voltage on melt electrospun fibers diameter is not well understood. While, some previous studies did not observed any strong correlation[271,272], but some studies do[273,266]. In our case, applied voltage is characterized as the most important process parameter to tune the fiber diameter. The strong correlation obtained in our study can be explained by increased electrostatic stretching on increasing the applied voltage during the flight of melt electrospun fibers before their solidification.

PCL with higher polydispersity displayed the lower viscosity as confirmed by the rheological measurements. In the range of applied voltage 10-20 kV, the material with higher viscosity dis-

played lower fiber diameter which is in contradiction with previous studies[253,274]. As previously explained by Nayak et al.[274] that the conductivity of polymers plays a important role along with the viscosity of polymers on the final diameter of melt electrospun fiber. To explain our contradicting result, the conductivity of the PCL (PDI=1.8) with high viscosity should be lower than the PCL (PDI= 1.5) because all other process parameters were kept constant.

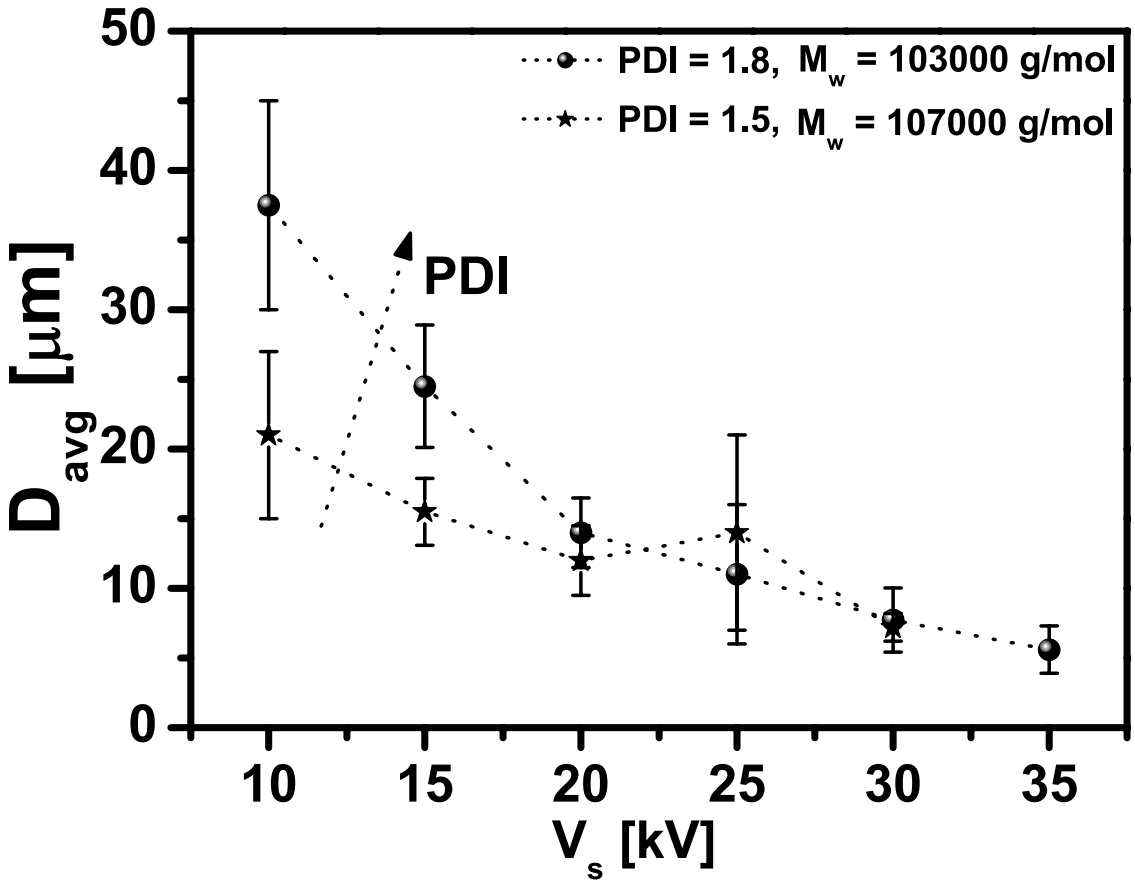

Figure 8.4: Influence of applied voltage (processing parameter), V_s, and polymer polydispersity (material property) on the fiber average diameter, D_{avg}.

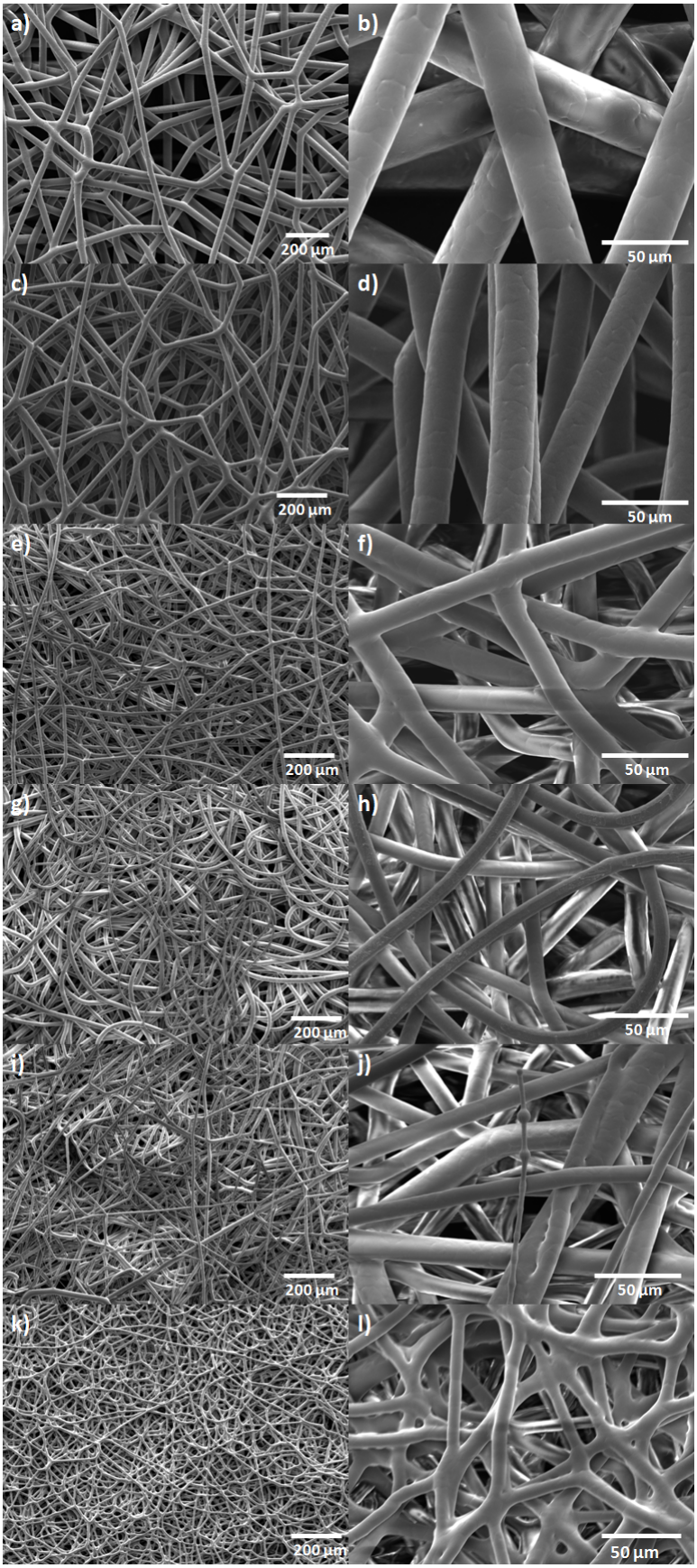

Figure 8.5: Influence of applied voltage on melt electrospun fibers of PCL (M_w = 107000 g/mol) (a-b) V_s = 10 kV (c-d) V_s = 15 kV (e-f) V_s = 20 kV (g-h) V_s = 25 kV (i-j) V_s = 30 kV (k-l) V_s = 35 kV.

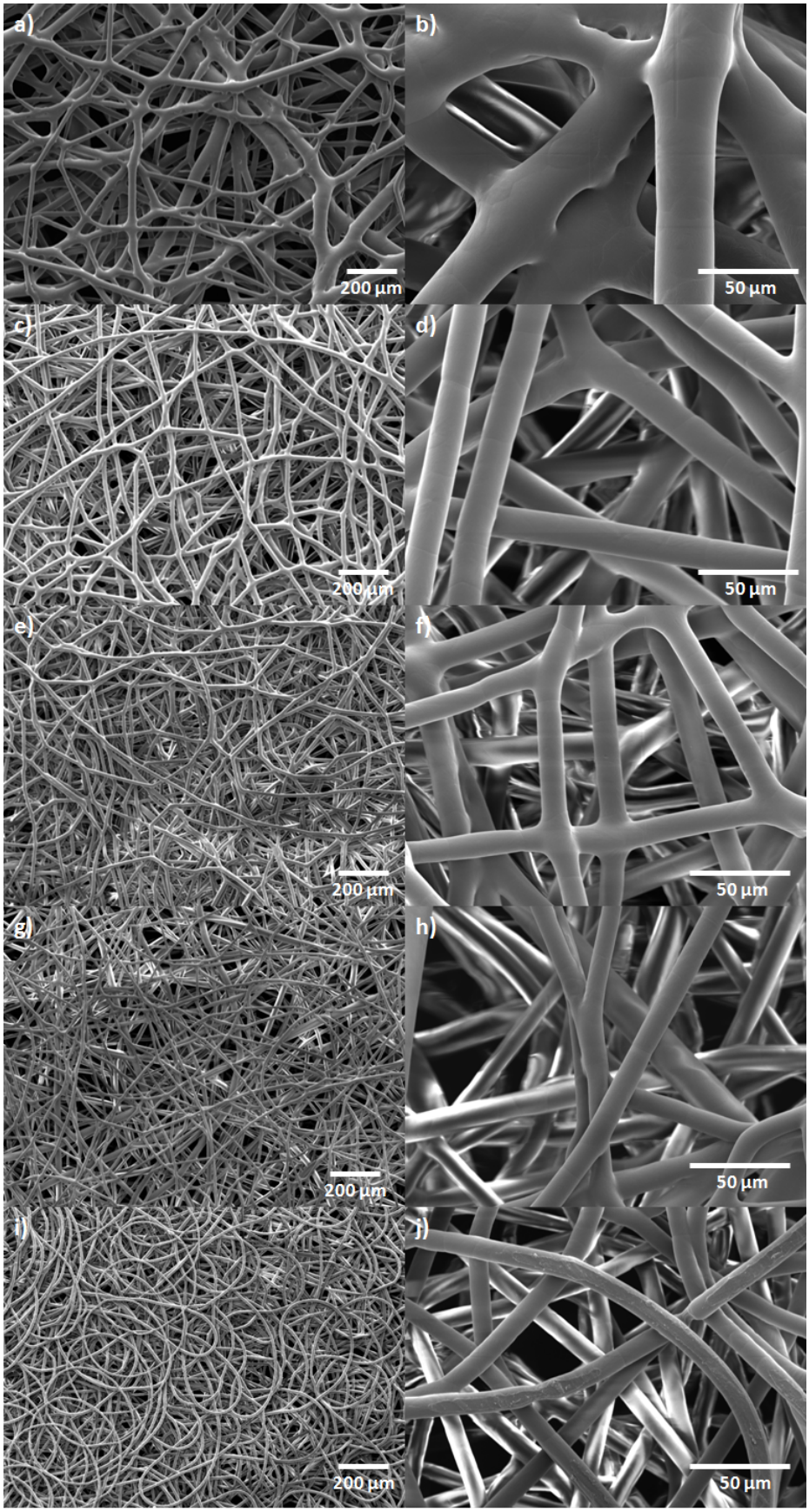

Figure 8.6: Influence of applied voltage on melt electrospun fibers of PCL (M_w = 103000 g/mol) (a-b) V_s = 10 kV (c-d) V_s = 15 kV (e-f) V_s = 20 kV (g-h) V_s = 25 kV (i-j) V_s = 30 kV.

Figure 8.7 shows the influence of distance between the syringe and collector (process parameter) and polydispersity (PDI) (material parameter). It could be observed that as the distance between the syringe and collector were increased, the melt electrospun average fiber diameter also increased. The SEM images is displayed in Fig. 8.8. The increase of fiber diameter with distance could be explained by the fact that as we increased the distance the applied electrostatic force decreased which resulted in increasing the fiber diameter.

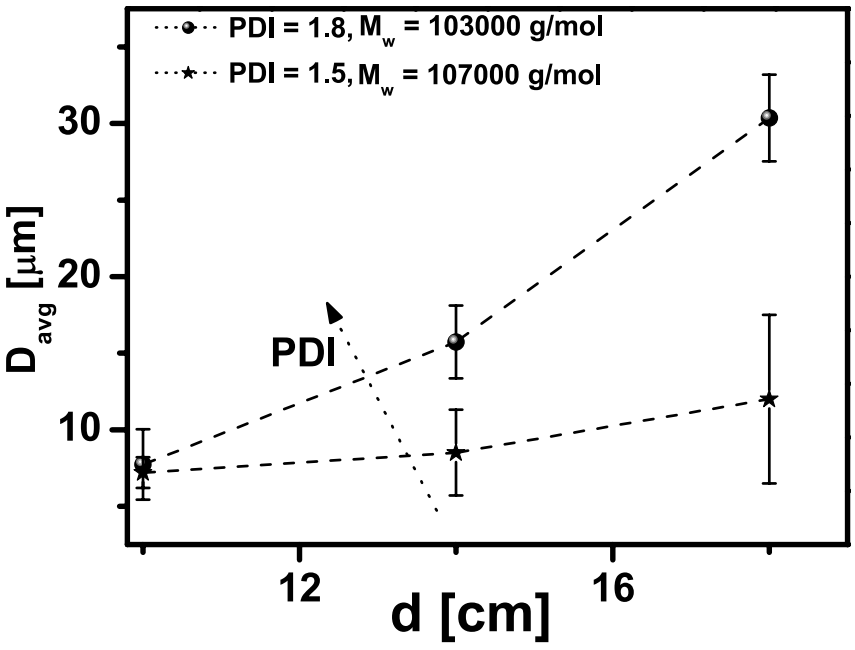

Figure 8.7: Influence of distance on the melt electrospun fibers of PCL.

Next, the blends of PCL-L-S (M_w = 40000 g/mol) and PCL-CAPA-6808 (M_w = 103000 g/mol) were melt electrospun. Using blending of PCL polymers, we were able to tune the zero shear viscosity, η_0, as can be seen by oscillatory shear rheology experiments. As the weight fraction of PCL-L-S (M_w = 40000 g/mol) was increased in the blends, the η_0 displayed the significant decrease. These blends provides ideal model system to study the effect of viscosity on fibers diameter.

Figure 8.9 shows the variation of average diameter of the melt electrospun fibers as a function of applied voltage and η_0 (by changing the weight fraction of PCL-L-S (M_w = 40000 g/mol) in the blends). It must be noticed that melt electrospinning, for blend, B_1, between 0 - 10 kV, for blend, B_2, between 10 - 15 kV, for blend, B_3, between 10-20 kV, and for blend, B_4, between 10-25 kV, did not work. The common voltage where melt electrospinning can be performed for all the

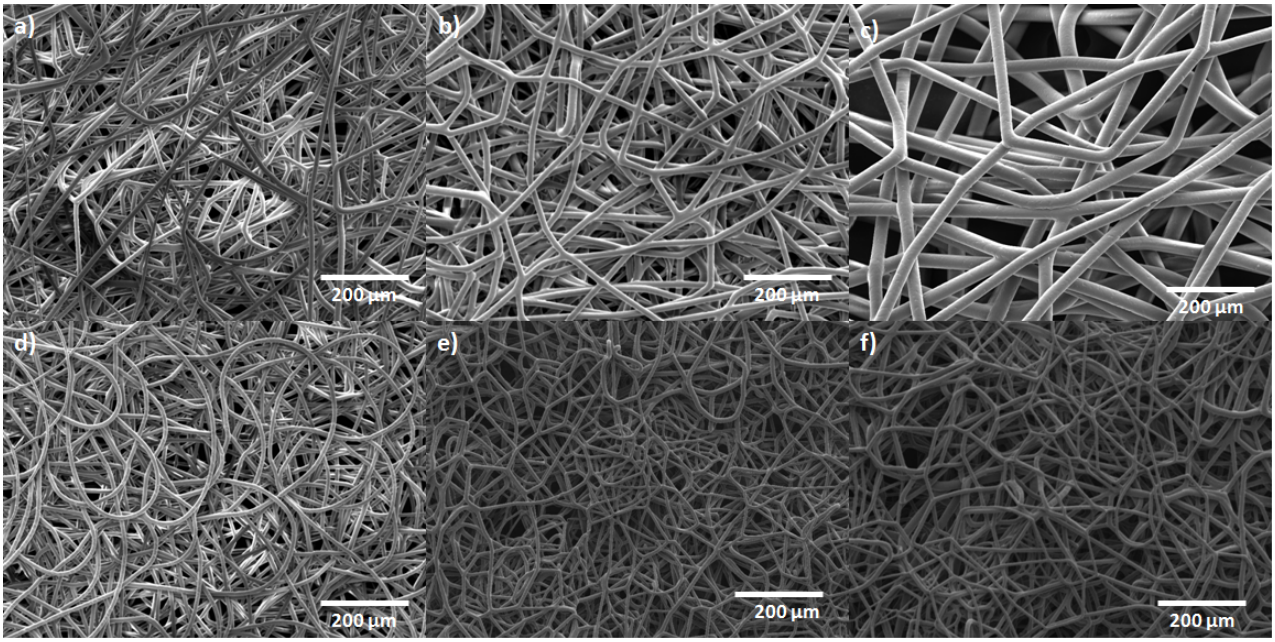

Figure 8.8: Influence of distance on melt electrospun fibers of PCL, (a) PCL(M_w=103000 g/mol, D=10 cm), (b) PCL(M_w=103000 g/mol, D=14 cm), (c) PCL(M_w=103000 g/mol, D=18 cm), (d) PCL(M_w=107000 g/mol, D=10 cm), (e) PCL(M_w=107000 g/mol, D=14 cm), (f) PCL(M_w=107000 g/mol, D=18 cm).

blends was 30 kV. The SEM images are displayed in Figure 8.10 for the blends obtained at 30 kV. D_{avg} measured for the blends obtained at 30kV displayed decreasing trend as a function of weight fraction of PCL-L-S (M_w = 40k), except for the case of 20 wt. % (B_4). The minimum average fiber diameter is observed for 12 wt. % (B_3).

In addition, the influence of collector temperature was also investigated for the first time. When increasing the collector temperature, failure of melt electrospun fibers is observed. Figure 8.11 shows the different kind of failure observed in our melt electrospinning. At 15 °C, rarely any kind of failure is observed but at the few instant we observed the failure (Fig. 8.11a). In this case, it appears that during the extension of the fiber in the electrostatic field, the Raleigh kind of instability originated and after deposition on collector due to crystallization fiber is exposed to extreme stretching which led to substantial reduction is aspect ratio of thinner fiber. However, when collector temperature is increased to 25 °C, transitional stage of failure as shown in Fig. 8.11b-c, along with the failure which were shown in Fig. 8.12b.

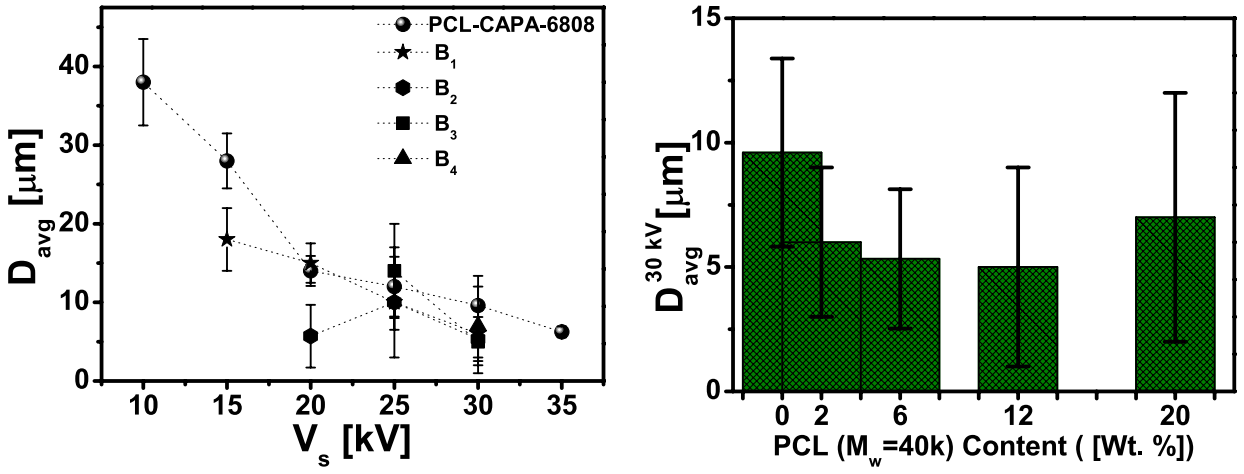

(a) (b)

Figure 8.9: Fiber diameter of blends as a function of applied voltage for the PCL blends, (a) average fiber diameter as a function of applied voltage and (b) average fiber diameter as a function of blends weight fraction at applied voltage of 30 kV.

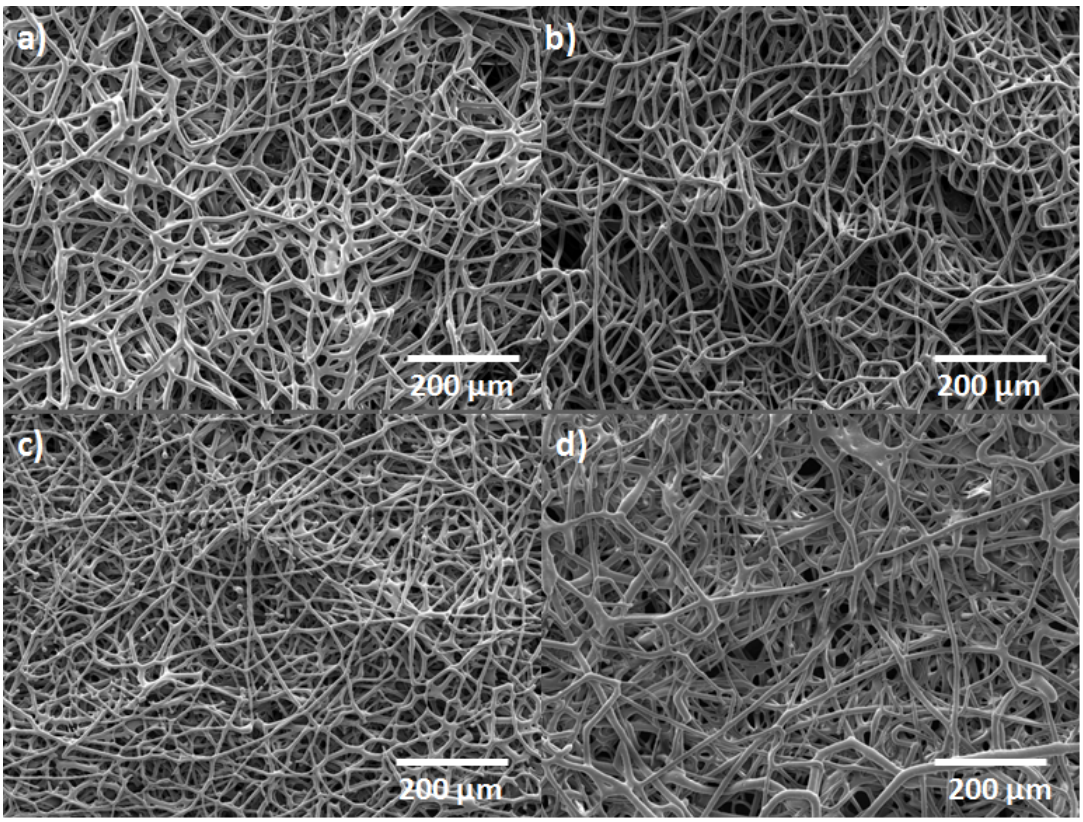

Figure 8.10: SEM image of blends at 30 kV, (a) 2 % weight fraction of PCL-L-S, (b) 6 % weight fraction of PCL-L-S, (c) 12 % weight fraction of PCL-L-S, (d) 2 % weight fraction of PCL-L-S.

For these experiments, the PCL with molecular weight, M_w = 103000 g/mol was chosen. The working distance was kept at 10 cm, applied voltage at 30 kV, flow rate of 0.05 ml/h and needle temperature of 110 °C. The obtained fibers is randomly deposited and no merging between the fibers is observed (Fig. 8.12a), when collector temperature is kept at 15 °C. However, on changing the collector temperature to 25 °C, the fibers displayed to merge in each other along with significant failure of fibers (Fig. 8.12b). As a result of these multiple failure, we were able to obtained a new kind of morphology.

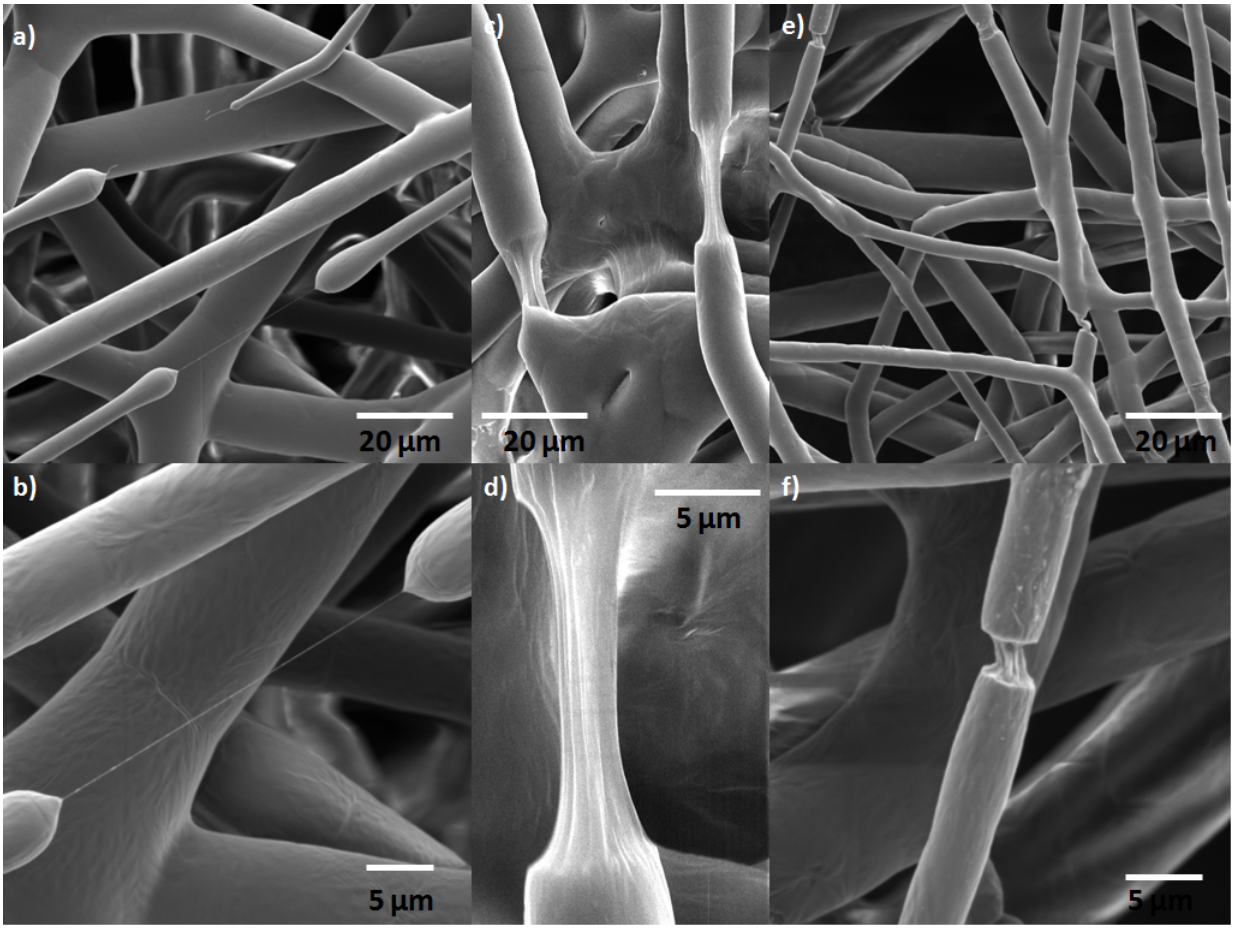

Figure 8.11: Failure mode in melt electrospun fibers [a-b] failure of fiber observed at 15 °C [c-d] failure of fibers (crazing) observed at 25 °C [e-f] failure of fibers (fracture) observed at 25 °C.

The mechanism of formation of this new morphology can be explained by the fact that at high temperature the fibers fuse together at multiple points. During the solidification of the deposited mats, few fibers gets broken, the load on the fiber must be transferred to its neighbouring fibers. Our observation was indicative of the fracture mode operative with increased fusion. The highly fused fibers creates stress concentration as individual fibers break and multi-axial tension leads to

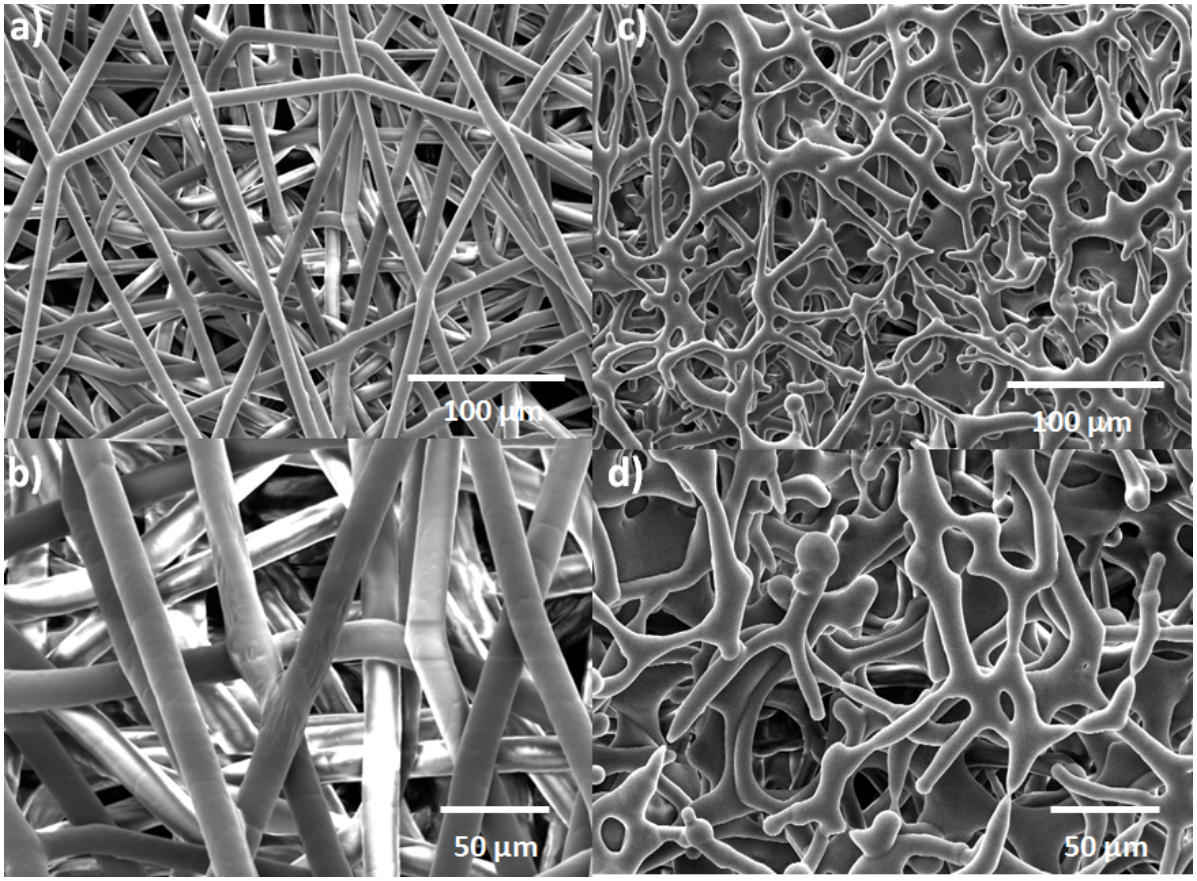

Figure 8.12: The influence on morphology of melt electrospun fiber as a function of applied collector temperature [a-b] uniform randomly collected temperature at a collector temperature of 15 °C [c-d] the new morphology obtained because of multiple failure of melt electrospun fibers at a collector temperature of 25 °C.

a catastrophic failure of the mats which results into new morphology.

8.3 Conclusion

Unique melt electrospinning equipment was developed and solvent free PCL scaffolds were fabricated. The influence of various process (applied voltage, working distance, and collector temperature) and material parameters (polydispersity and viscosity) were investigated. The applied voltage is found to have strong correlation with the fiber diameter. When increasing the applied voltage, the fiber diameter showed a decreasing trend. It is also concluded by experiments on PCL and its blends that alone viscosity reduction is not enough to reduce the fiber diameter. The minimum fiber average fiber diameter achieved using our set-up for PCL and blends was 5 μm

The influence of collector temperature was also investigated. When increasing the collector temperature, the merging of fibers with each other was observed resulting in the failure of the fibers during their final solidification. At intermediate temperature (25 C) of the collector, fiber failure appeared everywhere in the scaffold leading to the production of scaffold having a morphology with large open porosity. This new kind of morphology could open interesting applications for tissue engineering applications due to better cell infiltration.

Chapter 9

Summary and Outlook

This thesis focused on the characterization of polymer melts using shear and extensional rheology. The development of a novel self-assembling technique to fabricate hierarchical 3D cm-thick foams using electrospinning for tissue engineering applications. The research work presented in this thesis spans the spectrum from theory and modeling to experimental rheometry and the fabrication of scaffolds using solution and melt elecrospinning technology. The three questions motivating this thesis are: (i) how do we best describe the nonlinear viscoelasticity of polymer melts and polymer composites, (ii) how do we fabricate 3D cm-thick scaffolds using solution electrospinning and (iii) how do we fabricate solvent free scaffolds.

The first question was addressed by performing the experiments and simulations under the large deformation oscillatory shear and uniaxial extensional flow. Specifically, the large deformations oscillatory shear responses (shear stress and first normal stress difference) were analyzed using the FT-Rheology and Stress-Decomposition techniques. At first, to investigate the influence of entanglements on the stress response several linear monodisperse polystyrene (PS) melts were chosen. A new intrinsic nonlinear parameter, the zero shear-rate intrinsic nonlinearity, $\mu_0 = \lim_{\omega\to 0} Q_0/\omega^2$, was introduced using the FT-Rheology. In the linear viscoelastic regime, the zero shear-rate viscosity, η_0, displayed the following scaling, $\eta_0 \propto M_w^{3.4-3.6}$. However, in the non-linear viscoelastic regime the following scaling was displayed for the newly introduced parameter $\mu_0 \propto M_w^{8.85\pm0.15}$. Furthermore, polydispersity effects on linear and nonlinear viscoelastic properties were investigated under oscillatory shear flow. Blends of monodisperse PS are an ideal model system to investigate polydispersity effects because no other complexity is introduced to complicate the analysis. In the linear viscoelastic regime, the qualitative behaviour is similar to monodisperse PS melts. However, in nonlinear viscoelastic regime, the plot of $Q_0(\omega)$ as a function of ω shows two

distinct peaks corresponding to the two chain sizes in the binary blends. The intrinsic nonlinearity, $Q_0(\omega)$, was shown to be more sensitive for the characterization of blends and monodisperse PS relative to linear viscoelastic measurements in oscillatory shear flow.

The introduction of long-chain branching in linear polymers leads to a substantial improvement in the extensional and shear properties for industrial processing. To characterize the long-chain branching effects on rheological properties, linear and long-chain branched polyolefins blends were formulated. Based on linear and nonlinear viscoelastic properties measurements, a starlike topology with few branches for long-chain branched PP and a tree-like topology with a high degree of branching for long-chain branched PE were proposed. In the linear viscoelastic regime, the flow activation energy was calculated for the PP and PE blends. The differences in the evolution of flow activation energy with the fraction of long-chain branched polymer for the PP and PE blends were attributed to differences in the type of long-chain branching. In the nonlinear viscoelastic regime, the first normal stress response was measured using large amplitude oscillatory shear flow for PP and PE blends. The nonlinearity in the first normal stress measurements was quantified by the ratio of the fourth Fourier harmonic relative to the second Fourier harmonic, $N_{4/2}(\gamma_0, \omega)$. Motivated by the square scaling law, $N_{4/2} \propto \gamma_0^2$, a new intrinsic nonlinear parameter, $Q_0^{N_{4/2}}$, was introduced and used to characterize long-chain branching effects on PP and PE blends. The contrasting qualitative behaviour of $Q_0^{N_{4/2}}$ for PP and PE blends was attributed to differences in the type of long-chain branching. Furthermore, the stress response was also analyzed using the Stress-Decomposition technique. The following new parameters, the new intrinsic elastic nonlinearity, Q_0^e, and the intrinsic viscous nonlinearities, Q_0^v, were proposed. These new measures were more sensitive to long-chain branching than $Q_0^{3/1}$. The highest sensitivity was obtained by $Q_0^{5/1}$ for characterization of PP and PE blends. In the LAOS regime, the values for $e_{3/1}$ and $e_{5/1}$ at $\gamma_0 = 10$, and $\omega/2\pi = 0.1$ Hz showed the highest sensitivity to characterize the effect of addition of long-cain branched polymers in PP and PE blends. However, highest sensitivity was obtained using $Q_0^{5/1}$. Our hypothesis of the proposed structure is further confirmed by uniaxial extensional measurements. As in previous studies, decreasing strain hardening with increasing extensional rate is correlated with a small degree of branching for high molecular weight branches and an increasing trend with extensional rate is correlated with a high degree of branching for low molecular weight branches. In the end, characterization based on LAOS flow can be applied universally for linear polymers and polymers with small amounts of long-chain branching, but strain hardening factor (SHF) can only be determined for polymers with significant extensional hardening.

Polymer composites were prepared by dispersing single-walled carbon nanotubes (SWCNTs) and multi-walled carbon nanotubes (MWCNTs) in a PE matrix using a two step method to ensure homogeneous dispersion. The rheological properties [$G^{'}(\omega)$ and $Q_0(\omega)$] were significantly changed when the MWCNT weight fraction was increased from 1 wt.% to 3 wt.% in PE/MWCNTs composites. This substantial change in the rheological properties was attributed to the formation of percolation networks. The percolating network seemed to have alter results in the nonlinear viscoelastic regime compared to the linear viscoelastic regime. According to Palza et al.[2] observation for electrical conductivity, a minimum for $Q_0(\phi)$ was observed as we increased the weight fraction of MWCNTs (ϕ). This observation was explained through the higher stretching in the PE/MWCNTs composites due to interaction between the polymer-MWCNTs.

The second theme driving this thesis was the development of a scaffold for the tissue engineering applications. Using a single-step solution electrospinning, we were able to fabricate the hierarchical 3D cm-thick scaffolds of poly(ϵ-caprolactone) fibers. The self-organization strategy were exploited for the nanofibers which were deposited into honeycomb patterns. These patterns increase in size with deposition time, leading to increased porosity along with good physical and mechanical properties suitable for tissue engineering applications. In addition, we developed a melt electrospinning set-up for the fabrication of solvent free scaffolds. The influence of process and material parameters were investigated and the applied voltage on the needle was identified as the most important parameter to tailor the diameter of fibers. Furthermore, a new morphology were obtained, if the collector temperature is increased. The new morphology is result of the multiple failure of deposited melt electrospun fibers.

The work presented within this thesis introduces new concepts that have further possibilities. The newly introduced zero shear-rate intrinsic nonlinearity, μ_0, scaling with molecular weight were established for PS polymer melts system in limited range of molecular weight (M_w = 40-200 kg/mol). However, it would be interesting to calculate how the μ_0 scale with molecular weight for the different polymers in the unentangled and entangled regime, as well as what is the relationship with polydispersity and long-chain branching. Second, the new proposed material parameters based on the first normal stress measurements present new possibilities to investigate the behaviour of normal stress at large deformations and for characterization of the long-chain branching in industrial systems. As the experiments were conducted on industrial polymer melts which are inherently complex, the experiments on model systems could provide a new insight on the effect

of branching. Finally, the effects of network formation on the non-linear viscoelastic material parameter (zero strain intrinsic nonlinearity, Q_0) need to be further examined on the variety of polymer systems and also for different aspect ratios of carbon nanotubes.

The work based on the second theme of the thesis also presents many possibilities. At first, the fabricated hierarchical scaffold need to be tested for variety of tissue engineering applications. Furthermore, bio-functionalization of the scaffolds by protein adsorption or by the layer by layer (LbL) technique[247] could be envisaged to further promote cell adhesion and proliferation. At last, the melt electrospun scaffolds need to be tested for tissue engineering applications and a comparison with the performance of solution electrospun scaffolds would be next step forward.

Appendix A

Analytical Solution of MSF Model Under MAOS Flow

The shear stress can be expressed by power series as proposed by Pearson and Rochefort[275]:

$$\sigma_{xy}(t) = \gamma_0[G^{'}_{11}(\omega)\sin(\omega t) + G^{''}_{11}(\omega)\cos(\omega t)] + \gamma_0^3[G^{'}_{31}(\omega)\sin(\omega t) + G^{''}_{31}(\omega)\cos(\omega t) + G^{'}_{33}(\omega)\sin(3\omega t) + G^{''}_{33}(\omega)\cos(3\omega t)] + o(\gamma_0^5) \quad \text{(A.1)}$$

The analytical solution of MSF model proposed by Wagner et al.[71]:

$$G^{'}_{11}(\omega) = \sum_i g_i \frac{\omega^2\lambda_i^2}{1+\omega^2\lambda_i^2} \quad \text{(A.2)}$$

$$G^{''}_{11}(\omega) = \sum_i g_i \frac{\omega\lambda_i}{1+\omega^2\lambda_i^2} \quad \text{(A.3)}$$

$$G^{'}_{31}(\omega) = -\frac{3}{2}(\alpha-\beta)\left[2G^{'}_{11}(\omega) - \frac{1}{2}G^{'}_{11}(2\omega)\right] \quad \text{(A.4)}$$

$$G^{''}_{33}(\omega) = \frac{3}{4}(\alpha-\beta)\left[G^{'}_{11}(\omega) - G^{'}_{11}(2\omega) + \frac{1}{3}G^{'}_{11}(3\omega)\right] \quad \text{(A.5)}$$

$$G^{''}_{31}(\omega) = -\frac{3}{2}(\alpha-\beta)\left[G^{''}_{11}(\omega) - \frac{1}{2}G^{''}_{11}(2\omega)\right] \quad \text{(A.6)}$$

$$G^{''}_{33}(\omega) = \frac{3}{4}(\alpha-\beta)\left[G^{''}_{11}(\omega) - G^{''}_{11}(2\omega) + \frac{1}{3}G^{'}_{11}(3\omega)\right] \quad \text{(A.7)}$$

Appendix B

Analysis of PP and PE Blends Using Steady Shear and Lissajous-Bowditch Curves

In the chapter 5, the PP and PE blends were investigated under oscillatory shear and extensional flows. Here, steady shear rheology experimental results are presented and further analysis of oscillatory shear data are performed using a Lissajous-Bowditch curves.

B.1 Validity of Cox-Merz and Laun Rule for the PP and PE blends

The Cox-Merz rule[276] and Laun's rule[277] are two empirical relations that allow for an estimation of the steady state viscosity and first normal stress difference, respectively, using small amplitude oscillatory shear measurements. The validity of the Cox-Merz rule and Laun's rule implies that it is possible to predict a nonlinear viscoelastic property from measurements in the linear viscoelastic regime. The Cox-Merz rule has been validated experimentally for several polymeric materials[4,278]. However, deviations from this rule was also observed by Venkatraman et al.[279] for HDPEs. The Cox-Merz rule states that the modulus of the complex dynamic viscosity, $|\eta^*(\omega)|$, a linear viscoelastic material property, is equal to the steady shear viscosity $\eta(\dot{\gamma})$, a non-linear viscoelastic material property when $\omega = \dot{\gamma}$ for arbitrary shear rates/frequencies.

$$|\eta^*(\omega)|_{\omega=\dot{\gamma}} \equiv \eta(\dot{\gamma}) \tag{B.1}$$

The Laun rule states that the first normal stress difference $N_1(\dot{\gamma})$ measured using steady shear flow, which is a nonlinear viscoelastic property, can be calculated from the storage modulus

($G^{'}(\omega)$) and loss modulus ($G^{''}(\omega)$), which are linear viscoelastic properties, from the following empirical rule.

$$N_1(\dot{\gamma})|_{\omega=\dot{\gamma}} \equiv 2G^{'}(\omega)\left\{1+\left(\frac{G^{'}(\omega)}{G^{''}(\omega)}\right)^2\right\}^{0.7} \tag{B.2}$$

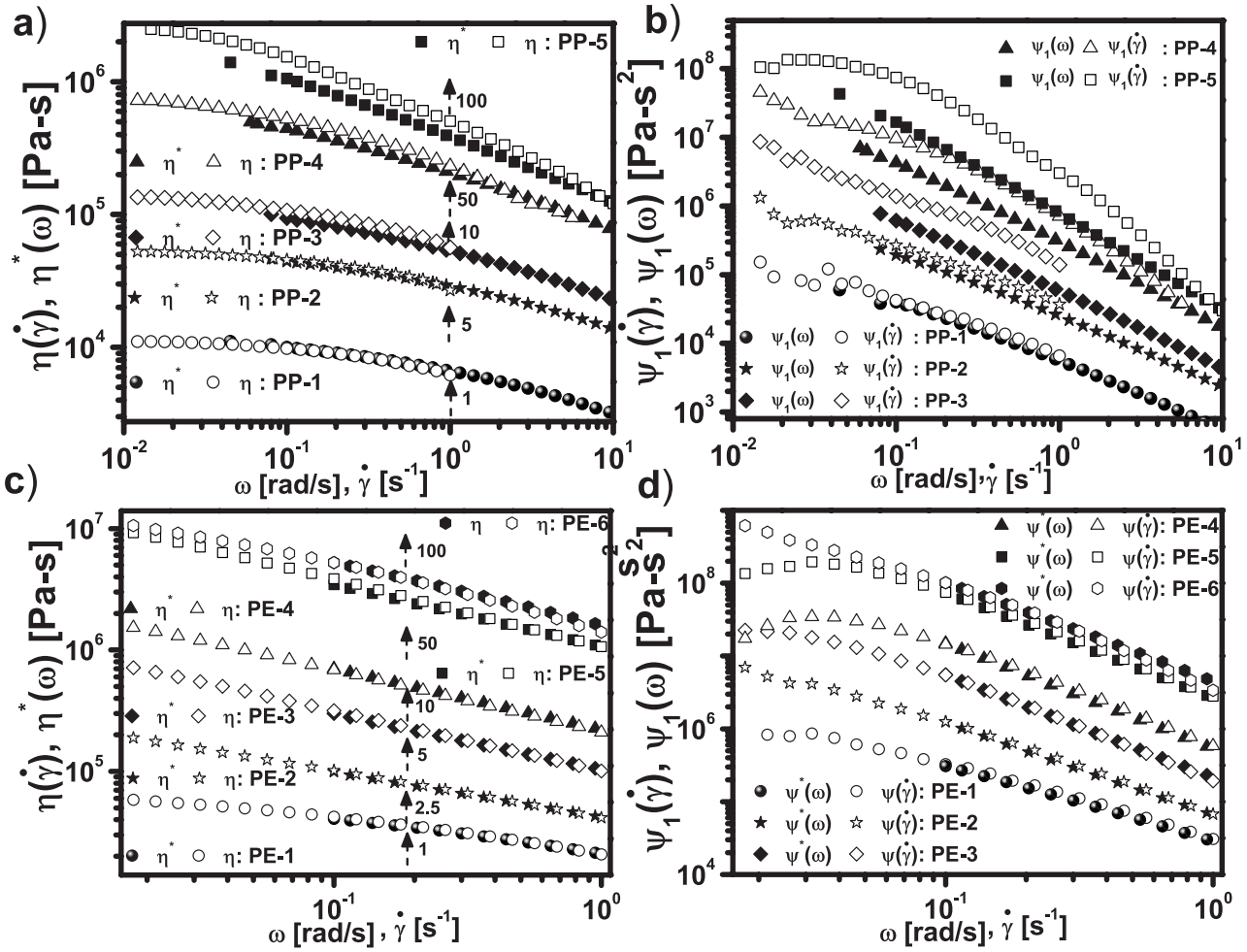

Figure B.1: Validity of the Cox-Merz and Laun rules for blends of linear and branched polypropylene, and linear and branched polyethylene (a) The Cox-Merz rule validity for PP-blends (b) The Laun rule validity for PP-blends (c) The Cox-Merz rule validity for PE-blends (d) Laun rule validity for PE-blends.

Figure B.1a shows the complex viscosity $|\eta^*|$, which is measured at small deformations in oscillatory shear, and the steady state viscosity $\eta(\dot{\gamma})$, which is measured in steady shear for PP-blends at 190°C. The vertical arrow represents the shift in vertical direction and number represents the

factor by which the curves were shifted vertically. The curves were shifted vertically for clarity. The ratio $|\eta^*|/\eta(\dot{\gamma})$ was close to one for the case of linear PP (PP-1), indicating the validity of Cox-Merz rule. In contrast, the LCB PP (PP-5) and blends were deviates from the Cox-Merz rule. Similarly, B.1b shows the normal stress difference coefficient $\psi(\dot{\gamma})$, which was measured in steady shear, and estimated $\psi(\dot{\gamma})$ from Laun's empirical rule. The ratio $|\psi^*(\omega)|/\psi(\dot{\gamma})$ was close to one for the case of linear PP (PP-1), indicating the validity of Laun rule. In contrast, the LCB PP (PP-5) and blends were deviates from the Laun rule. In case of LCB PP (PP-5) and blends, the ratios [$|\eta^*|/\eta(\dot{\gamma})$, $|\psi^*(\omega)|/\psi(\dot{\gamma})$] were smaller then one and it could be observed for the LCB PP (PP-5) and blend (PP-4) that as the shear rate was increased the ratio is approaching one. Figure B.1c-d show the ratios $|\eta^*|/\eta(\dot{\gamma})$ and $|\psi^*(\omega)|/\psi(\dot{\gamma})$ for PE-blends. For the PE-blends, these ratios are always approximately equal to 1, which confirmed the validity of both the Cox-Merz rule and Laun's rule for these systems.

B.2 Lissajous-Bowditch Curves

Lissajous-Bowditch curves are 2-D projections of the 3-D complex stress response onto the strain-stress and strain-rate-stress planes which helps in analyzing the stress response from both elastic and viscous perspective. In polymer melt rheology, experimentally these curves were used to confirm the absence of LCB through the presence of secondary loops in the 2-D projection onto the $\sigma(t)$-$\dot{\gamma}(t)$ plane[280]. Figure B.2 illustrates the 3-D complex stress response onto the strain-stress and strain-rate-stress planes as a function of applied deformation amplitudes γ_0, and branching parameter q in Pom-Pom model. Along with the stress projections in both planes (strain-stress and strain-rate-stress), the decomposed elastic and viscous stresses obtained by Chebyshev polynomials analysis were also displayed. At $\gamma_0 = 1$, it was seen from both 2-D projections that the shape of the curves were elliptical which are the expected response in the linear regime. But as seen in Figure 5.3 and Figure 5.4, the higher harmonics were observed in the range $\gamma_0 = 0.01 - 1$. This is the one of the disadvantage of using the Lissajous-Bowditch curves where it is hard to differentiate between the SAOS and MAOS response (detection and quantification of higher harmonic below $I_{3/1} \ll 0.03$ is difficult to characterize). At $\gamma_0 = 2$, or above this deformation, distortion from the elliptical shapes were observed in both the elastic and viscous representation which belongs to the similar deformation range where deviations in the scaling of the relative third higher harmonics of Fourier and Chebyshev polynomials coefficients occurs. The degree of branching q increase reduced the distortion in the response which means the nonlinearity was suppressed with higher

branching.

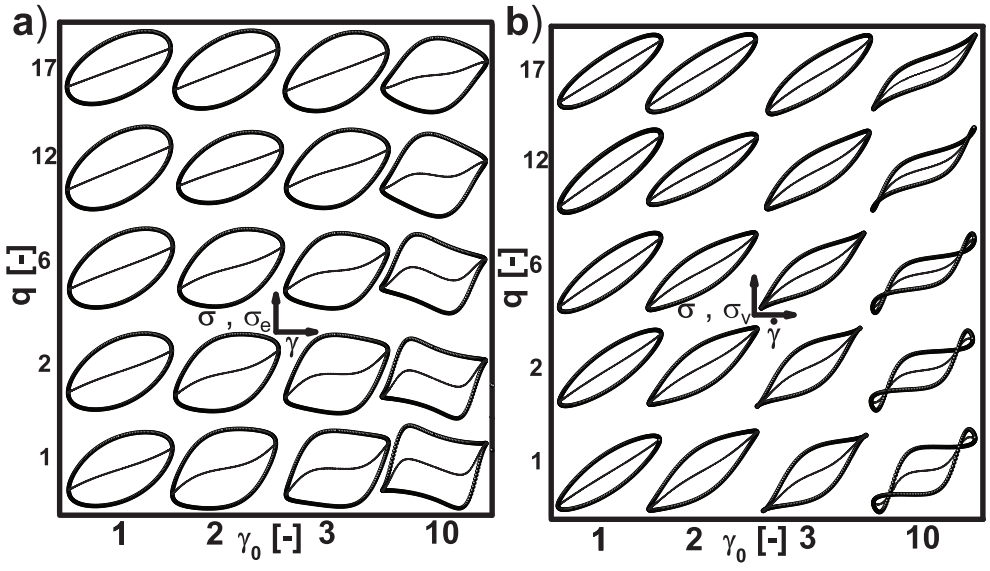

Figure B.2: Results for LAOS simulations using the Pom-Pom Model with parameters $G_n = 10^5$ Pa, $S_b = 10$, $S_a = 4$, $\tau_b = 1$ sec, and q = 1, 2, 6, 12, 17 for (a) elastic Lissajous-Bowditch curves (b) viscous Lissajous-Bowditch curves.

Interestingly at $\gamma_0 = 3$, for the lower degree of branching ($q = 1, 2$ and 6) the elastic stress (σ_e) is zero for the range of applied instantaneous strain (B.2a). However, at higher q (12 and 17) the elastic stress is zero only when the instantaneous strain is zero. The similar phenomenon can be seen in B.2b, at the corresponding shear-rate the pure viscous response were observed for $q = 1, 2, 6$. Recently, using a Chebyshev framework, a general condition was derived for the appearance of secondary loops in the $\sigma(\dot{\gamma}_0)$ plane projection as well as in the $\sigma(\gamma_0)$ plane projection of the total stress[281]. Here, we confirm that the presence of these secondary loops is correlated with the condition that $e_{3/1} > 1/3$. It was also realized that while branching delays the appearance of secondary loops, its absence at one fixed deformation cannot be used as proof of LCB in the system as discussed by Stadler et al.[280]

Figure B.3a shows the elastic Lissajous-Bowditch curves for different applied deformations, γ_0, and LCB content for PP-blends. An elliptical response at $\gamma_0 = 0.1$ was seen for all the PP-blends. However, as the applied deformation was increased, a gradual distortion in the total as well as the elastic stresses was seen. At deformations between $\gamma_0 = 5 - 10$, the elastic stress appeared to be zero over a large range of applied instantaneous deformations which as discussed

in the results for the single mode Pom-Pom model simulations is a necessary condition for the presence of secondary loops. This particular range where the elastic stress were zero, reduces as the LCB content increases is characteristic for these systems. Figure B.3b shows the viscous Lissajous-Bowditch curves at different applied deformations γ_0, and LCB content for PP-blends. At a small deformation of $\gamma_0 = 0.1$, the response was elliptical and afterwards there was a gradual distortion in the signal until a deformation of $\gamma_0 = 5$ was reached where, for PP-1, PP-2 and PP-3, there was a region where the total stress was independent of the instantaneous deformation. At $\gamma_0 = 10$ strain, secondary loops were present for PP-1 and, for PP-2 and PP-3 the range for the instantaneous strain-rate were increased where the total stress was independent of the instantaneous deformations, and for PP-4 and PP-5 this region gets disappeared.

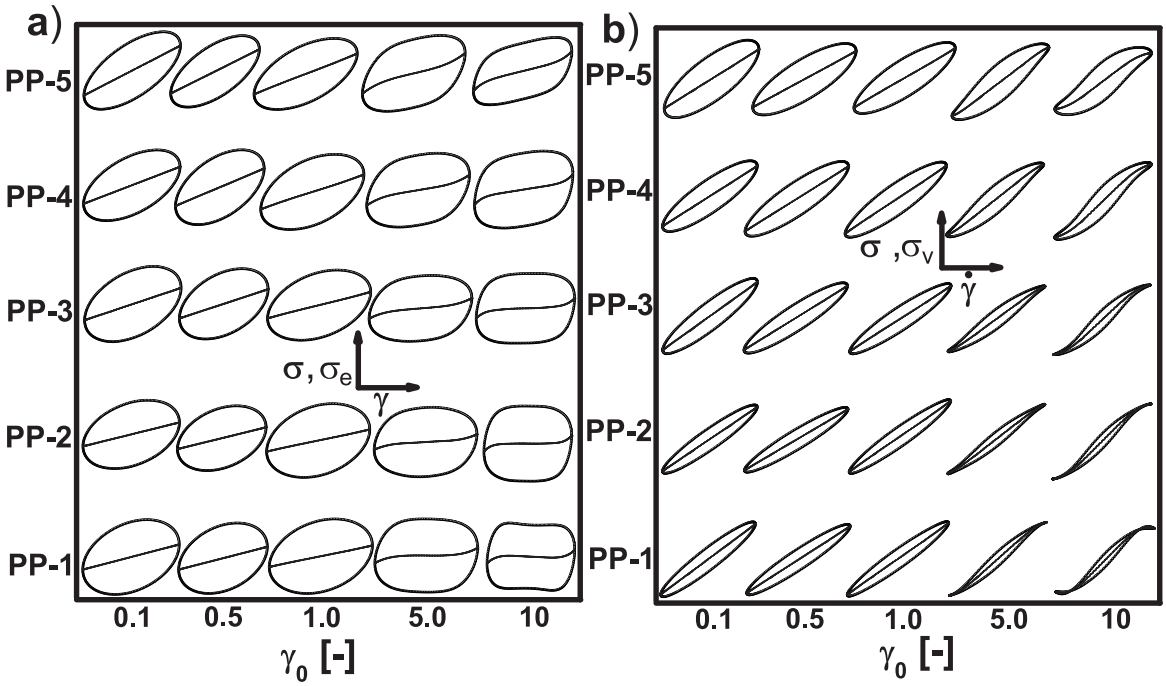

Figure B.3: Lissajous-Bowditch curves along with elastic and viscous stress as a function of applied deformation for PP-blends (a) elastic Lissajous-Bowditch curves (b) viscous Lissajous-Bowditch curves.

Figure B.4a shows the elastic Lissajous-Bowditch curves at different applied deformations γ_0, and LCB content for PE-blends. Similar to the PP-blends at small deformations, elliptical responses were observed. In addition, at $\gamma_0 = 10$, the elastic stress appeared to be zero over a very large range of instantaneous deformations and the size of this range decreased with increasing LCB content. Figure B.4b shows the viscous Lissajous-Bowditch curves at different applied de-

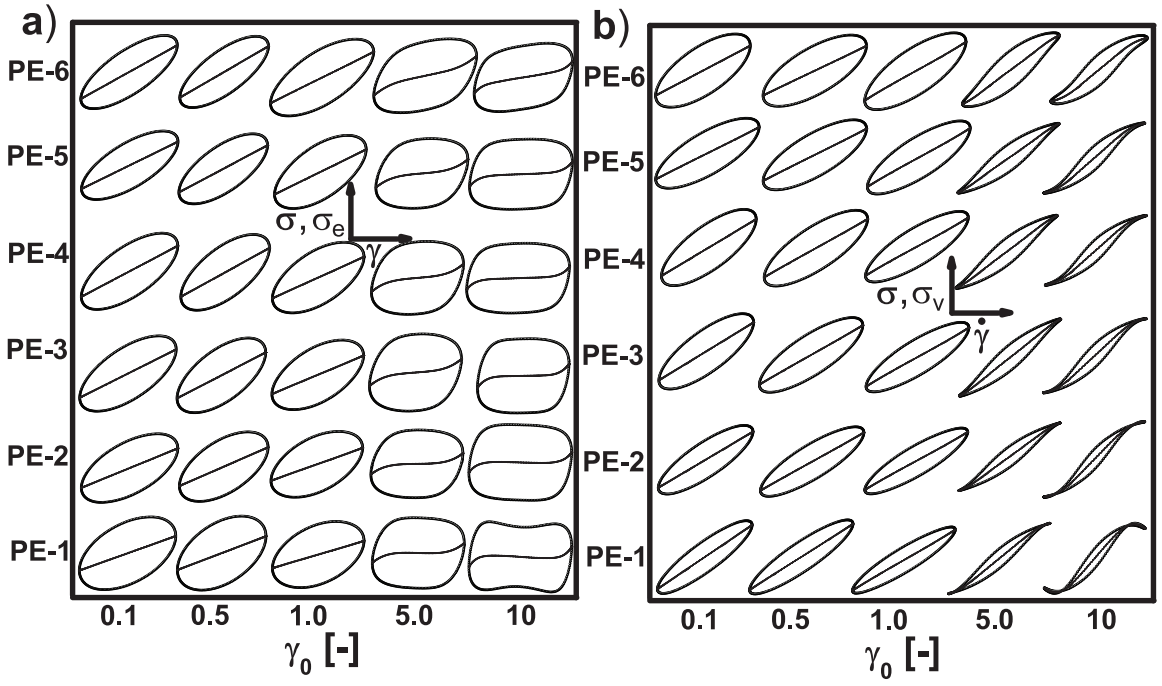

Figure B.4: Lissajous-Bowditch curves along with elastic and viscous stress as a function of applied deformation for PE-blends (a) elastic Lissajous-Bowditch curves (b) viscous Lissajous-Bowditch curves.

formations γ_0, and LCB content for PE-blends. Here as well, at small deformation around 10%, elliptical responses were seen, while at high deformations (γ_0 = 10), secondary loops were present in the curves for PE-1 and PE-2 and a pure viscous response seen for PE-3, PE-4 and PE-5. It is important to note here that secondary loops were seen for PE-2 which contains 10% of LCB and that this result is in direct contradiction with previous conclusion regarding secondary loops[280]. According to previous work, even a small amount of LCB helps in disappearing the secondary loops and secondary loops is the only signature of linear topological molecules. Our observation are in well agreement with the simulation which were performed using single Pom-Pom model where we observed the condition before appearances of secondary loops and appearance of secondary loops even for molecules where more elasticity is present. We concluded from this discussion that indeed LCB helps in disappearance of secondary loops when investigated at same deformation but appearance of secondary loops is no fingerprint of linear topology in LAOS.

Bibliography

1. http://www.purdue.edu/rem/rs/sem.htm, 2013.

2. Palza, H.; Kappes, M.; Hennrich, F.; Wilhelm, M. *Compos. Sci. Technol.* **2011**, *71*, 1361 – 1366.

3. A report by Plastic Europe 2013: Plastics - Champions of sustainble growth and innovation in Europe.

4. Dealy, J. M.; Larson, R. G. *Structure and Rheology of Molten Polymers: From Structure To Flow Behavior and Back Again*; Hanser Publishers, 2006.

5. Koo, J. *Polymer Nanocomposites : Processing, Characterization, And Applications: Processing, Characterization, And Applications*; Mcgraw-hill, 2006.

6. Tobita, H.; Saito, S. *Macromol. Theor. Simul.* **1999**, *8*, 513–519.

7. Hubner, G.; Fonseca, I.; Parkinson, M. *NMR Spectroscopy of Polymers: Innovative Strategies for Complex Macromolecules*; Chapter 26, pp 401–415.

8. Klimke, K.; Parkinson, M.; Piel, C.; Kaminsky, W.; Spiess, H. W.; Wilhelm, M. *Macromol. Chem. Phys.* **2006**, *207*, 382–395.

9. Macosko, C. *Rheology: Principles, Measurements, and Applications*; Advances in interfacial engineering series; VCH, 1994.

10. Gahleitner, M. *Prog. Poly. Sci.* **2001**, *26*, 895 – 944.

11. Dealy, J.; Wissbrun, K. *Melt Rheology and its Role in Plastics Processing: Theory and Applications*; Fluid Mechanics and its Applications Series; Springer, 1990.

12. Reneker, D. H.; Chun, I. *Nanotechnology* **1996**, *7*, 216–223.

13. Li, D.; Xia, Y. *Adv. Mater.* **2004**, *16*, 1151–1170.

14. Greiner, A.; Wendorff, J. *Angew. Chem. Int. Ed.* **2007**, *46*, 5670–5703.

15. Bose, G. M. *Recherches sur la cause et sur la véritable théorie de l'électricité,*; Wittenberg, 1745.

16. Rayleigh, L. *Philos. Mag.* **1882**, *14*, 184–186.

17. Morton, W. J. Patent US 705691, 1902.

18. Formhals, A. Patent US 1,975,504, 1934.

19. Larrondo, L.; St. John Manley, R. *J. Polym. Sci., Part B: Polym. Phys.* **1981**, *19*, 933–940.

20. Doshi, J.; Reneker, D. H. *J. Electrostatics* **1995**, *35*, 151 – 160.

21. Filatov, Y.; Budyka, A.; Kiričenko, V. *Electrospinning of Micro-and Nanofibers: Fundamentals and Applications in Separation and Filtration Processes*; Begell digital library; Begell House Publishers, Incorporated, 2007.

22. Agarwal, S.; Wendorff, J. H.; Greiner, A. *Adv. Mater.* **2009**, *21*, 3343–3351.

23. Liu, W.; Thomopoulos, S.; Xia, Y. *Adv. Healthcare Mater.* **2012**, *1*, 10–25.

24. Yang, D.; Niu, X.; Liu, Y.; Wang, Y.; Gu, X.; Song, L.; Zhao, R.; Ma, L.; Shao, Y.; Jiang, X. *Adv. Mater.* **2008**, *20*, 4770–4775.

25. Onozuka, K.; Ding, B.; Tsuge, Y.; Naka, T.; Yamazaki, M.; Sugi, S.; Ohno, S.; Yoshikawa, M.; Shiratori, S. *Nanotechnology* **2006**, *17*, 1026–1032.

26. Formo, E.; Lee, E.; Campbell, D.; Xia, Y. *Nano Lett.* **2008**, *8*, 668–672.

27. Liu, J.; Yue, Z.; Fong, H. *Small* **2009**, *5*, 536–542.

28. Di Benedetto, F.; Camposeo, A.; Pagliara, S.; Mele, E.; Persano, L.; Stabile, R.; Cingolani, R.; Pisignano, D. *Nat. Nanotech.* **2008**, *3*, 614–619.

29. Hagewood, J.; Wilkie, A. *Nonwovens World* **2003**, 69–73.

30. Barnes, H.; Hutton, J.; Walters, K. *An Introduction to Rheology*; Annals of Discrete Mathematics; Elsevier, 1989.

31. Skoog, D. *Principles of instrumental analysis*; Saunders golden sunburst series; Saunders College Pub., 1985.

32. Sommer, C.; Muller, G. *J. Liq. Chromatogr. Related Technol.* **2001**, *24*, 1047–1060.

33. DesLauriers, P. J.; Rohlfing, D. C.; Hsieh, E. T. *Polymer* **2002**, *43*, 159 – 170.

34. Striegel, A. M.; Krejsa, M. R. *J. Polym. Sci., Part B: Polym. Phys.* **2000**, *38*, 3120–3135.

35. Agarwal, P. K.; Somani, R. H.; Weng, W.; Mehta, A.; Yang, L.; Ran, S.; Liu, L.; Hsiao, B. S. *Macromolecules* **2003**, *36*, 5226–5235.

36. Yu, Y.; DesLauriers, P. J.; Rohlfing, D. C. *Polymer* **2005**, *46*, 5165 – 5182.

37. Egerton, R. *Physical Principles of Electron Microscopy: An Introduction to TEM, SEM, and AEM*; Springer, 2005.

38. Doi, M.; S. F. Edwards, M. *The Theory of Polymer Dynamics*; The International Series of Monographs on Physics Series; Clarendon Press, 1988.

39. Hansen, D. R.; Williams, M. C.; Shen, M. *Macromolecules* **1976**, *9*, 345–354.

40. Edwards, S. F. *Proc. Phys. Soc.* **1967**, *92*, 9.

41. de Gennes, P. G. *J. Chem. Phys.* **1971**, *55*, 572–579.

42. McLeish, T. C. B. *Adv. Phys.* **2002**, *51*, 1379–1527.

43. Likhtman, A. E.; McLeish, T. C. B. *Macromolecules* **2002**, *35*, 6332–6343.

44. http://www.reptate.com/,.

45. Giesekus, H. *J. Non-Newton Fluid* **1982**, *11*, 69 – 109.

46. Larson, R. *Constitutive Equations for Polymer Melts and Solutions*; Butterworths Series in Chemical Engineering; Elsevier Science & Technology Books, 1988.

47. Marrucci, G. *J. Non-Newton Fluid* **1996**, *62*, 279 – 289.

48. Larson, R. *The Structure and Rheology of Complex Fluids*; Topics in Chemical Engineering Series; Oxford University Press, 1999.

49. Wagner, M. H.; Yamaguchi, M.; Takahashi, M. *J. Rheol.* **2003**, *47*, 779–793.

50. Wagner, M. H.; Hepperle, J.; Münstedt, H. *J. Rheol.* **2004**, *48*, 489–503.

51. Wagner, M. H.; Rolon-Garrido, V. H.; Nielsen, J. K.; Rasmussen, H. K.; Hassager, O. *J. Rheol.* **2008**, *52*, 67–86.

52. McLeish, T. C. B.; Larson, R. G. *J. Rheol.* **1998**, *42*, 81–110.

53. Blackwell, R. J.; McLeish, T. C. B.; Harlen, O. G. *J. Rheol.* **2000**, *44*, 121–136.

54. Lee, K.; Mackley, M. R.; McLeish, T. C. B.; Nicholson, T. M.; Harlen, O. G. *J. Rheol.* **2001**, *45*, 1261–1277.

55. Hyun, K.; Wilhelm, M.; Klein, C. O.; Cho, K. S.; Nam, J. G.; Ahn, K. H.; Lee, S. J.; Ewoldt, R. H.; McKinley, G. H. *Prog. Polym. Sci.* **2011**, *36*, 1697 – 1753.

56. Ewoldt, R. H.; Clasen, C.; Hosoi, A. E.; McKinley, G. H. *Soft Matter* **2007**, *3*, 634–643.

57. Wilhelm, M.; Reinheimer, K.; Kübel, J. *Z. Phys. Chem.* **2012**, *226*, 547–567.

58. Reinheimer, K.; Grosso, M.; Hetzel, F.; Kübel, J.; Wilhelm, M. *J. Colloid Interf. Sci.* **2012**, *380*, 201 – 212.

59. Wilhelm, M.; Maring, D.; Spiess, H. *Rheol. Acta* **1998**, *37*, 399–405.

60. Wilhelm, M.; Reinheimer, P.; Ortseifer, M. *Rheol. Acta* **1999**, *38*, 349–356.

61. Wilhelm, M.; Reinheimer, P.; Ortseifer, M.; Neidhofer, T.; Spiess, H. . *Rheol. Acta* **2000**, *39*, 241–246.

62. Wilhelm, M. *Macromol. Mater. Eng.* **2002**, *287*, 83–105.

63. Klein, C. O.; Spiess, H. W.; Calin, A.; Balan, C.; Wilhelm, M. *Macromolecules* **2007**, *40*, 4250–4259.

64. Cho, K. S.; Hyun, K.; Ahn, K. H.; Lee, S. J. *J. Rheol.* **2005**, *49*, 747–758.

65. Ewoldt, R. H.; Hosoi, A. E.; McKinley, G. H. *J. Rheol.* **2008**, *52*, 1427–1458.

66. Yu, W.; Wang, P.; Zhou, C. *J. Rheol.* **2009**, *53*, 215–238.

67. Cho, K. S.; Song, K.-W.; Chang, G.-S. *J. Rheol.* **2010**, *54*, 27–63.

68. Rogers, S. A.; Erwin, B. M.; Vlassopoulos, D.; Cloitre, M. *J. Rheol.* **2011**, *55*, 435–458.

69. Hyun, K.; Baik, E. S.; Ahn, K. H.; Lee, S. J.; Sugimoto, M.; Koyama, K. *J. Rheol.* **2007**, *51*, 1319–1342.

70. Gurnon, A. K.; Wagner, N. J. *J. Rheol.* **2012**, *56*, 333–351.

71. Wagner, M. H.; Rolon-Garrido, V. H.; Hyun, K.; Wilhelm, M. *J. Rheol.* **2011**, *55*, 495–516.

72. Hyun, K.; Kim, W.; Park, S. J.; Wilhelm, M. *J. Rheol.* **2013**, *57*, 1–25.

73. Hyun, K.; Wilhelm, M. *Macromolecules* **2009**, *42*, 411–422.

74. Reinheimer, K.; Grosso, M.; Wilhelm, M. *J. Colloid Interf. Sci.* **2011**, *360*, 818 – 825.

75. Kempf, M.; Ahirwal, D.; Cziep, M.; Wilhelm, M. *Macromolecules* **2013**, *46*, 4978–4994.

76. Vittorias, I.; Lilge, D.; Baroso, V.; Wilhelm, M. *Rheol. Acta* **2011**, *50*, 691–700.

77. Hyun, K.; Kim, W. *Korea-Australia Rheol. J.* **2011**, *23*, 227–235.

78. Pearson, D. S.; Rochefort, W. E. *J. Polym. Sci., Part B: Polym. Phys.* **1982**, *20*, 83–98.

79. Nam, J. G.; Ahn, K. H.; Lee, S. J.; Hyun, K. *J. Rheol.* **2010**, *54*, 1243–1266.

80. Nam, J. G.; Hyun, K.; Ahn, K. H.; Lee, S. J. *J. Non-Newton Fluid* **2008**, *150*, 1 – 10.

81. Ferry, J. *Viscoelastic Properties of Polymers*; Wiley, 1980.

82. Ganeriwala, S. N.; Rotz, C. A. *Polym. Eng. Sci.* **1987**, *27*, 165–178.

83. Ewoldt, R.; Bharadwaj, N. *Rheol. Acta* **2013**, *52*, 201–219.

84. Watanabe, H.; Kotaka, T. *Macromolecules* **1984**, *17*, 2316–2325.

85. Watanabe, H.; Sakamoto, T.; Kotaka, T. *Macromolecules* **1985**, *18*, 1436–1442.

86. Struglinski, M. J.; Graessley, W. W. *Macromolecules* **1985**, *18*, 2630–2643.

87. Tsenoglou, C. *Macromolecules* **1991**, *24*, 1762–1767.

88. Colby, R. H.; Rubinstein, M. *Macromolecules* **1990**, *23*, 2753–2757.

89. Janzen, J.; Colby, R. *J. Mol. Struct.* **1999**, *485 - 486*, 569 – 584.

90. Shroff, R. N.; Mavridis, H. *Macromolecules* **1999**, *32*, 8454–8464.

91. Vega, J. F.; Santamaría, A.; Muñoz Escalona, A.; Lafuente, P. *Macromolecules* **1998**, *31*, 3639–3647.

92. Gabriel, C.; Kokko, E.; Löfgren, B.; Seppälä, J.; Münstedt, H. *Polymer* **2002**, *43*, 6383 – 6390.

93. Crosby, B. J.; Mangnus, M.; de Groot, W.; Daniels, R.; McLeish, T. C. B. *J. Rheol.* **2002**, *46*, 401–426.

94. Likhtman, A. E.; Milner, S. T.; McLeish, T. C. B. *Phys. Rev. Lett.* **2000**, *85*, 4550–4553.

95. Larson, R. G. *Macromolecules* **2001**, *34*, 4556–4571.

96. Wagner, M. H.; Rubio, P.; Bastian, H. *J. Rheol.* **2001**, *45*, 1387–1412.

97. Larson, R. G. *Science* **2011**, *333*, 1834–1835.

98. Read, D. J.; Auhl, D.; Das, C.; den Doelder, J.; Kapnistos, M.; Vittorias, I.; McLeish, T. C. B. *Science* **2011**, *333*, 1871–1874.

99. Wood-Adams, P. M.; Dealy, J. M.; deGroot, A. W.; Redwine, O. D. *Macromolecules* **200**, *33*, 7489–7499.

100. He, C.; Wood-Adams, P.; Dealy, J. M. *J. Rheol.* **2004**, *48*, 711–724.

101. Lai, S.; Plumley, T. A.; Butler, T. I.; Knight, G. W.; Kao, C. I. *SPE Antec Technol. Papers* **1994**, *40*, 1814–1815.

102. Trinkle, S.; Friedrich, C. *Rheol. Acta* **2001**, *40*, 322–328.

103. Trinkle, S.; Walter, P.; Friedrich, C. *Rheol. Acta* **2002**, *41*, 103–113.

104. Kessner, U.; Kaschta, J.; Münstedt, H. *J. Rheol.* **2009**, *53*, 1001–1016.

105. Kessner, U.; Kaschta, J.; Stadler, F. J.; Le Duff, C. S.; Drooghaag, X.; Münstedt, H. *Macromolecules* **2010**, *43*, 7341–7350.

106. Wasserman, S. H.; Graessley, W. W. *Polym. Eng. Sci.* **1996**, *36*, 852–861.

107. Auhl, D.; Stadler, F. J.; Münstedt, H. *Macromolecules* **2012**, *45*, 2057–2065.

108. Rogers, S. A.; Lettinga, M. P. *J. Rheol.* **2012**, *56*, 1–25.

109. Schlatter, G.; Fleury, G.; Muller, R. *Macromolecules* **2005**, *38*, 6492–6503.

110. Vittorias, I.; Wilhelm, M. *Macromol. Mater. Eng.* **2007**, *292*, 935–948.

111. Filipe, S.; Klimke, K.; Tran, A. T.; Reussner, J. *AIP Conf. Proc.* **2011**, *1375*, 114–126.

112. Eckstein, A.; Friedrich, C.; Lobbrecht, A.; Spitz, R.; Mülhaupt, R. *Acta Polym.* **1997**, *48*, 41–46.

113. Gabriel, C.; Münstedt, H. *J. Rheol.* **2003**, *47*, 619–630.

114. Auhl, D.; Stange, J.; Münstedt, H.; Krause, B.; Voigt, D.; Lederer, A.; Lappan, U.; Lunkwitz, K. *Macromolecules* **2004**, *37*, 9465–9472.

115. Rolón-Garrido, V.; Wagner, M. *Rheol. Acta* **2007**, *46*, 583–593.

116. Stadler, F. J.; Kaschta, J.; Münstedt, H. *Macromolecules* **2008**, *41*, 1328–1333.

117. Wood-Adams, P.; Costeux, S. *Macromolecules* **2001**, *34*, 6281–6290.

118. Eckstein, A.; Suhm, J.; Friedrich, C.; Maier, R.-D.; Sassmannshausen, J.; Bochmann, M.; Mülhaupt, R. *Macromolecules* **1998**, *31*, 1335–1340.

119. Stadler, F. J.; Piel, C.; Klimke, K.; Kaschta, J.; Parkinson, M.; Wilhelm, M.; Kaminsky, W.; Münstedt, H. *Macromolecules* **2006**, *39*, 1474–1482.

120. Mavridis, H.; Shroff, R. N. *Polym. Eng. Sci.* **1992**, *32*, 1778–1791.

121. Stadler, F. J.; Gabriel, C.; Münstedt, H. *Macromol. Chem. Phys.* **2007**, *208*, 2449–2454.

122. Férec, J.; Heuzey, M.; Ausias, G.; Carreau, P. *J. Non-Newton Fluid* **2008**, *151*, 89 – 100.

123. Labiausse, V.; Hohler, R.; Cohen-Addad, S. *J. Rheol.* **2007**, *51*, 479–492.

124. Münstedt, H. *Soft Matter* **2011**, *7*, 2273–2283.

125. Stange, J.; Uhl, C.; Münstedt, H. *J. Rheol.* **2005**, *49*, 1059–1079.

126. Rolon-Garrido, V. H.; Zatloukal, M.; Wagner, M. H. *J. Rheol.* **2013**, *57*, 105–129.

127. Laun, H.; Münstedt, H. *Rheol. Acta* **1978**, *17*, 415–425.

128. Malmberg, A.; Gabriel, C.; Steffl, T.; Münstedt, H.; Lüfgren, B. *Macromolecules* **2002**, *35*, 1038–1048.

129. Hepperle, J.; Münstedt, H. *Rheol. Acta* **2006**, *45*, 717–727.

130. Iijima, S.; Ichihashi, T. *Nature* **1993**, *363*, 603–605.

131. Baughman, R. H.; Zakhidov, A. A.; de Heer, W. A. *Science* **2002**, *297*, 787–792.

132. Ajayan, P. M.; Schadler, L. S.; Giannaris, C.; Rubio, A. *Adv. Mater.* **2000**, *12*, 750–753.

133. Kharchenko, S. B.; Douglas, J. F.; Obrzut, J.; Grulke, E. A.; Migler, K. B. *Nat. Mater.* **2004**, *3*, 1476–1122.

134. Huxtable, S. T.; Cahill, D. G.; Shenogin, S.; Xue, L.; Ozisik, R.; Barone, P.; Usrey, M.; Strano, M. S.; Siddons, G.; Shim, M.; Keblinski, P. *Nat. Mater.* **2003**, *2*, 1476–1122.

135. Ramasubramaniam, R.; Chen, J.; Liu, H. *Appl. Phys. Lett.* **2003**, *83*, 2928–2930.

136. Terrones, M. *Annu. Rev. Mater. Sci.* **2003**, *33*, 419–501.

137. Kota, A. K.; Cipriano, B. H.; Duesterberg, M. K.; Gershon, A. L.; Powell, D.; Raghavan, S. R.; Bruck, H. A. *Macromolecules* **2007**, *40*, 7400–7406.

138. Kashiwagi, T.; Grulke, E.; Hilding, J.; Groth, K.; Harris, R.; Butler, K.; Shields, J.; Kharchenko, S.; Douglas, J. *Polymer* **2004**, *45*, 4227 – 4239.

139. Vigolo, B.; Coulon, C.; Maugey, M.; Zakri, C.; Poulin, P. *Science* **2005**, *309*, 920–923.

140. Sahimi, M. *Applications of percolation theory*; Taylor & Francis, 1994.

141. Huang, C.-L.; Wang, C. *Carbon* **2011**, *49*, 2334 – 2344.

142. Sun, G.; Chen, G.; Liu, Z.; Chen, M. *Carbon* **2010**, *48*, 1434 – 1440.

143. Du, F.; Scogna, R. C.; Zhou, W.; Brand, S.; Fischer, J. E.; Winey, K. I. *Macromolecules* **2004**, *37*, 9048–9055.

144. McNally, T.; Ptschke, P.; Halley, P.; Murphy, M.; Martin, D.; Bell, S. E.; Brennan, G. P.; Bein, D.; Lemoine, P.; Quinn, J. P. *Polymer* **2005**, *46*, 8222 – 8232.

145. Lee, S. H.; Kim, M. W.; Kim, S. H.; Youn, J. R. *Eur. Polym. J.* **2008**, *44*, 1620 – 1630.

146. Winter, H.; Mours, M. *Neutron Spin Echo Spectroscopy Viscoelasticity Rheology*; Advances in Polymer Science; Springer Berlin Heidelberg, 1997; Vol. 134; pp 165–234.

147. Alig, I.; Lellinger, D.; Dudkin, S. M.; Ptschke, P. *Polymer* **2007**, *48*, 1020 – 1029.

148. Skipa, T.; Lellinger, D.; Bhm, W.; Saphiannikova, M.; Alig, I. *Polymer* **2010**, *51*, 201 – 210.

149. Alig, I.; Lellinger, D.; Engel, M.; Skipa, T.; Ptschke, P. *Polymer* **2008**, *49*, 1902 – 1909.

150. Alig, I.; Skipa, T.; Lellinger, D.; Ptschke, P. *Polymer* **2008**, *49*, 3524 – 3532.

151. Lim, H. T.; Ahn, K. H.; Hong, J. S.; Hyun, K. *J. Rheol.* **2013**, *57*, 767–789.

152. Hassanabadi, H. M.; Abbasi, M.; Wilhelm, M.; Rodrigue, D. *J. Rheol.* **2013**, *57*, 881–899.

153. Lebedkin, S.; Schweiss, P.; Renker, B.; Malik, S.; Hennrich, F.; Neumaier, M.; Stoermer, C.; Kappes, M. M. *Carbon* **2002**, *40*, 417 – 423.

154. Cipiriano, B. H.; Kashiwagi, T.; Raghavan, S. R.; Yang, Y.; Grulke, E. A.; Yamamoto, K.; Shields, J. R.; Douglas, J. F. *Polymer* **2007**, *48*, 6086 – 6096.

155. Langer, R.; Vacanti, J. *Science* **1993**, *260*, 920–926.

156. Griffith, L. G.; Naughton, G. *Science* **2002**, *295*, 1009–1014.

157. Macchiarini, P.; Jungebluth, P.; Go, T.; Asnaghi, M. A.; Rees, L. E.; Cogan, T. A.; Dodson, A.; Martorell, J.; Bellini, S.; Parnigotto, P. P.; Dickinson, S. C.; Hollander, A. P.; Mantero, S.; Conconi, M. T.; Birchall, M. A. *The Lancet* **2008**, *372*, 2023 – 2030.

158. Pham, C.; Greenwood, J.; Cleland, H.; Woodruff, P.; Maddern, G. *Burns* **2007**, *33*, 946 – 957.

159. Atala, A.; Bauer, S. B.; Soker, S.; Yoo, J. J.; Retik, A. B. *The Lancet* **2006**, *367*, 1241 – 1246.

160. Cen, L.; Liu, W.; Cui, L.; Zhang, W.; Cao, Y. *Pediatric res.* **2008**, *63*, 492–496.

161. Dvir, T.; Timko, B. P.; Kohane, D. S.; Langer, R. *Nat. Nanotech.* **2011**, *6*, 13–22.

162. Hartgerink, J. D.; Beniash, E.; Stupp, S. I. *Science* **2001**, *294*, 1684–1688.

163. Yang, Y.; Bolikal, D.; Becker, M. L.; Kohn, J.; Zeiger, D. N.; Simon, C. G. *Adv. Mater.* **2008**, *20*, 2037–2043.

164. Dehghani, F.; Annabi, N. *Curr. Opin. Biotechnol.* **2011**, *22*, 661–666.

165. Liu, X.; Smith, L. A.; Hu, J.; Ma, P. X. *Biomaterials* **2009**, *30*, 2252 – 2258.

166. Hollister, S. J. *Nat. Mater.* **2005**, *4*, 518–524.

167. Prabhakaran, M. P.; Ghasemi-Mobarakeh, L.; Ramakrishna, S. *J. nanosci. nanotech.* **2011**, *11*, 3039–3057.

168. Taylor, G. I. *Proc. R. Soc. London, Ser.A* **1964**, *280*, 383–397.

169. Han, T.; Reneker, D. H.; Yarin, A. L. *Polymer* **2007**, *48*, 6064 – 6076.

170. Reneker, D. H.; Yarin, A. L.; Fong, H.; Koombhongse, S. *J. Appl. Phys.* **2000**, *87*, 4531–4547.

171. Yarin, A. L.; Koombhongse, S.; Reneker, D. H. *J. Appl. Phys.* **2001**, *89*, 3018–3026.

172. Xin, Y.; Reneker, D. H. *Polymer* **2012**, *53*, 3629 – 3635.

173. Liu, K.; Ertley, C. D.; Reneker, D. H. *Polymer* **2012**, *53*, 4241 – 4253.

174. Shin, Y. M.; Hohman, M. M.; Brenner, M. P.; Rutledge, G. C. *Appl. Phys. Lett.* **2001**, *78*, 1149–1151.

175. Yarin, A. L.; Kataphinan, W.; Reneker, D. H. *J. Appl. Phys.* **2005**, *98*, 64501–64511.

176. Dzenis, Y. *Science* **2004**, *304*, 1917–1919.

177. Fridrikh, S. V.; Yu, J. H.; Brenner, M. P.; Rutledge, G. C. *Phys. Rev. Lett.* **2003**, *90*, 144502.

178. Yu, J. H.; Fridrikh, S. V.; Rutledge, G. C. *Polymer* **2006**, *47*, 4789 – 4797.

179. Shenoy, S. L.; Bates, W. D.; Frisch, H. L.; Wnek, G. E. *Polymer* **2005**, *46*, 3372 – 3384.

180. Deitzel, J.; Kleinmeyer, J.; Harris, D.; Tan, N. B. *Polymer* **2001**, *42*, 261 – 272.

181. McKee, M. G.; Wilkes, G. L.; Colby, R. H.; Long, T. E. *Macromolecules* **2004**, *37*, 1760–1767.

182. Pornsopone, V.; Supaphol, P.; Rangkupan, R.; Tantayanon, S. *Polym. Eng. Sci.* **2005**, *45*, 1073–1080.

183. Subbiah, T.; Bhat, G. S.; Tock, R. W.; Parameswaran, S.; Ramkumar, S. S. *J. Appl. Polym. Sci.* **2005**, *96*, 557–569.

184. Demir, M.; Yilgor, I.; Yilgor, E.; Erman, B. *Polymer* **2002**, *43*, 3303 – 3309.

185. Zong, X.; Kim, K.; Fang, D.; Ran, S.; Hsiao, B. S.; Chu, B. *Polymer* **2002**, *43*, 4403 – 4412.

186. He, J.-H.; Wan, Y.-Q.; Yu, J.-Y. *Fibers Polym.* **2008**, *9*, 140–142.

187. Jarusuwannapoom, T.; Hongrojjanawiwat, W.; Jitjaicham, S.; Wannatong, L.; Nithitanakul, M.; Pattamaprom, C.; Koombhongse, P.; Rangkupan, R.; Supaphol, P. *Eur. Polym. J.* **2005**, *41*, 409 – 421.

188. Son, W. K.; Youk, J. H.; Lee, T. S.; Park, W. H. *Polymer* **2004**, *45*, 2959 – 2966.

189. Lee, K.; Kim, H.; Khil, M.; Ra, Y.; Lee, D. *Polymer* **2003**, *44*, 1287 – 1294.

190. Jung, Y.; Kim, H.; Lee, D.; Park, S.; Khil, M. *Macromol. Res.* **2005**, *13*, 385–390.

191. Zeng, J.; Xu, X.; Chen, X.; Liang, Q.; Bian, X.; Yang, L.; Jing, X. *J. Controlled Release* **2003**, *92*, 227 – 231.

192. Choi, J. S.; Lee, S. W.; Jeong, L.; Bae, S.-H.; Min, B. C.; Youk, J. H.; Park, W. H. *Int. J. Biol. Macromol.* **2004**, *34*, 249 – 256.

193. Kim, S. J.; Lee, C. K.; Kim, S. I. *J. Appl. Polym. Sci.* **2005**, *96*, 1388–1393.

194. Aussawasathien, D.; Dong, J.-H.; Dai, L. *Synth. Met.* **2005**, *154*, 37 – 40.

195. Norris, I. D.; Shaker, M. M.; Ko, F. K.; MacDiarmid, A. G. *Synth. Met.* **2000**, *114*, 109 – 114.

196. McKee, M. G.; Hunley, M. T.; Layman, J. M.; Long, T. E. *Macromolecules* **2006**, *39*, 575–583.

197. Duan, B.; Dong, C.; Yuan, X.; Yao, K. *J. Appl. Polym. Sci.* **2004**, *15*, 797–811.

198. Ki, C. S.; Baek, D. H.; Gang, K. D.; Lee, K. H.; Um, I. C.; Park, Y. H. *Polymer* **2005**, *46*, 5094 – 5102.

199. Son, W. K.; Youk, J. H.; Lee, T. S.; Park, W. H. *Polymer* **2004**, *45*, 2959 – 2966.

200. Hsu, C.-M.; Shivkumar, S. *Macromol. Mater. Eng.* **2004**, *289*, 334–340.

201. Lee, K.; Kim, H.; Khil, M.; Ra, Y.; Lee, D. *Polymer* **2003**, *44*, 1287 – 1294.

202. Lee, K.; Kim, H.; Bang, H.; Jung, Y.; Lee, S. *Polymer* **2003**, *44*, 4029 – 4034.

203. Lee, K. H.; Kim, H. Y.; La, Y. M.; Lee, D. R.; Sung, N. H. *J. Polym. Sci., Part B: Polym. Phys.* **2002**, *40*, 2259–2268.

204. Wannatong, L.; Sirivat, A.; Supaphol, P. *Polym. Int.* **2004**, *53*, 1851–1859.

205. Celebioglu, A.; Uyar, T. *Mater. Lett.* **2011**, *65*, 2291 – 2294.

206. Beachley, V.; Wen, X. *Mater. Sci. Eng., C* **2009**, *29*, 663 – 668.

207. Megelski, S.; Stephens, J. S.; Chase, D. B.; Rabolt, J. F. *Macromolecules* **2002**, *35*, 8456–8466.

208. Wang, C.; Hsu, C.-H.; Lin, J.-H. *Macromolecules* **2006**, *39*, 7662–7672.

209. Pawlowski, K.; Belvin, H.; Raney, D.; Su, J.; Harrison, J.; Siochi, E. *Polymer* **2003**, *44*, 1309 – 1314.

210. Zhao, S.; Wu, X.; Wang, L.; Huang, Y. *J. Appl. Polym. Sci.* **2004**, *91*, 242–246.

211. Krishnappa, R.; Desai, K.; Sung, C. *J. Mater. Sci.* **2003**, *38*, 2357–2365.

212. Theron, S.; Zussman, E.; Yarin, A. *Polymer* **2004**, *45*, 2017 – 2030.

213. Ayutsede, J.; Gandhi, M.; Sukigara, S.; Micklus, M.; Chen, H.-E.; Ko, F. *Polymer* **2005**, *46*, 1625 – 1634.

214. Lee, J. S.; Choi, K. H.; Ghim, H. D.; Kim, S. S.; Chun, D. H.; Kim, H. Y.; Lyoo, W. S. *J. Appl. Polym. Sci.* **2004**, *93*, 1638–1646.

215. Hardick, O.; Stevens, B.; Bracewell, D. *J. Mater. Sci.* **2011**, *46*, 3890–3898.

216. Baumgarten, P. K. *J. Colloid Interface Sci.* **1971**, *36*, 71 – 79.

217. Yang, Y.; Jia, Z.; Li, Q.; Guan, Z. *Dielectrics and Electrical Insulation, IEEE Transactions on* **2006**, *13*, 580 –585.

218. Casper, C. L.; Stephens, J. S.; Tassi, N. G.; Chase, D. B.; Rabolt, J. F. *Macromolecules* **2004**, *37*, 573–578.

219. Katta, P.; Alessandro, M.; Ramsier, R. D.; Chase, G. G. *Nano Lett.* **2004**, *4*, 2215–2218.

220. Carnell, L. S.; Siochi, E. J.; Holloway, N. M.; Stephens, R. M.; Rhim, C.; Niklason, L. E.; Clark, R. L. *Macromolecules* **2008**, *41*, 5345–5349.

221. Li, D.; Ouyang, G.; McCann, J. T.; Xia, Y. *Nano Lett.* **2005**, *5*, 913–916.

222. Ding, Z.; Salim, A.; Ziaie, B. *Langmuir* **2009**, *25*, 9648–9652.

223. Dempsey, D. K.; Schwartz, C. J.; Ward, R. S.; Iyer, A. V.; Parakka, J. P.; Cosgriff-Hernandez, E. M. *Macromol. Mater. Eng.* **2010**, *295*, 990–994.

224. Lavielle, N.; Hbraud, A.; Mendoza-Palomares, C.; Ferrand, A.; Benkirane-Jessel, N.; Schlatter, G. *Macromol. Mater. Eng.* **2012**, *297*, 958–968.

225. Kameoka, J.; Orth, R.; Yang, Y.; Czaplewski, D.; Mathers, R.; Coates, G. W.; Craighead, H. G. *Nanotechnology* **2003**, *14*, 1124.

226. Chang, C.; Limkrailassiri, K.; Lin, L. *Appl. Phys. Lett.* **2008**, *93*, 123111.

227. Whitesides, G. M.; Grzybowski, B. *Science* **2002**, *295*, 2418–2421.

228. Deitzel, J.; Kleinmeyer, J.; Harris, D.; Tan, N. B. *Polymer* **2001**, *42*, 261 – 272.

229. Thandavamoorthy, S.; Gopinath, N.; Ramkumar, S. S. *J. Appl. Polym. Sci.* **2006**, *101*, 3121–3124.

230. Yan, G.; Yu, J.; Qiu, Y.; Yi, X.; Lu, J.; Zhou, X.; Bai, X. *Langmuir* **2011**, *27*, 4285–4289.

231. Sun, B.; Long, Y. .; Yu, F.; Li, M. .; Zhang, H. .; Li, W. .; Xu, T. . *Nanoscale* **2012**, *4*, 2134–2137.

232. Bonino, C. A.; Efimenko, K.; Jeong, S. I.; Krebs, M. D.; Alsberg, E.; Khan, S. A. *Small* **2012**, *8*, 1928–1936.

233. Kim, H.-Y.; Lee, M.; Park, K. J.; Kim, S.; Mahadevan, L. *Nano Lett.* **2010**, *10*, 2138–2140.

234. Blakeney, B. A.; Tambralli, A.; Anderson, J. M.; Andukuri, A.; Lim, D.-J.; Dean, D. R.; Jun, H.-W. *Biomaterials* **2011**, *32*, 1583 – 1590.

235. Tzezana, R.; Zussman, E.; Levenberg, S. *Tissue Eng.* **2008**, *14*, 281–288.

236. Cleveland, W. S.; Devlin, S. J. *J. Am. Stat. Assoc.* **1988**, *83*, 596–610.

237. Yoshizawa, K.; Okuzono, T.; Koga, T.; Taniji, T.; Yamanaka, J. *Langmuir* **2011**, *27*, 13420–13427.

238. Stavans, J. *Phys. Rev. A* **1990**, *42*, 5049–5051.

239. Ding, Z.; Salim, A.; Ziaie, B. *Langmuir* **2009**, *25*, 9648–9652.

240. Lavielle, N.; Hbraud, A.; Mendoza-Palomares, C.; Ferrand, A.; Benkirane-Jessel, N.; Schlatter, G. *Macromol. Mater. Eng.* **2012**, *297*, 958–968.

241. Gibson, L. J. *J. Biomech.* **2005**, *38*, 377 – 399.

242. Harley, B. A.; Hastings, A. Z.; Yannas, I. V.; Sannino, A. *Biomaterials* **2006**, *27*, 866 – 874.

243. Woodfield, T. B. F.; Van Blitterswijk, C. A.; De Wijn, J.; Sims, T. J.; Hollander, A. P.; Riesle, J. *Tissue Eng.* **2005**, *11*, 1297–1311.

244. Schwarz, K.; Epple, M. *Macromol. Rapid Commun.* **1998**, *19*, 613–617.

245. Oh, S. H.; Park, I. K.; Kim, J. M.; Lee, J. H. *Biomaterials* **2007**, *28*, 1664 – 1671.

246. Ji, W.; Sun, Y.; Yang, F.; Beucken, J.; Fan, M.; Chen, Z.; Jansen, J. *Pharmaceutical Research* **2011**, *28*, 1259–1272.

247. Mendoza-Palomares, C.; Ferrand, A.; Facca, S.; Fioretti, F.; Ladam, G.; Kuchler-Bopp, S.; Regnier, T.; Mainard, D.; Benkirane-Jessel, N. *ACS Nano* **2012**, *6*, 483–490.

248. Dalton, P. D.; Klinkhammer, K.; Salber, J.; Klee, D.; Mller, M. *Biomacromolecules* **2006**, *7*, 686–690.

249. Pham, Q. P.; Sharma, U.; Mikos, A. G. *Biomacromolecules* **2006**, *7*, 2796–2805, PMID: 17025355.

250. Larrondo, L.; St. John Manley, R. *J. Polym. Sci., Part B: Polym. Phys.* **1981**, *19*, 909–920.

251. Larrondo, L.; St. John Manley, R. *J. Polym. Sci., Part B: Polym. Phys.* **1981**, *19*, 921–932.

252. Lyons, J.; Ko, F. *Polym. News* **2005**, *30*, 170–178.

253. Dalton, P. D.; Grafahrend, D.; Klinkhammer, K.; Klee, D.; Müller, M. *Polymer* **2007**, *48*, 6823 – 6833.

254. Li, X.; Liu, H.; Wang, J.; Li, C. *Mater. Lett.* **2012**, *73*, 103 – 106.

255. Zhao, N.; Liu, T.; Liu, R. **2012**, *512-515*, 2424–2427.

256. Detta, N.; Brown, T. D.; Edin, F. K.; Albrecht, K.; Chiellini, F.; Chiellini, E.; Dalton, P. D.; Hutmacher, D. W. *Polym. Int.* **2010**, *59*, 1558–1562.

257. Li, X.; Liu, H.; Wang, J.; Li, C. *Polymer* **2012**, *53*, 248 – 253.

258. Zhmayev, E.; Cho, D.; Joo, Y. L. *Polymer* **2010**, *51*, 4140 – 4144.

259. Li, X.; Liu, H.; Wang, J.; Li, C. *Mater. Lett.* **2012**, *73*, 103–106.

260. Karchin, A.; Simonovsky, F. I.; Ratner, B. D.; Sanders, J. E. *Acta Biomater.* **2011**, *7*, 3277–3284.

261. Wang, X. .; Huang, Z. . *Chin. J. Polym. Sci.* **2010**, *28*, 45–53.

262. Hutmacher, D. W.; Dalton, P. D. *Chem. Asian J.* **2011**, *6*, 44–56.

263. Zussman, E.; Rittel, D.; Yarin, A. L. *Appl. Phys. Lett.* **2003**, *82*, 3958–3960.

264. Yoshioka, T.; Dersch, R.; Greiner, A.; Tsuji, M.; Schaper, A. K. *Macromol. Mater. Eng.* **2010**, *295*, 1082–1089.

265. Ye, H.; Lam, H.; Titchenal, N.; Gogotsi, Y.; Ko, F. *Appl. Phys. Lett.* **2004**, *85*, 1775–1777.

266. Dalton, P. D.; Grafahrend, D.; Klinkhammer, K.; Klee, D.; Mller, M. *Polymer* **2007**, *48*, 6823 – 6833.

267. Li, X.; Liu, H.; Wang, J.; Li, C. *Polymer* **2012**, *53*, 248 – 253.

268. Lyons, J.; Li, C.; Ko, F. *Polymer* **2004**, *45*, 7597 – 7603.

269. Hunley, M. T.; Karikari, A. S.; McKee, M. G.; Mather, B. D.; Layman, J. M.; Fornof, A. R.; Long, T. E. *Macromol. Symp.* **2008**, *270*, 1–7.

270. http://rsbweb.nih.gov/ij/,.

271. Zhou, H.; Green, T. B.; Joo, Y. L. *Polymer* **2006**, *47*, 7497 – 7505.

272. Tian, S.; Ogata, N.; Shimada, N.; Nakane, K.; Ogihara, T.; Yu, M. *J. Appl. Polym. Sci.* **2009**, *113*, 1282–1288.

273. Wang, X.-f.; Huang, Z.-m. *Chin. J. Polym. Sci.* **2010**, *28*, 45–53.

274. Nayak, R.; Padhye, R.; Kyratzis, I. L.; Truong, Y. B.; Arnold, L. *Textile Res. J.* **2013**, *83*, 606–617.

275. Pearson, D. S.; Rochefort, W. E. *J. Polym. Sci., Part B: Polym. Phys.* **1982**, *20*, 83–98.

276. Cox, W. P.; Merz, E. H. *J. Poly. Sci.* **1958**, *28*, 619–622.

277. Laun, H. M. *J. Rheol.* **1986**, *30*, 459–501.

278. Winter, H. *Rheol. Acta* **2009**, *48*, 241–243.

279. Venkatraman, S.; Okano, M. *Polym. Eng. Sci.* **1990**, *30*, 308–313.

280. Stadler, F.; Leygue, A.; Burhin, H.; Bailly, C. *235th ACS National Meeting* **2008**, *49*, 121–122.

281. Ewoldt, R.; McKinley, G. *Rheol. Acta* **2010**, *49*, 213–219.

Acknowledgments

I am extremely grateful to my supervisors Prof. Dr. Guy Schlatter and Prof. Dr. Manfred Wilhelm for their help, support and guidance during my PhD. I have benefitted greatly by their inputs into my research. I also acknowledge their emphasis on applying the gained knowledge during the PhD to industry by providing me an opportunity for an internship at Unilever PortSunlight United Kingdom. They always promoted me to present my research work at several conferences. I owe a large debt of gratitude to Prof. Dr. Norbert Willenbacher for his external supervision. I also owe a large debt of gratitude to Dr. Anne Hébraud for many useful discussion regarding the research related to electrospinning. I would like to extend my gratitude to Dr. Susana Filipe from Borealis Linz, Austria, Dr. Humberto Palza from the University of Chile, and Dr. Michael Kempf from 3M for providing me the polymeric materials for rheological characterization.

I am grateful to Prof. Dr. Kyu Hyun for helping me understand the Fourier Transform (FT) Rheology. I would like to thank Prof. Dr. Markus Busch for providing me the facilities to perform high temperature GPC measurements on polyethylene blends. I would like to extend my special thanks to Dr. Thomas Meins, Dr. Ingo Naue, and Dr. Kathrin Reinheimer for making me comfortable, when I arrived here at the start of my PhD. I am grateful to all my wonderful group members for numerous discussion related to my research. My special thanks to Dr. Jennifer Kubel and Dr. Roland Kadar for so many wonderful discussion and being the best office buddy. I also like to extend my special thanks to Ms. Sabine Weiland for helping me with all the administrative work and being so nice to me.

Curriculum Vitae

- **Name:** Deepak Ahirwal
- **Date of Birth:** 04/06/1984
- **Place of Birth:** Datiya, India
- **Nationality:** Indian

Education:

- **Dual Degree [B.Tech (Bachelor Degree) + M.Tech (Master Degree)]**: Indian Institute of Technology Bombay, India [July 2004- Aug. 2009]
- **Doctor of Philosophy**: Department of Chemical Engineering, Karlsruhe Institute of Technology, Germany [Oct. 2009- Aug. 2013]
- **Doctor of Philosophy**: Institute of Chemistry and Processes for the Energy, Environment and Health, University of Strasbourg, France [Oct. 2009- Aug. 2013]

Internships:

- Unilever PortSunlight, United Kingdom [Nov. 2011- Feb. 2012]
- Lyondelbasell Frankfurt, Germany [June 2008]
- IRC Polymer Leeds, United Kingdom [May 2007 - July 2007]